

Laboratório
Nacional de
Computação
Científica

Graduate program in Computational Modeling

**From medical image processing to in-vivo
mechanical characterization: A framework based
on IVUS studies**

By

Gonzalo Daniel Maso Talou

PETRÓPOLIS, RJ - BRASIL

MARCH, 2017

FROM MEDICAL IMAGE PROCESSING TO IN-VIVO MECHANICAL
CHARACTERIZATION: A FRAMEWORK BASED ON IVUS STUDIES

Gonzalo Daniel Maso Talou

TESE SUBMETIDA AO CORPO DOCENTE DA COORDENAÇÃO DE FORMAÇÃO
DE RECURSOS HUMANOS DO LABORATÓRIO NACIONAL DE COMPUTAÇÃO
CIENTÍFICA COMO PARTE DOS REQUISITOS NECESSÁRIOS PARA A
OBTENÇÃO DO GRAU DE DOUTOR EM MODELAGEM COMPUTACIONAL.

D.SC.

Aprovado por:

Prof. Pablo Javier Blanco, D.Sc. (PRESIDENTE)

Prof. Eduardo Alberto Fancello, D.Sc.

Prof. Carlos Augusto Homem de Magalhães Campos, Ph.D.

Prof. Antonio André Novotny, D.Sc.

Prof. Gilson Antônio Giraldi, D.Sc.

PETRÓPOLIS, RJ - BRASIL

MARCH, 2017

M398m Maso Talou, Gonzalo Daniel
From medical image processing to in-vivo mechanical characterization: A framework based on IVUS studies / Gonzalo Daniel Maso Talou. Petrópolis, RJ. : Laboratório Nacional de Computação Científica, 2017.
xxv, 216 p. : il.; 29.7 cm
Orientador: Pablo Javier Blanco
Co-Orientador: Raúl Antonino Feijóo
Tese (D.Sc.) – Laboratório Nacional de Computação Científica, 2017.
1. Image processing 2. IVUS 3. Cardiovascular diseases - Diagnostic
4. Inverse Problem I. Blanco, Pablo Javier II. MCT/LNCC III. From medical image processing to in-vivo mechanical characterization: A framework based on IVUS studies

CDD – 616.075 4

Resumo da tese submetida à Coordenação de Pós-Graduação do Laboratório Nacional de Computação Científica - LNCC/MCT como parte dos requisitos necessários para a obtenção do grau de Doutor em Ciências (D.Sc.)

DESDE O PROCESSAMENTO DE IMAGENS MÉDICAS ATÉ A CHARACTERIZAÇÃO IN-VIVO DAS PROPRIEDADES MECÂNICAS: UM FRAMEWORK BASEADO EM ESTUDOS IVUS.

Gonzalo Daniel Maso Talou

Março, 2017

Orientadores: Pablo Javier Blanco, Diretor de Tese
Raúl Antonino Feijóo, Co-Diretor de Tese

As doenças cardiovasculares são a principal causa de mortalidade e morbidade em todo o mundo, principalmente devido a acidentes vasculares tais como infarto de miocárdio e acidente cerebro-vascular. O entendimento da gênese, progressão e comportamento de tais doenças é fundamental para um eficaz diagnóstico, tratamento e avaliação de risco cirúrgico. Grandes avanços foram realizados na caracterização histológica da placa vulnerável que conduz a acidentes vasculares, embora as técnicas in-vivo para a visualização da mesma ainda constituam uma área de investigação extremamente activa.

Neste trabalho é proposta uma metodologia para estudar a caracterização in-vivo dos tecidos da parede arterial. Esta metodologia envolve: novos métodos de aprimoramento de imagens médicas (gating, registro e redução de ruído para imagens de ultrassom de alta frequência) e estimativa de fluxo óptico; modelos mecânicos detalhados para artérias coronárias; e um método eficiente de assimilação de dados para a caracterização de tecidos. A tese é dividida em três partes: i) processamento de imagens médicas; ii) estimação de parâmetros de material e iii) aplicações médicas. Particularmente, este trabalho foca-se no uso do ultrassom intravascular (IVUS) como técnica de imagens médicas, embora a segunda parte do manuscrito é suficientemente genérica para ser estendida para outros tipos de imagens médicas.

Na primeira parte, são apresentados diferentes métodos para melhorar e recuperar de medidas de deformações e descrição espacial das estruturas anatômicas dos vasos arteriais. Propõe-se um novo método de gating para extrair a descrição do vaso em cada instante do ciclo cardíaco. Devido ao movimento intrínseco dos sensores durante a aquisição da imagem de ultrassom, propomos um método de registro que corrige este deslocamento no plano transversal e no eixo axial de aquisição. Para melhorar a relação sinal-ruído das imagens geradas, propõe-se um método de redução de ruído baseado na estatística do ruído “speckle” (ruído intrínseco do ultrassom), que supera as estratégias clássicas de redução de ruído presentes na literatura. Usando os três métodos anteriores, apresentamos uma metodologia para estimar o fluxo óptico da seção transversal do vaso durante o ciclo cardíaco.

Na segunda parte, apresentamos um resumo do estado da arte sobre a anatomia arterial e o comportamento mecânico da parede arterial, com especial ênfase nas artérias coronárias. Assim, descrevemos a fisiopatologia da aterosclerose e as alterações mecânicas nos tecidos dos vasos afetados. Em seguida, o problema de caracterização de tecidos é abordado, estimando os parâmetros constitutivos de modelos mecânicos para tecidos arteriais via filtros de Kalman. Utilizando dados experimentais de espécimens ex-vivo e modelos

constitutivos apropriados, estuda-se a configuração do filtro de Kalman e avalia-se a capacidade da estratégia proposta para a estimação de tecidos. Por último, são empregadas técnicas de fluxo óptico desenvolvidas na primeira parte, para abordar a caracterização dos tecidos in-vivo.

A terceira parte da tese apresenta uma contribuição obtida com as técnicas desenvolvidas na primeira parte deste trabalho. Realiza-se uma comparação multimodal para a geração de modelos geométricos arteriais a partir de imagens médicas. Especificamente, comparamos a tomografia coronariana computadorizada (CCTA) versus a angiografia coronariana fundida com ultrassom intravascular em termos de descritores geométricos e índices hemodinâmicos derivados dos modelos geométricos. Neste estudo são empregadas técnicas de gating e registro para obter uma correta descrição geométrica dos vasos.

Abstract of a thesis submitted to the Postgraduate Department of the National Laboratory for Scientific Computing - LNCC/MCT as a partial fulfilment of the requirements for the degree of Doctor in Sciences (D.Sc.)

FROM MEDICAL IMAGE PROCESSING TO IN-VIVO MECHANICAL CHARACTERIZATION: A FRAMEWORK BASED ON IVUS STUDIES

Gonzalo Daniel Maso Talou

March, 2017

Advisors: Pablo Javier Blanco, Thesis Advisor
Raúl Antonino Feijóo, Thesis Co-Advisor

Cardiovascular diseases are the principal cause of mortality and morbidity worldwide mostly due to myocardial infarction and stroke. The understanding of the genesis, development and progression of such diseases is key for effective diagnosis, treatment and surgical risk assessment. Notorious advances have been performed in the histological characterization of culprit plaque for such events, although in-vivo techniques for tissue characterization still comprise an extremely active area of research.

In this work, a framework is proposed targeting the in-vivo characterization of the arterial wall tissues. The set of methodologies involves: novel image processing methods for medical image enhancement (gating, registration and denoising of high frequency ultrasonic images) and optical flow estimation; detailed mechanical models for coronary arteries; and an efficient data assimilation method for tissue characterization. The thesis is structured in three parts: i) medical image processing; ii) material parameter estimation and iii) medical applications. Particularly, this work makes use of Intravascular Ultrasound (IVUS) as medical image acquisition technique, even though, the second part of the thesis is generic and can be straightforwardly extended to other imaging techniques.

In the first part, different methods are presented to enhance and retrieve data of arterial vessel deformations and spatial description of anatomical structures. A novel gating method is proposed to obtain the vessel description at each instant along the cardiac cycle. Due to the intrinsic motion of the sensors during the image acquisition, we propose a registration method that corrects the sensor displacement in the transversal plane of acquisition and along the axis of the vessel. To improve the signal-to-noise ratio of the ultrasound, we propose a denoising method based on the speckle noise (ultrasound characteristic noise) statistics which outperforms classic denoising strategies. Using the three previous methods, we present a methodology to obtain the optical flow of the vessel cross-section during the whole cardiac cycle.

In the second part, we scrutinize state-of-the-art literature about the arterial anatomy and mechanical behavior of the arterial wall with particular focus on coronary arteries. Hence, we describe the pathophysiology of the atherosclerosis and the mechanical alterations of the components of the tissues in affected vessels. Then, the tissue characterization problem is addressed by estimating the constitutive parameters of constitutive mechanical models for arterial tissues with a reduced-order unscented Kalman filter. Using the surveyed data and adequate constitutive models, the appropriate setup for the data assimilation problem is studied, and the capabilities of the proposed strategy for tissue estimation are assessed. Then, optical flow techniques are employed to characterize the tissues in-vivo.

The third part of the thesis presents a side contribution related to the first part of this work,

that is a multimodality comparison for the generation of geometric arterial models from medical images. Specifically, we compare coronary computed tomography angiography (CCTA) versus coronary angiography fused with intravascular ultrasound in terms of geometric descriptors and hemodynamic indexes derived from the geometric models. In such study the gating and registration techniques developed in the first part of the thesis are employed.

Preface

The current manuscript is the culmination of the challenging, gratifying and inspiring work performed in the last 6 years, including my master and doctoral programs at the National Laboratory for Scientific Computing (LNCC). Since my admission, my knowledge in computer science was complemented with applied mathematics, mechanical engineering and medicine topics which helped me to understand science as a unity of knowledge instead of a tree of disassociated specialties and specialists. For this unbounded vision of science as well as for a large academic and personal growing, is that I gratefully acknowledge my advisors, Prof. Pablo Blanco and Prof. Raúl Feijóo, who also imparted the vocation and passion for what we do. I am deeply indebted for all time shared with them in discussions, reviews and lessons with incredible disposition and willingness. Hence, I thank the other members of the HeMoLab group, such as Gonzalo Ares, Carlos Bulant, Lucas Mueller, Felipe Figueredo, Alonso Álvarez, Mario Sansuke, Rafael Bomfim, Daniel Golbert and Paulo Trenhago, who shared their expertises and researches, along personal talks and seminars. All in all, I am specially grateful to Gonzalo Ares, Lucas Mueller, Carlos Bulant and Pablo Blanco for the daily discussions, opinions, team-work, patience and friendship along these years and through the endeavors of the theses and publications.

Related to the medical insights and knowledge acquired along this work, I would like to thank to Dr. Pedro Lemos and Dr. Cristiano Bezerra for receiving me in several occasions and dedicating their time during the stressful routine at Incor and Sírio Libanês health centers. Their dedication in clinical work, professionalism and desire to improve medicine through research, multi-disciplinarity and cross-functional knowledge is an important motivation for this thesis as well. Their contributions, teachings and peer-reviewing endowed this manuscript with a stronger medical background towards clinical needs and practices.

It is an important contribution to this thesis the support and affect of my close friends and family. As foreigner who is far away from his family, those personal spheres are daily intertwined where friends have a stronger and family-like bond. For this, I would like to thank my big Petropolitan family, Carlos, Lis, Gonzalo, Carla, Lucas, Wenddi, Serena, Pablo, Mariela, Benjamin and Valentina, for the happy moments, emotional support and unconditional friendship. I thank my loving parents and brother for the countless hours of Skype, cheering my goals and efforts that they made possible. Finally, I am deeply grateful to my girlfriend Camila, for being always by my side in each endeavor of life, for her friendship, patience and love.

GONZALO D. MASO TALOU
MARCH 2017, PETRÓPOLIS, RJ - BRAZIL

para mis padres

"Be the change that you wish to see in the world."

— *Mohandas K. Gandhi (1869-1948)*

Contents

Preface	ix
List of symbols and abbreviations	xix
1 Introduction	1
1.1 Motivation	1
1.1.1 The worldwide impact of cardiovascular diseases	1
1.1.2 Silent diseases and prognosis uncertainty	2
1.1.3 Challenges in diagnosis, risk assessment and treatment	3
1.2 State-of-the-art in in-vivo characterization of the vessel wall	4
1.3 Aims and goals	6
1.4 Structure of the thesis	7
I Image processing of IVUS studies	9
2 Gating	11
2.1 Background	11
2.2 Methodology	12
2.2.1 Integration of motion signals	12
2.2.2 Cardiac phase identification	14
2.2.3 Decomposition in cardiac phases	16
2.2.4 Parameter setup	17
2.2.4.1 Parameter α	17
2.2.4.2 Parameter δ	18
2.3 Results	18
2.3.1 Acquisition of IVUS studies	18
2.3.2 Features correlation	20
2.3.3 Error measurements	20
2.3.4 Method performance	21
2.3.5 Mean cardiac frequency estimation	24
2.3.6 Gating comparison	25
2.3.7 Computational cost	26
2.3.8 Limitations	26
2.4 Final remarks	27
3 Spatio-temporal registration	29
3.1 Background	29
3.2 Methodology	31
3.2.1 IVUS preprocessing	31
3.2.2 Maximum likelihood estimator for block matching	32
3.2.2.1 Normalized cross-correlation estimator	33
3.2.2.2 Rayleigh noise estimator	34

3.2.2.3	Generalized Gamma noise estimator	35
3.2.3	Transversal registration	36
3.2.4	Longitudinal registration	38
3.2.5	Numerical strategies	41
3.2.5.1	DLT implementation	42
3.2.5.2	DTL implementation	42
3.2.5.3	Coupled implementation	42
3.3	Results	43
3.3.1	Acquisition of IVUS studies	43
3.3.2	Computational cost	43
3.3.3	Validation of transversal registration	46
3.3.4	Validation of longitudinal registration	47
3.3.5	Longitudinal motion from <i>in-vivo</i> studies	52
3.3.6	Longitudinal motion characterization	54
3.4	Discussion	55
3.5	Final remarks	56
4	Denoising and optical flow	57
4.1	State-of-the-art in Optical Flow techniques	57
4.2	Despeckling of IVUS images	60
4.2.1	Total variation method	61
4.2.2	Maximum likelihood variation method	62
4.2.3	Parameter setup	66
4.3	Optical Flow methods	67
4.3.1	Horn-Schunck method (classic approach)	67
4.3.2	Farnebäck method	68
4.3.3	Zach method	69
4.3.4	Weickert method	70
4.3.4.1	Combining Global-Local (CGL)	70
4.3.4.2	Non-linear functions	71
4.3.4.3	Multi-resolution technique	71
4.3.4.4	Functional minimization	72
4.3.4.5	Numerical scheme	72
4.3.5	Comparative assessment for displacement field estimation	73
4.4	Performance analysis for IVUS tracking	76
4.4.1	Synthetic ring sequence	77
4.4.2	Synthetic artery sequence based on <i>in-vivo</i> scenario	81
4.4.2.1	Noiseless images	82
4.4.2.2	Speckled images	84
4.4.3	<i>In-vivo</i> artery sequence	87
4.5	Final remarks	88
II	Biomechanical characterization of the vessel wall	93
5	Anatomy and mechanical models	95
5.1	Arterial wall anatomy	95
5.1.1	Arterial wall architecture	96
5.1.2	Tunica intima	97
5.1.3	Tunica media	100
5.1.4	Tunica adventitia	101
5.1.5	Material behavior of vessel constituents	103

5.2	Atherosclerotic plaque anatomy	105
5.3	Mechanical models for the arterial wall	108
5.3.1	Preload problem	109
5.3.2	Forward problem	110
5.3.3	The preloaded forward problem	111
5.4	Constitutive models	111
5.4.1	Neo-Hookean material model	112
5.4.2	Neo-Hookean material model with collagen fibers	112
5.5	Coronary arteries settings	113
5.5.1	Model and physiological parameters	113
5.5.2	Model geometry	114
6	In-vivo estimation of biomechanical parameters	117
6.1	State-of-the-art in parameter estimation techniques	117
6.2	Kalman filters	119
6.2.1	Weighted least-square approximation	119
6.2.2	Kalman filter	122
6.2.3	Unscented Kalman filter	123
6.2.4	Reduced-order unscented Kalman filter (ROUKF)	125
6.3	Biomechanical parameter estimation with ROUKF	128
6.3.1	Initialization and tissue regions delimitation	130
6.3.2	ROUKF parameter setup	131
6.3.3	Media and adventitia modeling	135
6.4	Cases of study	138
6.4.1	Synthetic idealized artery	138
6.4.2	Synthetic artery with in-vivo geometry	141
6.4.3	In-vivo artery	146
6.5	Final remarks	146
III	Medical Applications	151
7	Geometric arterial models: IVUS vs. CCTA	153
7.1	Introduction	153
7.2	Methods	154
7.2.1	Study population	154
7.2.2	Acquisition and processing of medical images	155
7.2.2.1	Intra-vascular ultrasound	156
7.2.2.2	Coronary computed tomography angiography	159
7.2.3	Invasive FFR measurements	159
7.2.4	Flow Simulations	159
7.2.5	Statistical analysis	160
7.3	Results	161
7.3.1	Geometric comparison	161
7.3.2	Hemodynamic comparison	163
7.4	Discussion	165
7.4.1	Limitations	167
7.5	Final remarks	168

8	Conclusions	169
8.1	Contributions	169
8.2	Partial conclusions	171
8.2.1	Image processing of IVUS studies	171
8.2.2	Biomechanical characterization of the vessel wall	171
8.2.3	Medical applications	172
8.3	General conclusions	172
8.4	Future works	173
A	Guidewire detection	175
B	Discrete gradient ascendant method	177
C	Application of variational calculus	179
C.1	Maximum likelihood variations	179
C.2	Optical flow based on Weickert strategies	181
	Medical glossary	185
	Bibliography	215

List of symbols and abbreviations

Chapter 1

CVD	Cardiovascular disease	IB-IVUS	Integrated backscatter IVUS, tissue characterization technique introduced by YD Co.
DALYs	Disability-adjusted life years		
IVUS	Intravascular ultrasound		
VH-IVUS	Virtual histology IVUS, tissue characterization technique introduced by Volcano.	ADAN	Anatomically detailed arterial network.
iMAP	Tissue characterization technique introduced by Boston Scientific.		

Chapter 2

ECG	Electrocardiogram	$s_i(n)$	Normalized motion signal i at the n -th frame of the study
CCB	Combined correlation and blurring method		
AID	Absolute intensity difference method	w_i	Weight factor for s_i
		H, W	Height and width of the study images (in pixels)
CDM	Correlation dissimilarity matrix method	$\hat{s}_i(n)$	Motion signal i at the n -th frame of the study
MB	Motion blur method		
BPM	Beats per minute	$s_i^+(n)$	Positive motion signal i at the n -th frame of the study
FPS	Frames per second		
LAD	Left anterior descending artery	α	Mixture parameter for the case of only two signals
RCA	Right coronary artery	$\tilde{s}(k)$	k -th frequency of the signal s in the spectral domain
LCx	Left circumflex artery		
LA	Bland-Altman limits of agreement	f_m	Estimated mean cardiac frequency
%CV	Bland-Altman coefficient of variability	f_c	Cut-off frequency for the gating low-pass filter
RPC	Bland-Altman coefficient of reproducibility	δ	Deviation factor of the cardiac frequency
SD	Standard deviation	s_{low}	Low-pass filtered signal of s
s	Motion signal along the study	$f(n)$	Kernel in the spatial domain of the low-pass filter

$w(n)$	Rectangular unitary window function in the spatial domain	$\sigma_t^{\alpha_c}(i)$	Standard deviation of the heartbeat period of the study using α_c as mixture parameter
$h(n)$	Hamming window function in the spatial domain	\mathbf{w}	Vector of weight factors
f_{max}	Maximum sample frequency	$C_{\mathbf{w}}$	Set of \mathbf{w} candidates for the setup of the signal mixture
τ, ν	Offset and intensity parameters of the Hamming window	O_i	Observations of the i -th specialist
$p(i)$	i -th local minima of a signal s	\bar{O}_i	Mean of the observations of the i -th specialist
$HB(i, j)$	Frame number for the j -th image in the i -th heartbeat of the study	$p_m(i)$	Middle time instant of the i -th heartbeat of the study
$U^k(i)$	i -th image of the k -th cardiac phase	ε_{HBP}	Mean error per heartbeat
M	Amount of image features used to construct s	μ_{PD}	Mean offset of the estimated cardiac phases
P	Amount of gated cardiac phases in the study	ε_{PD}	Phase detection error
B	Amount of heartbeats in the study	ε_{HF}	Heart frequency error
C	Set of α candidates for the setup of the signal mixture	B^{ECG}	Amounts of heartbeats detected with ECG signal
A	Cardinality of C	B^{IB}	Amounts of heartbeats detected with an image based gating
$t_{\text{HB}}^{\alpha_c}(i)$	Period of the i heartbeat of the study using α_c as mixture parameter		

Chapter 3

RF	Radiofrequency	BPM	Beats per minute
CFD	Computational fluid dynamics	ECG	Electrocardiogram
MLE	Maximum likelihood estimators	LAD	Left anterior descending artery
SAD	Sum of absolute differences	LCx	Left circumflex artery
SSD	Sum of square differences	RCA	Right coronary artery
NCC	Normalized cross-correlation	MSGA	Multi-seed gradient ascend method
DTW	Dynamic time warping	LA	Bland-Altman limits of agreement
ROI	Region of interest	ICC	Intervals of cross-correlation
DLT	Decoupled strategy with longitudinal-transversal registration	SNR	Signal-to-noise ratio
DTL	Decoupled strategy with transversal-longitudinal registration	J_k	k -th frame of the IVUS study
VWR	Vessel wall region	M_k	Binary mask of the k -th frame of the IVUS study
FIR	Full image region	M^{DR}	Binary mask of the downring artifact
GG	Generalized Gamma distribution	M_k^{GW}	Binary mask of the guidewire in the k -th frame of the IVUS study

M_k^{VW}	Binary mask of the area comprised between the EEM and the lumen	$\mathcal{F}(J_n, J_m)$	Functional that measures the correlation between J_n and J_m .
M_k^{FIR}	Binary mask for the ROI FIR	\mathcal{U}	Space of admissible rigid motions of the transducer
M_k^{VWR}	Binary mask for the ROI VWR	$d_{\mathcal{U}}(\Xi_i, \Xi_j)$	Euclidean distance over \mathcal{U} between the elements Ξ_i and Ξ_j
\neg, \vee, \wedge	Logical operators for NOT, OR and AND operations	P	Amount of phases phases
$u(s), v(s)$	Intensity value of the image u, v at the pixel s	\mathcal{I}_i	Sequence of images corresponding to the i -th cardiac phase
$\varepsilon, \varepsilon_u$	Noise intensity function and noise intensity function for the image u	\mathcal{I}_{st}	Sequence of images corresponding to the end-diastolic cardiac phase
$L(\varepsilon, s)$	Log-likelihood function for noise ε	\mathcal{I}_{mo}	Sequence of images corresponding to the most moved cardiac phase
$P(u(s))$	Probability for intensity $u(s)$ in image u	$\mathcal{P}_{\text{motion}}$	Functional that quantifies the amount of motion in a sequence
$P_{\varepsilon}(\cdot)$	Probability density function at (\cdot) for the distribution of ε	H, W	Height and width (in pixels) of the IVUS image
$u_{\varepsilon}(s)$	Derivative of u with respect to ε	I_j^i	j -th image in the sequence corresponding to the i -th cardiac phase
$c(u, v)$	Correlation function	$s(I)$	Distance over the longitudinal axis (in mm) where the image I was acquired
μ, σ	Mean and standard deviation of quantity \cdot	s_0	Initial position of the transducer
\hat{u}, \hat{v}	Normalized versions of images u and v with null mean and normalized standard deviation	v_p	Pullback velocity
\tilde{u}, \tilde{v}	Log-compressed version of the images u and v	f_s	Frame rate of acquisition
Ω	Image domain	N_i	Amount of images in the sequence corresponding to the i -th cardiac phase
Γ	Complete gamma function	$c_w(I_i, I_j)$	Neighborhood likelihood estimator with w neighborhood length
α, γ, ν	Parameters of the generalized gamma distribution	ϕ	Gaussian weight function
J_n	n -th image of the IVUS study	σ_G	Standard deviation of the ϕ
M_n^Z	Binary mask of the J_n using the ROI Z	T	Cut-off threshold for w neighborhood
$M_{n,m}^Z$	Intersection of masks M_n^Z and M_m^Z	$\mathcal{R}_n^{(\cdot)}$	Set of frames located at the n -th frame position of the end-diastolic phase when using the registration strategy (\cdot)
$\mathcal{R}_{n,m}^Z$	Set of pixel coordinates where $M_{n,m}^Z = 1$	\mathcal{V}_j	Set composed by the j -th frame of each cardiac phase
$ \mathcal{R}_{n,m}^Z $	Cardinality of $\mathcal{R}_{n,m}^Z$		
Ξ_m^n	Rigid motion between frames J_n and J_m		
τ_x, τ_y, θ	Components of the rigid motion depicting the translation along x and y axis and the rotation angle.		

$\ \cdot\ _{\mathcal{U}}$	Norm associated to the distance function $d_{\mathcal{U}}$	ε_i	Longitudinal registration error of the i -th landmark
r_{eq}	Equivalent radius of the luminal area	$\mathcal{I}^j(i)$	Frame of the i -th landmark in the cardiac phase j
A_l	Area of the lumen	μ_{BA}	Bland-Altman mean
\overline{O}_i	Mean observations of the i -th specialist	d_k	Longitudinal motion in mm at the k -th frame of the end-diastolic phase
\overline{O}_i^E	Mean extended observations of the i -th specialist	p_d	Pre-defined motion of the IVUS study
O_{MSGA}	Observations obtained from MSGA		

Chapter 4

OF	Optical flow	\mathcal{R}_i	Sub-region i of the domain Ω
SNR	Signal-to-noise ratio		
MLV	Maximum likelihood variations	$ \mathcal{R}_i $	Cardinality of \mathcal{R}_i
TV-L1	Total variation with L_1 norm	$\mathcal{P}_{(\cdot)}$	Set of parameter instances associated with the denoising method (\cdot)
ROI	Region of interest	\mathcal{E}	Optical flow functional
CGL	Combining global-local strategy	$\ \mathbf{A}\ _F$	Frobenius norm of tensor \mathbf{A}
I_i	i -th image	G_{ρ}	Gaussian kernel of convolution with ρ standard deviation
$\mathbf{w} = (u, v)$	Optical flow field		
Ω	Image domain	∇_{ρ}	Gradient operator embedding the Gaussian convolution
$\partial\Omega$	Boundary of the domain Ω		
$ \Omega $	Cardinality of Ω	$\frac{\partial_{\rho}}{\partial t}$	Temporal derivative operator embedding the Gaussian convolution
α	Regularization factor		
p^k, τ, σ	step size parameters of TV-L1		
β	subrelaxation parameter	ψ	Non-linear weight function
\hat{I}_o, \hat{I}_d	Image with and without noise	ψ'	Derivative of the non-linear weight function
I_o, I_d	Log-compressed version of images \hat{I}_o and \hat{I}_d	κ	Non-linear factor associated with the function ψ
ε	Image noise	M	Amount of resolutions used in the multi-resolution approach
$\tilde{\varepsilon}$	Log-compressed image noise		
$P_{(\cdot)}$	Probability density function of the distribution associated with variable (\cdot)	I^m	Image I at the m level of image resolution
δ, γ, ν	Parameters of the generalized gamma distribution	\mathbf{w}^m	Optical flow associated to I^m
Δ	Laplacian operator	$\delta\mathbf{w}^m$	Optical flow increment between \mathbf{w}^m and \mathbf{w}^{m+1}
\mathbf{n}	Unit normal vector		
a, b, c	Reparametrization of parameters δ, γ, ν	ψ'_i	Derivative of the non-linear weight function of the i -th term of the optical flow functional
ε_d^H	Region-wise denoising error		
μ_i	Mean intensity of \mathcal{R}_i		

\mathbf{w}_T	Ground truth value of the optical flow	ε_d^{of}	Error in the norm L_2 of the optical flow estimation
ε_T	Ground truth value of the strain field		

Chapter 5

ECM	Extracellular matrix	$\chi(\cdot)$	Mapping function described in the (\cdot) configuration
GAG	Glycosaminoglycans		
PG	Proteoglycans	$\mathbf{F}_m, \mathbf{f}_s$	Gradient of χ in the material and spatial configurations, respectively
DAPI	4',6-diamidino-2-phenylindole staining		
EL	Elastic lamella	∇_m, ∇_s	Spatial gradient in the material and spatial configuration, respectively
IEL	Internal elastic lamella		
EEL	External elastic lamella		
Ox	Oxytalan	$\mathbf{t}(\cdot)$	Traction imposed over the boundary $\partial\Omega(\cdot)$
SMC	Smooth muscle cell		
LDL	Low density lipids	\mathbf{n}	Unit normal vector in the spatial configuration
HDL	High density lipids		
CeFb	Cell rich fibrotic tissue	\mathbf{P}	Tangential projection operator
HyFb	Hypocellular fibrotic tissue		
Ca	Calcified tissue	$\lambda(\cdot)$	Lagrange multiplier of the mechanical problem described in the (\cdot) configuration
Lip	Lipidic tissue		
HES	Haematoxylin, erythrosine, safran staining		
ROO	Oil red-O staining	$\boldsymbol{\sigma}(\cdot)$	Cauchy stress tensor described in the (\cdot) configuration
LM	Left main coronary artery		
RCA	Right coronary artery		
LAD	Left anterior descending coronary artery	$\boldsymbol{\varepsilon}(\cdot)$	Strain rate tensor described in the (\cdot) configuration
LCx	Left circumflex coronary artery	$\mathcal{L}(\cdot)$	Linear space for pressures in the (\cdot) configuration
CAD	Computer-aided design	$\mathcal{U}(\cdot)$	Space of kinematically admissible displacements in the (\cdot) configuration
$(\cdot)_s, (\cdot)_m$	Description of (\cdot) at the spatial and material configurations, respectively	$\mathcal{V}(\cdot)$	Space of kinematically admissible variations in the (\cdot) configuration
$\Omega(\cdot)$	Domain described in the (\cdot) configuration		
$\partial\Omega(\cdot)$	Boundary of the domain $\Omega(\cdot)$	$\mathbf{S}(\cdot)$	Second Piola-Kirchhoff stress tensor in the (\cdot) configuration
$\partial\Omega^W(\cdot)$	Luminal boundary of the domain $\Omega(\cdot)$		
$\partial\Omega^E(\cdot)$	Abluminal boundary of the domain $\Omega(\cdot)$	$\mathbf{E}(\cdot)$	Green-Lagrange deformation tensor in the (\cdot) configuration
$\partial\Omega^A(\cdot)$	Non-physical axial boundary of the domain $\Omega(\cdot)$	\mathbf{n}_0	Unit normal vector in the material configuration
$\mathbf{x}(\cdot)$	Coordinates at the configuration (\cdot)	α_{in}	Ratio between inertial and circumferential stresses
$\mathbf{u}(\cdot)$	Displacement field at the configuration		

ρ	Vessel wall density	\mathbf{C}_m	Cauchy tensor
r_i	Inner radius	k_1, k_2	Coefficients associated with the stiffness of the collagen fibers
h	Vessel wall thickness		
p_i	Internal pressure of the vessel wall	δ_i	Fiber activation coefficient
T	Time from diastole to peak pressure	λ_i^0	Recruitment stretch
ψ	Strain energy function	ρ	Mixture parameter of isotropic and anisotropic fiber contributions
c	Coefficient associated with the stiffness of a neo-hookean material	\mathbf{a}_i	Fiber orientation vector
		θ	Angle between fibers and the circumferential direction
I_1	First invariant of the Cauchy tensor		

Chapter 6

KKT	Karush-Kuhn-Tucker	\mathbf{P}_Z	Covariance of Z
FSI	Fluid structure interaction	$f(\cdot)$	Nonlinear forward operator
EKF	Extended Kalman filter	$h(\cdot)$	Nonlinear observation operator
ROUKF	Reduced order unscented Kalman filter	t	Time at which f and h are evaluated
PDF	Probability density function	\bar{X}	Mean state vector
LB	Lower bound	N	Number of components of X
UB	Upper bound	w_i	Weight of the i -th sigma-point
X	State vector		
Z	Observation vector	σ_i	i -th sigma-point
V	Observation error vector	$\hat{X}^{(i)}$	Estimate of the state vector using the i -th sigma point
V	Model error vector	$\hat{Z}^{(i)}$	Estimate of the observation vector using the i -th sigma point
\mathbf{H}	Lineal observation operator		
\hat{X}	Estimate of the state vector	\hat{X}^-	A priori estimate of the state vector
$\ \cdot\ _{L_2}$	L_2 norm		
\mathbf{H}^{-L}	Left inverse observation operator	\mathbf{P}^-	A priori covariance matrix of the state vector
$E(\cdot)$	Expectation of the random variable \cdot	\hat{Z}	Estimate of the observation vector
\mathbf{R}	Covariance matrix of the observations	\hat{X}^+	A posteriori estimate of the state vector
σ_i	Standard deviation of the uncertainty in the i -th observation	\mathbf{P}^+	A posteriori covariance matrix of the state vector
\mathbf{K}	Estimator gain matrix	X^a	Extended state vector
\mathbf{I}	Identity operator	θ	Parameter vector
\mathbf{P}, \mathbf{P}_X	Covariance matrix of the state vector	M	Amount of parameters
\mathbf{A}	Linear forward operator	\mathbf{L}, \mathbf{U}	Matrices obtained through the decomposition of \mathbf{P}
\mathbf{Q}	Covariance matrix of the model error		
\mathbf{P}_{XZ}	Cross-variance between X and Z	\mathbf{D}_w	Diagonal matrix containing the sigma-point weights

$\{\mathbf{HL}\}, \mathbf{P}_w$	Matrices obtained through the decomposition of the covariance matrices	$\hat{\theta}^+$	A posteriori estimate of the parameter vector
$(\cdot)^X$	Matrix (\cdot) associated only to the vector X contributions of X^a	$\mathbf{u}_{(\cdot)}^M$	Displacement field in the configuration (\cdot) computed by solving the mechanical problem of equilibrium
$(\cdot)^\theta$	Matrix (\cdot) associated only to the vector θ contributions of X^a	$\mathbf{u}_{(\cdot)}^{OF}$	Displacement field in the configuration (\cdot) computed by the optical flow with IVUS images
$\hat{\theta}^{(i)}$	Estimate of the parameter vector using the i -th sigma point	$\mathbf{0}$	Null operator
$\hat{\theta}^-$	A priori estimate of the parameter vector	σ_Z	Observation uncertainty
		σ_θ	Parameter uncertainty

Chapter 7

CCTA	Coronary computed tomography angiography	P_a	Aortic pressure
AX	Angiography	Ω	Domain occupied by the coronary vessel
FFR	Fractional flow reserve	Γ_w	Domain boundary corresponding to the arterial wall
AWSS	Average wall shear stress	Γ_p	Proximal domain boundary
OSI	Oscillatory shear index	Γ_i	i -th outlet boundary
CDF	Computational fluid dynamics	N_o	Amount of boundary outlets
RCA	Right coronary artery	\mathbf{n}	Unit normal vector
LAD	Left anterior descending coronary artery	\mathbf{v}	Velocity field
LCx	Left circumflex coronary artery	p	Pressure field
RI	Ramus intermedius	ρ	Blood density
%DS	Percentage of diameter stenosis	μ	Blood viscosity
MLA	Minimum lumen area	P_p	Mean systemic blood pressure
IQR	Interquartile range	\mathbf{t}_i	Traction imposed at Γ_i
CABG	Coronary artery bypass graft	γ	Murray's law exponent
PCI	Percutaneous coronary intervention	v	Velocity magnitude
LVEF	Left ventricular ejection fraction	A	Lumen area
VMTK	Vascular modelling toolkit	D	Lumen diameter
BA	Bland-Altman	Re	Reynolds number
Γ_s	Cross-sectional slice	Q	Flow rate
$\partial\Gamma_s$	Cross-sectional slice contour	FFOI	Ratio between flow at the outlets and flow in the inlet
$\overline{(\cdot)}$	Γ_s -averaged quantity	Ω_{FFR}	Sub-domain where FFR is computed
P_d	Distal pressure	ρ	Spearman's correlation value

Chapter 1

Introduction

In this chapter, the motivations and challenges behind this work are introduced. To place the contribution of this thesis within the state-of-the-art context, a survey about the characterization of the material properties of tissues composing the arterial wall is performed. Then, a detailed description of the steps and goals of this thesis is presented, highlighting the necessary methods that must be developed to achieve the mechanical characterization of the vessel. Finally, the structure of the manuscript is described, summarizing the specific motivation and contents of each chapter.

1.1 Motivation

This work is mainly motivated by the huge impact of cardiovascular diseases in our society, as the major cause of death worldwide, and also by the difficulties in its diagnosis, treatment and research, all of which can be eased by the use of computational mechanics as a complementary tool for research, risk assessment and prognosis. Particularly, we focus our research in the development of computational tools for the study, detection and description of atherosclerotic plaque lesions, motivated by their central role in the development of cardiovascular events.

1.1.1 The worldwide impact of cardiovascular diseases

In the last century, the technological revolution in medicine, biochemistry and sanitation achieved a substantial diminution of the worldwide deaths due to infectious and other transmissible diseases. As consequence, a larger percentage of the population attained elder stages where chronic diseases are naturally developed. Today, the principal causes of death and morbidity worldwide are the cardiovascular diseases (CVDs). In fact, myocardium ischemia and stroke are the worldwide leading causes of death in the last 15 years and just in 2015 accounted for a combined 15 million deaths [217]. Besides the fatal events, the morbidity caused by CVDs is responsible for 10% of the disability-adjusted life years (DALYs) lost in low and middle-income countries, and for 18% of DALYs lost in high-income countries [302]. The morbidity does not only attain at personal and familiar levels, it is a large social burden in terms of work-force lost and health economic expenditures. More precisely, the projected cumulative economic losses in the period of 2011-2025 from all noncommunicable diseases is \$7.28 trillion in low and middle-income countries [153]. From these losses, CVDs represents roughly the 50% and neglecting the investment for prevention and treatment of such diseases may cost \$47 trillion worldwide in the next 25 years [184].

In developed and developing countries, this impact is substantial to the economy due to the aging of its population. The decay of natality combined with the increase of

the life expectancy, projects a future decrease of the population ratio between work active and elder population. Thus, the rates of mortality and morbidity in our society due to CVDs will raise. To attenuate such consequences, it is of the utmost importance, socially and economically, the investment in: i) research about genesis, progression, causes and vulnerability of the atherosclerotic plaque to increase the insight on the related CVDs; ii) new medical techniques for early detection of these diseases whose early treatment would reduce the morbidity and decrease the disease progression; iii) diagnosis and visualization techniques to assess the arterial composition and functionality; iv) risk assessment tools to identify viable and effective treatments in combination with better therapeutic devices and procedures to improve the treatment outcome. In particular this work contributes in the items i), iii) and iv), where the arterial composition recovered from medical images can be used to study the plaque development along follow-ups of patient samples, as well as to elaborate patient-specific diagnosis and risk assessment based on the vessel state at the moment.

1.1.2 Silent diseases and prognosis uncertainty

Diagnosis and early detection of CVD is hindered by characteristic absence of symptoms. Many cardiovascular accidents occur due to advanced atherosclerotic plaque progression. The plaque is slowly developed during our whole life and can remain clinically silent [81]. During this progression, the cardiovascular system remodeling and the nervous system mechanisms of control adapt the organism to behave similarly as in a free-disease state. Although at some point the plaque reaches a critical condition when these mechanisms cannot sustain a healthy state for the individual and symptoms start to arise or even a cardiovascular event occurs. Even when the patient is symptomatic there is also uncertainty in its condition. Some cases exhibit acute coronary syndrome followed by a period of stability that can be short or last for years or decades [81] and the reasons of this variability is yet unknown. What is categorically evident is the fact that the mechanisms responsible for plaque growth and plaque instability (with a consequent cardiovascular accident) are different at some point. Some theories for these phenomena have been proposed ([30, 291, 292, 298, 305, 338], see Section 5.2 for further details), although there is no conclusive evidence to support any of them entirely [107].

The lack of in-vivo and patient specific tools for tissue identification in arteries hinders the follow-up of the progression and mechanical destabilization of the plaque [107]. As ex-vivo data of unstable plaque morphology have already been reported [55, 321], there is no reliable technique to identify such culprit patterns during in-vivo diagnosis. The CCTA and MRI techniques only may visualize the larger arteries with enough relevant details due to its low spatial resolution. Even more, the classification of soft tissues with CCTA is very challenging due to the low intensity contrast among them. Intravascular imaging, such as IVUS and OCT, solves the resolution issue delivering $\approx 1 - 17\mu\text{m}$ resolutions. Nevertheless, IVUS features low signal-to-noise ratio and close intensity values for lipidic and fibrotic materials, while OCT lacks of sufficient signal penetration to characterize the complete thickness of the vessel wall. For such reasons, conventional imaging techniques on their own do not allow an in-vivo examination of the vessel wall tissues.

On the contrary, data assimilation and numerical simulation enable the in-silico creation of patient models without resolution or invasiveness constraints. Using segmentation and reconstruction techniques, patient-specific geometrical models can be retrieved from medical imaging. Integrating these geometries with appropriate constitutive laws for the different tissue materials, allows the simulation of scenarios of interest for medical research such as plaque rupture, therapeutic procedures and vessel deformation. Even more, the numerical simulation of the vessel wall under the image acquisition conditions can be synergically combined with image data and data assimilation techniques to analyze

the vessel composition. Such methodology may unveil the in-vivo structure of the vessel from medical images, delivering a key tool for medical research (e.g. the follow-up of the progression and mechanical destabilization of the plaque, as discussed before). Also, it delivers a feedback to conduct more accurate patient-specific simulations since the behavior of the vessel wall is better described. Among other applications, risk assessment of therapeutic procedures and fluid structure interaction between blood and vessel wall on different patient conditions may lead to a better understanding and prognosis of the patient condition.

1.1.3 Challenges in diagnosis, risk assessment and treatment

Effective diagnosis, risk assessment and treatment of CVDs involve new challenges for the mainstream medical practices. The complexity of such diseases is given by: i) the multiple patient-specific factors that contribute to the progression and genesis of the CVDs; ii) the complex integrability between the cardiovascular components where local and systemic mechanisms affect the local vessel conditions.

The genesis, stability and progression CVD relies on patient-specific factors such as vascular geometry and composition, hemodynamics, phenotype, genotype and patient anamnesis. Each of these factors present a notorious variability from one patient to another, from anatomical differences, mechanical state of the vessels and hemodynamic variables, to previous medical procedures, conditions, daily routine and environmental conditions. For such reasons, indexes and generalizations derived from a population of patients usually lack of representativity for a specific patient. This does not imply that patient population studies are useless. On the contrary, valuable insights are obtained from these studies such as indicators for risk assessment or the characterization of the pathology, among many others. Nevertheless, it must be taken into account that patients, due to their particular conditions, may diverge from the population trend. At this point, the acquisition and analysis of patient-specific features is key for a robust and tailored evaluation of the patient. In clinical practice, patient monitoring and medical imaging techniques deliver large amounts of patient specific data although its effective analysis and complete comprehension is challenging. Here, new computational tools may enhance the data organization, analysis and assimilation. For instance, after the image acquisition segmentation, registration and gating tools rearrange the data to ease its interpretation and provide better suited inputs for data analysis. In turn, numerical simulation techniques for hemodynamics and vessel wall interaction can ease and extend the analysis of such data. Patient-specific hemodynamic simulations deliver a detailed description of the blood flow kinematics and, also, allow to analyze variability of the flow conditions (such as pressure, pulse wave, systemic resistance, among others) and the vessel geometry (e.g. increase or decrease stenoses levels, simulate stent implantation) and its state (e.g. choose its constitutive materials, its axial stretch) to analyze pathological scenarios. These customizations permit the analysis of the diseases in a patient-specific context, through a computational model of the patient, for any physiological or non-physiological condition and without accessibility or resolution constraints for measurements of any variable. Hence, the contribution of each patient-specific factor mentioned before, can be studied independently in these models by varying their influences and observing the outcomes. Such methodology will aid in the understanding of how these factors are combined in complex scenarios and which impact they actually have in hemodynamics and vessel wall mechanics.

The high integrability between components of the cardiovascular system impose another difficulty for the study of CVDs. In fact, the local conditions within a particular vessel are influenced by the systemic conditions. For example, suppose that the distal capillary beds of a vessel reduce their resistance because the irrigated tissue demands larger

blood supply. Such adjustment induces a local pressure drop and, in turn, may trigger a local vasomotor tone adaptation to avoid excessive pressure reduction. This is only one of numerous scenarios where systemic adaptations modify the local hemodynamics and/or the local mechanical conditions of the vessel. To study such complex integration among the cardiovascular components, highly detailed models of the cardiovascular system are required. The ADAN (Anatomically Detailed Arterial Network) model [42, 43] makes possible to study such complex contributions and the estimation of appropriate hemodynamic conditions for simulations in any given artery. The availability of such resource with the contents developed in the current thesis may lead to realistic recreation of the physical conditions in coronary arteries which will be fundamental for therapeutic procedure simulations, risk assessment and diagnosis.

The conception of the previous computational solutions described for preprocessing, numerical simulation or complex anatomical modeling are inherently created by a cross-functional team. The creation of such teams and the establishment of a common ground for brainstorming, critical discussion and exchange of knowledge is another big challenge. This multi-disciplinary paradigm requires teams where all members have a basic knowledge across all team areas of expertise to share a common language and understanding along their activities. Also, the delineation of common meaningful goals, synergically integrating the contributions of each expertise, is not a straightforward task. Nevertheless, the capabilities of such groups allowed the creation of specific tools and a deeper specialization for complex problems.

These challenges are an important motivation for this thesis because of the available resources to tackle them. The joint work with the medical professionals of Incor and S rio-Liban s health centers is materialized across all chapters of the current manuscript, from the medical data acquired in those centers to meaningful discussions and interpretation of the results. The expertise available in the HeMoLab¹ group concerning computational hemodynamics, solid mechanics, numerical simulations and modeling facilitates the materialization of the several methods here developed. The access to high performance computing resources (HPCMACC and Santos Dumont² clusters located at LNCC) endowed this work with substantial sensitivity analysis of the developed methods and the creation of computationally demanding scenarios to validate several methods and computational strategies.

1.2 State-of-the-art in in-vivo characterization of the vessel wall

The correlation between the vessel remodeling and rupture with the stresses of the arterial wall has awoken the interest in quantifying stresses in atherosclerotic lesions [72, 244, 274]. The methods usually used for these tasks are the elastography [63, 248] and palpography [62]. These approaches measure the strains in the arterial wall at different pressures to estimate the stress, considering the vessel as an isotropic, homogeneous, incompressible and linearly elastic material. Two feasible sources for the internal load are the arterial pressure [89] and the expansion of a compliant angioplasty balloon [296]. An advantage of these methods, in comparison with those commented in the previous paragraph, is the capability to differentiate soft fatty from stiff tissues because of their different mechanical properties [187, 198, 199]. However, because of mechanical hypotheses, the strains and, therefore, the stresses are calculated locally via image data polluted with speckle noise. As consequence, the observed global deformations of the vessel wall may not be in accordance with the estimated stresses.

¹HeMoLab web page at <http://hemolab.lncc.br/web/>

²More information about these clusters can be found at <http://www.cenapad-rj.lncc.br/>

Available methods to perform in-vivo tissue characterization in health facilities are image-based methods, namely: VH-IVUS (Volcano Corp., Rancho Cordova, CA, USA) [239], IB-IVUS (YD Co., Ltd., Nara, Japan) [172] and iMap (Boston Scientific, Natick, MA, USA) [287]. These methods analyze the radio-frequencies of the IVUS studies and extract data based on different features. Then, using ex-vivo vessel samples and the associated histology, a ground truth database is built to train a classifier (for VH-IVUS or iMap) or to estimate threshold values to determine the tissue characterization. The main problems from these approaches are that: (i) they are extremely sensitive to the training dataset; (ii) in-vivo and ex-vivo tissues may not present the same echogenic response [77] leading to inappropriate categories for the classifier; (iii) the tissue composition of the vessel wall is not necessarily compatible with the vessels strains observed. The comparison of these methods is not trivial given that they classify the tissue in different and not comparable categories [138, 345]. Furthermore, the validation against ex-vivo samples may not be appropriate due to item (ii) mentioned above.

Other image-based techniques have also appeared incorporating alternatives on the frequency analysis or the classifier. Different mathematical approaches for the feature extraction have been tested, such as discrete wavelet packet frame and a 2-D Hilbert transform of multiscale representations [169, 234], fractal theory [137], angle-dependence analysis [139] or moment invariants [342]. An interesting approach to reduce the drawback exposed in the item (ii) of the previous paragraph, is presented in [77] to integrate ex-vivo and in-vivo information at the training of the classifier, although the uncertainty of the in-vivo histological data limits the classifier efficiency for these tissues.

A promising approach for the characterization problem is the estimation of mechanical properties of biological tissues via data assimilation. In the last decades, several studies assumed the displacement field of the vessel wall as known and formulated the problem of estimating constitutive parameters trying to reproduce the measurements, i.e. the displacement field. The different strategies can be classified in any of the following two categories: i) variational approach or ii) sequential filtering approach. The variational approaches minimize a functional cost that measures the dissimilarities between the displacement field extracted from the images and the prediction of the mechanical problem. The problem is typically solved using the Karush-Kuhn-Tucker necessary conditions [32, 97, 179, 210, 255, 294] involving the solution of an adjoint problem. The main drawback of this approach is the amount of evaluations to the cost functional (or its derivative) that must be performed in order to solve the inverse problem (usually ranging from 10^2 to 10^3 [185]). For such scenarios, [185] proposes reduced order strategies to solve the Navier Stokes equations in combination with a domain parametrization technique that reduces both the geometrical and computational complexity. Other approach is taken in [32], applying model reduction techniques based on a proper orthogonal decomposition to accomplish the solution of 3D FSI in a computationally efficient way. Efficient implementations for solid mechanics problems have also been proposed in [25, 353] using a virtual fields method and a constitutive equation gap functional, respectively. In turn, sequential filtering approaches are naturally less computationally demanding and embarrassingly parallel. In the last decade several methods have been proposed for the estimation of cardiovascular model parameters [66, 228, 229, 230] and vessel tissue properties [33, 34, 195]. To adapt the traditional linear Kalman filter to such non-linear problems, the formulation of an extended Kalman filter (EKF) was employed where the first order derivative of the mechanical problem operator must be computed along the filtering [66, 195, 229, 230]. Immediately, a more accurate and faster strategy was proposed by using a reduced order unscented Kalman filter (ROUKF) which exploits the fact that the unscented transform tracks the mean and standard deviation of variables after being affected by a non-linear operator. An advantage of the ROUKF strategy is that the unscented transform guar-

antees at least second order approximation in its prediction step (similar to the use a higher order derivative operator in the variational approaches or non-linear Kalman filter) without the need for the estimate of any operator derivative.

A deeper literature review is performed in due time in each of the chapters of the thesis, surveying the state-of-the-art for each specific topic. Concerning the previously introduced data assimilation techniques, the reader may look into Chapter 6 for further details. Currently, there is still not work which presents a complete methodology from medical image acquisition to in-vivo mechanical characterization of the arterial tissues. In this thesis, we aim to establish the tools, methodology and knowledge targeting such need.

1.3 Aims and goals

The aim of the present thesis is the construction of a methodology to obtain the mechanical characterization of the vessel wall tissues from IVUS images. This requires the development of new image processing tools (see Part I) and a deeper understanding of the vessel wall composition and mechanical behavior combined with the use of data assimilation techniques (see Part II).

To achieve such goal, a novel methodology is here proposed with the following workflow. First, an IVUS study is acquired for the vessel of interest. Since this study acquires images at different instants of the cardiac cycle, a gating is performed to obtain the spatial configuration of the vessel during each cardiac phase. As the heart and the coronaries arteries are deformed during the cardiac cycle, all gated phases are registered to the end-diastolic phase configuration because it presents the lowest cardiac deformation. Then, we remove the characteristic ultrasonic noise (speckle noise) from the images to allow the use of optical flow techniques. At this stage, a cross-section of the vessel is chosen, where the tissue characterization is to be performed, e.g., an atherosclerotic lesion. The same cross-section is extracted from all the gated phases obtaining a sequence of the cross-section deformation along the cardiac cycle. Using an optical flow technique, the displacement of the vessel wall is estimated for each frame in the sequence. Finally, combining the optical flow displacement field, appropriate models for the tissues of the vessel wall and a data assimilation technique, the constitutive parameters of the tissue models are determined. The values of the constitutive parameters can be contrasted with experiments reported in the literature to identify the specific materials of the vessel wall.

Several methods have to be developed to obtain the necessary tools for the study of the mechanical characterization problem. Each of them is a goal and novel contribution by its own. In fact, we will present the use of such methods in other medical applications: i) the use of registration methods to assess the axial deformation of the vessel between two cardiac phases (see Chapter 3); and ii) the use of gating for an accurate geometrical reconstruction of the coronary vessels (see Chapter 7).

Thus, the goals of this thesis are the following

- The development and validation of image-based gating methods with sufficient robustness to deal with a wide range of cardiac frequencies, different coronary arteries, calcified and stented arteries and, also, with acceptable accuracy to gate several cardiac phases;
- The development and validation of a registration method that aligns each frame of the gated cardiac phases to the ones in the end-diastolic phase.
- The development and validation of a novel denoising method specially tailored for the reduction of speckle noise in IVUS images. The method must be compared with state-of-the-art methods for image denoising to highlight the advantages of the customized strategy.

- The analysis of the state-of-the-art optical flow methods to assess which one is the best suited alternative for the estimation of the displacement field when making use of IVUS images.
- The analysis of constitutive models for coronary vessel tissues and atherosclerotic plaque. Survey the medical and anatomic bibliography and the available experimental data to assess the best suited model and range of parameters for each type of material.
- The exhaustive analysis and validation of a data assimilation approach for the characterization of the mechanical properties of arterial vessels using full-field measurements as input data.

1.4 Structure of the thesis

The thesis is structured in three parts of cohesive contents:

- Image processing of IVUS studies: Presents all the contents associated with the post-processing of an IVUS study. It is divided in three chapters detailing the gating, registration, denoising and optical flow methods. It was decided to group the denoising and optical flow methods in the same chapter because both of these methods are closely tied in the successful estimation of the vessel wall displacements.
- Biomechanical characterization of the vessel wall: Presents all contents regarding the mechanical models and data assimilation techniques used for the biomechanical characterization of the vessel wall. The first chapter deals with the mechanical models chosen for the modelling of each arterial wall and atherosclerotic plaque tissues. To justify the chosen models, range of parameters and corresponding hypotheses during the data assimilation process, it is performed a bibliographic scrutiny of the arterial anatomy and histopathology of the plaque. Also, experimental data is gathered regarding the mechanical state and properties of the coronary vessels for the setup of the models. The second chapter details the data assimilation process for the biomechanical characterization of the vessel wall using a Kalman filter method and state-of-the-art mechanical models.
- Medical applications: Presents the summary of two comparative clinical studies performed with the use of the image processing methods developed in the first part of the manuscript. The studies are a geometrical and a hemodynamic comparison of models derived from IVUS and CCTA images for the same sample of patients. It aims to highlight the strength and weakness of each model and, also, the considerations that must be taken into account when drawing conclusions from models derived with each modality.

Furthermore, appendices with auxiliary signal processing methods, mathematical developments and a medical glossary are included at the end of the document. Lastly, we present the derived contributions from this thesis, published in international and national journals and conference proceedings.

Part I

Image processing
of
IVUS studies

Chapter 2

Gating

The reconstruction of vessel configuration at different cardiac phases is a key step to retrieve the vessel wall kinematics during the cardiac cycle. This data is present in non-gated IVUS studies. However, such data are unsorted in the study because the frames of different cardiac phases are intertwined during the pullback of the acquisition sensor (hereafter simply transducer). For this reason, in the present chapter we introduce a methodology to retrieve the set of images associated to each specific cardiac phase leading to a more accurate and time consistent arrangement of the IVUS data.

2.1 Background

In the case of coronary IVUS, the periodic contractions of the heart impose large displacements of the vessel structures and acquisition probe. In that scenario, the estimation of volumetric measurements and axial position of structures can be misleading due to this motion as shown in [235]. Consequently, non-homogeneous displacements and rotations are observed along the vessel in the axial as well as in the cross-sectional directions [21]. Since a typical IVUS study spans many cardiac cycles (≈ 2 minutes of acquisition time), the pseudo-periodic motion imposed by the heartbeat is clearly distinguishable throughout the entire study. Also, along the different heartbeats of the study, a similar motion pattern is seen, which suggests an association between each cardiac phase and the motion exerted to the structures by the cardiac contraction. Several approaches explored this aspect by sampling images of a particular cardiac phase during (on-line) or after (off-line) the IVUS acquisition [2, 57, 125, 155, 235, 284, 285, 286]. The resulting set of images presents a severe reduction of the motion phenomena delivering a static configuration of the vessel structures in a particular cardiac phase.

On-line ECG-gated techniques use the ECG signal to acquire images of one particular cardiac phase. This scheme increases the time of acquisition up to three times in comparison with the plain IVUS study [322]. Importantly, such online approach only presents information of one cardiac phase, thus neglecting all the others, which may be crucial for studies such as palpographies or 4-D reconstructions. As a final remark here, we point out that the cardiac phase acquired is expected to correspond to the end-diastolic phase, associated with the lowest motion imposition over the cardiac cycle, however, this is difficult to be achieved [235, 286]. Since the acquisition is gated in terms of R-peak offsets and due to the heart rate variability, ensuring a consistent cardiac phase acquisition is a challenging task.

To overcome the obstacles pointed out in the previous paragraph, an off-line ECG-gated can be performed over a plain IVUS study when the ECG signal is synchronized with the IVUS acquisition equipment. However, the necessary setup to perform this technique is not always available.

In the last decade, image-based techniques for off-line gating IVUS studies have been developed [2, 57, 125, 155, 284, 285, 286]. The independence of ECG acquisition permits an efficient low-cost implementation of these techniques. As proposed in [2], these methods usually present three steps for the gating process: 1) generation of a signal that measures the cardiac motion in each frame; 2) filtering and extraction of the extrema values over the motion signal and 3) off-line gating of the study. The first stage creates a signal which is intrinsically associated with the motion pattern previously described. In the second step, local extremal values related to a specific cardiac phase are extracted to obtain a partition of the study into cardiac cycles. Finally, in the last step, each cycle is divided into cardiac phases which are used to retrieve a specific cardiac phase from the whole study. The main differences among the available methodologies are in the implementation strategies of the first two steps.

Different strategies for the first step permit the classification of approaches based on lumen morphology variations [125, 155, 285] and based on image intensity features [2, 57, 284, 286]. The methods in the former category present dependence with the segmentation of the luminal area, which is still an active research field, and some approximations are time consuming due to the lack of an automatic and robust procedure [125, 285]. Also, luminal topological variations, such as bifurcations, induce spurious extremal values in the motion signal. For methods in the second category, a set of features are used to measure the variations between adjacent images: cross-correlation [284, 286], local mean variation [2] and Gabor associated features [57]. None of the previous approaches takes advantage of the blurring induced by the transducer probe motion, which is also a marker of cardiac motion and is insensitive to topological variations.

The second stage frequently involves the application of a bandpass filter centered in a fundamental frequency associated with the mean cardiac frequency along the study. This strategy neglects the high order frequencies of the motion signal, which might misalign local extrema.

In the current chapter, we propose an automatic gating method for synergical combination of image features. Also, a novel method for phase extraction is presented using an iterative signal reconstruction scheme. Specifically, the proposed method, hereafter referred as Combined Correlation and Blurring (CCB), is based on: (i) the definition of a combined motion signal that integrates the signals presented in [286] and [58] giving less sensitivity to topological variations and more accuracy for the cardiac phase extraction; (ii) a scheme for the identification of local extrema in the motion signal based on the progressive incorporation of harmonic components to gradually refine the position of extremal values; and (iii) a simple physiological criteria for the extraction of multiple phases. The method validation is conducted using 61 in-vivo IVUS studies from 21 patients including a wide range of functional and physiological situations (different degrees of stenosis, stent deployments and mild arrhythmias) through different coronary arteries.

2.2 Methodology

2.2.1 Integration of motion signals

Let us define the motion signal as a function $s(n)$ that measures the motion of the n -th image of the study. Then, $s(n)$ increases if the structures in the image change their distribution by translation, deformation or rotation with respect to the preceding/succeeding images. Besides, the image noise (speckle) produced by the micro-structures of the tissue [3] arises as a coherent pattern that varies through the different material composition in the vessel wall. For this reason, the noise variations that increment $s(n)$ are associated to movements or topological changes of the structures present in the images.

The signal $s(n)$ is chosen to be a linear combination of M image features, $s_i(n)$, $i = 0, \dots, M - 1$, characterizing the motion in an image. Then, the function $s(n)$ is defined as

$$s(n) = \sum_{i=0}^{M-1} w_i s_i(n), \quad (2.2.1)$$

where $w_i \in (0, 1)$ is the weight factor of the feature s_i and $\sum_{i=0}^{M-1} w_i = 1$.

In this work, we choose two features similar to those presented in [286] and [58], respectively. The first feature, $\hat{s}_0(n)$, is an inverse correlation between two consecutive images, that is

$$\hat{s}_0(n) = 1 - \frac{\sum_{i=1}^H \sum_{j=1}^W (u_n(i, j) - \mu_n)(u_{n+1}(i, j) - \mu_{n+1})}{\sigma_n \sigma_{n+1}}, \quad (2.2.2)$$

where $u_n(i, j)$ is the intensity at the i -th row and j -th column, μ_n and σ_n are mean and standard deviation of the intensity for the n -th frame (we refer to frames and images as synonyms) and H and W are the frame height and width, respectively. The choice of this feature is justified because the absence of movement is associated with two almost identical images, leading to a $\hat{s}_0(n) \approx 0$. When the motion between the frames increases, the matching of structures decreases leading to smaller correlation. Nevertheless, observe that \hat{s}_0 also can increase in motionless scenarios such as topological changes (e.g. bifurcations) or the appearance of new structures (e.g. stents or calcium deposits). To improve the treatment of these scenarios, we use another feature for motion assessment, insensitive to differences between adjacent frames. This second feature, called $\hat{s}_1(n)$, measures the blurring in the image,

$$\hat{s}_1(n) = - \sum_{i=1}^H \sum_{j=1}^W |\nabla u_n(i, j)|, \quad (2.2.3)$$

which exploits the fact that the transducer movement provokes a blurring effect at the borders of the structures.

To adequately combine the image features used to generate $s(n)$, we normalize their ranges as

$$s_i(n) = \frac{s_i^+(n)}{\sum_{n=1}^N s_i^+(n)}, \quad (2.2.4)$$

where

$$s_i^+(n) = \hat{s}_i(n) - \min_{1 \leq n \leq N} (\hat{s}_i(n)), \quad (2.2.5)$$

and N is the number of images in the IVUS study. This last step ensures that all s_i are positive and of the same order of magnitude. For the particular case of using two image features, the weighing factors can be reduced to only one parameter, α , defined as $w_0 = \alpha$ and $w_1 = 1 - \alpha$, thus

$$s(n) = \alpha s_0(n) + (1 - \alpha) s_1(n). \quad (2.2.6)$$

The image features and the integrated signal are presented in Figure 2.1 for a frame window in an in-vivo study. It is observed that several consecutive columns present a similar intensity pattern around the points of minima, which means that the transducer is acquiring a set of almost identical frames. A pseudo-periodic pattern with equally separated minima is observed for $s(n)$. These minima are also present in the individual features and are equally displaced to the end diastolic phase (P-wave, marked with green dashed vertical lines) in each heartbeat. Therefore, we can infer a direct relation between these minima and a specific cardiac phase in the study.

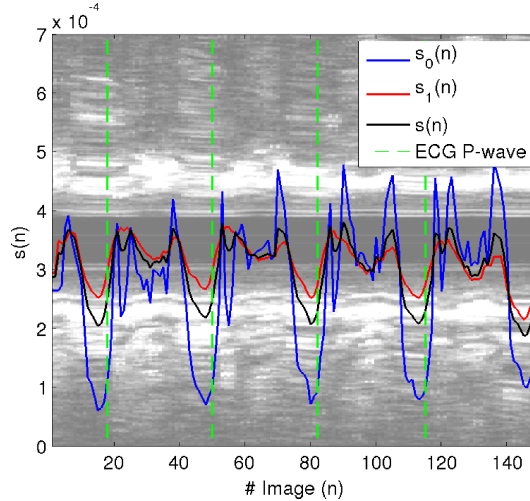


Figure 2.1: Partial longitudinal view (first 150 frames) of an IVUS study presenting the motion signal $s(n)$ and the associated features, $s_0(n)$ and $s_1(n)$, using $\alpha = 0.25$. Also the P-wave occurrence from the synchronized electrocardiogram is marked with a dashed green line.

2.2.2 Cardiac phase identification

The next goal is to detect the set of pseudo-periodic minima related to the specific cardiac phase previously described. As seen in Figure 2.1, $s(n)$ presents many local minima in each heartbeat making non-trivial the automatic gating of this cardiac phase. But taking advantage of the $s(n)$ pseudo-periodicity, the frequency spectrum of $s(n)$ is analyzed and a low frequency version of $s(n)$ is created, eliminating spurious minima. To maintain the direct relation between the remaining minima and the physiological cardiac phases, the filtered low frequency signal must include a minimum amount of frequencies such that the original pulsation pattern is preserved. Otherwise, the lack of high order frequencies can lead to a poor representation of the pseudo-periodicity of the signal local minima.

The frequency spectrum of the signal, $\tilde{s}(k)$, is computed as the discrete Fourier transform of $s(n)$. In Figure 2.2, the absolute value of the frequency spectrum $\tilde{s}(k)$ from an in-vivo IVUS study is presented. There, a local maximum frequency f_m in the range of physiologically valid heart frequencies is observed (0.75 Hz to 1.66 Hz or, equivalently, 45 BPM to 100 BPM). As will be shown later, f_m is a close approximation of the mean cardiac frequency along the study (see Section 2.3.5). The use of f_m as cutoff frequency for a low-pass filter over $s(n)$ yields a filtered signal that preserves an approximate amount of heartbeats from the study. Therefore, the automatic detection of f_m is performed by extracting the maximum frequency component of $s(n)$ in the physiological range, i. e.,

$$f_m = \max_{k \in [0.75, 1.66]} (\tilde{s}(k)), \quad (2.2.7)$$

where the physiological range is defined between 0.75 Hz and 1.66 Hz.

To consider the pseudo-periodicity of the signal we introduce a factor, δf_m , $\delta \in (0, 1)$, which models the deviation of the heartbeat frequency along the study. Then, the cutoff frequency for the low-pass filter is defined as

$$f_c = (1 + \delta)f_m. \quad (2.2.8)$$

The low frequency signal, $s_{low}(n)$, is constructed as the convolution of $s(n)$ against a

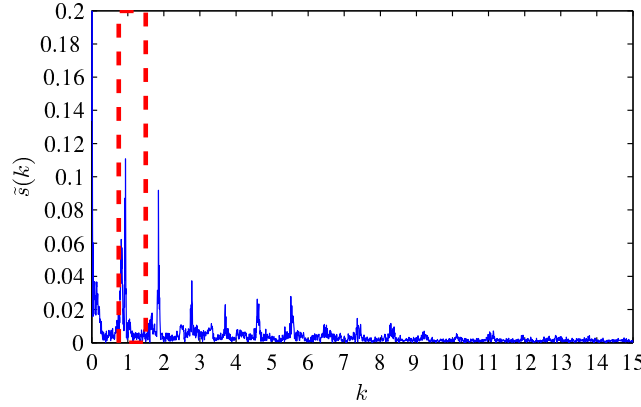


Figure 2.2: Motion signal in the frequency domain. Red lines depict the range of physiologically valid heart frequencies.

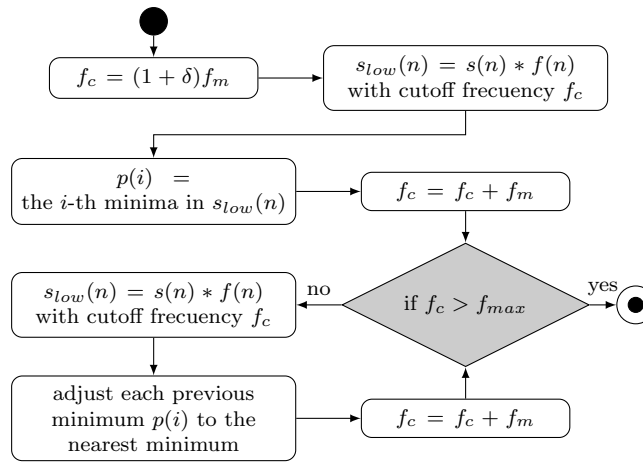


Figure 2.3: Activity diagram detailing the iterative adjustment of $p(i)$ from the initial signal $s_{low}(n)$ to $s(n)$.

low-pass kernel $f(n)$, namely

$$s_{low}(n) = s(n) * f(n), \quad (2.2.9)$$

where $*$ is the convolution operator. In turn, the low-pass kernel is defined as

$$f(n) = w(n)h(n), \quad (2.2.10)$$

where $w(n)$ is the equivalent of a rectangular unitary window for the frequencies $k \in [0, f_c]$ and $h(n)$ is a Hamming window of N points. The approximations involved with the Fourier discrete transform are avoided by applying this kernel in the time domain. Thus, the expression of $f(n)$ is given by

$$f(n) = \left[\frac{f_c}{f_{max}} \text{sinc} \left(\frac{f_c n}{f_{max}} \right) \right] \left[\tau - \nu \cos \left(2\pi \frac{n}{N} \right) \right], \quad (2.2.11)$$

where f_{max} is the maximum frequency in the study calculated as half of the transducer frame rate. In the equiripple sense, optimal values for the Hamming window are chosen as $\tau = \frac{25}{46}$ and $\nu = \frac{21}{46}$ (see [99, 129]).

The resulting signal $s_{low}(n)$ presents approximately one minimum for each heartbeat, which provides a first approximation for the local minima positions $p(i)$, at the i -th heartbeat. Using this initialization, the iterative scheme presented in Figure 2.3 is applied.

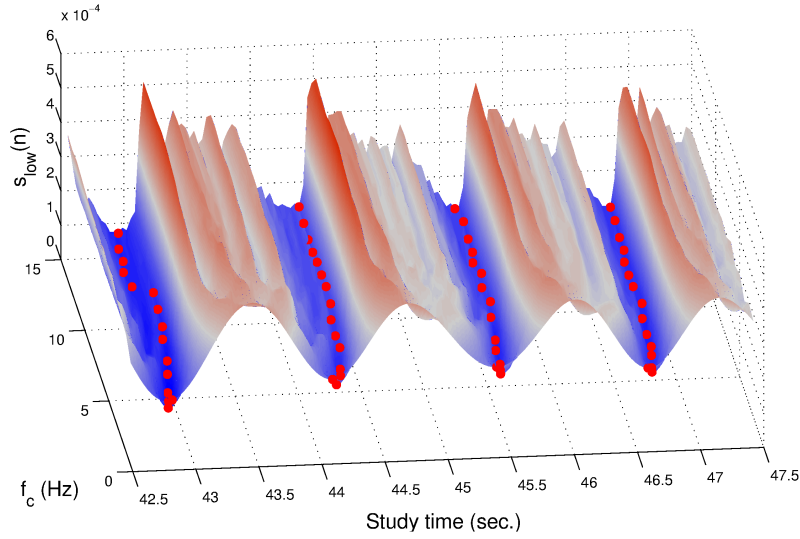


Figure 2.4: Evolution of the iterative scheme for adjusting the minima position. The axis f_c corresponds to the cutoff frequency of the low-pass filter and, at each fixed value of this axis, the $s_{low}(n)$ associated signal is presented. The red dots mark the position of the adjusted minima, $p(i)$, corresponding to the identified cardiac phase.

At each step, all frequencies up to the next harmonic component are incorporated in the definition of $s_{low}(n)$, and $p(i)$ is adjusted to the nearest local minimum. Note that, the adjusted value of $p(i)$ is not necessarily the i -th minimum of $s_{low}(n)$ because addition of higher frequencies may induce the appearance of additional minima. This process is repeated until $s_{low}(n)$ incorporates all harmonic components of f_m , obtaining the adjusted minimum for each heartbeat.

In Figure 2.4, the evolution of $s_{low}(n)$ through the incorporation of frequencies is observed along the f_c axis. It can be seen that the initialization of the minima in $s_{low}(n)$ can be heterogeneously shifted from the pseudo-periodic minima of $s(n)$ due to the absence of high frequency contributions. As we incorporate harmonic components of $s(n)$ progressively, the minima is adjusted smoothly (red points path in the f_c axial direction) to the associated minima position at the signal $s(n)$. This increases the precision of the $p(i)$ locations, for the cardiac phase detection.

2.2.3 Decomposition in cardiac phases

The identification of the images corresponding to the detected cardiac phase, i. e. the ones acquired at the $p(i)$ instants, allows the decomposition of the study in sets of images associated to each heartbeat. This is done by grouping the images between $p(i)$ and $p(i+1)$ as the set of images acquired in the i -th heartbeat. In this manner, the number of sets found, corresponds to the number of heartbeats identified in the IVUS study.

Over these new sets of images, we define $HB(i, j)$ as the index (frame number) in the original IVUS study of the j -th image corresponding to the i -th heartbeat in the study. In this indexation $HB(i, 1)$ represents the images at the first identified cardiac phase (i.e., the frames acquired at $p(i)$).

Since the cardiac frequency changes along the study, the heartbeats are sampled with a variable amount of frames. This variability in the heartbeat affects mainly the time of the diastole (more specifically the T-P interval), i. e. the heart relaxes during a longer or shorter period of time. However, the cardiac waves duration associated with the

cardiac phases remain almost invariant. As consequence, longer heartbeats feature more cardiac phases (more frames) than short heartbeats.

Then, P cardiac phases for the i -th heartbeat are identified as the first P frames. The value of P is chosen as the amount of frames of the shortest heartbeat in the study (the heartbeat composed by the smallest number of frames). The reason behind this choice was to preserve axial spacing as homogeneous as possible between images from different cardiac phases. This guarantees that each phase is represented by the same amount of information.

Finally, the set of images $U^k(i)$ corresponding to the k -th cardiac phase is defined as

$$U^k(i) = I(\text{HB}(i, k)), \quad i = 1, \dots, B, k = 1, \dots, P, \quad (2.2.12)$$

where $I(n)$ is the n -th image of the IVUS study and B is the quantity of heartbeats along the study.

2.2.4 Parameter setup

An analysis of parameters α and δ (see equations (2.2.6) and (2.2.8), respectively) is performed to ensure an appropriate and automatic execution of the method.

2.2.4.1 Parameter α

IVUS studies present small variations in the cardiac period during acquisition for patients without severe cardiac arrhythmia. For this reason, the criteria used to choose the optimal α is to reduce the heartbeat period variability detected with the gating method (see Section 2.3.8 for associated implications). This is simply done by minimizing the standard deviation of the set of values $p(i+1) - p(i)$ for $i = 1, \dots, B-1$.

In this manner, an optimization problem is solved to determine the optimal α parameter that efficiently combines the features s_0 and s_1 for a specific IVUS study. This minimization process is performed by testing a large number of candidates, say α_c , $c \in C$ being C the set of candidates, and then picking the best solution for the aforementioned criteria. Combining s_0 and s_1 with a particular α and computing the adjusted minima $p(i)$ are computationally cheap tasks, then we can apply a brute force minimization scheme with low computational cost.

To formalize this, let us define $t_{\text{HB}}^{\alpha_c}(i) = p(i+1) - p(i)$ as the period of the i -th heartbeat from the signal $s(n)$ calculated with α_c and $\sigma_t^{\alpha_c}$ as the standard deviation of the periods $t_{\text{HB}}^{\alpha_c}(i)$ for the entire study, then the optimal α is obtained as

$$\alpha = \arg \min_{\alpha_c \in C} \sigma_t^{\alpha_c}. \quad (2.2.13)$$

To determine an appropriate quantity of α_c values, we evaluate the sensitivity of the minimum $\sigma_t^{\alpha_c}$ from (2.2.13) with respect to different sizes of C . We define C as a set of equally spaced candidates $C = \{\alpha_c^i; \alpha_c^i = i/A, i = 0, \dots, A\}$ where A is the quantity of α_c candidates to be tested in (2.2.13). For the set of studies available (61 studies), a suitable size of C was given by $A = 10^3$, for which the error of estimating $\sigma_t^{\alpha_c}$ was smaller than 10^{-3} s.

The α value from (2.2.13) varies among studies due to their vessel topology and intensity of sensor motion. As commented before, s_0 does not accurately represent motion for studies with several topological changes (bifurcations, dissections, etc.) then a lower α is expected for these cases. On the other hand, studies with poor blurring (usually associated with low sensor motion during acquisition) will produce an unreliable signal s_1 , increasing the value of α .

This setup is straightforwardly generalized for the integration of M motion signals by performing the same optimization scheme over the M dimensional space defined by the weight factors $\mathbf{w} = w_1, w_2, \dots, w_M$ (see (2.2.1)). The optimal weights factors of the features are obtained as

$$\mathbf{w} = \arg \min_{\mathbf{w} \in C_{\mathbf{w}}} \sigma_t^{\mathbf{w}} \quad (2.2.14)$$

where $C_{\mathbf{w}} = C_{w_1} \times C_{w_2} \times \dots \times C_{w_M}$ and C_{w_i} is the set of candidates for the weight factor w_i .

2.2.4.2 Parameter δ

The range $\delta \in (0, 1)$ guarantees no harmonic contributions in each low-pass filter iteration. This ensures that the signal $s(n)$ contains only one minima at each heartbeat. Meanwhile, the variability in the heartbeat frequency can mislead the detection of the heartbeats for values of δ close to the range limits.

For the inferior limit, when δ is close to 0, the heartbeats with frequency above f_m are not recovered in $s_{low}(n)$. For the superior limit, when δ is close to 1, we are recovering in $s_{low}(n)$ a harmonic contribution for the heartbeats with frequency below f_m . As result, we would be generating two local minima for the heartbeats with duration larger than the mean heartbeat duration. Both cases are unacceptable because they introduce inaccuracies to the initialization of our minima adjustment scheme (Figure 2.3).

For these reasons, intermediate values render better results. Concretely, a good agreement was empirically obtained for $\delta = 0.4$, which resulted in neither omission nor addition of minima in comparison with the data retrieved from the ECG signal. Theoretically this value is also valid given that variability in the heartbeat frequency above 40% of the mean is not usually seen in patients without severe cardiac arrhythmia.

2.3 Results

The proposed method was validated using IVUS images with a synchronized ECG signal. A manual offline ECG gating was taken as ground truth for comparison purposes, where a specialist determined the frames at the R-wave peak by inspection of the ECG signal. Moreover, other state-of-the-art methods described in the literature were also implemented, namely Absolute Intensity Difference (AID) [125], Correlation Dissimilarity Matrix (CDM) [286] and Motion Blur (MB) [58]. It is worth noting that the image features combined by our method are the ones presented in CDM and MB. A direct comparison between the three methods is useful to assess the improvement introduced by the proposed strategy.

2.3.1 Acquisition of IVUS studies

The IVUS studies were acquired with the AtlantisTMSR Pro Imaging Catheter 40 MHz synchronized with an ECG signal and connected to an iLabTM Ultrasound Imaging System (both by Boston Scientific Corporation, Natick, MA, USA), at the Heart Institute (InCor), University of São Paulo Medical School and Sírio-Libanês Hospital, São Paulo, Brazil. The acquisition frame rate was of 30 FPS performing for each frame 256 radial scans with 256 intensity measurements. The generated frames of 512×512 pixels in cartesian coordinates present a resolution of $17.5 \mu\text{m} \times 17.5 \mu\text{m}$ per pixel.

The acquisition was performed during a diagnostic or therapeutic percutaneous coronary procedure. Vessels were imaged during automated pullback at 0.5 mm/s, but additional manual runs, not used in the subsequent analysis, were performed. Overall, multiple

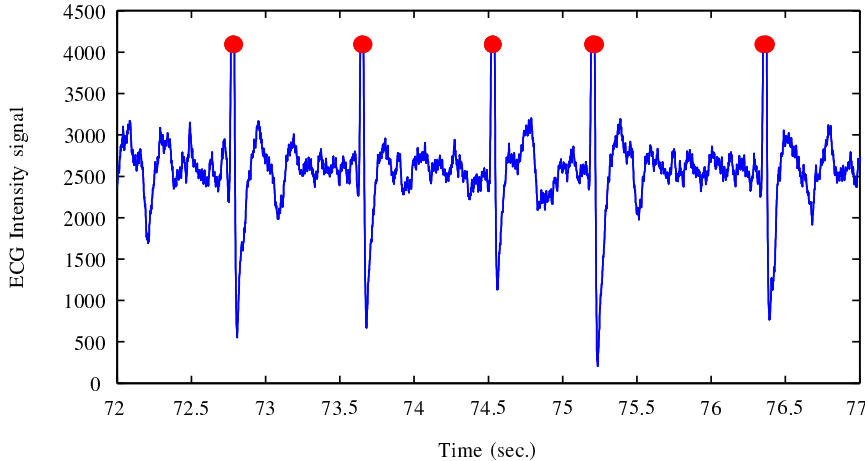


Figure 2.5: Electrocardiogram (ECG) signal depicting red marks made by the specialist at R-wave peak instants. The marks are then associated to the frames acquired at these instants according to the IVUS DICOM header. This example shows 5 seconds of the ECG signal synchronously acquired during the IVUS pullback by the iLabTM Ultrasound Imaging System.

runs where performed on 21 patients leading to 61 IVUS studies with synchronized ECG signal. The IVUS sequence length reported in these studies comprises 2974.8 ± 1133.8 frames (mean \pm SD). Images from different coronary arteries (left anterior descending artery - LAD, 31 studies; right coronary artery - RCA, 8 studies; left circumflex artery - LCx, 12 studies; and obtuse marginal and diagonal arteries, 10 studies) at different mean cardiac frequencies (from 65 BPM to almost 105 BPM) including cases with severe stenosis, stent deployment and mild arrhythmia (presence of ≤ 5 extrasystole in 9 studies) were analyzed.

After the procedure, a manual offline ECG gating was performed for each study. Specifically, a specialist marks, as shown in Figure 2.5, the elapsed time at each R-wave peak over the ECG signal of each study. Using that information, the period of each cardiac cycle in the studies is calculated. As the IVUS study is synchronized with the ECG signal, the R-wave peak frames are identified and the gating of this phase is used as ground truth. As the time between the beginning P-wave and the R-wave peak rarely varies, it is reasonable to infer the period between the steady phase as the period between the R-wave peaks.

Manual R-wave peak segmentation reliability was estimated by calculating intra- and inter-observer variability in terms of the Bland-Altman limits of agreement (LA) and the coefficient of variability (%CV). Thus, 3 specialists processed 3 times 5 studies (with 77, 112, 130, 130 and 165 R-wave peaks giving $N = 614$ samples). For intra-observer variability, we compare among the repeated segmentations of a fixed specialist to observe the degree of variation. The results are presented in Table 2.1 where it is seen that variations within each specialist are less than 1 frame (maximum variation of 0.3634 frames for the specialist 3 between segmentations 1 and 3), showing negligible variability in the segmentation process. Inter-observer variability was addressed by estimating the mean observation, \bar{O}_i , corresponding to the i -th specialist. The values of \bar{O}_i are simply the mean values of each R-wave peak time from the 3 repeated segmentations of the i -th specialist. Then, \bar{O}_i represents the mean intra-observer value which minimize intra-observer bias. The results presented in Table 2.2 suggest even lower variability than intra-observer analysis (worst case presented a discrepancy of 0.184 frames between specialists 2 and 3), indicating a high level of agreement between specialists about this ground truth.

	S_1 vs S_2		S_1 vs S_3		S_2 vs S_3	
	LA (in frames)	%CV	LA (in frames)	%CV	LA (in frames)	%CV
O_1	-0.0130 ± 0.2351	0.012	-0.0098 ± 0.2553	0.014	0.0033 ± 0.2285	0.012
O_2	-0.0081 ± 0.2647	0.014	0.0016 ± 0.2457	0.013	0.0098 ± 0.2210	0.012
O_3	0.0033 ± 0.3521	0.019	0.0163 ± 0.3471	0.018	0.0130 ± 0.3425	0.018

Table 2.1: Intra-observer variability from 3 segmentations (S_1 , S_2 and S_3) per specialist (O_1 , O_2 and O_3). Bland-Altman limits of agreement (LA) and coefficient of variations (%CV) are presented for each comparison.

	LA	%CV
\bar{O}_1 vs \bar{O}_2	-0.0141 ± 0.1196 frames	0.006
\bar{O}_1 vs \bar{O}_3	-0.0038 ± 0.1729 frames	0.009
\bar{O}_2 vs \bar{O}_3	0.0103 ± 0.1737 frames	0.009

Table 2.2: Inter-observer variability from mean values of the 3 intra-observer segmentations. Bland-Altman limits of agreement (LA) and coefficient of variations (%CV) are presented for each comparison.

2.3.2 Features correlation

The main purpose of constructing a combined signal from two image features is to increase the robustness of the heart motion estimation. Thus, we seek for features uncorrelated that at the same time present a close motion pattern associated with the heartbeat. As the features present a low correlation, their combination presents minimal redundancy, implying that the motion is characterized in different manners by each feature.

In that manner, we analyze the correlation between the features s_0 and s_1 , by computing the Pearson’s linear correlation between them. As result, we obtain a mean correlation of -0.164 ± 0.266 (mean \pm SD), presenting scarce redundancy of information. Meanwhile, both features present a similar motion frequency, characterized by f_m from (2.2.7), showing a subtle absolute difference of 0.0146 ± 0.0263 heartbeats per second (mean \pm SD) along the studies. The resemblance in f_m allows us to infer that both feature reproduce a pseudo-periodic pattern closely associated with the transducer motion.

2.3.3 Error measurements

The proposed image-based gating method was assessed using two quality measures. For the sake of simplicity, we introduce some definitions first. Let us generalize the definition of $p(i)$ as the time at which a particular cardiac event occurs at the i -th heartbeat of the study, e. g., the R-wave peak in the ECG signal ($p^{\text{ECG}}(i)$) or the minima in an image-based method ($p^{\text{IB}}(i)$). From $p(i)$ then we can derive $t_{\text{HB}}(i)$ and $p_m(i)$, the heartbeat period and the middle time instant of the i -th heartbeat of the study, as

$$t_{\text{HB}}(i) = p(i+1) - p(i)$$

$$p_m(i) = \frac{t_{\text{HB}}(i)}{2} + p(i).$$

The **mean error per heartbeat**, ε_{HBP} , measures the mean period difference between the image-based and the offline ECG gating method. For each heartbeat its period, obtained from the image-based gating, is compared with the nearest period from the ECG

gating as

$$\varepsilon_{\text{HBP}} = \frac{\sum_{i=1}^M \left| t_{\text{HB}}^{\text{IB}}(i) - t_{\text{HB}}^{\text{ECG}} \left(\min_j (|p_m^{\text{IB}}(i) - p_m^{\text{ECG}}(j)|) \right) \right|}{M} \quad (2.3.1)$$

where M is the quantity of cardiac events detected by the image-gating method and $(\cdot)^{\text{IB}}$ and $(\cdot)^{\text{ECG}}$ are quantities associated with the image-based gating method and the offline ECG gating method, respectively. Using this error measurement, the omission or erroneous detection of the $p(i)$ event does not affect the error estimation in the next cardiac cycles. Notice that the quantity of heartbeats in a study according to the gating method is equal to $M - 1$.

The **phase detection error**, ε_{PD} , measures the difference between the R-wave peak detected by the image-based and the ECG gating methods. As previously mentioned, the time elapsed between the P-wave and the R-wave peak rarely varies (independently of the heartbeat frequency variations), then we can identify the R-wave peak frames in the image-based gating by displacing all P-wave frames with the same offset. As we want to retrieve the most similar phase to the R-wave peak, we calculate this offset as the mean distance between $p^{\text{IB}}(i)$ events to the p^{ECG} , given by

$$\mu_{\text{PD}} = \frac{\sum_{i=1}^M \left[p^{\text{ECG}} \left(\min_j (|p_m^{\text{IB}}(i) - p_m^{\text{ECG}}(j)|) \right) - p^{\text{IB}}(i) \right]}{M}. \quad (2.3.2)$$

Thus, we calculate the error at each heartbeat as the distance between the p^{ECG} instant and the p^{IB} displaced by μ_{PD} , namely

$$\varepsilon_{\text{PD}}(i) = p^{\text{IB}}(i) + \mu_{\text{PD}} - p^{\text{ECG}} \left(\min_j (|p_m^{\text{IB}}(i) - p_m^{\text{ECG}}(j)|) \right), \quad (2.3.3)$$

with $i = 1, \dots, M$.

2.3.4 Method performance

The performance of the CCB method was evaluated through comparisons with the following methods: Absolute Intensity Difference (AID), Correlation Dissimilarity Matrix (CMB) and Motion Blurring (MB). The comparison of our method against [286] and [58] shows the improvement obtained by the proposed integration of both motion signals.

In the first comparison, the capability of the different methods for predicting the cardiac cycles periods is compared. The heartbeat periods estimated via the ECG offline method were used as ground truth. In Figure 2.6 the error ε_{HBP} for the four methods is shown. The CCB method presents the best behaviour as indicated by the linear fitting in the same figure, followed by the AID method. The variability of the error is also smaller for the CCB method, while higher cardiac frequencies tend to increment the error.

An additional comparison between the image-based methods and the ECG offline gating method is displayed in Figure 2.7. In this case, we present the heartbeat period estimation for each heartbeat in every study (61 studies). The Bland-Altman coefficient of reproducibility ($\text{RPC} = 1.96 \times \text{SD}$) is the smallest for CCB, $\text{RPC}(\%) = 0.23 \text{ sec. (26\%)}$, followed by AID with $\text{RPC}(\%) = 0.36 \text{ sec. (41\%)}$. This implies that the CCB method is the closest one to the manual offline ECG gating. The proposed method also presents a more robust estimation of the heartbeat period evidenced by the reduced dispersion and range of samples in the y-axis (see Figure 2.7).

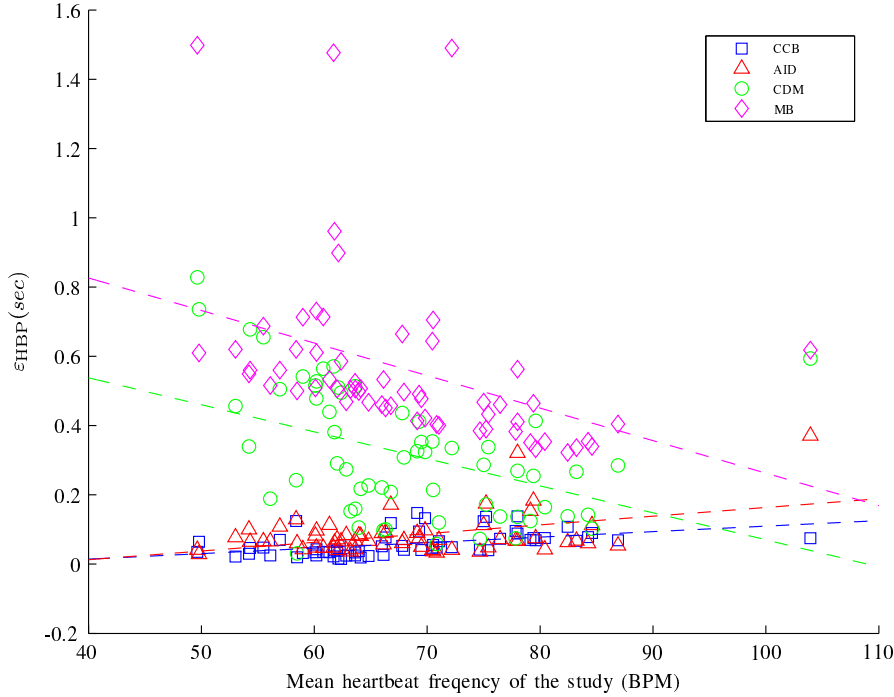


Figure 2.6: Mean error per heartbeat, ε_{HBP} , at each study for the different gating methods. The dashed lines represent a linear fitting (via linear least-squares) to describe the error trend in each method.

Using the acquisition time of frames at R-wave peak according to the manual offline ECG gating, we evaluate the performance of the methods. Since the R-wave peak is the only cardiac phase that we can extract precisely from the ECG, this is the only indicator where the success in recognizing a specific cardiac phase can be measured. For this reason, the ε_{PD} error is a trustful indicator of success when using p^{ECG} as the R-wave peaks. As the mean of this error is zero by construction, we are interested in its standard deviation along each study as given by the offline gating and by the ground truth. The value of this indicator is presented in Figure 2.8 where the mean and maximum standard deviation for the 61 studies using each of the 4 methods are shown. The CCB method presents the most accurate results, with mean SD of ε_{PD} being 0.165, 0.251, 0.282 and 0.475 for the CCB, AID, CDM and MB methods, respectively.

From the analysis of these results, it is seen that MB presents outliers exceeding 0.8 seconds (see Figure 2.6) caused by the omission of several frames associated with the steadiest phase. In these studies the transducer motion is too low to produce the blurring effect, at least not along the full study. Then, the motion signal poorly represents the cardiac pulsatility and does not present the characteristic quasi-periodic pattern (the frames extracted do not represent any specific phase, see Figure 2.8). CCB circumvents this issue by the adjustment of α as proposed in (2.2.13). As s_1 shows high variation of heartbeat periods, α is adjusted to values closer to 1 giving major weight to s_0 data (which resembles the signal used in AID).

In addition, we compare the number of heartbeats estimated by each method against the ground truth. Here, it is evident that the methods using band pass filter around the mean cardiac frequency (i.e. CCB and AID) delivered better results (see Table 2.3). This is given by the low heartbeat frequency variation within a study. As extra systoles may occur in a study from time to time, the cardiac frequency remains almost invariant and the use of this information is fundamental to provide robustness to the method. Methods like CDM and MB do not assume low variation of the cardiac frequency, making

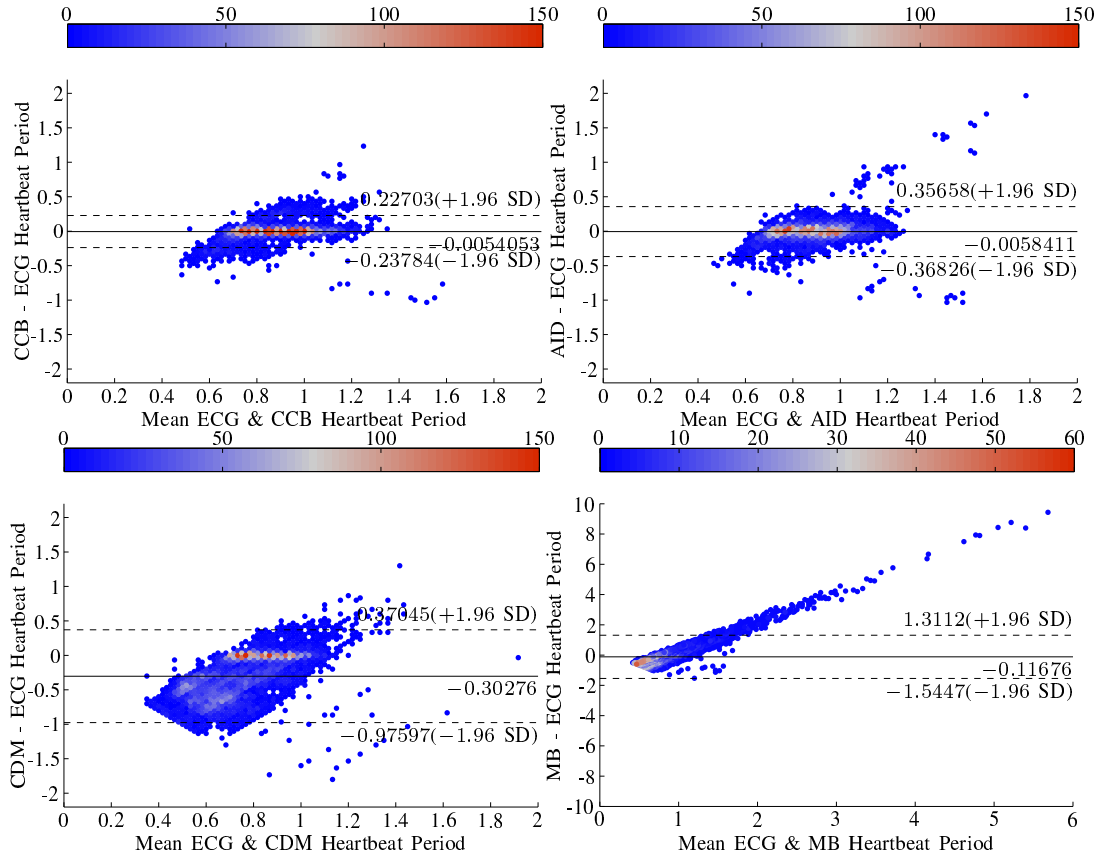


Figure 2.7: Bland-Altman plots comparing the heartbeat periods measured by the offline electrocardiogram method (assumed as ground truth) and : (a) the CCB method presenting $\text{RPC}(\%) = 0.23 \text{ sec}$ (26%); (b) the AID method presenting $\text{RPC}(\%) = 0.36 \text{ sec}$ (41%); (c) the CDM method presenting $\text{RPC}(\%) = 0.67 \text{ sec}$ (90%); (d) the MB method presenting $\text{RPC}(\%) = 1.4 \text{ sec}$ (170%). Each sample represents one heartbeat period in one of the studies. The color indicates the amount of samples overlapped in the same position of the diagram, horizontal solid line stands for the mean difference and dashed line depict the limits of agreement ($1.96 \times$ standard deviation of the differences). Plots (a)-(d) contain respectively 6802, 6614, 10077 and 7651 samples corresponding to 61 studies. RPC: reproducibility coefficient; AID: absolute intensity difference method; CMB: correlation dissimilarity matrix method; MB: motion blurring; CCB: combined correlation and blurring method.

them potentially capable of detecting any kind of cardiac variations. Nevertheless, these methods would also be capable of detecting extremely shorts heartbeats (most of the times physiologically meaningless) which would yield an incoherent phase gating. Particularly, CCB method presents a better performance compared to the other methods (even against AID) diminishing the number of frames omitted or oversampled for the extracted cardiac phase. For the CCB, less than 6 beats per study are missed or overestimated presenting a mean error of 1.492 ± 0.977 heartbeats (mean \pm SD) along all the studies. As consequence, the proposed method presents a larger proportion of phase coherent data extracted from the study for a specific cardiac phase.

From the different comparisons, AID and CCB reported the closest heartbeat period detection mainly because the use of a band filter around the mean cardiac frequency of the study. Their motion signals present low heartbeat period variations (as higher frequencies were removed), which is physiologically expected. Thus, an accurate prediction of mean heartbeat periods and number of heartbeats present in the study is obtained. However,

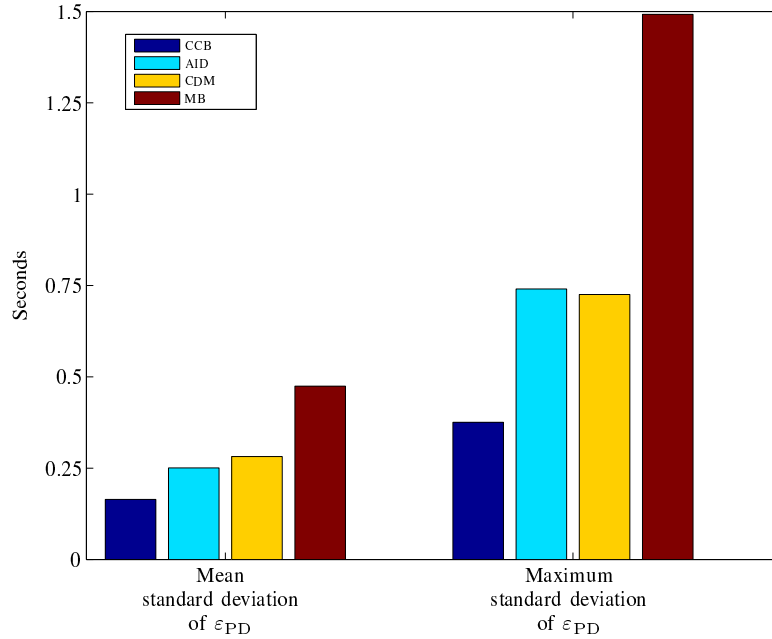


Figure 2.8: Mean and maximum standard deviation of the phase detection error, ϵ_{PD} , for each of the gating methods.

Id	CCB	AID	CDM	MB
Mean error	1.492	4.246	52.984	24.623
SD error	0.977	3.567	48.028	19.068
Maximum error	6	22	219	80

Table 2.3: Error in the number of heartbeats (frames in the longitudinal view) detected by each gating method. The error in the i -th study is calculated as $|B^{\text{ECG}} - B^{\text{IB}}|$ where B^{ECG} and B^{IB} are the heartbeats estimated in the ground truth and in the image based method, respectively.

note that AID is not phase consistent, i.e. the identified frames are not necessarily associated with the same cardiac phase, as can be shown in Figure 2.8. In turn, CCB underpins this issue by combining the motion signal s_0 (associated with frames correlation) with another uncorrelated motion signal (associated with blurring). The resulting signal intensity decreases at the steadiest phase frames while increases at the remaining phases frames. Then, when minima are adjusted by the iterative harmonic scheme, we obtain a more accurate steadiest phase identification.

2.3.5 Mean cardiac frequency estimation

Using the ground truth, we computed the mean cardiac frequency, f^{ECG} , as the quantity of heartbeats detected over the study time duration. Then, we compared f^{ECG} against f_m calculated using (2.2.7) in terms of their absolute difference, i. e., $\epsilon_{\text{HF}} = |f^{\text{ECG}} - f_m|$. The comparison shows an error of 1.109 ± 0.861 BPM (mean \pm SD), and always minor than 4.126 BPM. This allows estimating the mean cardiac frequency of the patient with reasonable accuracy, only by using the IVUS image data.

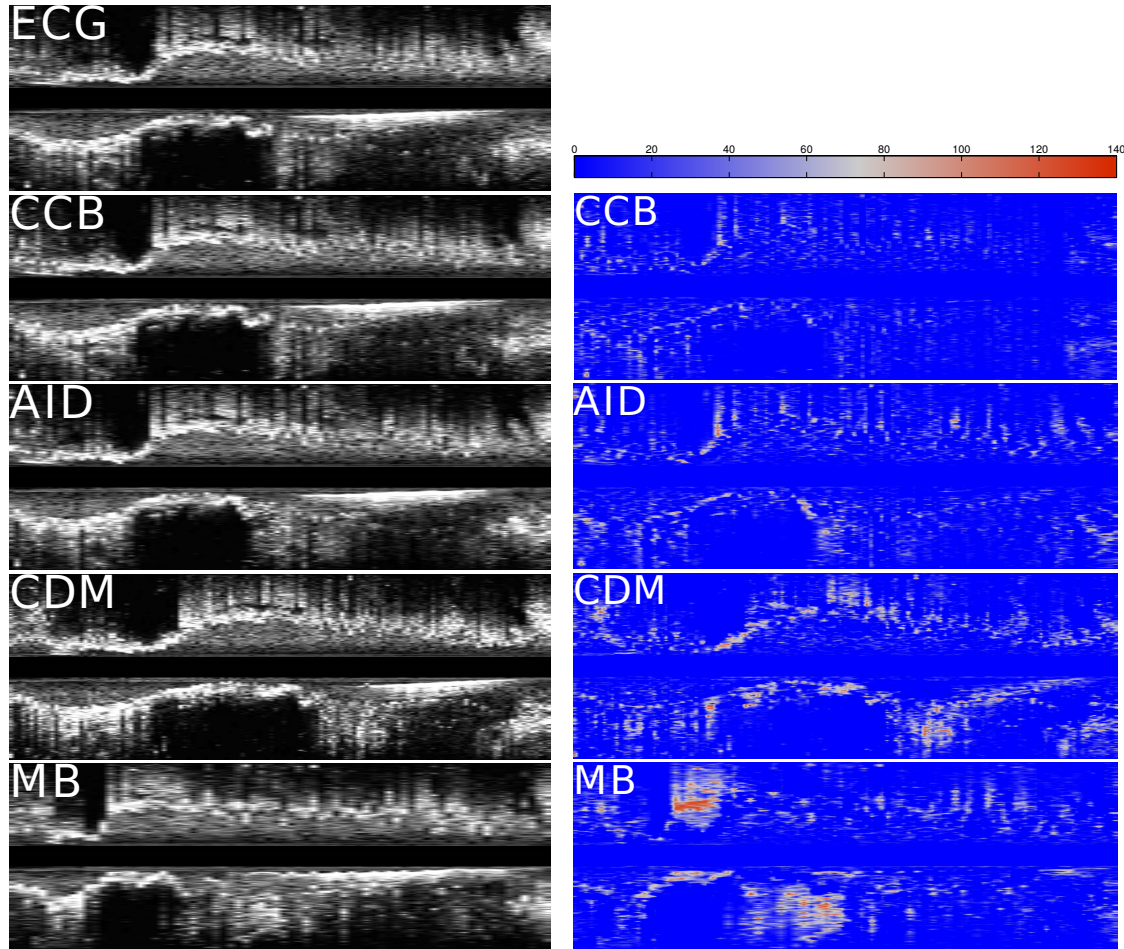


Figure 2.9: Longitudinal views of an IVUS study processed with the different gating methods: (left column) standard longitudinal view; (right column) absolute pixel-to-pixel difference versus the electrocardiogram (ECG) offline method.

2.3.6 Gating comparison

As a qualitative comparison, the corresponding longitudinal views after the gating process with the different methods for a particular IVUS study are shown in Figure 2.9. The endothelial layer gated by the offline ECG method clearly resembles the result of the CCB method more than those obtained with other methods. This comparison is accentuated when looking at the pixel-to-pixel differences between the ground truth (ECG) and the different methods (see Figure 2.9, right column). This can be particularly appreciated at the bifurcation presented in the middle section of the sequence, where delay or anticipation of the branch origin occurs for other methods (CDM, AID and BM). Moreover, a substantial reduction of *saw tooth artifact* is particularly appreciated CCB and AID methods.

The distribution of the differences between the image based and the offline gating method is not homogeneous. As shown in Figure 2.10 the maximum differences are located at the middle part of the vessel where the bifurcation is located. This encourages the use of features that correctly measure the motion at places where topological changes occur. In fact, small differences are seen for the CCB method, where blurring information reduces motion misidentification.

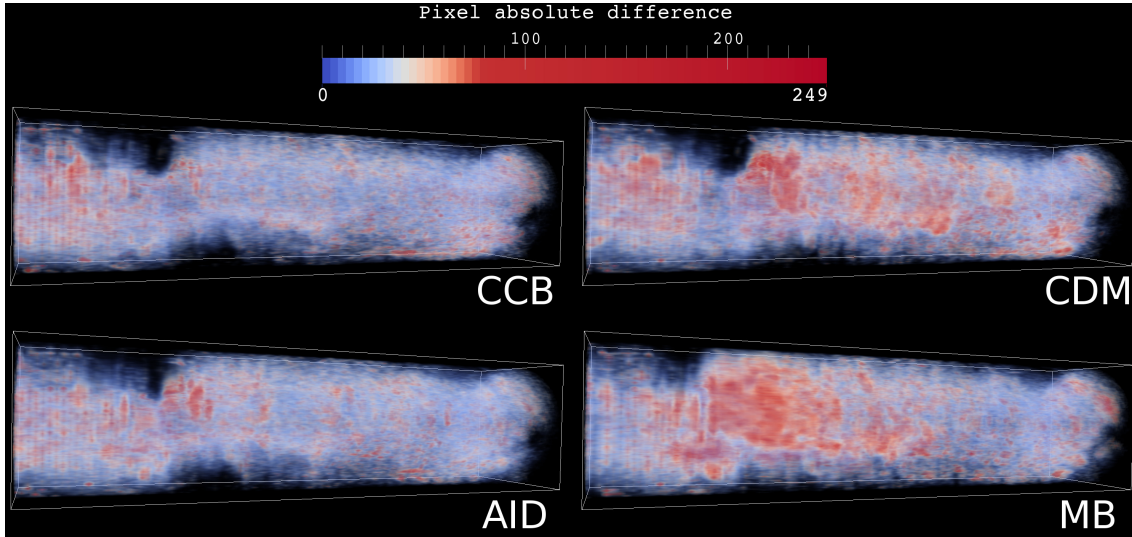


Figure 2.10: Volume rendering corresponding to the absolute pixel-to-pixel difference of the volumes gated by the image based gating method and the manual offline electrocardiogram (ECG) gating. The study visualized is the same as in Figure 2.9.

2.3.7 Computational cost

The CCB method was implemented partially in MATLAB and C++ languages. The signal s_i calculation is performed in C++ parallelized at frame level with OpenMP. Parameter α estimation (see equation (2.2.13)) and the iterative filtering scheme are performed in MATLAB using *parfor* parallelization for α estimation.

For the execution of the method, we used a workstation with an Intel Xeon CPU E5-2620 at 2.00 GHz processor and Kingston 99U5471-031.A00LF at 1333 MHz (latency of 27 ns) RAM memory over Ubuntu 14.04.1 LTS. The method execution process was parallelized into 12 threads for all the measurements reported in this section. As performance measurement, we use the wall clock time because we are interested in showing that the execution time is reasonable for clinical use. To diminish the operative system time variations during the method execution, we run 5 times each study processing, and store only the mean wall clock time from these executions.

The results show that the execution time is 20.63 ± 8.11 seconds (see Figure 2.11) which in comparison to the acquisition time of the study (99.16 ± 37.79) represents 20%. This overhead is found to be suitable for medical practice since it allows to perform image gating during the diagnostic or therapeutic procedure. In a closer analysis, it is seen that the time consuming tasks are the α estimation and signal computation (see Figure 2.11 and 2.12). Both tasks could be fully parallelized with a maximum of A and N threads, respectively, where A is the number of α candidates to be tested in (2.2.13) and N is the quantity of frames in the IVUS study. As reported in Section 2.2.4.1 and 2.3.1, $A = 1000$ and $N = 2974.8 \pm 1133.8$ frames which allows a theoretical speed up of the methods until two order of magnitude from the reported results. Finally, almost all the estimation time for the value of α is spent in the iterative adjustment of $p(i)$ (see Figure 2.12). This task is implemented in MATLAB and parallelized using *parfor*. Clearly, its performance can be improved by reimplementing the task in C++ with OpenMP parallelization.

2.3.8 Limitations

Known limitations of this method, as well as for other methods using a low/band-pass filters for the spectral filtering of a motion signal, are related to the treatment of

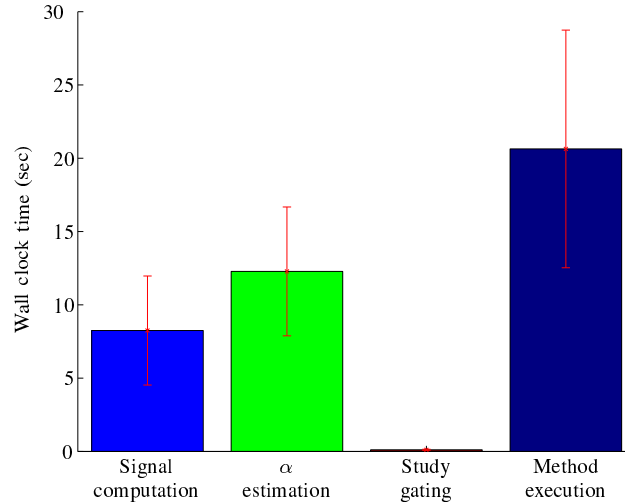


Figure 2.11: Mean processing time of the 61 IVUS studies showing the time for: the signal computation (see equations (2.2.2) and (2.2.3)), α estimation (see equation (2.2.13)), study gating (Section 2.2.2 and 2.2.3) and total method execution time.

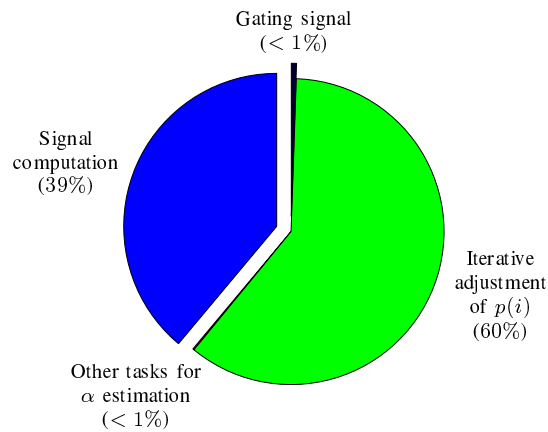


Figure 2.12: Percentage consumed by each method subtask during the execution. The task α estimation presented in Figure 2.11 here is subdivided in the tasks: iterative adjustment of $p(i)$ and other tasks for α estimation.

IVUS studies in patients with large heart rate variability, such as cardiac dysrhythmia, or at locations with no vessel movement at all, such as infarcted areas of the heart.

2.4 Final remarks

A novel method to improve the IVUS gating by combining different image motion features has been presented in this chapter. Particularly, the proposed strategy, called Combined Correlation and Blurring (CCB), has shown to outperform other methods that use the same image features separately for the 61 processed IVUS studies. The proposed method is capable of identifying cardiac phases, heartbeats and mean cardiac frequency along the studies in an accurate and robust manner for a wide range of situations (severe stenoses, stents, different coronary vessels and studies from 65 to almost 105 BPM). This has been verified through direct comparison with the cardiac phase associated to the

R-wave peak, retrieved from a manual offline ECG gating with scarce intra-inter observer variability.

In terms of heartbeat detection and cardiac period estimation, the CCB method showed more accurate results than the other gating techniques. The cardiac phase detection performed by the CCB method presents the smallest error between the image-based gating methods, rendering the most accurate gating for IVUS study. From the comparisons carried out in this work, it presents the lowest frame omission and/or oversampling at each heartbeat, as direct consequence of the correct identification of the heartbeats along the study.

In contrast to the time consuming manual offline ECG gating, it is worthwhile to highlight that our method is fully automatic, independent from other studies or equipment and it is applicable to pre-existing IVUS studies. Also, the computational overhead of this method to the IVUS acquisition time is a 20%, allowing its use for medical practice during diagnosis as well as during therapeutic coronary procedures. All these aspects permit the direct application of the CCB method as a pre-processing stage for filtering, segmentation or reconstruction methods, which would be greatly benefited from the increase of accuracy and time consistency of the so-extracted cardiac phases from the IVUS study.

Chapter 3

Spatio-temporal registration

After the IVUS gating presented in the previous chapter, a new problem arises from the so-obtained image volume data: the gated volumes are spatially inconsistent. To correctly map one region of the vessel across different cardiac phases, e.g. to estimate the deformation of the atherosclerotic plaque or the motion of a stent, a spatial registration between the volumes corresponding to the different cardiac phases is required.

In this chapter, we address the registration problem in IVUS studies by proposing a novel methodology based on a block matching variational approach. We identify the key ingredients for the registration process (vessel wall specificity for transversal registration, longitudinal locality for comparison, maximum likelihood estimators for ultrasonic imaging) and study their sensitivity to deliver an optimal cardiac phase registration.

3.1 Background

During the IVUS acquisition, the piezo-electric sensor records the cross-sections of the vessel at a constant known pullback velocity. Although a spatial arrangement of vessel cross-sections is available after an IVUS procedure, the heart contraction imprints an undesired relative motion occurring between the transducer and the vessel (usually referred to as cardiac dynamic component), misleading frame location during non-diastolic phases as well as the position and rotation of the wall structures with respect to the transducer. The transducer relative motion to the vessel can be decomposed in two spatial components, the transversal (or in-plane) motion and the longitudinal (or axial) motion. The former produces the translation and rotation of the vessel structures between two different corresponding images, while the latter induces a proximal/distal displacement in addition to the a priori known motion imposed by the transducer pullback. As consequence, the reconstruction of the vessel wall is hindered for non-diastolic phases since vessel cross-sections are not equally spaced in the longitudinal direction and the transversal motion distorts the geometrical description of the vessel wall. This affects the processing of image-derived quantities either for diagnosis or for setting input data for computational models such as those used in CFD simulations or in tissue characterization (e.g. virtual histology, elastographies or palpographies).

Early approaches for IVUS study registration have focused only on the transversal motion component. The goal of these works was the enhancement of vessel structures alignment to improve elastography outcomes. The main problem for IVUS registration is to deal with low signal-to-noise ratio of the ultrasound and the speckle noise characteristics. Early works ([94, 158, 189, 225]) performed a rigid registration of two adjacent images using the underlying radiofrequency (RF) data of the IVUS study and block matching strategies with different maximum likelihood estimators (MLE) such as sum of absolute differences (SAD) ([94, 158, 189]), sum of square differences (SSD) ([158, 189])

or normalized cross-correlation (NCC) ([158, 225]). Subsequent approaches focused on IVUS image data which are available from traditional ultrasonic equipments. Several works applied SAD ([85, 87]), SSD ([243]), NCC ([174, 355, 356]) and mutual information ([174]) as MLE to match tissue patches between different IVUS images. Although these approaches delivered an improvement for registration, the MLE used were not suitable for speckle noise tracking. This issue can be circumvented by using ultrasound specific estimators as proposed in [324], which account for the log-compressed multiplicative noise within the images. Other approaches performed the transversal registration by aligning the centroids of the lumen in the two images ([116, 134, 193, 194, 281, 297, 310, 356]). To estimate the lumen centroid, a segmentation of the lumen is needed which is a time consuming task difficult to automatize. To overcome this, some authors proposed to approximate the lumen centroid as a gray intensity centroid ([134]) or the centroid of a simplified lumen geometry ([116, 281]). Some cross-section registration methods may present inaccurate results due to substantial variations in the lumen geometry (inaccuracy in lumen estimation, sites of branching or stent boundaries) given that in these cases the centroids alignment is not associated with the vessel wall alignment. Particularly, [116, 134] estimated the rotation component of the rigid motion using a Fourier analysis, resulting in a more robust approach. Non-rigid registration approaches were also developed in [13, 14, 15, 83, 84, 85, 86, 87, 170, 273]. Amores et al. ([13, 14, 15]) proposed the use 1D correlograms to analyze local and global features of the image and its gradient field to find the best correspondence between frames, although it requires lumen segmentation. Kautozian et al. ([170]) presented a Markov random field discrete multi-labeling scheme to match histological and IVUS image data. Other authors ([83, 84, 85, 86, 87, 273]) formulated an optimization problem to find the displacement field that maps the reference frame to the target one. Finally, a comparison study between different transversal registration approaches (rigid transformation, affine transformation, B-spline-based non-rigid free form deformation and daemons) was presented in [20], assessing their performances to map calcified lesions.

In turn, the longitudinal motion component has usually been neglected. In [21], an average axial displacement from 1.5 ± 0.8 mm in a 0.016 mm interframe acquisition was observed. Due to the catheter migration, the cross-sectional region observed in systolic phases is more proximal than expected (a mean offset of 93.75 frames) and, in the context of elastography, the derivation of associated strains occurring in the arterial wall can become extremely inaccurate because of the changes in the topological and tissue composition at these sites. Contributions addressing the longitudinal registration were reported in [7, 8, 218, 323]. In [218], a method for rigid longitudinal motion was proposed to align each cardiac phase with the diastolic phase of the study. Non-rigid approaches based on dynamic time warping (DTW) were proposed such as the extremes path search ([7, 8]) and minimal variance matching ([323]) methods.

More complete schemes that treat both motion components were presented in [193, 194, 310, 354, 355]. These works performed longitudinal prior transversal registration of two cardiac phases of the study. The longitudinal registration in [193, 194, 310, 354] requires user interaction to determine the frames at carina bifurcations (landmarks used to pair the bifurcation frames) and assumes a linear fitting for the remaining frames. The first non-rigid longitudinal registration method was proposed in [355] using a 3D graph path finding process where the segmentation of the lumen and external elastic membrane is a compulsory step.

In the present chapter we address the problem of transversal and longitudinal registration so that both motion components can be suitably compensated by using MLE specifically tailored for ultrasound speckle noise (see [78, 324]). Transversal registration is performed through the formulation of an optimization problem for which the rigid transver-

sal motion identified is the one that maximizes a given cost functional depending on the MLE. In addition, longitudinal registration is performed with a weighted MLE function that allows to align two different IVUS cardiac phase sub-sequences. Three strategies are considered to solve the problem. The first one is a strongly coupled (computationally demanding) method in which both motion components (transversal and longitudinal) are obtained simultaneously. The second and third strategies solve both motion components in a decoupled manner (resulting in computationally cheaper procedures), either considering first the longitudinal and then the transversal registration problems, or first the transversal and just then the longitudinal. Preliminary results of a decoupled approach (which performs longitudinal and then transversal registration with a normalized cross-correlation function as MLE) were reported in [211, 213]. All strategies are compared in terms of performance and accuracy on in-vivo patients, and descriptions of transducer longitudinal displacement along the IVUS acquisition are discussed. The results obtained by these strategies show that no segmentation of the vessel wall is required for the registration process, which improves reproducibility.

3.2 Methodology

In this section, we introduce the mathematical framework for the registration process. This is composed by the IVUS preprocessing, the longitudinal registration and the transversal registration. Firstly, we define the region of interest (ROI) used during the registration process. The subsequent stages deal with the longitudinal and transversal components of the transducer motion.

Then, through the integration of these stages, three registration algorithms are proposed. Two decoupled strategies are tested, namely solving first the longitudinal registration and then the transversal (DLT technique), and inverting the registration stages (DTL technique). A fully coupled strategy is also considered. More details are given in Section 3.2.5.

3.2.1 IVUS preprocessing

The arterial wall is better characterized by the structures lying in the region between the lumen and the external elastic lamina [192, 224]. However, the identification of this region through any image segmentation procedure requires, to some extent, manual setting and it is also time-consuming. Moreover, the development of robust and reproducible computational methods to accomplish this task is still an open problem [169]. Therefore, to analyze the sensitivity of the registration with respect to the vessel wall specificity, we define two ROIs: (i) a manually segmented vessel wall region (VWR) and (ii) the full image region (FIR) which does not require segmentation. The manual segmentation for the VWR ROI is performed by a specialist to obtain an accurate and robust description of the vessel wall, which is not guaranteed by automatic segmentation methods.

Let J_k be the k -th frame of the IVUS study ordered according to the original acquisition sequence. The ROI for the k -th frame $J_k(x, y)$, is defined as a binary mask $M_k(x, y)$ with the same size of an IVUS frame. Each value of M_k indicates whether the associated pixel in J_k belongs to the ROI or not. Similarly, we define $M^{\text{DR}}(x, y)$ and $M_k^{\text{GW}}(x, y)$ as the binary masks associated to the down-ring and the guidewire artifacts. These masks contain 1s at the positions where the artifact is found and 0s at remaining locations. The construction of the artifact masks is detailed in the Chapter A.

The FIR for the k -th frame is defined as

$$M_k^{\text{FIR}} = \neg(M^{\text{DR}} \vee M_k^{\text{GW}}). \quad (3.2.1)$$

where \neg and \vee are the logical operators NOT and OR respectively.

The VWR requires the elimination of regions outside the external elastic lamina and inside the vessel lumen from the ROI defined above. For this task, the user manually performs a segmentation of the EEM and lumen areas by picking points which are then interpolated with a cubic spline curve. To avoid lack of pixels in the mask, especially in cross-sections corresponding to healthy arterial tissues, the EEM curves are radially displaced by 20 pixels. Then, we create a mask, M_k^{VW} , where the area comprised between the EEM and lumen has value of 1, and 0 otherwise. Thus, the VWR is defined as

$$M_k^{\text{VWR}} = M_k^{\text{FIR}} \wedge M_k^{\text{VW}}. \quad (3.2.2)$$

where \wedge is the logical operator AND. The resulting masks for a given frame in an IVUS study are shown in Figure 3.1.

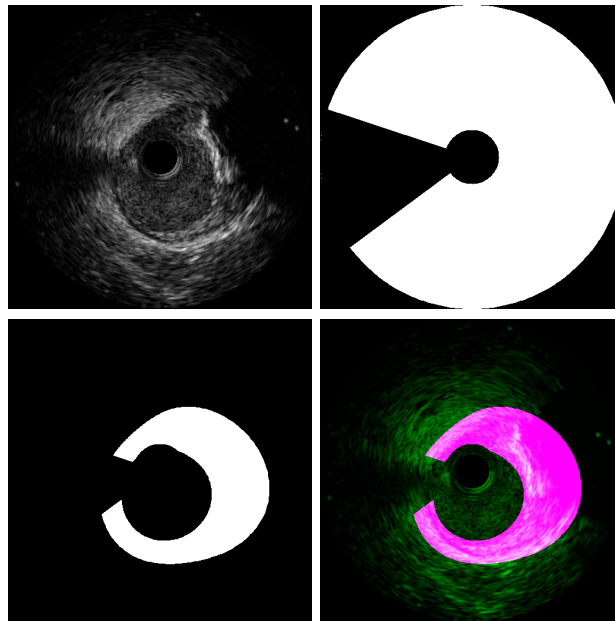


Figure 3.1: Binary masks used for each region of interest (ROI): (top-left) original IVUS image; (top-right) M_k^{FIR} ; (bottom-left) M_k^{VWR} ; (bottom-right) M_k^{VWR} overlapped with the original IVUS image.

3.2.2 Maximum likelihood estimator for block matching

For the development of a registration mechanism that effectively tracks the tissue vessel displacements, we require a function capable of identifying the same tissue composition region in different images. This task is not trivial due to the speckle noise present in the ultrasonic images.

Based on the assumption that the noise is coherent and correlated to the microstructures of tissues [3], some authors justify the use of normalized cross-correlation, sum of absolute differences or sum of squared differences functions as appropriate maximum likelihood estimator (MLE) for speckle tracking. However, this assumption assumes that local speckle noise is only generated by local micro-structure factors, neglecting the contribution of surrounding tissues, reflexions, proximal signal absorption, among others. Modeling all the sources of speckle noise in an MLE is a challenging task, and for this reason other authors have treated it simply as uncorrelated noise.

In this second approach, other authors suggest that the speckle phenomena is characterized by a Rayleigh distribution [327]. Evidence for this assumption is well documented

for low frequency ultrasound probes (< 20 MHz), although this distribution seems not be as precise for higher frequencies [111, 313]. For this latter case, distribution such as Rician [154], Nakagami [295], K [96, 157], Weibull [106] and Generalized Gamma (GG) [222, 267, 303] have presented a better fit against experimental measures. Particularly, we choose to employ the GG distribution because it has shown an accurate fit for high frequency transducers similar to IVUS (28 MHz in the work of [267]).

Then, we developed three alternative MLEs to establish the best likelihood function for IVUS registration: i) a normalized cross-correlation; ii) an estimator for Rayleigh noise distribution; and iii) an estimator for GG noise distribution. To derive the MLEs associated with each noise distribution, we introduce some useful notation. Let us define an IVUS images u and a noiseless image v of the same vessel cross-section related as

$$u(s) = v(s) \odot \varepsilon \quad (3.2.3)$$

where ε is the noise intensity in the images and \odot is the operator addition or multiplication depending on the noise model. We look for the maximum log-likelihood estimator such that maximizes the data entropy between the two noisy images (similarly as presented in [324]). Recalling the log-likelihood function from information theory with the assumption of conditionally independent noise at each pixel, it follows that

$$\begin{aligned} L(\varepsilon) &= \log P(u|v, \varepsilon) \\ &= \sum_{s \in \Omega} \log P(u(s)), \end{aligned} \quad (3.2.4)$$

where Ω is the image domain containing all pixels and $P(u(s))$ is the probability for intensity $u(s)$ in image u , which in turn depends of image v and the error ε due to (3.2.3). Hence, using the probability theorem to express the image intensity probability based on the error probability density function (PDF), see [252] for more details,

$$P(u(s)) = \frac{P_\varepsilon(\varepsilon(s))}{|u_\varepsilon(s)|}, \quad (3.2.5)$$

where $P_\varepsilon(\varepsilon(s))$ is the error intensity probability, $u_\varepsilon(s)$ is the derivative of u according to ε . Then, we formulate the maximum log-likelihood estimator as

$$L(\varepsilon) = \sum_{s \in \Omega} \log \left(\left(\frac{du}{d\varepsilon}(s) \right)^{-1} P(\varepsilon(s)) \right). \quad (3.2.6)$$

Using this estimator, we derive the Rayleigh and Generalized Gamma MLE functions used for the block matching registration.

3.2.2.1 Normalized cross-correlation estimator

The normalized cross-correlation is defined as follows

$$c(u, v) = \sum_{s \in \Omega} \frac{(u(s) - \mu_u)(v(s) - \mu_v)}{\sigma_u \sigma_v}. \quad (3.2.7)$$

where μ_i and σ_i are the mean and standard deviation of the intensity for the i image. This function is widely used in the literature for texture tracking because the normalization of u and v given by

$$\hat{u}(s) = \frac{u(s) - \mu_u}{\sigma_u}, \quad \hat{v}(s) = \frac{v(s) - \mu_v}{\sigma_v} \quad (3.2.8)$$

allows invariance against additive (normalization of the mean intensity to zero) and multiplicative (normalization of the dynamic range of the image with its standard deviation) constant valued differences.

The works of [320], [279] and [324] suggest that the normalized cross-correlation can be interpreted as a MLE for additive Gaussian noise with mean $E[uv]$.

3.2.2.2 Rayleigh noise estimator

Let us suppose a multiplicative Rayleigh noise over two IVUS images u_1 and u_2 of the same cross-section described by the noiseless image v , i.e., $u_1(s) = v(s) \varepsilon_1(s)$ and $u_2(s) = v(s) \varepsilon_2(s)$. Then, expression (3.2.3) is defined as

$$\begin{aligned} u_1(s) &= u_2(s) \frac{\varepsilon_1}{\varepsilon_2} \\ u_1(s) &= u_2(s) \varepsilon(s), \end{aligned} \quad (3.2.9)$$

where $\varepsilon = \frac{\varepsilon_1}{\varepsilon_2}$. Given that the IVUS images are log-compressed to adjust the dynamic range, we rewrite the previous expression as

$$\begin{aligned} \log u_1(s) &= \log u_2(s) + \log \varepsilon(s), \\ \tilde{u}_1(s) &= \tilde{u}_2(s) + \log \varepsilon(s), \\ \varepsilon(s) &= e^{\tilde{u}_1(s) - \tilde{u}_2(s)}, \end{aligned} \quad (3.2.10)$$

where \tilde{u}_1 and \tilde{u}_2 are the IVUS images. As ε_1 and ε_2 follow a Rayleigh distribution noise given by the PDF

$$P_{\varepsilon_y}(y) = \frac{y}{\sigma^2} e^{-\frac{y^2}{2\sigma^2}}, \quad y > 0, \quad (3.2.11)$$

then ε 's distribution is defined by the division of Rayleigh distributions. In [252] it is shown that the PDF of a random variable z , defined as the ratio of two random variables x and y with the same PDF (P_{ε_y}), is obtained as

$$P_{\varepsilon_z}(z) = \int_{-\infty}^{\infty} |y| P_{\varepsilon_y}(zy) P_{\varepsilon_y}(y) dy. \quad (3.2.12)$$

In our case $P_{\varepsilon_y}(y)$ is Rayleigh distributed, then

$$P_{\varepsilon_z}(z) = \int_0^{\infty} |y| \frac{z}{\sigma^4} y^2 e^{-\frac{z^2+1}{2\sigma^2} y^2} dy, \quad (3.2.13)$$

leading to the following PDF for the ratio of Rayleigh distributions

$$P_{\varepsilon}(y) = \frac{2y}{(y^2 + 1)^2}, \quad y > 0. \quad (3.2.14)$$

Using this noise model, we construct the associated MLE as proposed in (3.2.6) as

follows

$$\begin{aligned}
e(\tilde{u}_1, \tilde{u}_2) &= \sum_{s \in \Omega} \log \left[\frac{1}{\varepsilon(s)^{-1}} P_\varepsilon(e^{\tilde{u}_1(s) - \tilde{u}_2(s)}) \right] \\
&= \sum_{s \in \Omega} \log \left[e^{\tilde{u}_1(s) - \tilde{u}_2(s)} \frac{2 e^{\tilde{u}_1(s) - \tilde{u}_2(s)}}{\left((e^{\tilde{u}_1(s) - \tilde{u}_2(s)})^2 + 1 \right)^2} \right] \\
&= |\Omega| \log 2 + 2 \sum_{s \in \Omega} \left[\tilde{u}_1(s) - \tilde{u}_2(s) - \log \left(e^{2(\tilde{u}_1(s) - \tilde{u}_2(s))} + 1 \right) \right],
\end{aligned} \tag{3.2.15}$$

Similar MLEs may be found in [78] and [324]. Then, we normalize the MLE and neglect the constant contributions to obtain our similarity function

$$c(\tilde{u}_1, \tilde{u}_2) = \frac{1}{|\Omega|} \sum_{s \in \Omega} \left[\tilde{u}_1(s) - \tilde{u}_2(s) - \log \left(e^{2(\tilde{u}_1(s) - \tilde{u}_2(s))} + 1 \right) \right]. \tag{3.2.16}$$

3.2.2.3 Generalized Gamma noise estimator

Now, let us suppose a multiplicative noise over both images u_1 and u_2 , following a GG distribution. The relationship between the IVUS images \tilde{u}_1 and \tilde{u}_2 presented in (3.2.10) still holds. Now, ε_1 and ε_2 are distributed by the PDF

$$P_{\varepsilon_y}(y) = \frac{\gamma}{\alpha^\gamma \nu \Gamma(\nu)} y^{\gamma \nu - 1} e^{-\left(\frac{y}{\alpha}\right)^\gamma}, \quad \alpha, \gamma, \nu, y \geq 0 \tag{3.2.17}$$

where $\Gamma(x) = \int_0^\infty y^{x-1} e^{-y}$. As both images u and v are affected by multiplicative noise, ε is distributed by the division of GG distributions. Following (3.2.12), we calculate the PDF for ε as follows

$$\begin{aligned}
P_{\varepsilon_z}(z) &= \int_{-\infty}^{\infty} |y| \frac{\gamma}{\alpha^\gamma \nu \Gamma(\nu)} (zy)^{\gamma \nu - 1} e^{-\left(\frac{zy}{\alpha}\right)^\gamma} \frac{\gamma}{\alpha^\gamma \nu \Gamma(\nu)} y^{\gamma \nu - 1} e^{-\left(\frac{y}{\alpha}\right)^\gamma} dy \\
&= \left(\frac{\gamma}{\alpha^\gamma \nu \Gamma(\nu)} \right)^2 z^{\gamma \nu - 1} \int_0^\infty y^{2\gamma \nu - 1} e^{-y^\gamma \left(\frac{z^\gamma + 1}{\alpha^\gamma}\right)} dy \\
&= \left(\frac{\gamma}{\alpha^\gamma \nu \Gamma(\nu)} \right)^2 z^{\gamma \nu - 1} \frac{\Gamma(2\nu)}{\gamma \left(\frac{z^\gamma + 1}{\alpha^\gamma}\right)^{2\gamma}} \\
&= \frac{\gamma \Gamma(2\nu)}{\Gamma(\nu)^2} \frac{z}{(z^\gamma + 1)^{2\nu}},
\end{aligned} \tag{3.2.18}$$

obtaining the PDF for the ratio of GG distributions

$$P_\varepsilon(y) = \frac{\gamma \Gamma(2\nu)}{\Gamma(\nu)^2} \frac{y}{(y^\gamma + 1)^{2\nu}}, \quad y \geq 0. \tag{3.2.19}$$

Using this noise model, we construct the associated MLE as proposed in (3.2.6) as

follows

$$\begin{aligned}
e(\tilde{u}_1, \tilde{u}_2) &= \sum_{s \in \Omega} \log \left[\frac{1}{\varepsilon(s)^{-1}} P_\varepsilon(e^{\tilde{u}_1(s) - \tilde{u}_2(s)}) \right] \\
&= \sum_{s \in \Omega} \log \left[e^{\tilde{u}_1(s) - \tilde{u}_2(s)} \frac{\gamma \Gamma(2\nu)}{\Gamma(\nu)^2} \frac{e^{\tilde{u}_1(s) - \tilde{u}_2(s)}}{((e^{\tilde{u}_1(s) - \tilde{u}_2(s)})^\gamma + 1)^{2\nu}} \right] \\
&= |\Omega| \log \frac{\gamma \Gamma(2\nu)}{\Gamma(\nu)^2} + 2 \sum_{s \in \Omega} \left[\tilde{u}_1(s) - \tilde{u}_2(s) - \nu \log (e^{\gamma(\tilde{u}_1(s) - \tilde{u}_2(s))} + 1) \right],
\end{aligned} \tag{3.2.20}$$

Then, we normalize the MLE and disregard the constant contributions to obtain our similarity function

$$c(\tilde{u}_1, \tilde{u}_2) = \frac{1}{|\Omega|} \sum_{s \in \Omega} \left[\tilde{u}_1(s) - \tilde{u}_2(s) - \nu \log (e^{\gamma(\tilde{u}_1(s) - \tilde{u}_2(s))} + 1) \right]. \tag{3.2.21}$$

Note that for the special case of $\nu = 1$ and $\gamma = 2$, we retrieve the Rayleigh noise similarity function (3.2.16). In fact, the Rayleigh distribution is a particular case of the GG where $\nu = 1$, $\gamma = 2$ and $\alpha = \sqrt{2}\sigma$. The tuning of the additional parameters in GG distribution may allow a better characterization of the noise.

3.2.3 Transversal registration

The transversal registration consists in finding the rigid motion that better aligns the structures between two frames, say J_m and J_n . For the given frames J_n and J_m of the IVUS study and the corresponding ROIs M_n^Z and M_m^Z , $Z \in \{\text{FIR}, \text{VWR}\}$, we define the common ROI between these images as

$$M_{n,m}^Z = M_n^Z \wedge M_m^Z. \tag{3.2.22}$$

Using this common ROI we identify the set $\mathcal{R}_{n,m}^Z = \{(x, y), M_{n,m}^Z(x, y) = 1\}$ and its cardinality $|\mathcal{R}_{n,m}^Z|$. Then, we modify the MLE function presented in previous sections by defining $\Omega = \mathcal{R}_{n,m}^Z$.

Thus, we have to find the rigid motion that maximizes the similarity function between the two given frames. The rigid motion, called Ξ , is described by the horizontal and vertical displacements, τ_x and τ_y , and a rotation around the center of the frame θ . Then, Ξ that registers J_m to J_n is defined as

$$\begin{aligned}
\Xi_m^n &= \arg \max_{\Xi^* \in \mathcal{U}} \mathcal{F}(J_n, J_m) \\
&= \arg \max_{\Xi^* \in \mathcal{U}} c(J_n, J_m(x(\Xi^*), y(\Xi^*)))|_{\mathcal{R}^Z},
\end{aligned} \tag{3.2.23}$$

where \mathcal{U} is the space of admissible rigid motions of the transducer and $J_m(x(\Xi^*), y(\Xi^*))$ is the frame J_m after applying the rigid motion Ξ^* . Because of the acquisition sampling, the space \mathcal{U} is discrete. The translations and rotations only make sense for multiples of one pixel and $\frac{2\pi}{256}$ radians, respectively. Furthermore, the transducer is confined to the lumen, which imposes bounds to the horizontal and vertical displacements. Thus, we characterize

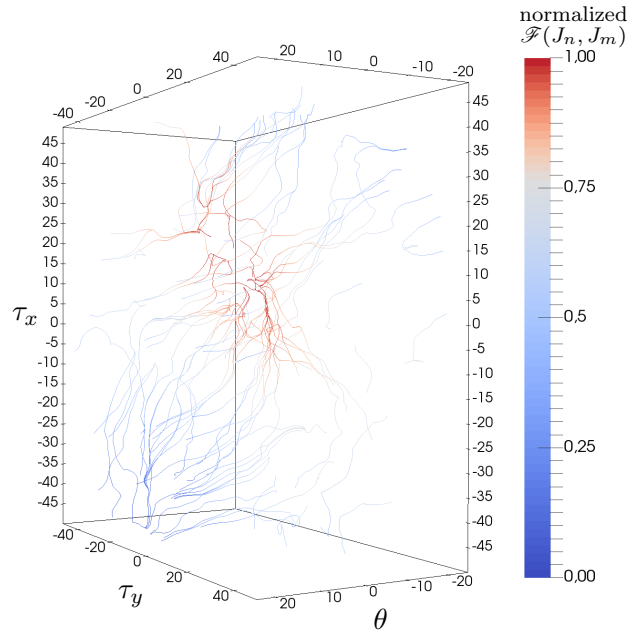


Figure 3.2: Streamlines associated to the vector field $\frac{d\mathcal{F}}{d\Xi}$ across the space \mathcal{U} for the comparison of two IVUS frames using the Rayleigh noise estimator. These streamlines show the gradient ascend capabilities from zones with low (in blue) to high (in red) \mathcal{F} values. Similar results are obtained with normalized cross-correlation and gamma generalized (GG) noise estimator.

\mathcal{U} as

$$\mathcal{U} = \left\{ \Xi = (\tau_x, \tau_y, \theta); \theta = i \frac{\pi}{128}, i = 0, \dots, 255; \right. \\ \left. \tau_x \in [\tau_x^{\text{MIN}}, \tau_x^{\text{MAX}}] \subset \mathbb{Z}; \tau_y \in [\tau_y^{\text{MIN}}, \tau_y^{\text{MAX}}] \subset \mathbb{Z} \right\}. \quad (3.2.24)$$

Expression (3.2.23) involves the maximization of a non-convex functional. The lack of convexity arises from the presence of speckle noise and because of the partial (incomplete) matching of the aligned structures. Notice that, the space \mathcal{U} is finite-dimensional, enabling the computation of the cost functional \mathcal{F} for each element $\Xi \in \mathcal{U}$. For this reason, a brute force algorithm simplifies the solution for the maximization problem.

In turn, the regularity of \mathcal{F} over \mathcal{U} allows the maximization through less expensive strategies. As seen in Figure 3.2, the streamlines across \mathcal{F} (using as velocity field $\frac{d\mathcal{F}}{d\Xi}$) yield to the same area with the minimum values (colored in red), showing the functional space adequacy for minimization by gradient methods. Also, the regularity of \mathcal{F} enables to use a gradient method without the need of a regularization terms. To deal with the lack of convexity and multiple solutions, an heuristic method called multi-seed gradient ascend (MSGA) is proposed. Here, multiple initializations are used to ascend and the instance that reaches the highest value of \mathcal{F} is retained as the solution for the maximization problem. A suitable trade-off between accuracy and performance is found for a 5-seed initialization procedure as described in Figure 3.3 (see also Section 3.3.2). Some considerations about this approach are presented in the Appendix B.

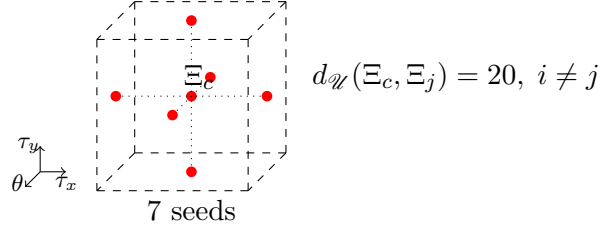


Figure 3.3: Initialization pattern over the space of admissible rigid motions, \mathcal{U} , used for the multi-seed gradient ascend (MSGA) method. The seeds are equidistant to the central seed positioned at Ξ_c . The dashed box is aligned with τ_x , τ_y , θ axes of the \mathcal{U} .

3.2.4 Longitudinal registration

During IVUS pullback, cardiac contraction strongly affects the longitudinal motion of the transducer with respect to the vessel ([21, 235, 322]). For this reason, IVUS frame sequence is not spatially ordered from distal to proximal positions. Also, the estimation of each frame spatial location based on the pullback velocity is not possible for frames acquired during cardiac contraction. To address this motion artifact, the study is gated to properly identify the frames in each cardiac phase. From the gating process presented in Chapter 2, P image sets are generated, where each set corresponds to a specific cardiac phase (see Figure 3.4). Although the images within each set are longitudinally ordered, the displacements between the frames may not necessarily be homogeneous because of the large variability in the transducer motion. Particularly, the phase previous to the cardiac contraction, hereafter referred to as *steady phase*, is assumed to present the most homogeneous displacement field as a result of the reduced cardiac motion. Because frames during the cardiac contraction present blurring due to the motion of the ultrasonic transducer [58, 214], we quantify vessel movement as the negative sum of the intensity gradient along each image (proportionally inverse to the image sharpness). Then, from the \mathcal{I}_i , $i = 1, \dots, P$ cardiac phases, we define the steady phase \mathcal{I}_{st} as

$$\mathcal{I}_{st} = \arg \min_{i=1, \dots, P} \mathcal{P}_{\text{motion}}(\mathcal{I}_i) = \arg \min_{i=1, \dots, P} \left\{ -\frac{1}{N_i} \sum_{j=1}^{N_i} \sum_{y=1}^H \sum_{x=1}^W |\nabla I_j^i(x, y)| \right\}, \quad (3.2.25)$$

where I_j^i denotes the j -th frame of the IVUS study in the i -th phase, N_i is the number of frames for that i -th cardiac phase, and H and W are the height and width of the images in the IVUS study.

As counterpart, we define the phase featuring maximal motion \mathcal{I}_{mo} as the maximum of $\mathcal{P}_{\text{motion}}$ (see Figure 3.5). Clearly, it will be denoted I_j^{st} and I_j^{mo} the frames of the steady phase and those in the maximal motion phase, respectively.

Assuming no motion by the cardiac contraction at the steady phase, the longitudinal location of its frames along the catheter is characterized as

$$s(I_j^{\text{st}}) = s_0 + \frac{j v_p}{f_s}, \quad (3.2.26)$$

where I_j^{st} is the j -th frame of the IVUS study in the steady frame \mathcal{I}_{st} , s_0 is the initial position of the transducer over the longitudinal axis, v_p is the pullback velocity in $\frac{\text{mm}}{\text{s}}$ and f_s is the framerate of the study in $\frac{\text{frames}}{\text{s}}$.

The steady phase \mathcal{I}_{st} , and the known spatial location of each frame I_j^{st} , $j = 1, \dots, N_{st}$, are used to perform a non-linear longitudinal registration of the remaining phases, hereafter referred to as *non-steady phases*. The registration process consists in

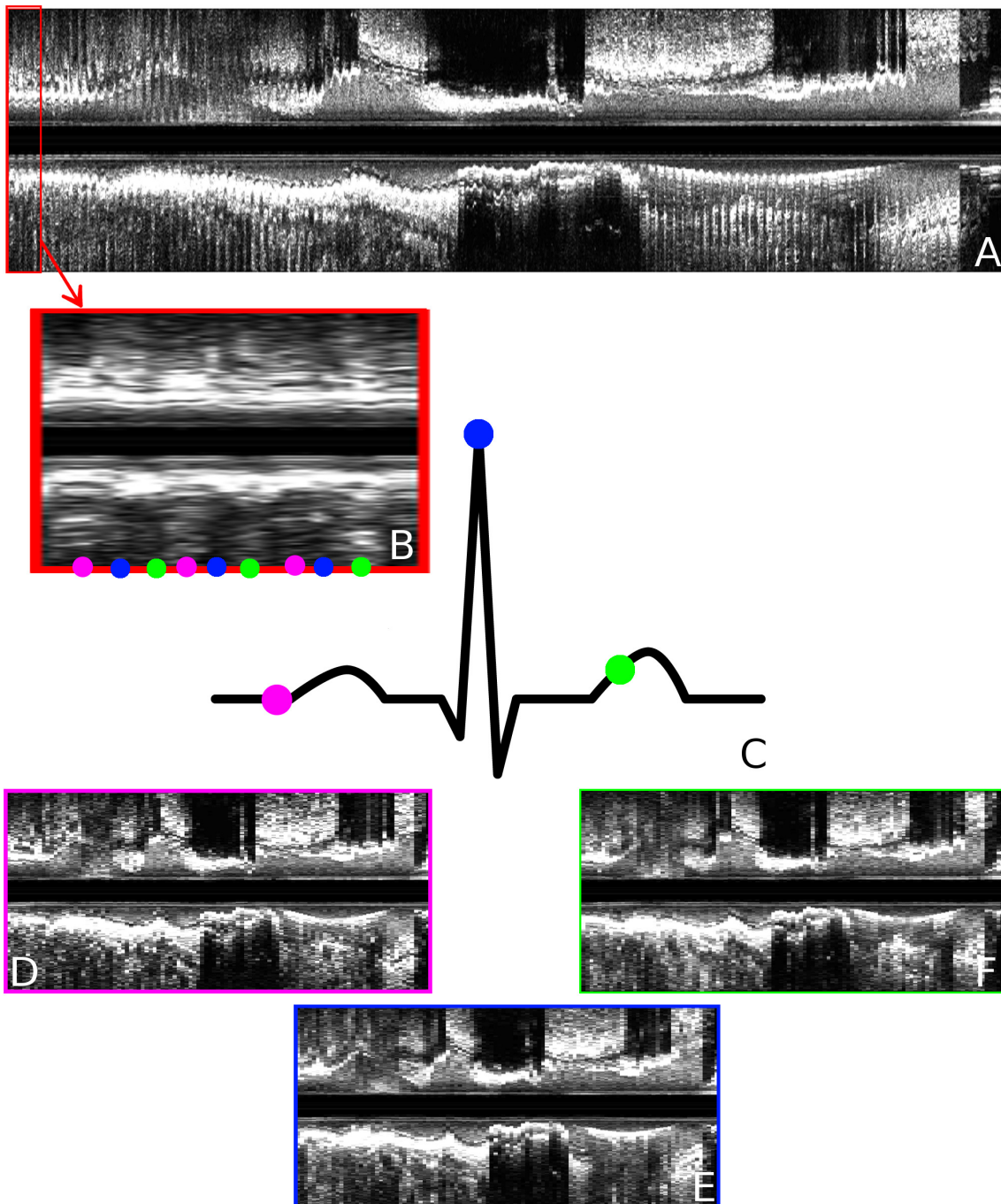


Figure 3.4: Gating process description. Given the IVUS study, longview presented in (A), and phase identification signal (C), e.g. the electrocardiogram or a motion signal for image-based gating, each frame is tagged accordingly to the cardiac phase at which it was acquired (B). Finally, images sets with frames at a specific cardiac phases are obtained (D, E, F).

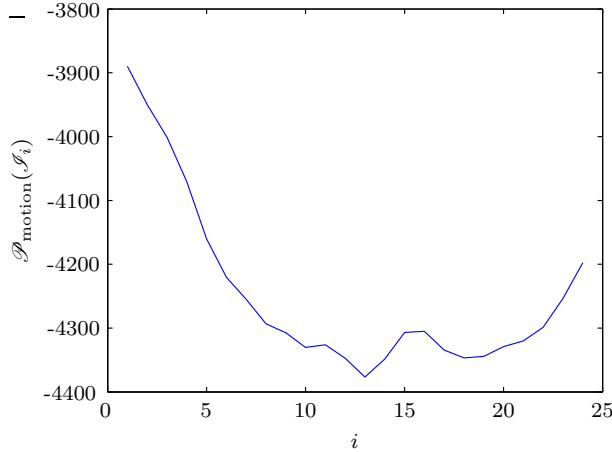


Figure 3.5: Function $\mathcal{P}_{\text{motion}}$ evaluated at each cardiac phase \mathcal{S}_i . The \mathcal{S}_i phases were retrieved from the image-based gating of an in-vivo IVUS study. For this gating, $\mathcal{S}_{\text{st}} = \mathcal{S}_{13}$ and $\mathcal{S}_{\text{mo}} = \mathcal{S}_1$.

assessing the similarity of each non-steady phase frame against the steady phase frames. The most similar steady phase frame is used to place the non-steady one. For the i -th cardiac phase, the degree of similarity between the j -th frame I_j^i and I_k^{st} , $k = 1, \dots, N_{\text{st}}$, is measured through a neighborhood likelihood estimator defined as follows

$$c_w(I_j^i, I_k^{\text{st}}) = \frac{\sum_{d=-w}^w \phi(d, \sigma_G) c(I_{j+d}^i, I_{k+d}^{\text{st}}) |_{\mathcal{R}^Z}}{\sum_{d=-w}^w \phi(d, \sigma_G)}, \quad (3.2.27)$$

where w is the longitudinal neighborhood width, d is the frame index within that neighborhood, and ϕ is a Gaussian weight function with σ_G standard deviation. The parameter w defines the domain used by the estimator c weighted by the value σ_G . Specifically, we want to neglect the contributions from frames whose weights are smaller than a factor T of the maximum weight value $\phi(0, \sigma_G)$. This would offer a weighting function of compact support with low computational effort. Empirically, we set $T = 10^{-1}$ to approximate c_w . Then, w is defined in terms of σ_G and T as

$$w(\sigma_G, T) = \left\lceil \sigma_G (-2 \log(T))^{\frac{1}{2}} \right\rceil. \quad (3.2.28)$$

Once we choose a suitable tolerance, the only parameter left is σ_G . As the value of σ_G is increased, information from adjacent frames is more relevant. Then, σ_G should be small enough to be representative of the local structures and large enough to incorporate information about the longitudinal structure to achieve robustness. In this way, the function ϕ in (3.2.27) introduces a low-pass filter regularization in the longitudinal motion and σ_G adjusts the low-pass frequencies to be included (the smaller the σ_G the more frequencies pass through the filter). The setup of this parameter is studied in Section 3.3.4.

Finally, the position in space of the frame I_j^i , which belongs to a *non-steady phase*, i.e. $i \neq \text{st}$, is defined as

$$s(I_j^i) = s(I_m^{\text{st}}), \quad (3.2.29)$$

where

$$m = \arg \max_{k=1, \dots, N_{\text{st}}} c_w(I_j^i, I_k^{\text{st}}). \quad (3.2.30)$$

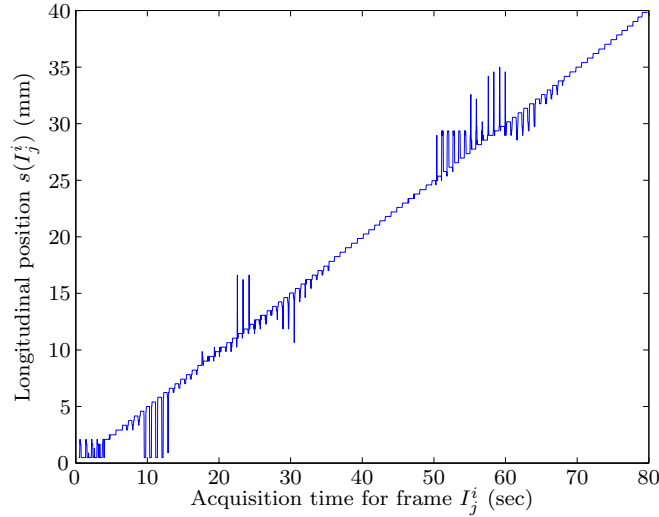


Figure 3.6: Results of the longitudinal registration process with $w = 3$: Transducer displacement along the longitudinal axis of the vessel for an in-vivo IVUS study.

Figure 3.6 shows the longitudinal registration of an in-vivo IVUS study according to the proposed method. The estimated motion of the transducer resembles the motion pattern observed in-vivo. In [21], the longitudinal displacements of the transducer were studied for a group of 31 patients using angiographies and IVUS at coronary bifurcations. The obtained longitudinal displacements are within the experimentally recorded ranges reported in [21]. Furthermore, a specific position in the longitudinal axis is represented by a set of frames in the different cardiac phases.

A formal definition for the set of frames located at the n -th frame position of the steady phase, is given by

$$\mathcal{X}_n = \{I_j^i; s(I_j^i) = s(I_n^{\text{st}}), j = 1, \dots, N_i, i = 1, \dots, P\}. \quad (3.2.31)$$

3.2.5 Numerical strategies

The strategies described next, present three alternative longitudinal registration schemes, two decoupled and another coupled with the transversal registration. As input for these implementations, we provide the N sets of gated volumes from the original IVUS study, i. e., $\mathcal{I}_i, i = 1, \dots, N$. Then, the registration task is to transversally and longitudinally register all phases $\mathcal{I}_i, i \neq \text{st}$, against \mathcal{I}_{st} .

For all the strategies, the preprocessing of the study is performed either using FIR or VWR. The first decoupled implementation (DLT implementation), defines \mathcal{X}_n sets through the longitudinal registration of all phases, as described in Section 3.2.4 and, then, performs the transversal registration in each \mathcal{X}_n independently, as explained in Section 3.2.3. The second decoupled strategy (DTL implementation), performs the transversal registration of each set $\mathcal{Y}_j = \{I_j^i; i = 1, \dots, P\}$ against I_j^{st} and, then, performs the longitudinal registration of all phases. The coupled strategy, aligns the cross-sections prior to the calculation of the correlation presented in (3.2.30). Once the minimum is found it provides not only the longitudinal coordinates, but also the transversal motion that aligns the structures, leading to a fully coupled frame registration method.

3.2.5.1 DLT implementation

The DLT implementation is composed of three serial and independent stages: the preprocessing, the longitudinal and transversal registration. As input, the last stage receives the \mathcal{X}_n sets from the longitudinal registration. Here for each one of these sets, the non-steady frames are registered against the steady frame. Formally, we define the transversal registration of the set \mathcal{X}_n as

$$\begin{aligned}\Xi_m^n &= \arg \max_{\Xi^* \in \mathcal{U}} \mathcal{F}(I_n^{\text{st}}, J_m) \\ &= \arg \max_{\Xi^* \in \mathcal{U}} c(I_n^{\text{st}}, J_m(x(\Xi^*), y(\Xi^*)))|_{\mathcal{A}^Z},\end{aligned}\quad (3.2.32)$$

where $J_m \in \mathcal{X}_n$ and $J_m \neq I_n^{\text{st}}$. Finally, the aligned set of frames located at the n -th frame position of the steady phase, is given by

$$\mathcal{X}_n^{\text{DLT}} = \{J_m(x(\Xi^*), y(\Xi^*)); J_m \in \mathcal{X}_n \setminus \{I_n^{\text{st}}\}\} \cup \{I_n^{\text{st}}\}.\quad (3.2.33)$$

3.2.5.2 DTL implementation

The DTL implementation is also composed of three serial and independent stages: the preprocessing, the transversal and longitudinal registration. The second step performs the transversal registration of the j -th frame across all phases (\mathcal{Y}_j) against the frame in \mathcal{I}_{st} . Formally, we define the transversal registration of the set $\mathcal{Y}_j = \{I_j^i; i = 1, \dots, P\}$ as

$$\begin{aligned}\Xi_i^j &= \arg \max_{\Xi^* \in \mathcal{U}} \mathcal{F}(I_j^{\text{st}}, I_j^i) \\ &= \arg \max_{\Xi^* \in \mathcal{U}} c(I_j^{\text{st}}, I_j^i(x(\Xi^*), y(\Xi^*)))|_{\mathcal{A}^Z},\end{aligned}\quad (3.2.34)$$

where $I_j^i \in \mathcal{Y}_j$ and $I_j^i \neq I_j^{\text{st}}$. The transversally registered frames $\tilde{I}_j^i = I_j^i(x(\Xi_i^j), y(\Xi_i^j))$ are the inputs for the longitudinal registration in which the longitudinal position for each frame \tilde{I}_j^i is given by

$$s(\tilde{I}_j^i) = s(I_n^{\text{st}}),\quad (3.2.35)$$

where

$$n = \arg \max_{k=1, \dots, N_{\text{st}}} c_w(\tilde{I}_j^i, I_k^{\text{st}}).\quad (3.2.36)$$

Finally, the aligned set of frames located at the n -th frame position of the steady phase, is given by

$$\mathcal{X}_n^{\text{DTL}} = \{\tilde{I}_j^i; s(\tilde{I}_j^i) = s(I_n^{\text{st}}), j = 1, \dots, N_i, i = 1, \dots, P\} \cup \{I_n^{\text{st}}\}.\quad (3.2.37)$$

3.2.5.3 Coupled implementation

The coupled implementation is composed of two stages: the preprocessing and the coupled longitudinal and transversal registration. The second stage, performs the transversal registration prior the comparison presented in (3.2.27). In that manner, the position in space of the frame I_j^i , which belongs to a *non-steady phase* and the applied transversal rigid motion Ξ_j^i to that frame are defined as

$$s(I_j^i(x(\Xi_j^i), y(\Xi_j^i))) = s(I_n^{\text{st}}),\quad (3.2.38)$$

where

$$n = \arg \max_{k=1, \dots, N_{\text{st}}} c_w(I_j^i(x(\Xi_j^i), y(\Xi_j^i)), I_k^{\text{st}}), \quad (3.2.39)$$

and

$$\Xi_j^i = \arg \max_{\Xi^* \in \mathcal{U}} \sum_{d=-w}^w \mathcal{F}(I_{k+d}^{\text{st}}, I_{j+d}^i). \quad (3.2.40)$$

Note that the transversal registration performed in (3.2.40) is now coupled with the longitudinal registration given by (3.2.39). Evidently, this implementation is computationally more expensive. To reduce the computational cost, we confine the search space in (3.2.39) to $k \in [\max(j - 11, 1); \min(j + 11, N_{\text{st}})]$ which represents longitudinal displacements of approximately 5.5mm forward and backward. According to [21], this range of displacement encloses those observed in-vivo. The same assumption is taken into account for the decoupled implementation for an objective cost and accuracy comparison in the forthcoming sections.

Finally, the aligned set of frames located at the n -th frame position of the steady phase, is given by

$$\begin{aligned} \mathcal{X}_n^{\text{C}} = \{ & I_j^i(x(\Xi_j^i), y(\Xi_j^i)); s(I_j^i(x(\Xi_j^i), y(\Xi_j^i))) = s(I_n^{\text{st}}), \\ & j = 1, \dots, N_i, i = 1, \dots, P \} \cup \{ I_n^{\text{st}} \}. \end{aligned} \quad (3.2.41)$$

3.3 Results

3.3.1 Acquisition of IVUS studies

The IVUS studies were acquired with the AtlantisTMSR Pro Imaging Catheter at 40 MHz synchronized with an ECG signal and connected to an iLabTM Ultrasound Imaging System (both by Boston Scientific Corporation, Natick, MA, USA), at the Heart Institute (InCor), University of São Paulo Medical School and Sírio-Libanês Hospital, São Paulo, Brazil.

The procedure was performed during a diagnostic or therapeutic percutaneous coronary procedure. Vessels were imaged using automated pullback at 0.5 mm/s. Overall, multiple runs were performed on 28 patients leading to 52 IVUS studies with synchronized ECG signal. We analyzed images from different coronary arteries (left anterior descending artery - LAD, 27 studies; left circumflex artery - LCx, 12 studies; right coronary artery - RCA, 10 studies; and other coronary arteries, 3 studies) spanning different mean cardiac frequencies (from 65 BPM to almost 90 BPM) including cases with severe stenoses and deployment (22 studies) or not (30 studies) of stents.

After the procedure, a specialist performed a manual offline ECG gating of the studies. Specifically, an operator marked the frame number at each R-wave peak in the IVUS study aided by the synchronized ECG signal. Hence, images in a specific cardiac phase (the R-wave peak phase) can be identified. Then, we use the criteria presented in Chapter 2 to decompose the IVUS study in several cardiac phases.

3.3.2 Computational cost

The computational cost is proportional to the number of seeds used in the gradient ascend method for transversal registration. For this reason, we analyzed the trade-off

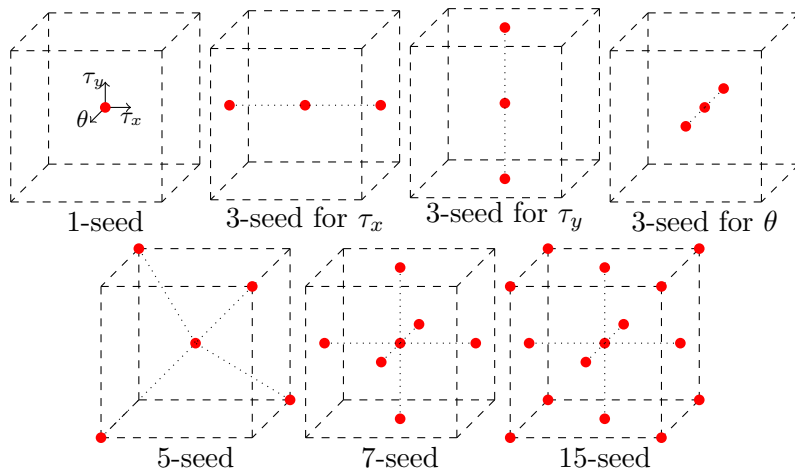


Figure 3.7: Initialization patterns over the space \mathcal{U} . The dashed box is aligned with the τ_x, τ_y, θ axes.

between computational load and maximization accuracy of (3.2.23) for seven different patterns of initialization. To precisely define the initializations, let us define

$$\|\Xi\|_{\mathcal{U}} = \sqrt{(\tau_x)^2 + (\tau_y)^2 + \left(\frac{128\theta}{\pi}\right)^2} \quad (3.3.1)$$

as the norm over \mathcal{U} and the associated distance defined as $d_{\mathcal{U}}(\Xi_1, \Xi_2) = \|\Xi_1 - \Xi_2\|_{\mathcal{U}}$, $\Xi_1, \Xi_2 \in \mathcal{U}$. Then, seven patterns were tested to deploy the seeds along \mathcal{U} , where a central seed is positioned at $(0, 0, 0)$ and the remaining seeds are distributed as presented in Figure 3.7.

The hardware for these tests consists of an Intel Xeon CPU E5-2650 v2 at 2.60GHz processor and Samsung 1866 MHz (latency of 13 ns) RAM memory over Red Hat Enterprise Linux Server release 6.3. All methods were executed in their serial versions with high CPU affinity for the measurements reported in this section. As performance measurement, we use the mean wall-clock time averaged from five executions to attenuate operative system time variations. Overall, we perform the registration of 52 bifurcation frames, each frame belonging to a randomly selected bifurcation of a different study.

To assess the maximization accuracy of (3.2.23) obtained with each initialization, we compared the MSGA solutions against the brute force search solution. The disagreement between the brute force and the MSGA method (hereafter assumed as MSGA error) is defined as follows

$$\varepsilon = \sqrt{\left(\frac{\tau_x - \hat{\tau}_x}{\mu_{\hat{\tau}_x}}\right)^2 + \left(\frac{\tau_y - \hat{\tau}_y}{\mu_{\hat{\tau}_y}}\right)^2 + \left(\frac{r_{eq}(\theta - \hat{\theta})}{\mu_{\hat{\theta}}}\right)^2} \quad (3.3.2)$$

where τ_x, τ_y, θ and $\hat{\tau}_x, \hat{\tau}_y, \hat{\theta}$ triplets are the rigid motion estimated with MSGA and brute force method, respectively, $r_{eq} = \sqrt{A_l/\pi}$ is the equivalent radius for the lumen in the analyzed frame, A_l is the area of the lumen in the analyzed frame and $\mu_{\hat{\tau}_x}, \mu_{\hat{\tau}_y}, \mu_{\hat{\theta}}$ are the means of $\hat{\tau}_x, \hat{\tau}_y$ and $r_{eq}\hat{\theta}$ for the 52 cases analyzed. The normalization applied by the factors $\mu_{\hat{\tau}_i}^{-1}$ equalizes the contribution of the three motion components to ε .

From the analysis (see Figure 3.8), it is confirmed that the accuracy improves as more seeds are added to the initialization process. The 3-seed pattern has shown that τ_x is the dimension that requires more initialization to minimize the optimization error because of the local minima in the functional produced by the partial matching of the

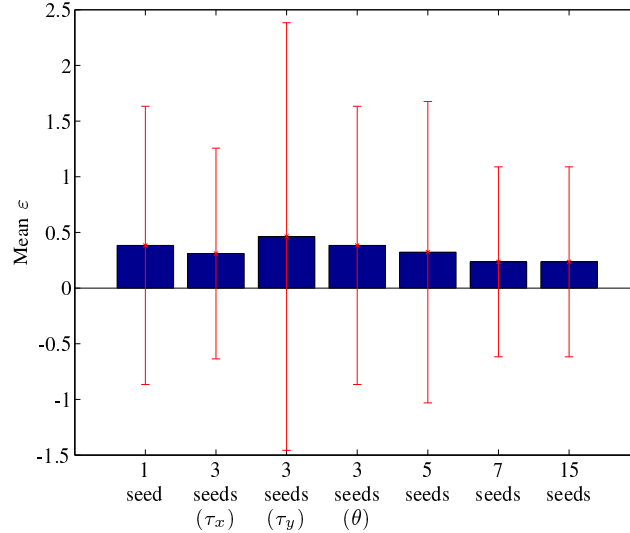


Figure 3.8: Standard deviation (whiskers) and mean (bars) of the multi-seed gradient ascend (MSGGA) error for the 7 initialization patterns along 52 bifurcation frames registrations. The normalization factors are $\mu_{\hat{\tau}_x}^{-1} = 5.827$, $\mu_{\hat{\tau}_y}^{-1} = 4.769$, $\mu_{\hat{\theta}}^{-1} = 0.152$.

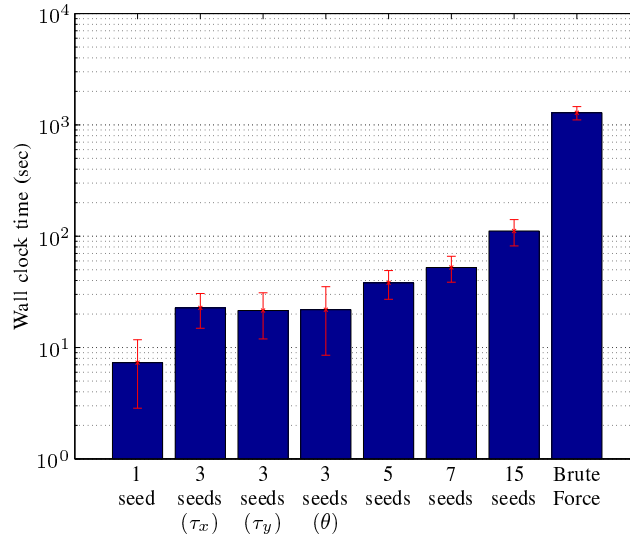


Figure 3.9: Standard deviation (whiskers) and mean (bars) computational cost of the proposed multi-seed gradient ascend (MSGGA) initializations and the brute force method for 52 bifurcation frames registrations.

structures registered. Note that the 7 seeds and the 15 seeds patterns present the same error ε in terms of mean and standard deviation, although the computational cost of 15-seed doubles the one of the 7-seed pattern (see Figure 3.9). For these reasons, we use the 7-seed pattern in the following analysis because it presents the better trade-off between accuracy and computational cost.

Lastly, we assess the performance of the decoupled and coupled strategies. We do not differentiate the two decoupled alternatives because their computational complexity in terms of frames registrations and comparisons (quantity of transversal registration and frame comparisons performed with the proposed MLE within a study) is the same and its computational cost does not present significant variations. In this case, we choose to parallelize the implementations to judge their potential use in medical practice. The implementations coded in C++ compiled with GNU compilers were parallelized at frame

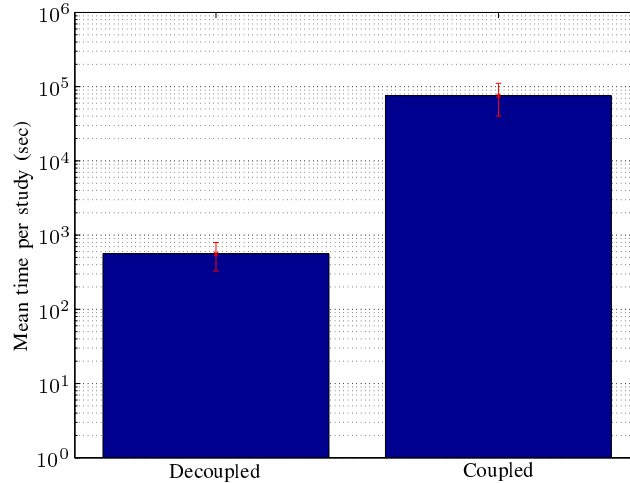


Figure 3.10: Standard deviation (whiskers) and mean (bars) computational cost per study of the parallelized decoupled and coupled strategies. The wall-clock times were estimated using the 52 IVUS studies.

level with OpenMP. Each execution was parallelized across the 16 threads of the aforementioned processors. The registration was carried along the 52 studies using the FIR ROI, $\sigma = 0.4$ and the MSGA with 7-seed pattern for both implementations. Results show that the decoupled strategy is 134 times faster than the coupled strategy (see Figure 3.10) with an execution time per study of 562 ± 233 sec and 75521 ± 35356 sec, respectively. As the execution times suggests, the decoupled method is capable to assess longitudinal motion during medical procedure whereas the coupled method must necessarily be regarded as an offline method.

3.3.3 Validation of transversal registration

To validate our method, we construct a ground truth based on registrations performed by medical image experts. Thus, two specialist perform the rigid registration of 30 distinguishable anatomical landmarks (each landmark is characterized by a pair of IVUS frames at the same cross-section in different cardiac phases) such as bifurcations, extreme points of stent or calcified regions. We study the intra- and inter-observer variability for this ground truth in terms of Bland-Altman limits of agreement (LA) and intervals of cross-correlation (ICC, only for inter-observer analysis).

The intra-observer variability (see Table 3.1) shows that manual registration (here performed twice for each landmark) is a hardly reproducible task even for image experts (p -value > 0.33 for the Bland-Altman mean). The identification at pixel precision of landmarks within an image was not entirely successful (LA smaller than 11 pixels for translations and 2.25 radians for rotations). Causes of these inaccuracies include the poor SNR, polar-to-cartesian interpolation within the image and the blurring of landmark structures provoked by heart contraction.

The inter-observer variability was estimated by comparing the average of the two manual registrations performed by each observer at each landmark (\bar{O}). Table 3.2 presents a good agreement between the specialists in the identification of τ_x and θ (ICC of 0.93 and 0.87 with p -value of $2 \cdot 10^{-10}$ and $3 \cdot 10^{-7}$, respectively) and a low correlation in the identification of τ_y (ICC of 0.49 with p -value of $4 \cdot 10^{-2}$). The LA show lower inter-observer than intra-observer variation.

Lastly, we extended the observations of one specialist (\bar{O}_1^E) from 30 to 50 landmarks, to obtain a bigger set for comparison against the proposed MSGA method. As result

(see Table 3.2) it is seen that the specialist 1 presents a higher correlation against the MSGA (ICC of 0.89, 0.94 and 0.93) than against specialist 2 (ICC of 0.93, 0.49 and 0.87). Moreover, the LA are narrower in the case \overline{O}_1^E vs O_{MSGA} for τ_y (LA < 2.3 pixels) while τ_x and θ remain within the same limits as in \overline{O}_1 vs \overline{O}_2 .

3.3.4 Validation of longitudinal registration

To complement the study of previous section, we now focus on the longitudinal registration error. For this task, we identified \mathcal{I}_{st} and \mathcal{I}_{mo} phases (as described in Section 3.2.4) for each IVUS study and performed the registration between the two phases. The reason to perform the registration against \mathcal{I}_{mo} and not against other intermediate phase is because the largest displacements and vessel deformations occur in this phase, turning the registration more challenging and prone to bigger errors.

To construct a ground truth, an expert manually identified the frames corresponding to 212 anatomical landmarks (such as carina bifurcation, calcium lesions or stent extremes) across all IVUS studies in both cardiac phases. Using the expert identifications as the registration ground truth, we define the longitudinal registration error in the i -th landmark as

$$\varepsilon_i = |s(l^{st}(i)) - s(l^{mo}(i))|, \quad (3.3.3)$$

where $l^j(i)$ is the manually identified frame of the i -th landmark in the cardiac phase j and $s(\cdot)$ is the spatial position of frame (\cdot) as described in Eqs. (3.2.26) and (3.2.29). Note that $s(l^{st}(i))$ is calculated with (3.2.26) without using any registration process while $s(l^{mo}(i))$ is estimated using the proposed strategies (see Section 3.2.5), and thus is responsible for the error presented by each strategy. Additionally, we estimate the Bland-Altman mean (μ_{BA}) and limits of agreement (LA) to assess conformity between the registrations performed by the expert and the proposed implementations (see Tables 3.4, 3.6, 3.8).

The longitudinal error was calculated for the 52 IVUS studies described in Section 3.3.1 using the MSGA with 7 seeds for transversal registration (see Tables 3.3, 3.4, 3.5, 3.6, 3.7 and 3.8). The MLE for the GG noise distribution closely improves the MLE for Rayleigh noise (that can be interpreted as GG with $\nu = 1$ and $\gamma = 2$) when parameters are adjusted to $\nu = 1.5$ and $\gamma = 1.5$. The improvement from these two MLE strategies is about 7% in mean. To find the appropriate parameters for the GG, we performed a sensitivity analysis over a subsample of 4 IVUS studies varying the parameters ν and γ in 0.5 units from case to case. Experimental essays may improve the insight of the ν and γ values specifics for different groups of tissues. It is important to note that as the noise is coherent signature of the underlying material, leading that different materials will present specific values that optimize their noise distribution. Related to the implementation strategies, the results clearly show that DTL presents the smallest error (0.30 ± 0.63 for $w = 3$), followed by the coupled implementation (0.40 ± 1.09 for $w = 5$) and lastly the DLT (0.62 ± 1.76 for $w = 5$). Even more, the results are in agreement with the Bland-Altman LA showing the same order for the narrower limits to zero. This strongly suggests that prior alignment of the transversal planes is relevant for the longitudinal registration. Also, the VWR mask renders less accurate registrations than FIR in all cases, which reflects the importance of including the perivascular tissue for the frame registration task. In terms of the neighborhood of frames used for the registration, it is seen that the inclusion of frames provides robustness to the registration strategy, improving the performance when compared to the one-to-one frame comparison, i.e., when $w = 0$. In terms of the μ_{BA} , it is seen that the proposed strategies are not strongly biased regarding sub- or over-estimation of the frame spatial position (in FIR cases is $|\mu_{BA}| < 0.2$ frames of bias which is always smaller than 10% of the LA).

Observer	τ_x		τ_y		θ	
	LA (pixels)	p	LA (pixels)	p	LA (radians)	p
O_1	-0.34 ± 5.68	0.75	-0.34 ± 10.37	0.86	-0.40 ± 2.23	0.33
O_2	-1.06 ± 7.57	0.45	-0.34 ± 5.69	0.75	-0.41 ± 2.25	0.33

Table 3.1: Intra-observer variability for two observers which perform the manual registration twice for the IVUS frame pairs. The variability is described in terms of the Bland-Altman limits of agreement (LA, expressed as mean \pm SD) and the p -value associated with the Bland-Altman mean, for each component of the rigid motion Ξ .

Observers	τ_x			τ_y			θ		
	LA (pixels)	ICC	p	LA (pixels)	ICC	p	LA (radians)	ICC	p
\overline{O}_1 vs \overline{O}_2	-0.26 ± 5.28	0.93	$< 2 \cdot 10^{-10}$	0.89 ± 5.90	0.49	$< 4 \cdot 10^{-2}$	0.20 ± 1.13	0.87	$< 3 \cdot 10^{-7}$
\overline{O}_1^E vs O_{MSGA}	-0.42 ± 5.31	0.89	$< 3 \cdot 10^{-12}$	0.18 ± 2.22	0.94	$< 2 \cdot 10^{-16}$	-0.19 ± 0.97	0.93	$< 2 \cdot 10^{-16}$

Table 3.2: Inter-observer variability in terms of the Bland-Altman limits of agreement (LA), interclass correlation coefficient (ICC) and p -value associated to ICC value. The observer \overline{O}_i are the mean observations of observer i and \overline{O}_1^E the mean observations for 50 landmarks instead of 30. O_{MSGA} represents the 50 landmark transversal registrations using the proposed method.

Validation for normalized cross-correlation estimator

σ	w	DLT Strategy		DTL Strategy		Coupled Strategy	
		ε with FIR (mean \pm SD)	ε with VWR (mean \pm SD)	ε with FIR (mean \pm SD)	ε with VWR (mean \pm SD)	ε with FIR (mean \pm SD)	ε with VWR (mean \pm SD)
0.4	0	0.76 \pm 1.81	1.01 \pm 2.14	0.41 \pm 0.83	0.43 \pm 0.81	0.41 \pm 1.08	1.56 \pm 2.99
0.8	1	0.69 \pm 1.69	0.78 \pm 1.92	0.37 \pm 0.88	0.66 \pm 1.55	0.47 \pm 1.24	0.73 \pm 2.02
1.2	2	0.69 \pm 1.77	0.67 \pm 1.79	0.36 \pm 0.86	0.56 \pm 1.40	0.44 \pm 1.17	0.73 \pm 1.94
1.6	3	0.65 \pm 1.78	0.70 \pm 1.86	0.33 \pm 0.79	0.76 \pm 1.92	0.46 \pm 1.29	0.70 \pm 2.00
2.0	4	0.61 \pm 1.71	0.68 \pm 1.86	0.31 \pm 0.69	0.72 \pm 1.77	0.50 \pm 1.34	0.63 \pm 1.76
2.4	5	0.61 \pm 1.66	0.79 \pm 2.06	0.40 \pm 1.00	0.79 \pm 1.95	0.56 \pm 1.61	0.61 \pm 1.82
2.8	6	0.72 \pm 1.97	0.77 \pm 2.03	0.42 \pm 1.12	0.81 \pm 1.93	0.58 \pm 1.68	0.66 \pm 1.66

Table 3.3: Mean and standard deviation of the longitudinal registration error measured at 212 landmark sites along 52 in-vivo IVUS studies.

σ	w	DLT Strategy		DTL Strategy		Coupled Strategy	
		BA with FIR ($\mu_{BA} \pm LA$)	BA with VWR ($\mu_{BA} \pm LA$)	BA with FIR ($\mu_{BA} \pm LA$)	BA with VWR ($\mu_{BA} \pm LA$)	BA with FIR ($\mu_{BA} \pm LA$)	BA with VWR ($\mu_{BA} \pm LA$)
0.4	0	0.10 \pm 3.84	0.01 \pm 4.66	0.08 \pm 1.82	0.20 \pm 1.76	0.03 \pm 2.27	-0.00 \pm 6.63
0.8	1	-0.01 \pm 3.59	0.07 \pm 4.06	0.09 \pm 1.86	-0.11 \pm 3.30	0.00 \pm 2.61	-0.09 \pm 4.21
1.2	2	-0.00 \pm 3.73	0.06 \pm 3.76	0.08 \pm 1.82	-0.07 \pm 2.96	-0.07 \pm 2.44	-0.26 \pm 4.05
1.6	3	-0.07 \pm 3.71	0.05 \pm 3.90	0.04 \pm 1.68	0.05 \pm 4.05	-0.10 \pm 2.68	-0.12 \pm 4.16
2.0	4	-0.07 \pm 3.56	-0.04 \pm 3.90	0.04 \pm 1.48	-0.23 \pm 3.72	-0.14 \pm 2.79	0.09 \pm 3.67
2.4	5	-0.11 \pm 3.47	-0.17 \pm 4.33	-0.03 \pm 2.11	0.06 \pm 4.13	-0.20 \pm 3.32	-0.14 \pm 3.76
2.8	6	-0.17 \pm 4.10	-0.14 \pm 4.26	-0.07 \pm 2.35	0.05 \pm 4.12	-0.16 \pm 3.48	-0.11 \pm 3.50

Table 3.4: Bland-Altman (BA) mean (μ_{BA}) and limits of agreement (LA) for longitudinal registrations with the proposed strategies against the expert ground truth (212 anatomical landmarks used as samples).

Validation for Rayleigh noise estimator

σ	w	DLT Strategy		DTL Strategy		Coupled Strategy	
		ε with FIR (mean \pm SD)	ε with VWR (mean \pm SD)	ε with FIR (mean \pm SD)	ε with VWR (mean \pm SD)	ε with FIR (mean \pm SD)	ε with VWR (mean \pm SD)
0.4	0	0.78 \pm 1.72	0.83 \pm 1.94	0.42 \pm 0.78	0.45 \pm 0.85	0.49 \pm 1.26	1.82 \pm 2.99
0.8	1	0.69 \pm 1.74	0.68 \pm 1.77	0.38 \pm 0.85	0.54 \pm 1.14	0.51 \pm 1.42	1.38 \pm 2.78
1.2	2	0.64 \pm 1.68	0.67 \pm 1.78	0.32 \pm 0.75	0.67 \pm 1.46	0.45 \pm 1.36	1.02 \pm 2.24
1.6	3	0.62 \pm 1.65	0.67 \pm 1.84	0.30 \pm 0.63	0.69 \pm 1.33	0.51 \pm 1.54	1.08 \pm 2.43
2.0	4	0.58 \pm 1.63	0.70 \pm 1.97	0.31 \pm 0.68	0.83 \pm 1.84	0.42 \pm 1.22	1.18 \pm 2.51
2.4	5	0.57 \pm 1.52	0.72 \pm 1.97	0.33 \pm 0.73	0.90 \pm 1.90	0.42 \pm 1.15	1.06 \pm 2.44
2.8	6	0.64 \pm 1.69	0.69 \pm 1.87	0.33 \pm 0.66	0.99 \pm 2.02	0.52 \pm 1.45	1.03 \pm 2.27

Table 3.5: Mean and standard deviation of the longitudinal registration error measured at 212 landmark sites along 52 in-vivo IVUS studies.

σ	w	DLT Strategy		DTL Strategy		Coupled Strategy	
		BA with FIR (μ_{BA} \pm LA)	BA with VWR (μ_{BA} \pm LA)	BA with FIR (μ_{BA} \pm LA)	BA with VWR (μ_{BA} \pm LA)	BA with FIR (μ_{BA} \pm LA)	BA with VWR (μ_{BA} \pm LA)
0.4	0	0.13 \pm 3.69	0.17 \pm 4.13	0.19 \pm 1.71	0.23 \pm 1.84	-0.07 \pm 2.66	0.27 \pm 6.85
0.8	1	0.14 \pm 3.67	0.17 \pm 3.71	0.12 \pm 1.80	0.09 \pm 2.47	-0.08 \pm 2.96	0.29 \pm 6.07
1.2	2	0.11 \pm 3.53	0.22 \pm 3.72	0.06 \pm 1.60	-0.02 \pm 3.16	-0.09 \pm 2.82	-0.04 \pm 4.83
1.6	3	0.09 \pm 3.46	0.28 \pm 3.80	0.00 \pm 1.38	-0.06 \pm 2.94	-0.14 \pm 3.18	-0.33 \pm 5.18
2.0	4	0.05 \pm 3.39	0.12 \pm 4.11	-0.01 \pm 1.46	0.13 \pm 3.96	-0.18 \pm 2.51	-0.19 \pm 5.43
2.4	5	0.00 \pm 3.19	0.09 \pm 4.11	-0.02 \pm 1.58	-0.14 \pm 4.13	-0.10 \pm 2.40	-0.50 \pm 5.13
2.8	6	-0.01 \pm 3.55	0.04 \pm 3.91	-0.01 \pm 1.45	-0.24 \pm 4.39	-0.19 \pm 3.01	-0.36 \pm 4.85

Table 3.6: Bland-Altman (BA) mean (μ_{BA}) and limits of agreement (LA) for longitudinal registrations with the proposed strategies against the expert ground truth (212 anatomical landmarks used as samples).

Validation for Generalized Gamma noise estimator with $\nu = 1.5$ and $\gamma = 1.5$

σ	w	DLT Strategy		DTL Strategy		Coupled Strategy	
		ε with FIR (mean \pm SD)	ε with VWR (mean \pm SD)	ε with FIR (mean \pm SD)	ε with VWR (mean \pm SD)	ε with FIR (mean \pm SD)	ε with VWR (mean \pm SD)
0.4	0	0.67 \pm 1.51	0.87 \pm 2.09	0.45 \pm 0.91	0.42 \pm 0.84	0.40 \pm 0.87	1.74 \pm 2.96
0.8	1	0.58 \pm 1.51	0.66 \pm 1.75	0.31 \pm 0.68	0.52 \pm 1.16	0.41 \pm 1.14	1.28 \pm 2.56
1.2	2	0.58 \pm 1.52	0.60 \pm 1.78	0.29 \pm 0.63	0.63 \pm 1.44	0.38 \pm 1.17	0.91 \pm 2.18
1.6	3	0.48 \pm 1.40	0.65 \pm 1.87	0.29 \pm 0.65	0.82 \pm 1.92	0.40 \pm 1.18	0.93 \pm 2.35
2.0	4	0.51 \pm 1.52	0.69 \pm 2.06	0.28 \pm 0.55	0.85 \pm 1.85	0.42 \pm 1.24	1.03 \pm 2.39
2.4	5	0.58 \pm 1.57	0.61 \pm 1.82	0.33 \pm 0.63	0.92 \pm 2.05	0.38 \pm 1.08	1.05 \pm 2.36
2.8	6	0.66 \pm 1.74	0.69 \pm 1.96	0.32 \pm 0.64	0.97 \pm 2.08	0.45 \pm 1.27	0.94 \pm 2.14

Table 3.7: Mean and standard deviation of the longitudinal registration error measured at 212 landmark sites along 52 in-vivo IVUS studies.

σ	w	DLT Strategy		DTL Strategy		Coupled Strategy	
		BA with FIR ($\mu_{BA} \pm LA$)	BA with VWR ($\mu_{BA} \pm LA$)	BA with FIR ($\mu_{BA} \pm LA$)	BA with VWR ($\mu_{BA} \pm LA$)	BA with FIR ($\mu_{BA} \pm LA$)	BA with VWR ($\mu_{BA} \pm LA$)
0.4	0	0.08 \pm 3.24	0.08 \pm 4.45	0.17 \pm 1.97	0.16 \pm 1.82	0.04 \pm 1.88	0.31 \pm 6.72
0.8	1	0.05 \pm 3.18	0.15 \pm 3.65	0.12 \pm 1.45	-0.01 \pm 2.51	-0.05 \pm 2.37	0.12 \pm 5.61
1.2	2	0.08 \pm 3.18	0.17 \pm 3.67	0.03 \pm 1.37	-0.15 \pm 3.07	-0.03 \pm 2.41	-0.21 \pm 4.63
1.6	3	-0.00 \pm 2.91	0.07 \pm 3.88	0.07 \pm 1.40	-0.15 \pm 4.10	-0.11 \pm 2.43	-0.07 \pm 4.96
2.0	4	-0.07 \pm 3.16	0.03 \pm 4.28	0.01 \pm 1.21	-0.07 \pm 4.00	-0.14 \pm 2.55	-0.23 \pm 5.09
2.4	5	-0.06 \pm 3.28	0.01 \pm 3.77	0.00 \pm 1.40	0.05 \pm 4.41	-0.12 \pm 2.23	-0.39 \pm 5.02
2.8	6	-0.06 \pm 3.66	-0.05 \pm 4.08	0.00 \pm 1.42	-0.25 \pm 4.48	-0.17 \pm 2.63	-0.21 \pm 4.57

Table 3.8: Bland-Altman (BA) mean (μ_{BA}) and limits of agreement (LA) for longitudinal registrations with the proposed strategies against the expert ground truth (212 anatomical landmarks used as samples).

3.3.5 Longitudinal motion from *in-vivo* studies

To analyze the factors that contribute to the appearance of longitudinal motion, we compare groups of IVUS studies using different criteria. Since we map the systolic frames to the diastolic frames whose locations are known, we use this mapping as a non-linear description of the longitudinal motion between the diastole and systole, i. e., the vessel displacement between \mathcal{I}_{st} and \mathcal{I}_{mo} . Then, we define the longitudinal motion in mm units at the k -th frame as follows

$$d_k = |s(I_k^{st}) - s(I_k^{mo})|. \quad (3.3.4)$$

where s is the function of frame space location defined in (3.2.26) and (3.2.29). Then, we define three longitudinal motion features: the fraction of the study with a pre-defined motion (p_d), the motion mean (μ_d) and the motion standard deviation (σ_d). The p_d feature is calculated as

$$p_d = \frac{\sum_{k=1}^N m^i(d_k)}{N} \quad (3.3.5)$$

where $m^i(d_k)$ is 1 if $d_k \geq i$ otherwise is 0, and N is the amount of heartbeats in the study such that contains the phases \mathcal{I}_{st} and \mathcal{I}_{mo} . We decide to measure the rate that represents the fraction of the study that spans with longitudinal displacement of $i = 0.6$ mm or more. The use of 0.6mm as threshold for longitudinal motion is given by the fact that I^{st} frames are spaced by ≈ 0.5 mm and errors of this magnitude are expected for the discretization of $s(I_k^{mo})$. Then, we choose to add 0.1mm to avoid the oscillations of the discretization error to guarantee the motion detection. The remaining features, μ_d and σ_d , are trivially defined as the mean and standard deviation of $d_k \geq 0.6$ mm in the study.

In the first analysis, we grouped the studies by coronary arteries. Additionally, the studies were separated by presence or not of a stent to avoid that longitudinal motion is affected by stent deployment, which may interfere with coronary artery local effects. According to the results reported in Table 3.9, a general reduction of motion was seen in all the features for the cases in which there was stent deployment. A minor portion of the study presented longitudinal motion and even in the locations where the motion persisted, a reduction in the mean and standard deviation was observed. In the case with no stent deployment, it was seen that as the longitudinal motion was less frequent (smaller values of p_d), the intensity of the motion also decreased (μ_d and σ_d). Particularly, LAD arteries presented the smallest longitudinal motion, followed by the RCA and LCx. All these results are consistent with those reported by [21] using different IVUS and AX techniques for longitudinal displacement estimation.

In the second study, we choose 5 patients with multiple IVUS studies on different arteries to assess whether the longitudinal motion is related to a specific patient, or not. The analysis did not show a clear correlation between the patient and the longitudinal motion. A study with a bigger patient population is necessary to evaluate this issue.

A last study is performed for patients before and after stent deployment to assess the influence of the arterial longitudinal stiffening and the longitudinal motion. To visualize the longitudinal displacement provoked by the heart contraction, we subtracted the pullback longitudinal displacement. As result, we observed (see Figure 3.11) that the stenting procedure suppressed the longitudinal displacement at the stent location and its surroundings. Also, the bifurcations outside the stent moved towards the stent center as well as some of the motion patterns (e.g. Case 2 in the distal half). In terms of quantitative indexes, Table 3.10 shows that the percentage of the vessel under motion (according to p_d estimator) decreases. Only the Case 5 shows the contrary, although as its mean displacement (μ_d) suggests this motion is due to transducer pullback (which is in ≈ 0.5 mm between cardiac cycles). Also, the displacements mean and standard deviation (μ_d and σ_d , respectively) presented a decreasing trend after stent deployment.

Artery label	With Stent			Without Stent			
	$\langle p_d \rangle$	$\langle \mu_d \rangle$ (in mm)	$\langle \sigma_d \rangle$ (in mm)	S	$\langle \mu_d \rangle$ (in mm)	$\langle \sigma_d \rangle$ (in mm)	S
LAD	0.09	1.10	0.38	12	1.33	0.63	15
LCx	0.20	1.74	0.84	6	2.25	1.14	6
RCA	0.08	1.03	0.25	3	1.66	0.81	7

Table 3.9: Mean longitudinal motion features for different coronary arteries with and without stent deployment. The S value stands for the amount of samples in the population used for the calculation and $\langle (\cdot) \rangle$ is the mean of $\langle \cdot \rangle$ for the S samples.

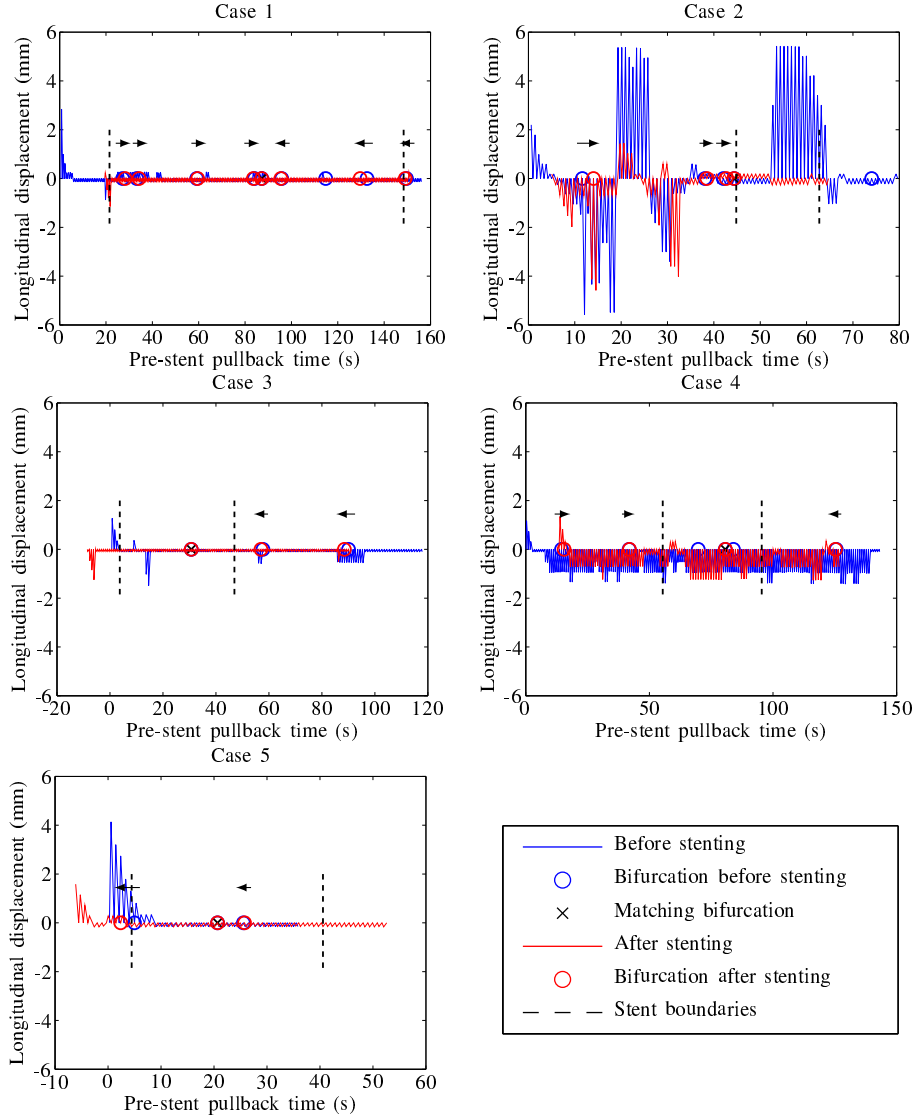


Figure 3.11: Longitudinal displacement estimated before and after stent deployment in 5 different patients. The bold \times marks the bifurcation used for rigid registration of the studies. The black arrows depict the longitudinal displacement of the remaining bifurcation due to stenting deformations in the vessel.

3.3.6 Longitudinal motion characterization

The insights given by the longitudinal motion before and after stent deployment, suggest that the observed longitudinal motion is directly related to the longitudinal vessel strain. As it is known, the estimated longitudinal motion represents the relative displacement between the vessel wall and the IVUS transducer. If longitudinal motion were to be dominantly determined by the transducer migration, the expansion of the lumen would increase the longitudinal motion. Instead, the five cases presented in Figure 3.11 have shown the opposite phenomenon (see Table 3.10). This behavior is compatible with the hypothesis that longitudinal motion is connected to the longitudinal strain (i.e. the longitudinal displacement of the vessel wall), which was suppressed by the stent deployment. Even more, the results reported in Table 3.9 show a reduction of longitudinal motion for arteries with stent and similar results are reported by [21] with different IVUS and AX imaging techniques. All this evidence is also compatible with the previous hypothesis.

Case	Pre-stent			Post-stent		
	p_d	μ_d (in mm)	σ_d (in mm)	p_d	μ_d (in mm)	σ_d (in mm)
1	0.16	0.51	0.47	0.03	0.56	0.30
2	0.89	2.20	1.98	0.69	1.10	1.14
3	0.16	0.58	0.31	0.03	0.68	0.37
4	0.85	0.90	0.15	0.22	1.04	0.15
5	0.24	1.81	1.41	0.93	0.45	0.12

Table 3.10: Longitudinal motion features for 5 different cases before and after stent deployment. The features were only computed along the vessel part where the stent was deployed.

By assuming this hypothesis to hold, the presented method becomes more than a mere longitudinal registration solution for IVUS. As a matter of fact, it allows the estimation of longitudinal strain distribution along the vessel. With this data at hand, and making use of proper tissue characterization methods, the longitudinal stress over atherosclerotic lesions could be inferred once suitable constitutive models for the vessel wall are available. Also, we could be able to predict areas more susceptible to stent fracture which is a late adverse event related to local shear forces [75].

Finally, the suppression of the longitudinal motion at the stenting area may be a temporal collateral effect associated to the angioplasty procedure. In fact, it is well known that during angioplasty the arteries tends to contract, reacting to the balloon inflation [121, 127, 311]. In a study by Togni et al.[311], implantation of a bare-metal stent does not affect physiologic response to exercise proximally and distally to the stent. However, sirolimus-eluting stents are associated with exercise-induced paradoxical coronary vasoconstriction of the adjacent vessel segments, although vasodilatory response to nitroglycerin is maintained. These observations suggest (drug-induced) endothelial dysfunction as the underlying mechanism. To better characterize the absence of longitudinal motion in stenting areas, longitudinal studies with pre-stent, post-stent and follow up IVUS acquisitions need to be performed.

3.4 Discussion

Several authors base their registration strategies on the segmentation of the whole arterial wall to obtain a more reliable representation of the vessel, although the outcomes of the present study suggest that this task is ineffective and, moreover, does a disservice to the registration. In contrast, the inclusion of perivascular tissue to the ROI aids the identification of the location of the vessel cross-section. In that sense, the ROI FIR avoids the segmentation task which is time consuming and, in some cases, questionable (e.g. bifurcations or calcium rings). Circumventing this task is fundamental towards achieving automation of the registration procedure, as in the present approach when using the FIR mask. In this last point, studies with guidewire artifact may demand the artifact segmentation (see Chapter A) which is the only not fully automatic task, although it is far less time demanding than vessel wall segmentation.

The transducer motion model is such that the fully coupled and the DTL decoupled method render similar results, being slightly better the latter technique. Both strategies, substantially outperform the DLT strategy, pointing out the importance of performing transversal registration prior longitudinal registration. Remarkably, the frames that rendered better results with DTL than with the coupled implementation feature significant

variation of the cross-section geometry between systole and diastole, e.g. bifurcations, and other neighboring contours, which attained a major MLE value than the expected (correct) frame. The use of transversal non-rigid registration may improve these cases, although it is important to highlight that the registration error was acceptably low even in these cases. The reason for DTL to slightly outperform the coupled implementation is that successive frames of the same phase present a similar transversal motion from diastolic phase, then DTL favors the longitudinal registration against near location frames which in most cases present the correct solution. On the contrary, the coupled implementation performs transversal registration against each one of the longitudinal candidate frames, which gives the best alignment to near or far frames without favoring any in particular. When the correct frame matches with low MLE value due to non-rigid deformations, the coupled implementation may result in larger errors than the DTL.

Another interesting insight from the registration analysis was the poor reproducibility of registration results obtained from medical imaging experts. This is consequence of the poor quality of ultrasound images which hinders the registration task for the human inspection. In contrast, computational models, as proposed here, ensure reproducibility, giving less uncertainty to the quality of the registration. Also, we demonstrated that the transversal error was competitive with the experts alignment and that mean longitudinal error was smaller than a single frame. These results indicate that our registration approach (particularly DTL) is less time consuming, offering reproducibility and high accuracy, which makes it more convenient for medical practice than manual registration by experts.

In Section 3.3.5, we have shown the capabilities of using the proposed method to measure local longitudinal strains along the vessel, which were in agreement with previously reported observations ([21]). This application of the method may help for the characterization of the vessel properties and for the better understanding of the vessel deformation in different scenarios.

As final remark, note that the normalized cross-correlation and Rayleigh MLEs have rendered larger errors for both registrations (transversal and longitudinal) than Generalized Gamma MLE. The latter estimator models better the log-compressed multiplicative noise which is the case of IVUS images. As result, the MLE is less sensitive to this noise along the registration process, improving the similarity measurements across the vessel structures.

3.5 Final remarks

Methods for longitudinal and transversal registration and longitudinal motion estimation were proposed in this chapter. Insights from applying the methodology before and after stenting procedures suggests that the longitudinal motion is associated with the longitudinal strain of the vessel wall, something that can benefit the construction of new culprit plaque indicators adding physical magnitude.

From the proposed methods, it was shown that a decoupled strategy of transversal prior longitudinal registration is the best option in terms of accuracy and computational cost. To reduce even more the computational cost involved in the transversal registration stage, the so-called MSGA method was developed and exhaustively tested. Also, it is concluded that the best choice of ROI used for registration is the one that makes use of both vessel wall and perivascular tissue, discarding the need for image segmentation.

Estimation of longitudinal motion across 52 IVUS studies showed that stenting procedures tend to suppress the local longitudinal motion and the overall motion within the study. In arteries without stent, LAD arteries present the smaller amount of longitudinal motion, followed by LCx and RCA.

Chapter 4

Denoising and optical flow

The mechanical characterization of biological tissue, as will be seen later, requires information about the kinematics of the arterial wall (i.e. the displacements of the vessel wall). The IVUS imaging modality is an excellent candidate to provide such information because it captures a spatio-temporal description of the artery. As presented in the previous chapters, we sorted the study data in time and space, so we are capable to retrieve a sequence along the cardiac cycle for each cross-section of the vessel. The remaining step to endow the study with data describing the kinematics, is to determine the arterial wall displacement along the cardiac cycle.

The optical flow (OF) is a well established and robust method for image tracking. Many formulations and implementations for this technique have been proposed since early the 80s. Actually, there is not a better method for this task, but a method that performs better depending on the characteristics of the image sequence. For this, we present an extensive review of the state-of-the-art in Section 4.1 and identify the more suitable methods for IVUS modality in Section 4.3.

The main drawback of OF when applied to IVUS images is that its capability to retrieve accurate displacement fields degrades remarkably because of the low signal-to-noise ratio (SNR) of the image sequence. Then, an effective denoising mechanism to improve SNR is essential to obtain reliable results. In Section 4.2, we address this issue contributing with a novel technique, called *maximum likelihood variations*, which is tailored to diminish speckle noise.

Finally, we analyze the performance of the denoising process combined with optical flow techniques using idealized (a ring geometry without image noise), in-silico (in-vivo based geometries with and without noise) and in-vivo image sequences. The final remarks in Section 4.5, summary the performance and insights of the proposed techniques and present potential future research in these areas.

4.1 State-of-the-art in Optical Flow techniques

Optical flow techniques (OF) have been actively studied since the beginning of the 80s. Its many applications in human-computer interaction, engineering and medicine increased the efforts of the computer vision community to render more efficient and accurate methods to solve these tasks. For these reasons, a wide variety of OF solutions are present in the literature which are optimal in different scenarios or for specific image characteristics, and users must be careful to select the one that is more appropriate for its own problem.

The first OF technique was introduced by Horn and Schunck [147]. The work presents an estimation of the displacement field that registers two images based on the minimization of the material derivative of the image intensities. As the problem is ill-posed

due to the denominated aperture problem (only the normal iso-brightness component of the flow can be estimated), a Tikhonov spatial regularization is proposed for the propagation of the solution from areas of high gradient modulus to zones where the gradient nearly vanishes. Other approximations, such as [201], do not make use of regularization to avoid low confidence flows (i.e. zones where the aperture problem arises), instead the flow in that locations is left as undetermined. As the outcomes suggest, the former methods were denominated as dense flow approaches and the latter as sparse flow approaches.

The Tikhonov regularizer in the Horn-Schunck formulation restricts the identification of discontinuous flows at the interfaces between objects with different trajectories. At these regions, the quadratic variations of the flow are penalized due to the regularizer and, as consequence, the discontinuities are over-smoothed. Several authors proposed different alternatives to surpass this inconvenient. In [12, 16, 238], a regularizer in terms of the curvatures allows an anisotropic diffusion of the flow leading to a discontinuous flow along long object boundaries (the shorter the boundary, the less the discontinuity is preserved). Other approaches, as proposed in [38, 241] impose a discontinuity penalization term and an estimator of the discontinuities presence. [314] proposes a solution of the aperture problem by considering objects in the scene with Lambertian surfaces and constant velocity at the local region. Alternatively, [299] propose a regularization term based on the theory of robust statistics to overcome the misspecification of the probability distribution associated to the intensity discontinuities. A more general regularizer is presented in [288] where Tikhonov and curvature approaches are special cases. The most popular solution, used even in the most recent works, is the one proposed in [79]. In that work, the regularization term is the L_1 norm of the flow gradient, which penalizes less the discontinuities in detriment of the functional regularity.

The flow discontinuity preservation was also tackled by identifying the objects boundaries. In [133] an edge motion constraint equation is added to track potential discontinuities. Also, the OF at regions with major uncertainty is improved by a global Bayesian decision using a maximum a posteriori criterion over different estimators. [260] proposed to resolve the OF forward and backward between a pair of images and then use the inconsistencies between the obtained fields to identify the occlusion regions. To preserve the flow discontinuities, an anisotropic diffusion regularization is used, similar to [16, 238]. Other authors suggest to segment the image in areas with homogeneous flows and match the discontinuities with the areas boundaries. In [40], the image is partitioned in patches where the flow is approached with a parametric model with local deformations. In that manner, the discontinuities at the inter-patch boundaries are naturally represented due to the lack of flow continuity constraints. In [220], a segmentation algorithm is coupled with the OF, and in an extended cost functional a term relaxes the flow smoothness at the segmentation boundaries and a second term increases the smoothness in the interior of subdomains. In [254] a similar approach is presented where the OF is calculated by a convex combination of the forward and backward flows. The obtained flow is more robust against occlusions in the scene.

In addition to the spatial regularization, some authors proposed the temporal regularization [37, 39, 40, 98, 344] assuming that the time between the images is small enough to deliver a small motion variations of the objects.

All the previous approaches regularize the OF based on mathematical predictions for border detection and, then, a diffusion process is imposed in the zones where flow uncertainty increases, disregarding the material properties. These approaches were conceived for general purpose and, because of that, there is no further knowledge about the nature of the objects in the scene. In turn, the knowledge of the mechanical models that describe objects behavior in the scene may improve this regularization leading to a mechanically compatible flow. In this field only few works such as [159, 160] and [112] have

shown contributions. In [160], a Lucas-Kanade approach is used to estimate an sparse flow over the domain, which is then imposed as constraint over an unstructured mesh where the nodes, which compose the mesh that describes the domain of analysis, are attached by springs. By minimizing the potential energy stored in the springs, where the spring stiffness is related to the mechanical properties of the underlying material, regularized displacements are obtained over the whole domain. [112] computes the flow only where the intensity gradients are high enough, i.e., regions with no aperture problem. Here, the mechanical properties are searched in terms of solid mechanics numerical simulation such that the resulting displacement field minimizes the data term of the optical flow. As we can see, no regularization term is used because the zones with aperture problem are neglected, and also, a dense field can be derived in terms of the mechanical problem although not enterily supported by image data.

In turn, several modifications have been suggested for the data term (represented in Horn-Schunck method by the material derivative). The material derivative is valid for OF identification as long as intensity remains constant on the surfaces between frames and as displacements are small enough, such that the material derivative of the intensity represents the image constancy between two images. The intensity constancy is usually violated due to noise or brightness variance of the surfaces. To tackle this issue, [37, 38, 39, 46, 47, 344] propose different normalization functions over the data term (and also the regularization term) which eliminate the contribution of outlier pixel values (uncorrelated motion of a pixel caused by intensity constancy violation). Alternatively, [180, 245] propose the addition of a data term based on the image gradients, increasing the gradient constancy constraint to the model. In the latter, a confidence estimator of the gradient is proposed in order to weigh the contributions of image and gradients data terms. Other authors treat these issues in an over-constrained equation system similar to [201], estimating the OF in the sense of total least square [333], least median of square orthogonal distances [27] or weighted total least square [27]. In all the three previous approaches, the outliers are identified and neglected for the OF calculation. For cases with large displacements between the two images, the material derivative in the data term is not enough, because it is simply a first order Taylor expansion for the OF problem and lacks the high order information required. For this reason many OF methods employ the denominated multiresolution scheme, proposed in [16, 247]. The method consists in progressively estimating the frequencies of the displacement field using coarse resolutions of the image, the coarser the resolution, the lower the frequency of the displacement that is calculated. The final flow is estimated by superposition of all calculated displacements. As an additional advantage, this method usually speeds up the convergence due to the decomposition in smaller (and computationally cheaper) OF problems.

Other less popular approximations for the OF problem are the frequency domain approaches. Few authors explore the capabilities of using a family of Gabor filters or Fourier analysis to track objects in time [36, 109, 132]. As commonly seen in image processing, the frequency domain eases the noise detection for diverse classes of noise and distributions. Nevertheless, these methods do not yield accurate and robust flows such as the time domain approaches.

Most renowned methods for general purpose OF are the ones developed by Farneback [102, 103, 104], Weickert [46, 47, 48, 49, 50, 51, 334, 335] and Zach [348].

The Farneback method exploits the orientation tensor (linear transformation that assesses the variation of the intensity in the direction of the applied vector) constructed at each pixel from a local quadratic approximation. In this method, the optical flow is obtained as the intensity invariant directions, i.e., the eigenvector with minor eigenvalue modulus. Note that for this approach the aperture problem rises when the minor eigenvalue has a multiplicity $\mathcal{M} \geq 2$. To avoid a noisy representation of the field, the author

proposes a parametric piecewise fitting for the representation of the field. In [102], it is proposed to define motion coherent regions by an heuristic approach over which the parametric fitting is applied. This method also features multiresolution characteristics to efficiently identify large displacements in the image sequence.

With the Weickert method, several improvements for OF have been proposed. The first contribution is the use of a nonlinear regularizer with the idea of reducing the flow diffusivity in regions with small flow. The correct tuning of this method allows discontinuous flows at the interfaces maintaining the well-posedness at constant intensity regions. The second is the combined local-global approach in which the image gradients and temporal derivatives are low-pass filtered to obtain a smooth and dense gradient field. In order to preserve boundary discontinuities, low-pass filtering must be carefully selected, i.e., through setting a cut frequency as large as possible. It has been demonstrated that this method presents a good performance when dealing with Gaussian noise. Additionally, such contributions were combined with a multiresolution methodology for robustness in large displacements scenarios.

The Zach method is methodologically simpler, although it delivers robust and discontinuous flows. The method uses the L_1 norm over each term of the classic Horn-Schunck formulation, i.e., a total variation with L_1 norm (TV-L1). The discontinuity of the functional derivative is treated by introducing a factor which smoothes the gradient near the minimum of the cost functional, making it differentiable. In [348], a duality based approach is proposed for an efficient minimization process. As simple as it is, this method has shown to increase the robustness of Horn-Schunck technique for constancy intensity violations, occlusions and noise within the image.

In the wider context of medical ultrasound, some authors have proven applicability of OF to solve tracking problems. In early 2000, several works demonstrated its applicability for tracking endocardial surface [17, 95, 223, 264] and cardiac valves [223] using a 5 MHz ultrasonic probe. In these applications, OF assisted the initialization of the segmentation contours in order to improve the initial prediction in a large displacement context. [309, 349] conducted a carotid elastography with an ultrasonic biomicroscope at 40 MHz presenting reasonable displacements for the arterial wall. Also, recent applications for tracking muscle landmarks have been presented [167]. Even more, the increasing attention for the OF in speckle polluted images (speckle tracking) has led to the creation of benchmark synthetic tests in the literature [10].

Although the advance in such applications shows a maturity of the OF in speckle scannerios, less applications are present for high frequency transducers where the speckle noise degrades even more the image (lower SNR due to bigger number of scatters of the ultrasound beam). Specifically in IVUS studies, OF has poorly been explored. In our knowledge, only the works of Danilouchkine et al. [83, 84, 85, 86, 87] have used these techniques for the assessment of the mean rotation of each IVUS frame. In the context of the present thesis, it is important to remark that the use of OF techniques to quantify the displacement field of arterial walls had been unexplored so far.

4.2 Despeckling of IVUS images

Ultrasonic image processing is a challenging task through its low signal-to-noise ratio (SNR). Particularly, optical flow techniques rely on the brightness constancy constraint which is far from being met in these conditions. However, we may circumvent this problem in two different manners: (i) we improve the SNR with a denoising technique in order to satisfy the brightness constancy constraint; or (ii) we develop new optical flow techniques robust to such image noise.

On the one hand, the former approach allows the use of mature optical flow techniques whose performance has been improved since the 90s. On the other hand, the latter approach allows the estimation of the flow over the raw data of the image, which is more efficient in terms of computational cost because treats the noise at the same time it estimates the optical flow.

Even though, we propose to explore the first approach as a preliminary work to in the future address the approach (ii). The first approach requires for a denoising method that can be improved by incorporating statistical information of the image noise. As previously seen in Chapter 3, functions based on maximum likelihood estimator permit to quantify similarity between two images with known noise involved. By endowing classic denoising strategies [64, 282] with specific noise recognition capabilities, we may obtain a tailored method to appropriately denoise IVUS images. This stands for the approach (i) mentioned above, allowing the optical flow computation over denoised IVUS images. Hence, the insight gained for IVUS noise characterization and the similarity functions used for denoising can be key for the development of new optical flow methods as discussed in (ii). The brightness constancy constraint is imposed by the data term, which approximates the intensity variation of the pixels between two images connected by a mapping function (the optical flow), i.e., $\|I_0(\mathbf{x} - \mathbf{w}) - I_1(\mathbf{x})\|$ where I_0 and I_1 are successive images, \mathbf{w} is the flow between them, and $\|\cdot\|$ is a given norm. Instead of minimizing the absolute difference of the pixel intensity, we propose to minimize a similarity function which considers the specific IVUS noise statistics.

In this chapter, we propose a new denoising technique more appropriate for IVUS noise, i.e., the solution for (i). A comparison against total variation method is performed in order to evaluate the improvement of such approach.

4.2.1 Total variation method

Firstly proposed in [282], the total variation method allows the image denoising for a wide spectrum of noise distributions. The method yields a denoised image by minimizing the total variation against the original noisy image. Particularly, the use of norm L_1 over the total variation term (method known as TV-L1) leads to major discontinuities while maintains the same level of denoising in the image. To formally define the TV-L1 method, let us define $I_o(x, y)$ as the original image and $I_d(x, y)$ as the denoised image, then $I_d(x, y)$ is estimated as follows

$$I_d = \arg \min_{\tilde{I}} \int_{\Omega} \left(|I_o(x, y) - \tilde{I}(x, y)| + \alpha |\nabla \tilde{I}(x, y)| \right) d\Omega, \quad (4.2.1)$$

where Ω is the image domain. Note that the functional defined in (4.2.1) is composed by a data term that measures the sum of absolute differences between the images and by a regularization term that imposes the continuity for the denoised image. The α parameter is key for the expected outcome of the method, small values of α do not denoise the image, while large values do not preserve image structures. For this reason the optimal value of α must be small enough to preserve the structures of interest in the image and large enough to deal with the maximum amount of noise. In this particular method the α parameter has not physical or experimental association.

To efficiently minimize (4.2.1), [65] proposed the Primal-Dual method in which a saddle point formulation of the functional is adopted. Convergence and numerical analysis for this method is presented in [64]. The discretized scheme for this approach, considering that $\Omega \subset \mathbb{R}^{m \times n}$, is given by the following iterative procedure, for $k = 0, 1, 2, \dots$, until convergence is achieved

$$p^{k+1} = \frac{p^k + \sigma \nabla I_d^k}{\max(\|p^k + \sigma \nabla I_d^k\|, 1)} \quad (4.2.2)$$

$$\hat{I}_d^{k+1} = g(I_d^k - \tau \nabla^T p^{k+1}, I_o, \alpha \sigma) \quad (4.2.3)$$

$$I_d^{k+1} = \hat{I}_d^{k+1} + \beta(\hat{I}_d^{k+1} - I_d^k) \quad (4.2.4)$$

where $p^k \in \mathbb{R}^{m \times n \times 2}$, τ and σ are the step size associated to the numerical scheme, β is the subrelaxation parameter for the minimization and $g(x, y, z)$ is defined as

$$g(x, y, z) = \begin{cases} x - z & \text{if } x > y + z \\ x + z & \text{if } x < y - z \\ y & \text{if } |x - y| \leq z \end{cases}. \quad (4.2.5)$$

In the study cases presented in forthcoming sections, we choose $p^0 = \nabla I_o$ and $I_d^0 = I_o$ as initialization and $\beta = 1$ for subrelaxation.

As presented in (4.2.1), a linear penalization for discrepancies between I_o and I_d is used, then noises that impose high intensities differences are successfully treated (e.g. salt-and-pepper noise). On the contrary, noises with low intensity are reduced, in part, for the contributions of the regularization term which tends to homogenize the local region and smooth image discontinuities as α increases. Then, the sharpness and local mean values of the image could be sacrificed to deal with low intensity noises.

An example of these scenarios is presented in Figure 4.1 where salt-and-pepper noise and generalized gamma (GG) distributed noise illustrate the high intensity and low intensity cases, respectively. In fact, the latter noise distribution presents low and high intensity differences, however the former case shows that the high intensity contributions are successfully treated by TV-L1. The multiplicative GG distributed noise is close to the noise observed in IVUS images. As we can see, TV-L1 over smooths the image, missing the brighter region (which is characteristic of a calcified area). For this reason, we will introduce a novel method for IVUS image denoising to deal with this problem.

4.2.2 Maximum likelihood variation method

From the TV-L1, we see that denoising methods behave appropriately as long as noise manifests a high contribution in the penalization energy proposed in (4.2.1). In that scenario, it is seen how the regularization term imposes smoothness to denoise the places with such high penalization energies. Then, it would be desirable for penalization contribution to be proportional to the probability of noise appearance at each place.

Then, we propose to coin a data term proportional to the noise probability of ultrasonic images. As previously discussed in Chapter 3, the generalized gamma (GG) distribution seems to be the most likely noise distribution for high frequency ultrasonic imaging. Thus, we derive the maximum likelihood estimator that compares one image, \hat{I}_o , with GG distributed noise versus a noiseless image, \hat{I}_d , which represents the denoised image. We know that

$$\hat{I}_o(x, y) = \hat{I}_d(x, y) \varepsilon(x, y) \quad (4.2.6)$$

where $\varepsilon(x, y)$ is a noise with GG distribution. As IVUS images I_o and I_d are log-compressed, then

$$\begin{aligned} \log(\hat{I}_o(x, y)) &= \log(\hat{I}_d(x, y) \varepsilon(x, y)) \\ \log(\hat{I}_o(x, y)) &= \log(\hat{I}_d(x, y)) + \log(\varepsilon(x, y)) \\ I_o(x, y) &= I_d(x, y) + \tilde{\varepsilon}(x, y) \end{aligned} \quad (4.2.7)$$

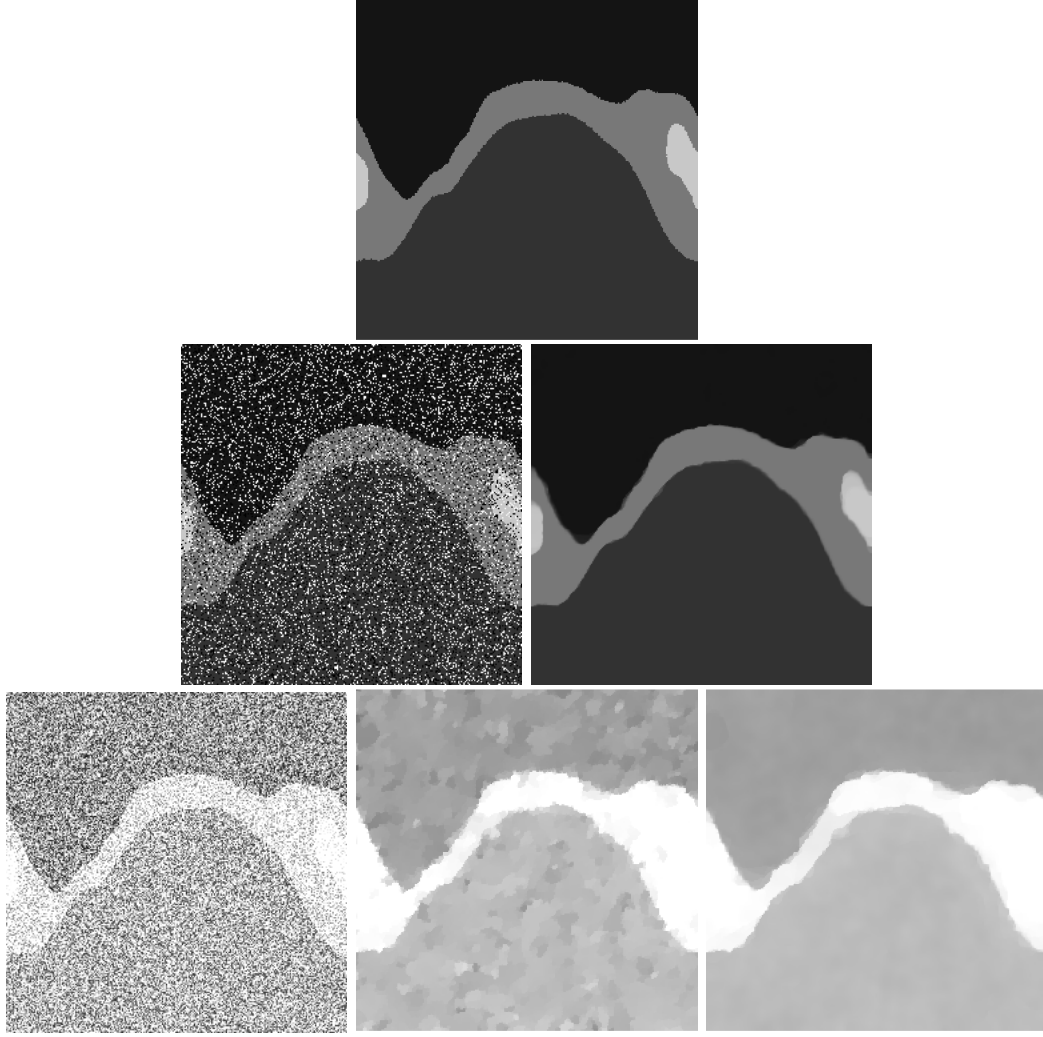


Figure 4.1: Denoising of a synthetic image using TV-L1 method with $\tau = 0.01$, $\sigma = \frac{1}{8\tau}$: (top) synthetic image; (middle, from left to right) image with pepper-and-salt noise and denoised image using $\alpha = 1$; (bottom, from left to right) image with multiplicative generalized gamma distributed noise, image denoised using $\alpha = 1$ and $\alpha = 0.5$, respectively.

where $\tilde{\varepsilon}(x, y)$ is distributed by $P_{\tilde{\varepsilon}}(y)$ probability density function derived from the GG distribution $P_{\varepsilon}(x)$ as

$$P_{\tilde{\varepsilon}}(\varepsilon)dP_{\tilde{\varepsilon}}, \quad \varepsilon = e^{\tilde{\varepsilon}} \text{ and } dP_{\varepsilon} = e^{\tilde{\varepsilon}}dP_{\tilde{\varepsilon}}. \quad (4.2.8)$$

Changing variables in the GG probability density function, we obtain that

$$\begin{aligned} P_{\tilde{\varepsilon}}(\tilde{\varepsilon})dP_{\tilde{\varepsilon}} &= P_{\varepsilon}(\varepsilon)dP_{\varepsilon} \\ &= P_{\varepsilon}(e^{\tilde{\varepsilon}})e^{\tilde{\varepsilon}}dP_{\tilde{\varepsilon}} \\ &= \frac{\gamma}{\delta^{\gamma\nu}\Gamma(\nu)} (e^{\tilde{\varepsilon}})^{\gamma\nu-1} e^{-\left(\frac{e^{\tilde{\varepsilon}}}{\delta}\right)^{\gamma}} e^{\tilde{\varepsilon}}dP_{\tilde{\varepsilon}} \end{aligned}$$

Finally, we obtain the log-compressed GG distribution as follows

$$P_{\tilde{\varepsilon}}(y) = \frac{\gamma}{\Gamma(\nu)} e^{\gamma\nu(y-\log \delta) - e^{\gamma(y-\log \delta)}}, \quad \gamma, \delta, \nu > 0. \quad (4.2.9)$$

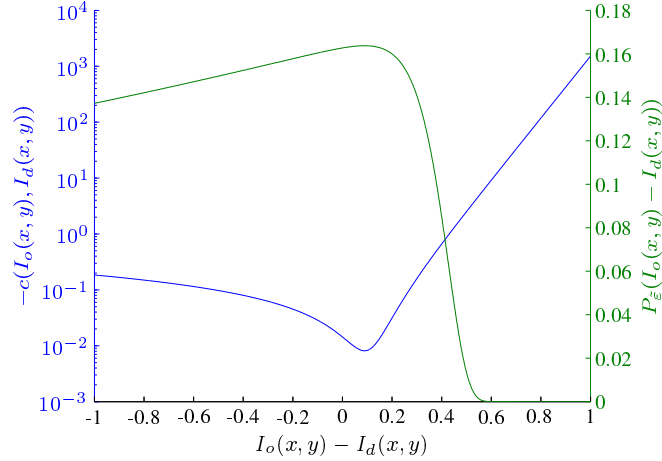


Figure 4.2: Probability density function for log-compressed noise in IVUS (green line) versus the data term value in (4.2.12) (blue line). Parameters used both functions are $\gamma = 12.75$, $\nu = 0.014$ and $\delta = 1.53$.

Using this model of noise, we construct the associated MLE as proposed in (3.2.6),

$$\begin{aligned}
e(I_o, I_d) &= \sum_{(x,y) \in \Omega} \log \left[P_{\varepsilon}(I_o(x, y) - I_d(x, y)) \right] \\
&= \sum_{(x,y) \in \Omega} \log \frac{\gamma}{\Gamma(\nu)} e^{\gamma \nu (I_o(x, y) - I_d(x, y) - \log \delta) - e^{\gamma (I_o(x, y) - I_d(x, y) - \log \delta)}} \\
&= |\Omega| \left(\log \frac{\gamma}{\Gamma(\nu)} - \gamma \nu \log \delta \right) \sum_{(x,y) \in \Omega} \left[\gamma \nu (I_o(x, y) - I_d(x, y)) - \frac{1}{\delta^\gamma} e^{\gamma (I_o(x, y) - I_d(x, y))} \right].
\end{aligned} \tag{4.2.10}$$

Discarding the constant contributions, we create a pixel-wise function for comparison given by

$$c(I_o(x, y), I_d(x, y)) = \gamma \nu (I_o(x, y) - I_d(x, y)) - \frac{1}{\delta^\gamma} e^{\gamma (I_o(x, y) - I_d(x, y))}. \tag{4.2.11}$$

Then, we modify the data term in cost functional (4.2.1) using the negative function of (4.2.11) to measure the discrepancies between IVUS images in an appropriate manner. The new optimization problem is given by

$$I_d = \arg \min_{\tilde{I}} \int_{\Omega} \left(-c(I_o(x, y), \tilde{I}(x, y)) + \alpha |\nabla \tilde{I}(x, y)| \right) d\Omega. \tag{4.2.12}$$

Note that the integration of the data term leads to (4.2.10) negated, up to a constant factor. As seen in Figure 4.2, as the difference between the original image and the restored image has higher probability to be given by the noise distribution (P_{ε}), the smaller is the penalization value in the data term. Assuming a smooth variation of $|\nabla I_d(x, y)|$, the Euler-Lagrange equations that minimize the cost functional (4.2.12) (see details in Appendix C.1) are the following

$$\gamma \nu - \frac{\gamma}{\delta^\gamma} e^{\gamma (I_o(x, y) - I_d(x, y))} - \alpha \frac{\Delta I_d(x, y)}{|\nabla I_d(x, y)|} = 0 \quad \text{in } \Omega \tag{4.2.13}$$

$$\nabla I_d(x, y) \cdot \mathbf{n} = 0 \quad \text{in } \partial\Omega \tag{4.2.14}$$

where $\partial\Omega$ is the boundary of the image domain and \mathbf{n} is the unit normal vector pointing

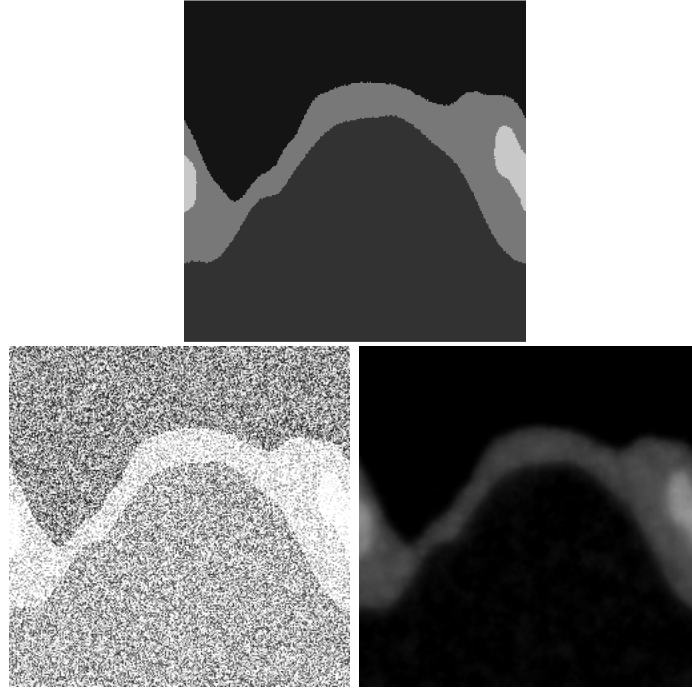


Figure 4.3: Denoising of a synthetic image using MLV method with $\alpha = 40$, $\gamma = 3.2$, $\nu = 0.22$, $\delta = 3.67$: (top) synthetic image; (bottom, from left to right) image with multiplicative generalized gamma distributed noise and image denoised, respectively. The image dynamic range is normalized between $[0,1]$ for the current parameters.

outwards to that boundary. To deal with the non-linearities introduced by the exponential term, we use a fixed-point iteration scheme with sub-relaxation (the latter to avoid overshooting problems). The discrete linear system of equations is given by

$$I_d^{n+1}(x, y) = \beta I_d^n(x, y) - (1 - \beta) \left[\frac{\gamma\nu - \frac{\gamma}{\delta\gamma} e^{\gamma(I_o(x,y) - I_d^n(x,y))}}{4\alpha} |\nabla_h I_d^n(x, y)| + I_d^n(x+1, y) + I_d^n(x, y+1) + I_d^n(x-1, y) + I_d^n(x, y-1) \right] \quad (4.2.15)$$

using a finite difference discretization with spatial spacing $\Delta x = \Delta y = 1$ pixels, and the gradient operator is discretized as

$$|\nabla_h I_d^n(x, y)| = \sqrt{(I_d^n(x+1, y) - I_d^n(x, y))^2 + (I_d^n(x, y+1) - I_d^n(x, y))^2}. \quad (4.2.16)$$

The proposed method, called Maximum Likelihood Variation method (or simply MLV), was applied to the synthetic image of the previous section (see Figure 4.3). It is seen that the 4 different regions are preserved after the denoising process. As the noise characteristics are embedded in the data term, the method search for the more probable intensity that degraded by speckle noise yields the observed intensity. Then, image areas with higher noise probability are easily recovered. Complementary, image areas with lower noise probability are recovered due to the regularization term and the surrounding intensity values. In the TVL1 denoising, it was seen that the brightest region was merged with the surrounding regions due to the brightness increase provoked by the TVL1 smoothing. On the contrary, MLV correctly identifies the noise components and reduces the image intensity variations due to smoothing.

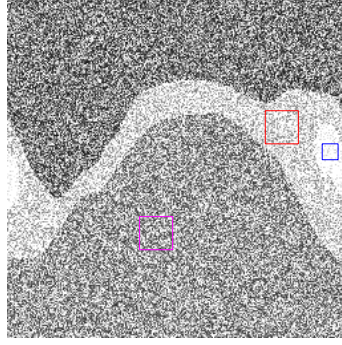


Figure 4.4: Synthetic image polluted with generalized gamma distributed noise $\alpha = 1.5$, $\gamma = 1.5$ and $\nu = 0.8$. The red, blue and magenta areas depict the regions of interest representing the intima, calcified and adventitia, respectively.

4.2.3 Parameter setup

The parameters that characterize the MLV method are divided in two groups, the noise distribution parameters and the smoothing and relaxation parameters. For the first group, we choose a reparametrization in terms of more meaningful parameters for the denoising process. Thus, we replace γ , ν and δ by the following parameters

$$a = \gamma \nu, \quad b = \frac{\gamma}{\delta \gamma}, \quad c = \gamma, \quad (4.2.17)$$

that allows to rewrite the Euler-Lagrange equation (4.2.13) over the domain, simply as

$$a - b e^{c(I_o(x,y) - I_d(x,y))} - \alpha \frac{\Delta I_d(x,y)}{|\nabla I_d(x,y)|} = 0, \quad (4.2.18)$$

where a , b and c model the weight of linear penalization, the weight of the exponential penalization and the exponential growing rate for the differences between $I_o(x,y)$ and $I_d(x,y)$, respectively.

Most applications using IVUS images (for example medical visualization of the vessel), demand a reduction of the speckle noise, recovering homogeneous intensity regions for each tissue. Then, we search the values of a , b , c and α such that minimize the intensity variations in the speckled image over regions that contain constant intensity in the original image (see Figure 4.4).¹

To achieve this, we minimize the following denoising error

$$\varepsilon_d^H = \frac{1}{|\mathcal{R}_1|} \sum_{x \in \mathcal{R}_1} (x - \mu_1)^2 + \frac{1}{|\mathcal{R}_2|} \sum_{x \in \mathcal{R}_2} (x - \mu_2)^2 + \frac{1}{|\mathcal{R}_3|} \sum_{x \in \mathcal{R}_3} (x - \mu_3)^2 \quad (4.2.19)$$

where \mathcal{R}_1 , \mathcal{R}_2 and \mathcal{R}_3 are the set of pixels over the intima-media, adventitia and calcium regions presented in Figure 4.4, μ_i is the mean intensity of \mathcal{R}_i and $|\mathcal{R}_i|$ is the amount of pixels in \mathcal{R}_i . For the set of parameters given by

$$\mathcal{P}_{MLV} = \{(\alpha, a, b, c); \alpha = 1, 2, \dots, 20; a, b, c = 0.1, 0.2, \dots, 2\} \quad (4.2.20)$$

$$\mathcal{P}_{TVL1} = \{(\tau, \alpha); \alpha = 10^i, i = -5, \dots, 0; \tau = 10^i, i = -5, \dots, 0\} \quad (4.2.21)$$

¹The specific application of optical flow will not necessarily require the absolute denoising of the image because the noise is related with the echogenic tissue and may aid its tracking. For such reason, we present a second parameter setup in the Section 4.4.2 where we find the optimum parameters in the sense of an optical flow global error.

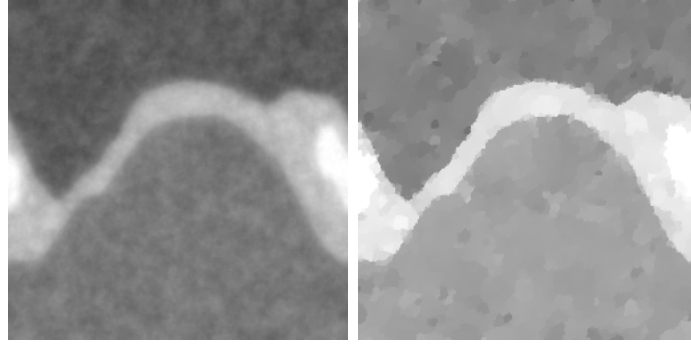


Figure 4.5: Best denoising in terms of error ε_d^H over the regions depicted in Figure 4.4: (left) the proposed MLV method presenting $\varepsilon_d^H = 0.191$; (right) the TV-L1 method presenting $\varepsilon_d^H = 0.284$. The image without denoising features an error of $\varepsilon_d^H = 0.496$.

we compute ε_d^H for MLV and TV-L1 methods². The minimum error was achieved using $\alpha = 4$, $a = 1.1$, $b = 1$, $c = 0.5$ for MLV and $\tau = 0.01$, $\sigma = \frac{1}{8\tau}$, $\lambda = 0.01$ for TV-L1 yielding to $\varepsilon_d^H = 0.191$ and $\varepsilon_d^H = 0.284$ respectively (see Figure 4.5). The method reduced the noise to 38.40% (ratio between ε_d^H after and before denoising) in the specified ROIs whereas the TV-L1 method reduced to 57.26%, showing better performance for the proposed MLV method.

4.3 Optical Flow methods

Next, we present the most popular optical flow methods to estimate flow between a pair of frames. The application of these methods to image sequences is by processing each pair of images at a time or by treating time as another spatial dimension (for example in Weickert 3D methods). This may lead to some difficulties in the parameter setting, e.g. the step in time is uncorrelated with the spatial spacing, which impacts in a set of critical parameters that cannot be properly adjusted. From the methods presented next, the Weickert method has been implemented by the author, while the Zach and Farneback methods were used from OpenCV library.

4.3.1 Horn-Schunck method (classic approach)

Let us define the image intensity function as $I(x, y, t)$. Then, the classical optical flow approach introduced by [147] is defined as the vector field \mathbf{w} that minimizes the following cost functional

$$\mathcal{E}(\mathbf{w}) = \int_{\Omega} \left[\left(\nabla I \cdot \mathbf{w} + \frac{\partial I}{\partial t} \right)^2 + \alpha \|\nabla \mathbf{w}\|_F^2 \right] d\Omega \quad (4.3.1)$$

where $\|\cdot\|_F$ is the Frobenius norm and $\mathbf{w} = (u, v)$ is the velocity intensity field, hereafter, the image flow. The first term is the material or total time derivative of the image intensity and the second term is a Tikhonov regularization of the first order derivatives. The functional without regularization term is ill-posed (usually referred in the literature to the aperture problem) because multiple solutions across iso-bright lines satisfy that optimization. Then, regularization provides the well-posedness of the problem imposing smoothness over \mathbf{w} , which in several scenarios is desirable.

²Both set of parameters were chosen to enclose the error minimum value and their spacing was such that no significant variations of error (minor than 0.01) occur among adjacent values

In that sense, the optical flow tracks iso-bright particles between two images, constraining the regularity of the solution vector field \mathbf{w} . Thus, some deficiencies of this method must be highlighted:

- the displacements of the particles must be infinitesimal so they can be tracked by the method;
- the method assumes that the particles (structure underlying at each pixel) remain with the same intensity (or at least suffer small intensity variations) which is improbable in images with noise;
- the method can not estimate spatial discontinues within flow field \mathbf{w} due to the constraint imposed by the regularization term.

Several modifications for this OF method have been proposed to circumvent these deficiencies. The next sections present those which we adopted to deal with IVUS sequences.

4.3.2 Farnebäck method

The Farnebäck method approximates the intensity field in the images with local quadratic polynomial expansions and then estimates the local displacement. The expansion is defined over a neighborhood of $P \times P$ pixels, denoted by η , satisfying

$$I(\mathbf{x}) \approx \mathbf{x} \cdot \mathbf{A}\mathbf{x} + \mathbf{b} \cdot \mathbf{x} + c \quad (4.3.2)$$

where \mathbf{A} is a symmetric matrix. The values of \mathbf{A} , \mathbf{b} and c are optimally calculated in the sense of weighted least squares to fit the \mathbf{x} pixels of a neighborhood. Then, the optical flow between I_1 and I_2 is formulated as

$$\begin{aligned} I_2(\mathbf{x}) &= I_1(\mathbf{x} - \mathbf{w}) = (\mathbf{x} - \mathbf{w}) \cdot \mathbf{A}_1(\mathbf{x} - \mathbf{w}) + \mathbf{b}_1 \cdot (\mathbf{x} - \mathbf{w}) + c_1 \\ &= \mathbf{x} \cdot \mathbf{A}_1\mathbf{x} + (\mathbf{b}_1 - 2\mathbf{A}_1\mathbf{w}) \cdot \mathbf{x} + \mathbf{w} \cdot \mathbf{A}_1\mathbf{w} - \mathbf{b}_1 \cdot \mathbf{w} + c_1 \\ &= \mathbf{x} \cdot \mathbf{A}_2\mathbf{x} + \mathbf{b}_2 + c_2 \end{aligned} \quad (4.3.3)$$

where \mathbf{w} is the optical flow and suffixes 1 and 2 stand for polynomial coefficients defined in images 1 and 2, respectively. From (4.3.3), we obtain the following identities

$$\mathbf{A}_2 = \mathbf{A}_1 \quad (4.3.4)$$

$$\mathbf{b}_2 = \mathbf{b}_1 - 2\mathbf{A}_1\mathbf{w} \quad (4.3.5)$$

$$c_2 = \mathbf{w}^T \mathbf{A}_1\mathbf{w} - \mathbf{b}_1^T \mathbf{w} + c_1 \quad (4.3.6)$$

and, if \mathbf{A}_1 is non-singular, we can estimate the optical flow from (4.3.5) as

$$\mathbf{w} = -\frac{1}{2}\mathbf{A}_1^{-1}(\mathbf{b}_2 - \mathbf{b}_1). \quad (4.3.7)$$

Obviously the identity 4.3.4 is hardly satisfied due to the polinomial assumption of the intensity signal, noise and image sampling. For these issues, the assumption is relaxed to

$$\mathbf{A}(\mathbf{x}) = \frac{\mathbf{A}_1(\mathbf{x}) + \mathbf{A}_2(\mathbf{x})}{2} \quad (4.3.8)$$

that replaces \mathbf{A}_1 in (4.3.7).

To improve the robustness of the solution given by (4.3.7), neighborhood informations are incorporated by applying a weighting function $w(\mathbf{n})$ proportional to neighbor distance. Then, all local flows $\mathbf{d}(\mathbf{x})$ must minimize the following cost functional

$$\sum_{\mathbf{n} \in \eta} w(\mathbf{n}) \left\| \mathbf{A}(\mathbf{x} + \mathbf{n}) \mathbf{w}(\mathbf{x}) - \frac{1}{2} (\mathbf{b}_1(\mathbf{x} + \mathbf{n}) - \mathbf{b}_2(\mathbf{x} + \mathbf{n})) \right\|^2. \quad (4.3.9)$$

Further details of the method and its minimization strategy can be found in [102, 103, 104, 105].

Note that the size of the local neighborhood, P , determines the structures size that the method is capable to track. As P increases the image is approximated with smoother surfaces, yielding more robust algorithm but a more blurred optical flow. An efficient implementation involves the use of a hierarchical scheme of separable convolutions [105]. In such convolutions, a Gaussian kernel of standard deviation σ smoothes the input images. The σ parameter has a similar effect to P , blurring the obtained flow but producing a more robust algorithm.

4.3.3 Zach method

The Zach method proposes a TV-L1 formulation for the optical flow cost functional, i.e.,

$$\mathcal{E}(\mathbf{w}) = \int_{\Omega} \left[|I_0(\mathbf{x}) - I_1(\mathbf{x} + \mathbf{w}(\mathbf{x}))| + \alpha |\nabla \mathbf{w}(\mathbf{x})| \right] d\Omega. \quad (4.3.10)$$

The minimization of the current formulation presents a major challenge than the classical Horn-Schunk approach because data and regularization term are not continuously differentiable. To face such difficulty, the [64] strategy is applied as we explained before in Section 4.2.1. For this, the cost functional (4.3.10) is linearized as

$$\mathcal{E}(\mathbf{w}) = \int_{\Omega} \left[|\nabla I_1 \cdot \mathbf{w} + I_1 - I_0| + \alpha |\nabla \mathbf{w}| \right] d\Omega \quad (4.3.11)$$

where spatial indexation of I and \mathbf{w} has been dropped for the sake of readability. Additionally, an auxiliary field $\mathbf{s} = (r, t)$ is introduced and the following convex approximation of (4.3.11) is adopted to solve the optimization problem,

$$\mathcal{E}_{\theta}(\mathbf{w}) = \int_{\Omega} \left[|\rho(\mathbf{s})| + \frac{1}{2\theta} |\mathbf{w} - \mathbf{s}|^2 + \alpha |\nabla \mathbf{w}| \right] d\Omega \quad (4.3.12)$$

where $\rho(\mathbf{w}) = \nabla I_1 \cdot \mathbf{w} + I_1 - I_0$.

To minimize (4.3.12), we perform 2 alternating updating steps:

1. For fixed \mathbf{s} , solve

$$\mathbf{w} = \arg \min_{\tilde{\mathbf{w}}} \int_{\Omega} \left[\frac{1}{2\theta} |\tilde{\mathbf{w}} - \mathbf{s}|^2 + \alpha |\nabla \tilde{\mathbf{w}}| \right] d\Omega \quad (4.3.13)$$

where the solution is given by

$$\mathbf{w} = \mathbf{s} - \theta \operatorname{div} \mathbf{P}, \quad (4.3.14)$$

where $\mathbf{P} \in \mathbb{R}^{2 \times 2}$ is composed by row vectors \mathbf{p}_1 and \mathbf{p}_2 that satisfy

$$\nabla(\theta \operatorname{div} \mathbf{p}_1 - r) = |\nabla(\theta \operatorname{div} \mathbf{p}_1 - r)| \mathbf{p}_1 \quad (4.3.15)$$

$$\nabla(\theta \operatorname{div} \mathbf{p}_2 - t) = |\nabla(\theta \operatorname{div} \mathbf{p}_2 - t)| \mathbf{p}_2 \quad (4.3.16)$$

and are obtained by solving by the following iterative fixed-point scheme

$$\mathbf{p}_1^{k+1} = \frac{\mathbf{p}_1^k + \tau \nabla(\operatorname{div} \mathbf{p}_1^k - \frac{r}{\theta})}{1 + \tau \nabla(\operatorname{div} \mathbf{p}_1^k - \frac{r}{\theta})} \quad (4.3.17)$$

$$\mathbf{p}_2^{k+1} = \frac{\mathbf{p}_2^k + \tau \nabla(\operatorname{div} \mathbf{p}_2^k - \frac{t}{\theta})}{1 + \tau \nabla(\operatorname{div} \mathbf{p}_2^k - \frac{t}{\theta})} \quad (4.3.18)$$

with $\tau \leq 1/8$ and $\mathbf{p}_i^0 = \mathbf{0}$.

2. For fixed \mathbf{w} , solve

$$\mathbf{s} = \arg \min_{\mathbf{s}} \left\{ \frac{1}{2\theta} |\mathbf{w} - \mathbf{s}|^2 + |\rho(\mathbf{s})| \right\} \quad (4.3.19)$$

where the solution is given by

$$\mathbf{s} = \mathbf{w} + \begin{cases} \theta \nabla I_1 & \text{if } \rho(\mathbf{w}) < -\theta |\nabla I_1|^2 \\ -\theta \nabla I_1 & \text{if } \rho(\mathbf{w}) > \theta |\nabla I_1|^2 \\ -\rho(\mathbf{w}) \nabla I_1 / |\nabla I_1|^2 & \text{if } |\rho(\mathbf{w})| \leq \theta |\nabla I_1|^2 \end{cases}. \quad (4.3.20)$$

The steps are sequentially repeated until convergence of the \mathbf{w} field is achieved.

Further details of the method and its minimization strategy can be found in [64, 256, 348].

4.3.4 Weickert method

The Weickert method was developed by successive improvement over a half of decade [46, 47, 48, 49, 50, 51, 334, 335]. Here, we present an implementation which makes use of the 2D formulation of the problem, adopting the strategies of combined global-local, non-linear weights and multi-resolution. As result the method manages to deal with the restrictions aforementioned to the Horn-Schunck formulation allowing to estimate finite size flows with certain discontinuity preservation.

4.3.4.1 Combining Global-Local (CGL)

This strategy is based on the assumption that a local neighborhood around a pixel presents a similar flow. Obviously, this is only valid when the image spatial resolution is higher than the structures in the image. By doing so, we obtain increased robustness of the flow against pixel interpolations and noise. The implementation is performed by the convolution product between the differential operators in the developed data term, i.e.,

$$\begin{aligned} \mathcal{E}(u, v) = \int_{\Omega} & \left[G_{\rho} * \left(\frac{\partial I}{\partial x} \right)^2 u^2 + G_{\rho} * \left(\frac{\partial I}{\partial y} \right)^2 v^2 + G_{\rho} * \left(\frac{\partial I}{\partial t} \right)^2 + 2 G_{\rho} * \left(\frac{\partial I}{\partial x} \frac{\partial I}{\partial y} \right) uv \right. \\ & \left. + 2 G_{\rho} * \left(\frac{\partial I}{\partial x} \frac{\partial I}{\partial t} \right) u + 2 G_{\rho} * \left(\frac{\partial I}{\partial y} \frac{\partial I}{\partial t} \right) v + \alpha \|\nabla \mathbf{w}\|_F^2 \right] d\Omega. \end{aligned} \quad (4.3.21)$$

Note that only image differential operators have been modified by the CGL strategy. For the sake of simplicity, we embed the Gaussian convolution process in the differential

operators ∇_ρ and $\frac{\partial \rho}{\partial t}$, rewriting the previous functional as follows

$$\mathcal{E}(\mathbf{w}) = \int_{\Omega} \left[\left(\nabla_\rho I \cdot \mathbf{w} + \frac{\partial \rho I}{\partial t} \right)^2 + \alpha \|\nabla \mathbf{w}\|_F^2 \right] d\Omega. \quad (4.3.22)$$

4.3.4.2 Non-linear functions

The smoothing imposed by the regularization term hinders the estimation of discontinuous flows, mainly at the object boundaries. This restriction can be relaxed (although not completely avoided) by diminishing the regularization for outliers values (usually associated with such objects boundaries). Then, a weight function proposed by [67] is applied to the functional,

$$\mathcal{E}(\mathbf{w}) = \int_{\Omega} \left[\psi \left(\left(\nabla_\rho I \cdot \mathbf{w} + \frac{\partial \rho I}{\partial t} \right)^2 \right) + \alpha \psi(\|\nabla \mathbf{w}\|_F^2) \right] d\Omega \quad (4.3.23)$$

where

$$\psi(x) = 2\kappa^2 \sqrt{1 + \frac{x}{\kappa^2}}. \quad (4.3.24)$$

4.3.4.3 Multi-resolution technique

The multi-resolution scheme solves the optical flow iteratively from coarse (or low frequency) to fine (or high frequency) resolutions between the two images (image source and target, respectively). At each iteration, the scheme estimates the flow component for a given spatial scale and then it is applied to the source image. Let us define $I^m(x, y, t)$, $m = 0, \dots, M$ as the volume compose by both images $I(x, y, t)$ at the m resolution level. In our notation, $m = 0$ is the coarsest resolution of $\frac{H}{2^{M-m}} \times \frac{W}{2^{M-m}}$ pixels and $m = M$ represents the original full resolution with $H \times W$ pixels. Then, we calculate I^m as

$$I^m(x, y, t) = \frac{\sum_{r=1}^{2^{M-m}} \sum_{s=1}^{2^{M-m}} I\left((x-1)2^{M-m} + r, (y-1)2^{M-m} + s, t\right)}{2^{M-m} 2^{M-m}} \quad (4.3.25)$$

where each pixel of the coarse resolution is the mean value of a subregion of the original images.

In the coarse resolution each pixel represents a set of finer scale pixels, and the associated infinitesimal displacements in an m resolution level, are displacement of 2^{M-m} pixels at the 0 resolution level. From the point of view of the original image, the estimated displacements are no longer infinitesimal. Thus, we iteratively solve the optical flow from coarse to fine resolutions using the obtained displacement of each iteration to warp the source image. In that manner, each iteration removes a set of low spatial frequencies of the displacement between images and advances to the next finer scale to process the higher frequencies.

The warping process takes the source image, $I(x, y, 0)$, and applies a deformation using the flow obtained at the previous iteration (i.e., at the previous resolution), \mathbf{w}^{m-1} , generating the image $I^m(\mathbf{x} + \mathbf{w}^{m-1}, 0) = I(\mathbf{x}, 0)$ used in the next iteration. As I and \mathbf{w}^{m-1} are defined over a discrete domain, we use bilinear interpolation to obtain the values of I^m at the center of each pixel. The images I^m can be interpreted as a version of I after removing the displacements described by \mathbf{w}^{m-1} .

The optical flow formulation to estimate the increments of flow (according to the

functional (4.3.1)) at $m + 1$ -th resolution is given by

$$\mathcal{E}(\delta \mathbf{w}^m) = \int_{\Omega} \left[\left(\nabla I^m \cdot \delta \mathbf{w}_j^m + \frac{\partial I^m}{\partial t} \right)^2 + \alpha \|\nabla(\mathbf{w}^m + \delta \mathbf{w}^m)\|_F^2 \right] d\Omega, \quad (4.3.26)$$

where $\delta \mathbf{w}^m$ is the optimization variable, $\mathbf{w}^{m+1} = \mathbf{w}^m + \delta \mathbf{w}^m$ and I^m is the warped representation of the original image after applying the mapping given by the displacement field \mathbf{w}^{m-1} . Also, the differential operator changes to track the corrections performed by the warping process. In this case ∇ and $\frac{\partial(\cdot)}{\partial t}$ are the differential operators between the source image after the warping process and the original target image (not warped) defined over the domain Ω . Thus, the operators only assess the variations due to the current high frequencies of the displacement, that is, the one-pixel variations occurring in the resolution level m .

4.3.4.4 Functional minimization

The obtained formulation for the Weickert strategy to obtain the increments of flow at a scale m , is presented as the minimization of the following cost functional

$$\mathcal{E}(\delta \mathbf{w}^m) = \int_{\Omega} \left[\psi \left(\left(\nabla_{\rho} I^m \cdot \delta \mathbf{w}^m + \frac{\partial_{\rho} I^m}{\partial t} \right)^2 \right) + \alpha \psi \left(\|\nabla(\mathbf{w}^m + \delta \mathbf{w}^m)\|_F^2 \right) \right] d\Omega. \quad (4.3.27)$$

The minimization is performed by solving the associated Euler-Lagrange equations (see details in Appendix C.2) given by

$$\begin{aligned} \left[\psi'_1 \phi_{\rho}^m(\delta \mathbf{w}^m) \nabla_{\rho} I^m \right] - \alpha \operatorname{div} \left(\psi'_2 \nabla(\mathbf{w}^m + \delta \mathbf{w}^m) \right) &= 0, \quad \text{in } \Omega \\ \left[\nabla(\mathbf{w}^m + \delta \mathbf{w}^m) \right] \mathbf{n} &= \mathbf{0}, \quad \text{in } \partial\Omega \end{aligned} \quad (4.3.28)$$

where

$$\begin{aligned} \phi_{\rho}^m(\mathbf{w}) &= \nabla_{\rho} I^m \cdot \mathbf{w} + \frac{\partial_{\rho} I^m}{\partial t} \\ \psi'_1 &= \psi' \left(\left(\nabla_{\rho} I^m \cdot \delta \mathbf{w}^m + \frac{\partial_{\rho} I^m}{\partial t} \right)^2 \right) \\ \psi'_2 &= \psi' \left(\|\nabla(\mathbf{w}^m + \delta \mathbf{w}^m)\|_F^2 \right) \\ \psi'(x) &= \frac{1}{\sqrt{1 + \frac{x}{\kappa^2}}}. \end{aligned}$$

Note that the Neumann boundary condition in (4.3.28) can be rewritten as $(\nabla \delta \mathbf{w}^m) \mathbf{n} = \mathbf{0}$ because $(\nabla \mathbf{w}^m) \mathbf{n} = \mathbf{0}$ by construction (previous resolution increments already satisfy the boundary condition).

4.3.4.5 Numerical scheme

The numerical scheme used for solving (4.3.28), applies a Jacobi scheme for space discretization. The convergence of the explicit formulation converge faster with a Gauss-Seidel approach, conversely the paralellization of the Jacobi alternative proves to be more efficient and scalable. Additionally, we incorporate relaxation in the iterative process to accelerate convergence.

In such manner, we derive the following numerical scheme to estimate the increment of flow (according with the multi-resolution scheme presented in Section 4.3.4.3) at the spatial position \mathbf{x} , as

$$\begin{aligned}\delta u^{n+1} &= (1 - \beta) \delta u^n + \beta \delta \hat{u}^{n+1}, \\ \delta v^{n+1} &= (1 - \beta) \delta v^n + \beta \delta \hat{v}^{n+1},\end{aligned}\tag{4.3.29}$$

where β is the relaxation factor and

$$\begin{aligned}\delta \hat{u}^{n+1} &= \frac{\frac{\alpha}{\Delta x^2} L_u^n - \psi'_1 (G_\rho * (\frac{\partial I}{\partial t} \frac{\partial I}{\partial x}) + G_\rho * (\frac{\partial I}{\partial x} \frac{\partial I}{\partial y}) \delta v^n)}{\psi'_1 G_\rho * (\frac{\partial I}{\partial x})^2 + \frac{\alpha}{\Delta x^2} \sum_{\mathbf{y} \in \mathcal{N}} \frac{\psi'_{2,\mathbf{y}} + \psi'_{2,\mathbf{x}}}{2}}, \\ \delta \hat{v}^{n+1} &= \frac{\frac{\alpha}{\Delta x^2} L_v^n - \psi'_1 (G_\rho * (\frac{\partial I}{\partial t} \frac{\partial I}{\partial y}) + G_\rho * (\frac{\partial I}{\partial x} \frac{\partial I}{\partial y}) \delta u^{n+1})}{\psi'_1 G_\rho * (\frac{\partial I}{\partial y})^2 + \frac{\alpha}{\Delta x^2} \sum_{\mathbf{y} \in \mathcal{N}} \frac{\psi'_{2,\mathbf{y}} + \psi'_{2,\mathbf{x}}}{2}},\end{aligned}\tag{4.3.30}$$

$$\begin{aligned}L_u^n &= \sum_{\mathbf{y} \in \mathcal{N}} \frac{\psi'_{2,\mathbf{y}} + \psi'_{2,\mathbf{x}}}{2} (u_{\mathbf{y}} + \delta u_{\mathbf{y}}^n - u_{\mathbf{x}}), \\ L_v^n &= \sum_{\mathbf{y} \in \mathcal{N}} \frac{\psi'_{2,\mathbf{y}} + \psi'_{2,\mathbf{x}}}{2} (v_{\mathbf{y}} + \delta v_{\mathbf{y}}^n - v_{\mathbf{x}}),\end{aligned}\tag{4.3.31}$$

where \mathcal{N} are the neighbor pixels, called \mathbf{y} , to \mathbf{x} and all image gradients are evaluated at \mathbf{x} . In our particular case, we use the four closest neighbors in the Cartesian directions. The ψ'_i operator is the derivative of the function ψ introduced in Section 4.3.4.2, and is defined as

$$\begin{aligned}\psi'_1 &= \psi' \left(\left(\nabla_\rho I \cdot \delta \mathbf{w} + \frac{\partial_\rho I}{\partial t} \right)^2 \right) \\ \psi'_{2,\mathbf{x}} &= \psi' \left(\left\| \nabla (\mathbf{w}_{\mathbf{x}} + \delta \mathbf{w}_{\mathbf{x}}) \right\|_F^2 \right)\end{aligned}$$

Note that we avoided the multi-resolution indexation for ψ' , I , \mathbf{w} and $\delta \mathbf{w}$ to ease the already complex notation, but it must be remembered that equations (4.3.29) are for one multi-resolution step only. After obtaining the flow increments, \mathbf{w} is updated as $\mathbf{w} + \delta \mathbf{w}$ and I is warped with the new flow \mathbf{w} as detailed in Section 4.3.4.3.

To solve the non-linear system (4.3.29), we use a fixed point scheme. To remove the non-linearities, we fix the values of ψ'_i functions at the current known solution $\delta \mathbf{w}^n$. The remaining linear system is solved with the proposed set of equations. Then, we update the value of ψ'_i functions using the new solution $\delta \mathbf{w}_{\mathbf{x}}^n$ from the linear system and repeat until a convergence criterion is satisfied.

For the image differential operators, we use finite difference approximations of sixth order in space (stencils are presented in Table 4.1) and first order in time (performed by forward differences) approximation. Also, we compute the forward differences not at the center of the pixel but at the shared vertex with the forward neighbors (in space and time), which results in a more robust estimation at the expense of losing locality.

4.3.5 Comparative assessment for displacement field estimation

Our main goal is the use of an optical flow method to estimate the displacement field between two images degraded by speckle noise. Usually, the previously described methods are validated in terms of flow orientation because flow is not used as a mapping function between frames as in our case. For this reason, we assess the vector orientation as well as its modulus for the Farneback, Zack and Weickert methods in a simple 2D example where the displacement field is known.

Position	Distance to stencil center (in pixels)												
	-6	-5	-4	-3	-2	-1	0	1	2	3	4	5	6
$i = 1$	0	0	0	0	0	0	-147	360	-450	400	-225	72	10
$i = 2$	0	0	0	0	0	-10	-77	150	-100	50	-15	2	0
$i = 3$	0	0	0	0	2	-24	-35	80	-30	8	-1	0	0
$i = 4, \dots, N-3$	0	0	0	-1	9	-45	0	45	-9	1	0	0	0
$i = N-2$	0	0	1	-8	30	-80	35	24	-2	0	0	0	0
$i = N-1$	0	-2	15	-50	100	-150	77	10	0	0	0	0	0
$i = N$	-10	-72	225	-400	450	-360	147	0	0	0	0	0	0

Table 4.1: Stencil coefficients used to compute a sixth order approximation of the spatial derivative. All coefficients must be multiplied by $\frac{1}{60\Delta x}$. i is the pixel coordinate in the image along the dimension the image is derived, e.g., for $\frac{\partial I}{\partial x}$, i corresponds to the x coordinate of the pixels at which the derivative is computed.

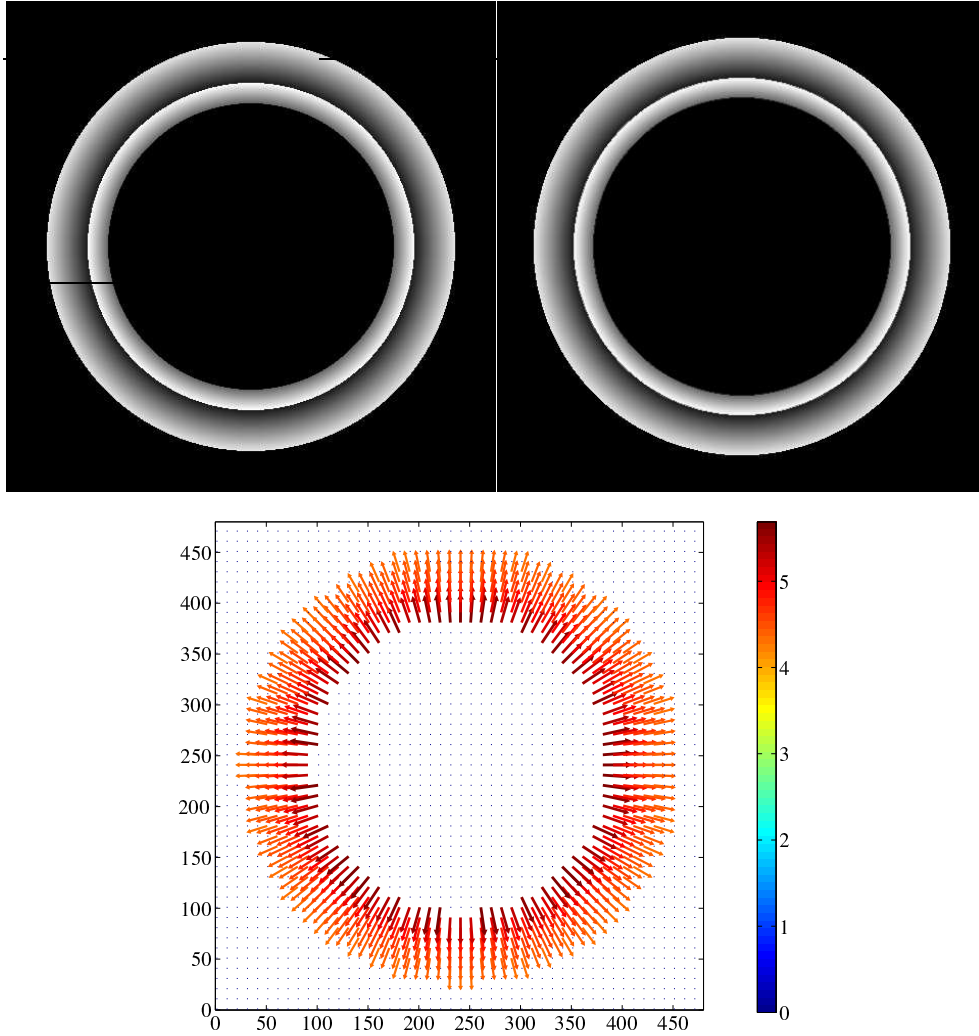


Figure 4.6: Case of study for the comparison of the optical flow methods. (Top) Images 1 and 2 of the sequence, before and after radial expansion (inflation), respectively; (bottom) displacement field between images 1 and 2, the color of the arrows stands for the magnitude of the displacement in pixel units.

The case of study is a ring subjected to inflation (see Figure 4.6) where the displacement field is known. Using the ring image before and after the inflation, we calculate the flow with each of the proposed methods. To perform a fair comparison, we optimize the parameters for each method to minimize the L_2 error against the ground truth of the displacement field. The optimization for the choice of parameters is achieved by brute force over a discretized parameter space, similar to that performed in Section 4.2.3.

As presented in Figure 4.7, the Weickert and Zach methods yield accurate flows with mean errors of $2.59 \pm 1.14\%$ and $2.00 \pm 1.39\%$ (mean \pm SD) over the displacement field, respectively. The bigger errors with both methods are localized along the intensity discontinuities where errors due to interpolation are expected in image processing and acquisition stages. Overall, the methods do not degrade the solution above 6.46% and 11.64% (maximum error in the flow in Figure 4.7) for Weickert and Zach methods respectively. The Fanebäck method fails to deliver a correct solution in the outer layer of the ring due to the lack of intensity variation (as result of the small strains in this area). The two other methods circumvent this difficult by the diffusive action of the regularization term which fills the uncertainty flow zones using the flow from neighbor areas.

As the main outcome of this study, we choose to work with the Weickert method for

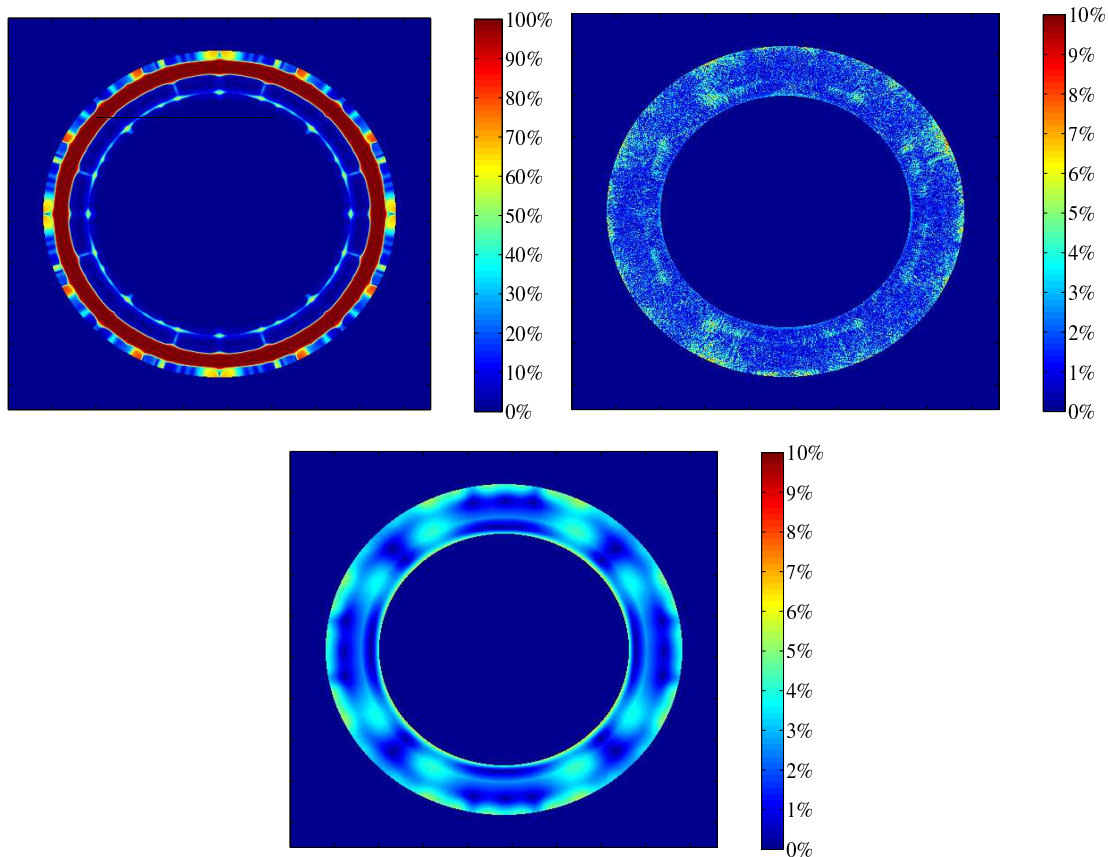


Figure 4.7: Relative error between estimated flow and the ground truth for the ring case. Flows estimation obtained after parameter optimization: (top-left) Farnebäck method with neighborhood size $P = 7$ and $\sigma = 1.5$ for Gaussian smoothing; (top-right) TV-L1 method with $\tau = 0.001$, $\alpha = 10$ and $\theta = 0.5$; (bottom) Weickert method with $\alpha = 0.2$, $\rho = 8$, $\beta = 0.5$; all methods use multi-resolution scheme 2-folding the image resolution 3 times, i. e., $M = 3$, (thus capturing displacements up to 15 pixels) and convergence was achieved when absolute error variation between successive steps was smaller than 10^{-5} .

the IVUS applications due to its more reduced error range, as well as because of the availability of in-house code and its potentiality for customization (changes to the non-linear weight functions, regularization term, or even the data term formulation). Nevertheless, the differences when compared to Zach are small, and further analysis and applications could shed light on the right choice.

4.4 Performance analysis for IVUS tracking

To analyze the capabilities of the denoising strategy combined with the optical flow method, we create synthetic images corresponding to spatial configurations of arterial walls before and after a deformation process. To simulate a realistic deformation process, we use an in-house numerical solver for solid mechanics [22, 41] that numerically solves, using the finite element method, the equilibrium equations for an homogeneous, isotropic, hyperelastic and incompressible solid bodies. The equilibrium equations for this problem are introduced in Section 5.4.1, where only one constitutive parameter, c , defines the hyperelastic behavior of each piece of arterial tissue.

The synthetic images are scales to a fixed lattice of 512×512 (480×480 only for the synthetic ring case). Additionally, each node of the mesh that discretizes the domain is

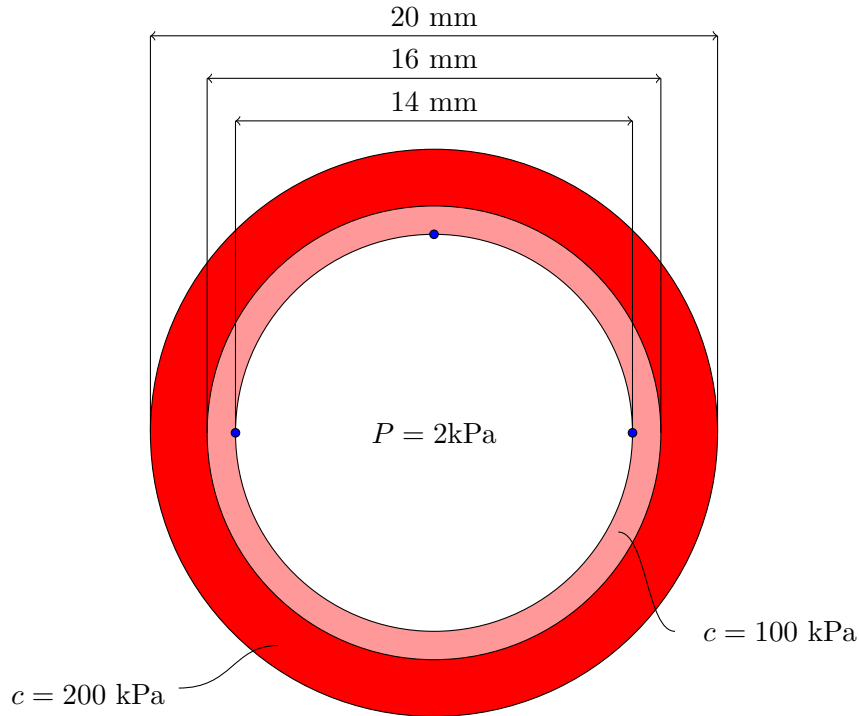


Figure 4.8: Scheme of the ring geometry and mechanical properties for the synthetic ring case.

enriched with an intensity value. Then, for a given spatial configuration of the mesh (e.g. before or after deformation), the intensity field of the mesh is projected over the image lattice using bilinear interpolation functions to generate the corresponding synthetic image.

As follows, different synthetic examples aim to analyze the optical flow using the proposed methodology. Firstly, an idealized synthetic ring without image noise is presented to perform a sensitivity analysis of the parameters in the OF method. Secondly, a synthetic vessel cross-section based on an in-vivo geometry (with and without image noise) is used to evaluate the capabilities of our method to retrieve the displacement field in presence of physiological conditions. Finally, the methodology is applied over an in-vivo pair of images showing the obtained displacement fields, where we discuss the variations over the flow and the possible correspondence to biological materials.

4.4.1 Synthetic ring sequence

Before applying our method to a synthetic or in-vivo model of an artery, we analyze the sensitivity of the parameters in order to establish the correct ranges for each one of them. As byproduct, we highlight some characteristics of the model such as flow magnitude loss and over smoothing due to improper parameter setting.

For this purpose, we create a sequence of a ring composed of two concentric material layers. To generate an image sequence with physical coherence, we solve the mechanical problems at given pressure levels. Zero tangent displacements on three luminal vertexes (location of the vertex are depicted with blue dots in Figure 4.8) are prescribed to avoid rigid motions. The constitutive parameters and pressure values are reported in Figure 4.8. The resulting displacement field \mathbf{w}_T will be used as ground truth to assess the capabilities of the OF method. Finally, we project the ring mesh before and after the deformation over an image lattice of 480×480 pixels, obtaining the synthetic images presented in Figure 4.9.

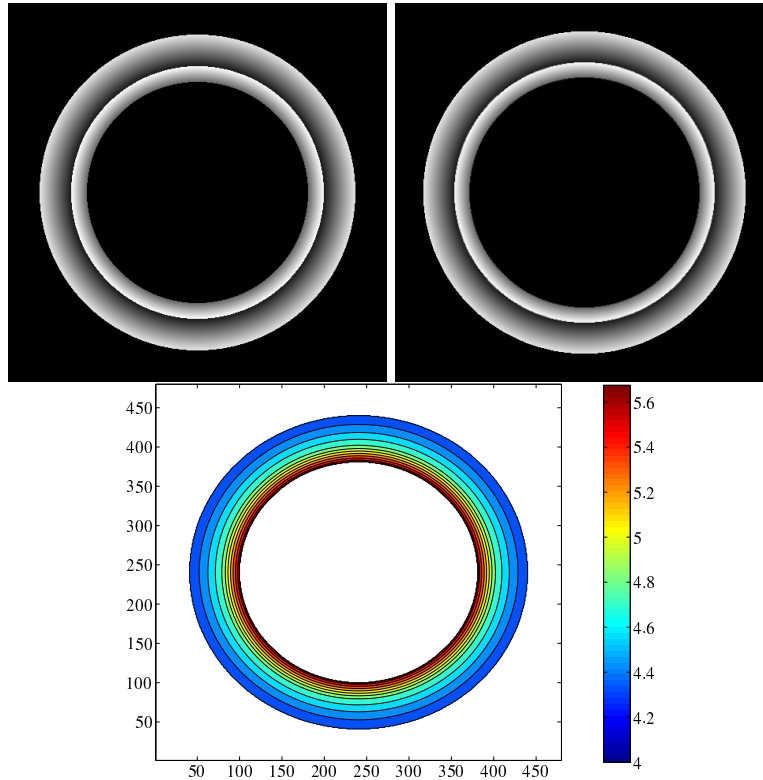


Figure 4.9: Synthetic image sequence for the ring example: (left-top) frame before the deformation; (right-top) frame after the deformation; (bottom) radial displacement between initial and final frame (in pixels).

The displacement field observed in the synthetic images is higher than the one observed in coronary arteries under physiological pressure values. This example is carried out to test the multi-resolution capabilities of the method when large displacements are involved and also to evidence more clearly the losses in flow magnitude given by diffusion (from the regularization term or CGL's Gaussian convolution).

An important factor is to estimate the optimal regularization weight α . As α increases, the problem is better posed although image term data is ignored in favor of smoother solutions. Another parameter that has a similar role is the ρ for the CGL coupling of local neighbors. As this factor increases, we indicate that there is a larger neighborhood of pixels which share the same flow, and, therefore, smoother flows are privileged. Sensitivity of the error in displacements and strains to parameters α and ρ is presented in Figure 4.10. As aforementioned, lower values of α turn the problem into an ill-posed problem ($\alpha < 0.05$) where the flow is not successfully recovered. For $\alpha \geq 0.15$, we obtain flows with mean errors of 1.5 – 6% and maximum error below 16%. Also larger values of α start to degrade the quality of the solution because of the poor contribution of the image data term. The CGL strategy shows low sensitivity for the displacements and improves the estimation of strains by increasing the coupled neighborhood (increase of ρ). Conversely, the use of larger values of ρ degrades locality of the solution.

Even more, the regularization undermines the estimation of the correct flow in the inner perimeter of the ring. As the regularization increases, we penalize spatial variations of the flow, as if we indicate the viscosity of the flow. Such artificial viscosity does not allow to develop the velocity profile estimated by the data term. This phenomenon can be seen in Figure 4.11 where the solution for low values of α recovers a more accurate description of the flow at the inner perimeter of the ring.

The non-linear weights have no significant contribution in our problem. In Figure

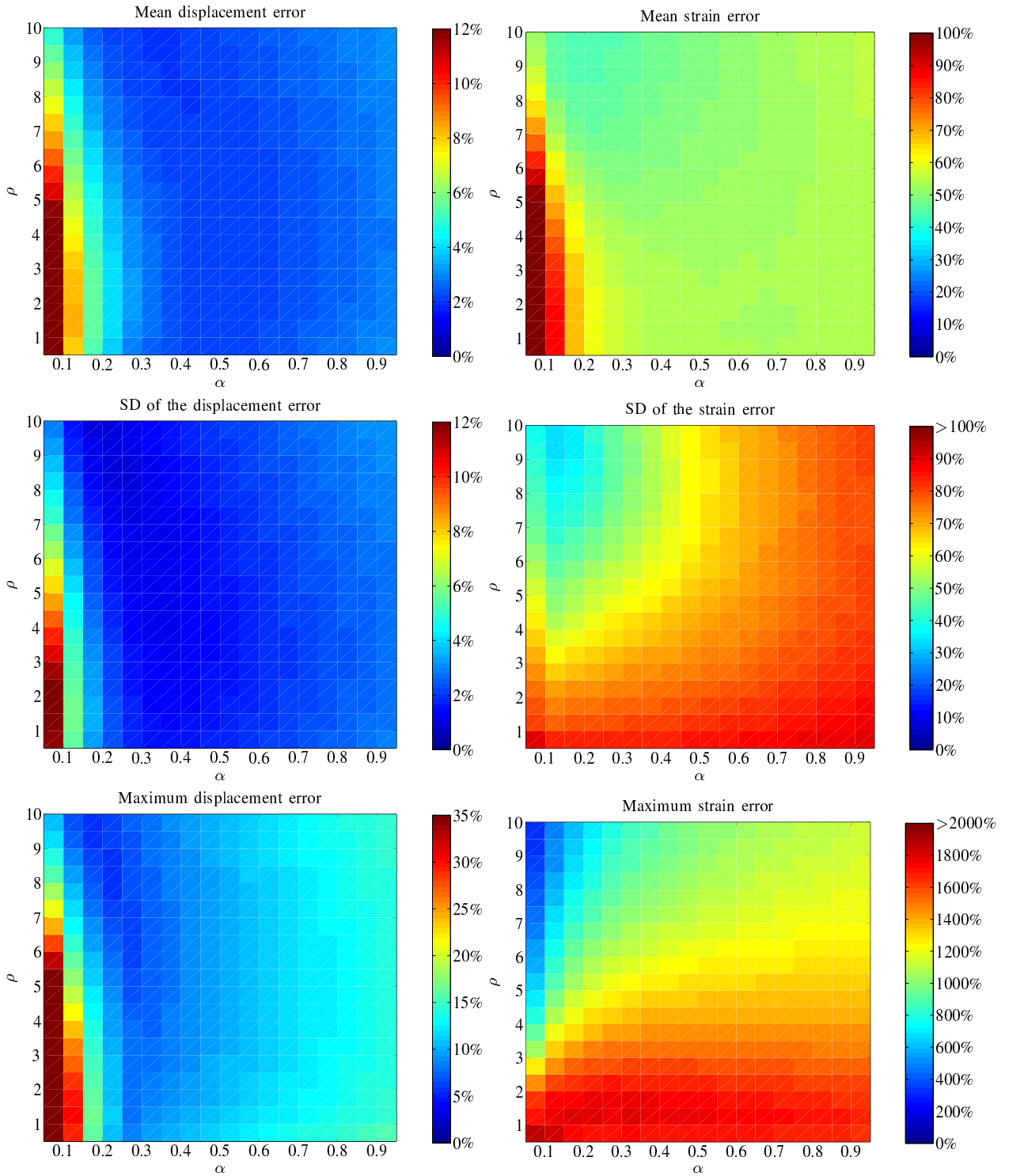


Figure 4.10: Sensitivity analysis of relative errors in displacements and strains with respect to parameters α and ρ . The values for the remaining parameters are $\beta = 0.5$, $\kappa^2 = 0.5$, $M = 3$ and tolerance of $1 \cdot 10^{-5}$ using absolute error between the last two iterations. The relative error is obtained as $\frac{|\mathbf{w} - \mathbf{w}_T|}{|\mathbf{w}_T|}$ for the displacements and $\frac{\|\varepsilon - \varepsilon_T\|_F}{\|\varepsilon_T\|_F}$ for the strains.

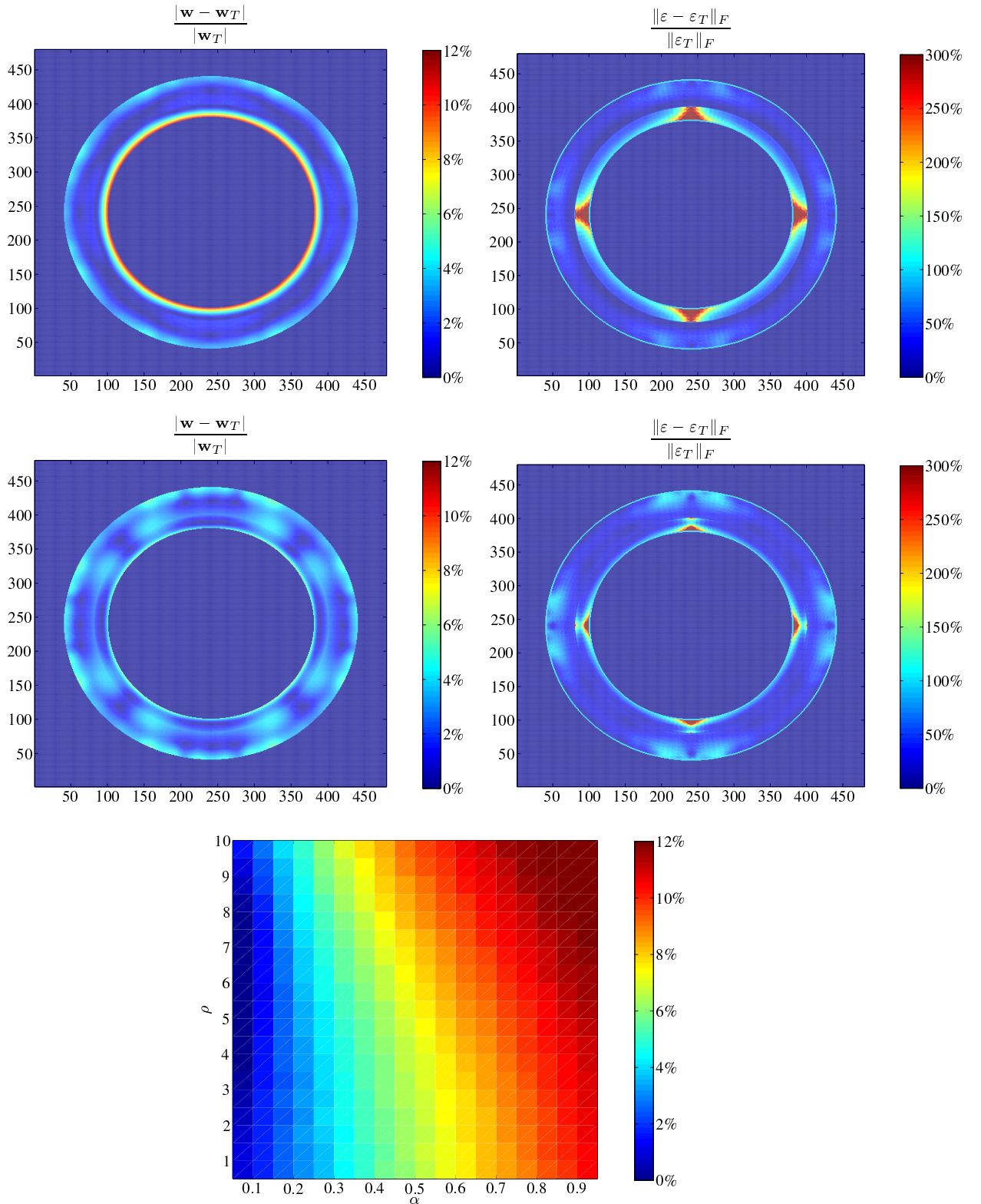


Figure 4.11: Example of error decrease by the relaxation of the regularization term: (top) errors for $\alpha = 0.6$ and $\rho = 8$; (middle) errors for $\alpha = 0.2$ and $\rho = 8$; (bottom) sensitivity of maximum inner radial displacement error to the parameters α and ρ . The values for the remaining parameters are $\beta = 0.5$, $\kappa^2 = 0.5$, $M = 3$ and tolerance of $1 \cdot 10^{-5}$ using absolute error between the last two iterations. \mathbf{w} and ε are the displacement vector field and strain tensor field respectively, and suffix $(\cdot)_T$ stands for the ground truth data.

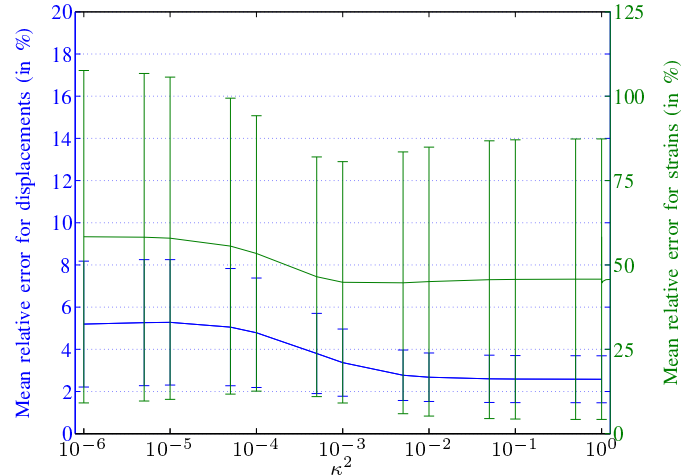


Figure 4.12: Mean relative error in the displacement field and strain field for different values of κ^2 (parameter for the non-linear weights). Whiskers mark the mean standard deviation for the entire image. The relative error is obtained as $\frac{\|\mathbf{w} - \mathbf{w}_T\|}{\|\mathbf{w}_T\|}$ for the displacements and $\frac{\|\varepsilon - \varepsilon_T\|_F}{\|\varepsilon_T\|_F}$ for the strains.

4.12 it is shown that the optical flow error is not significantly sensitive to variations in κ parameter (less than 2% of error for $10^{-3} \leq \kappa \leq 1$). Hence, the use of values smaller than $\kappa^2 = 10^{-3}$ (the smaller κ , the less penalized the discontinuities) degrades the optical flow estimation.

The multi-resolution parameter shows an important contribution for the flow estimation. For the current case, the sensitivity analysis demonstrated that using $M \geq 2$ allows an estimation with displacement errors below 3%. Note that $M = 2$ means that the coarser image pixels represent the mean of 4 pixels in the finer image, the next scale represents 2 pixels and the finer scale represents 1. With this value of M , solving infinitesimal displacements (i.e. 1 pixel) at each scale yields to an effective estimation of displacements of up to 7 pixels. As seen in Figure 4.9, the current case presents displacements up to 5.6 pixels. This is why values of $M \geq 2$ estimate them correctly with only mild oscillations due to down sampling and interpolation errors involved in the multi-resolution scheme.

4.4.2 Synthetic artery sequence based on in-vivo scenario

A more realistic synthetic case was generated based on an in-vivo geometry and tissue distribution of the vessel obtained from an IVUS image (see Figure 4.14). Firstly, we manually segment the vessel wall and we separate 3 areas of materials based on the acoustic impedance of the tissues (presumably fibrotic, lipidic and calcified tissues). The segmentation was employed to construct the vessel mesh using the softwares Salome v7.8.0 and Netgen, as shown in Figure 4.14.

Based on several experimental works that measure coronary artery elasticity in ex-vivo conditions [28, 44, 71, 90, 168, 188, 319, 331], we summary the physiological ranges for each coronary tissue in Table 4.2. From such ranges, we choose two synthetic sets of parameters denominated stiffer and compliant cases. From such sets of parameters, we solve the mechanical problem for a transmural pressure difference of 5.3 kPa, generating two image sequences, called the stiffer and the compliant sequences (see Figure 4.15).

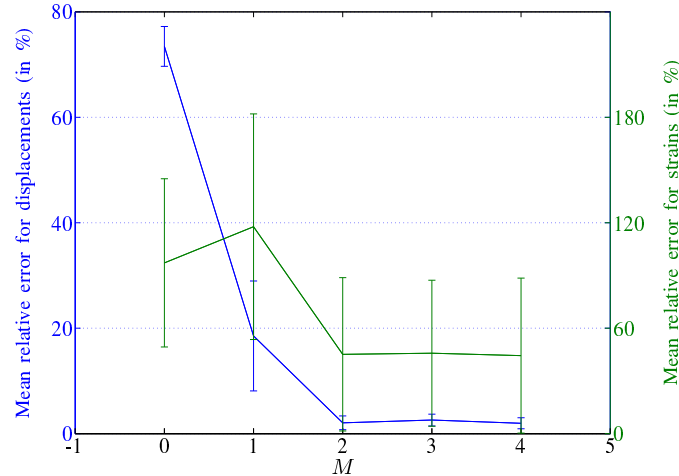


Figure 4.13: Mean relative error in the displacement field and strain field for different multi-resolution levels (M). Whiskers mark the mean standard deviation for the entire image. The relative error is obtained as $\frac{|\mathbf{w} - \mathbf{w}_T|}{|\mathbf{w}_T|}$ for the displacements and $\frac{\|\varepsilon - \varepsilon_T\|_F}{\|\varepsilon_T\|_F}$ for the strains.

	Fibrotic	Lipidic	Calcified
Ex-vivo ranges	500 – 2300	5 – 400	4000 – 18000
Stiff case	600	100	12000
Compliant case	500	10	4000

Table 4.2: Values of constitutive parameter c (in kPa) for coronary artery tissues.

4.4.2.1 Noiseless images

Using the sensitivity analyses presented in the previous section, we select the OF parameters as $\alpha = 0.05$, $\beta = 0.5$, $\rho = 2$, $\kappa^2 = 0.5$ and $M = 2$ to solve both cases. Note that α is smaller than in the previous case because the flow gradients magnitudes are smaller. To estimate a suitable α , we compute the optical flow with the lowest α that still converges to a solution and that does not present any sort of artifact (e.g. spatial oscillations). Also, as ρ presented a small sensitivity in the previous example, we choose to use a smaller value which allows to capture more local behavior of the flow.

As shown in Figures 4.16 and 4.18, the obtained flow is in agreement with the ground truth in terms of displacement vector orientation and modulus. All errors are smaller than a pixel in both cases, even in the second case where the flow magnitude increased from 1.7 to 2.6 pixels in the calcium area. Also, it must be noticed that greater errors (all those greater than 50%) are localized over the boundary, where the projection and interpolation mechanisms used to generate the image may have a strong influence. In the second scenario (the compliant case), the choice of a smaller value for ρ helped to localize the error. In terms of the error in the strain field, they are localized over the boundaries of the domain and in the calcium interface at the top-right direction. This is explained by the fact that the strain over boundaries is defined exclusively in the interior of the domain. In turn, at the interface between two different components, the strains are discontinuous because of the jump in the material property (see Figures 4.17 and 4.19). This is why the OF method is less accurate on those internal interfaces. Although the strain moduli disagree with the ground truth, the strain distribution is maintained, which is key to identify different materials in the scene. This last observation will be later explored in Chapter 6 for demarcation of tissue territories.

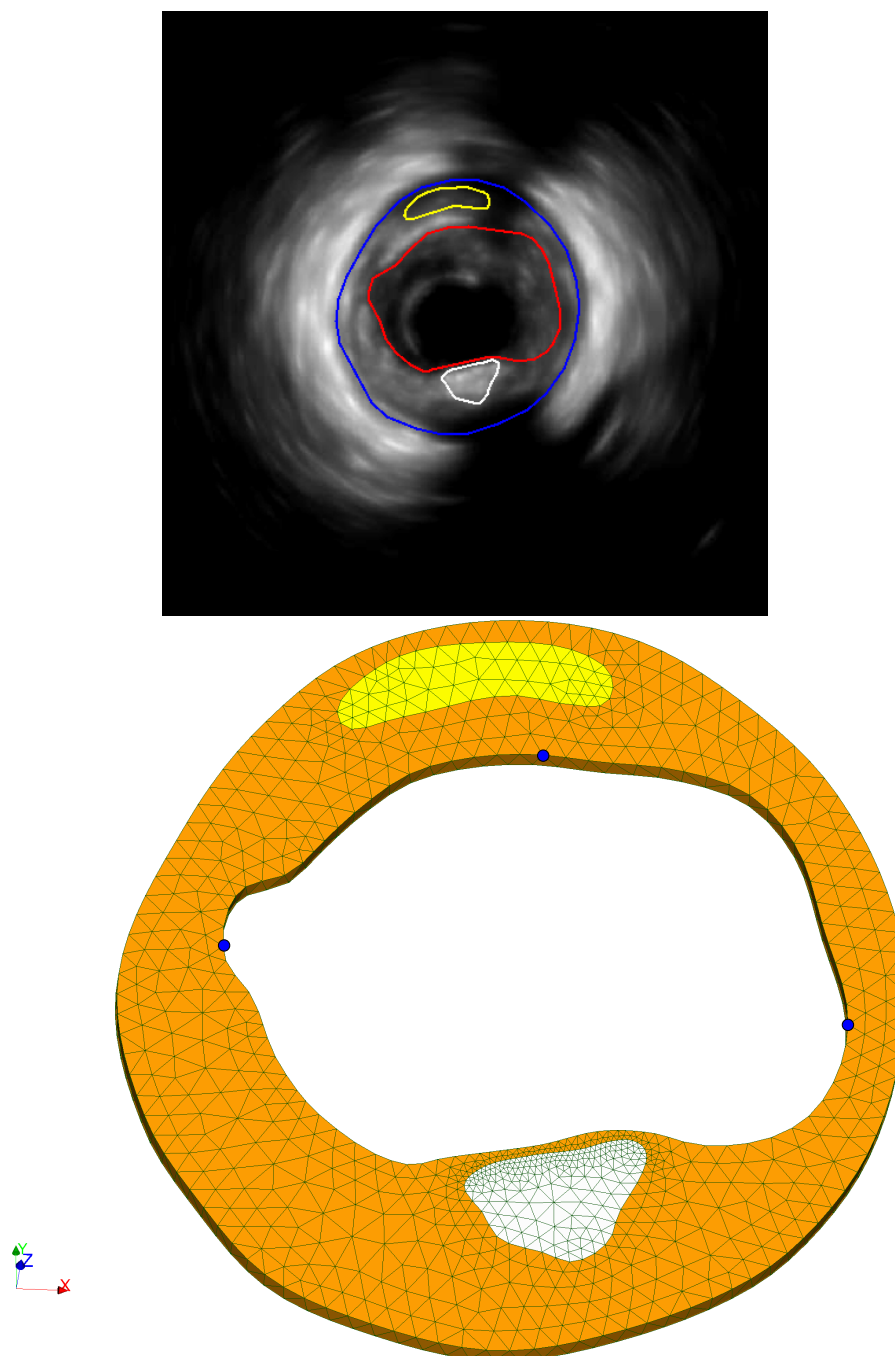


Figure 4.14: Synthetic artery generation based on in-vivo IVUS images: (top) IVUS image with segmented lumen (red), external elastic lamella (blue), lipid pool (yellow) and calcified region (white); (bottom) mesh generated for the mechanical problem and for the optical flow strategy, the blue dots depict the nodes with boundary conditions.

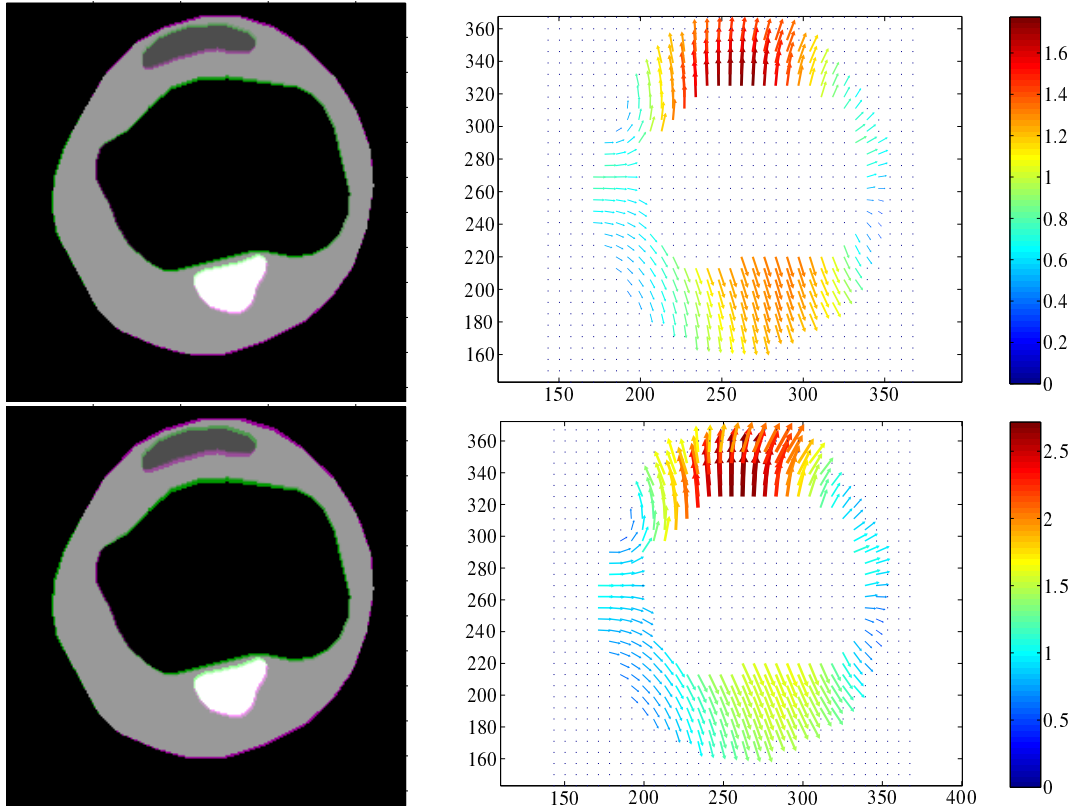


Figure 4.15: Synthetic sequences based on in-vivo IVUS images: (top) stiffer case sequence; (bottom) compliant case sequence. Each image of the first column presents the artery deformation in false-color³ using the color bands green and magenta for the image before and after deformation, respectively. The second column shows the displacements (in pixels, $1\text{px} = 16\mu\text{m}$) obtained from the mechanical problem which establishes our ground truth for optical flow estimation.

4.4.2.2 Speckled images

The images from the previous stiff and compliant cases are now polluted with statistically appropriate US noise. For this, we apply a speckle noise modeled by a generalized gamma (GG) distribution with parameters $\alpha = 1.5$, $\gamma = 1.5$ and $\nu = 0.8$ (values that outperform the registration process with GG MLE operator presented in Section 3.3.3) over each synthetic image of the sequences. These sequences are denoised with the MLV method presented in Section 4.2.2 and then the optical flow is estimated.

Previously, in Section 4.2.3, we derived the optimal denoising parameter in the sense of intensity homogeneity for a statistically known speckle noise. Analogously, we search for the optimal set of denoising parameter such that it minimizes the a posteriori optical flow estimation errors. In this analysis, we use a parameter space discretization given by

$$\mathcal{P} = \{(\alpha, a, b, c); \alpha \in \{1, 2, 4, 8, 16, 32\}, a, b, c \in \{0.1 \cdot i, i = 1, \dots, 25\}\} \quad (4.4.1)$$

and we minimize the mean absolute error in terms of the optical flow solution computed as

$$\varepsilon_d^{of} = \|\mathbf{w} - \mathbf{w}_T\|_{L_2}. \quad (4.4.2)$$

Using a sequence of the speckled compliant case, we found the optimal set of parameter

³The false-color visualization creates a composite RGB image showing images 1 and 2 overlaid in different color bands. Gray regions in the composite image show where the two images have the same intensities. Magenta and green regions show where the intensities are different.

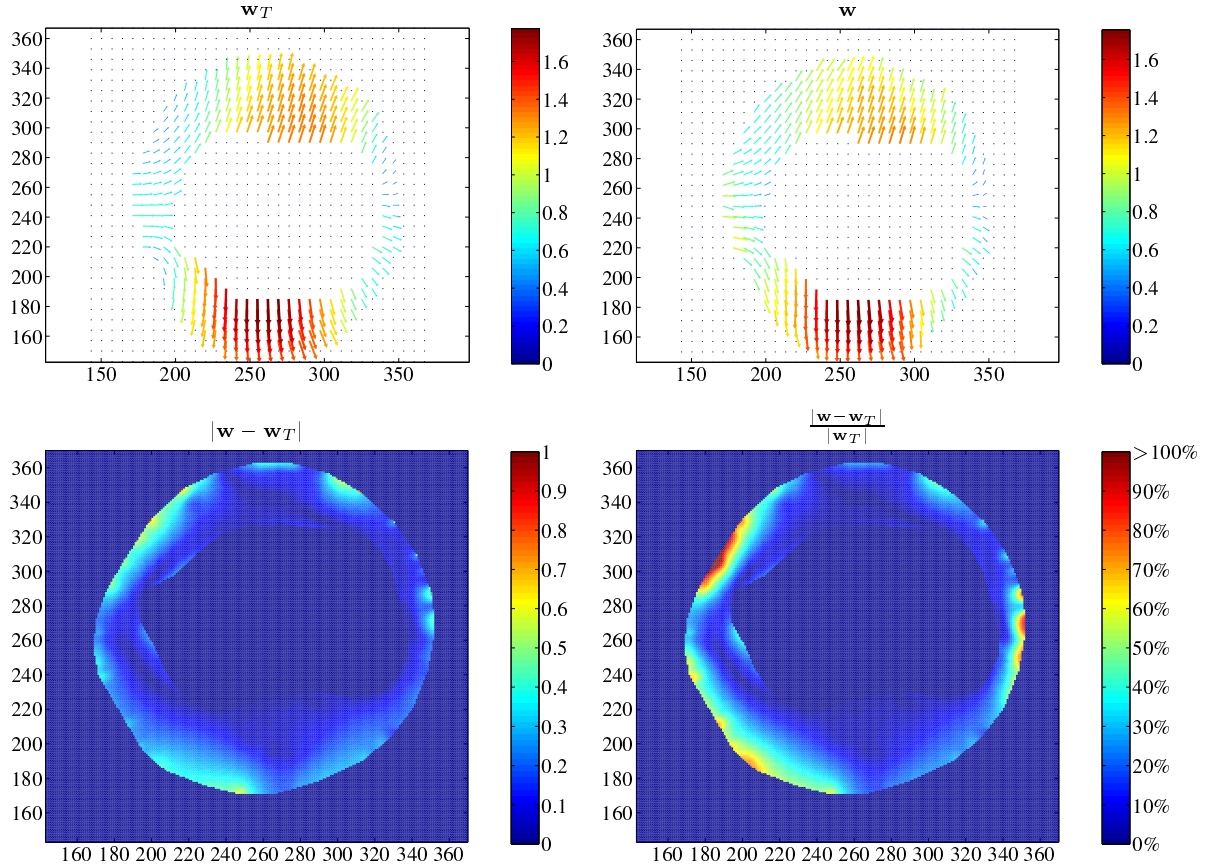


Figure 4.16: Stiff case displacements for the synthetic artery model. (Top-left) Displacement field, \mathbf{w}_T , obtained by solving the mechanical problem (ground truth); (top-right) displacement field, \mathbf{w} , obtained by solving the optical flow (OF) of the sequence (bottom-left) absolute error of the OF displacement field against the ground truth (in pixels); (bottom-right) relative error of the OF displacement field against the ground truth.

for $\alpha = 8$, $a = 1.5$, $b = 1.4$ and $c = 0.1$ with an error $\varepsilon_d^{of} = 0.305$ pixels. As shown in Figure 4.20, the larger errors are placed on the left-top region of the artery as occurs in the noiseless case (see Figure 4.18 but more spread. For the same sequence and using the optimal set of parameter in the sense of pixel homogeneity ($\alpha = 4$, $a = 1.1$, $b = 1$ and $c = 0.5$), an error of $\varepsilon_d^{of} = 0.342$ pixels is obtained and the bigger errors are spatially distributed with similar patterns as the presented in Figure 4.20.

To gain insight about the denoised optical flow performance when using the optimal parameters in the sense of optical flow error ε_d^{of} , we generate 10 sequences for each case, stiff and compliant, and with different noise instances (all instance have the same statistical distribution, GG distribution with parameters $\alpha = 1.5$, $\gamma = 1.5$ and $\nu = 0.8$). Then, we apply the denoising method with the parameters that optimize the sensitivity analysis ($\alpha = 8$, $a = 1.5$, $b = 1.4$ and $c = 0.1$) and performed a pixel-wise mean of the relative and absolute displacement errors. As presented in Figure 4.21, the errors localize again in the same places as in the noiseless cases, i.e., at the top-left and at the bottom left areas, and, again, all errors are below 1 pixel obtaining a sub-pixel precision level for the method (even in the presence of noise). The mean absolute error of the displacements obtained across the 10 sequences was 0.34 ± 0.07 and 0.38 ± 0.06 for the stiff and compliant cases and from the relative error plots of the displacements it is seen a mean error of $36.52 \pm 7.1\%$ and $31.19 \pm 5.15\%$ for the stiffer and the compliant cases, respectively. Looking at the relative errors of the strains, it is seen that errors above 300% localize in the calcified tissue while

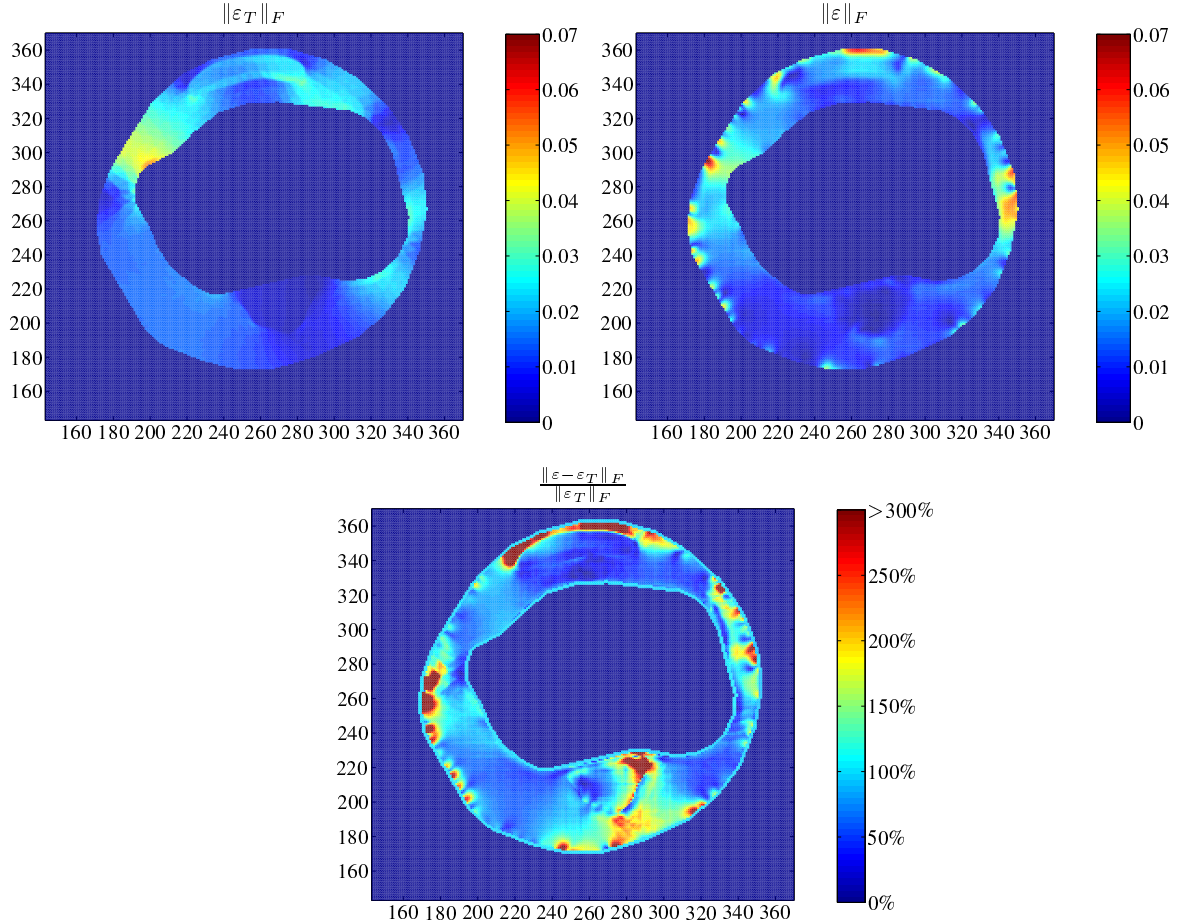


Figure 4.17: Stiff case strains for the synthetic artery model. (Top-left) Norm of the strain field, $\|\varepsilon_T\|_F$, obtained by solving the mechanical problem (ground truth); (top-right) norm of the strain field, $\|\varepsilon\|_F$, obtained by solving the optical flow (OF) of the sequence; (bottom) relative error of the OF strain field against the ground truth. The norm $\|\cdot\|_F$ stands for the Frobenius norm.

the remaining tissues present errors around 100%. To interpret this observation, consider that calcified tissue undergoes smaller deformations due to its high elastic module, and thus relative errors are more sensitive than in more compliant materials.

Note that the statistically analysis of different noise instances in the compliant sequence shows a mean absolute error of 0.38 ± 0.06 when using the optimal parameters in the sense of OF and 0.35 ± 0.03 when using the optimal parameters in the sense of homogeneity. Obviously, the sensitivity analysis can be conducted using more noise instances than just one to improve the parameter optimization, although this will be meaningful when using experimentally supported noise values for the IVUS speckle, which exceeds the focus of the current work. Although, this insight allow us to infer that the use of the optimal parameters in the sense of homogeneity is as good as the one obtained by OF error minimization. This last is understandable because we consider an statistically homogeneous speckle across all tissues when really each tissue has its own statistical set of parameters [3, 293, 327]. This consideration implies that noise is not correlated with the tissue, then its presence is not useful for tissue tracking and, conversely, it degrades the intensity assumption of the optical flow.

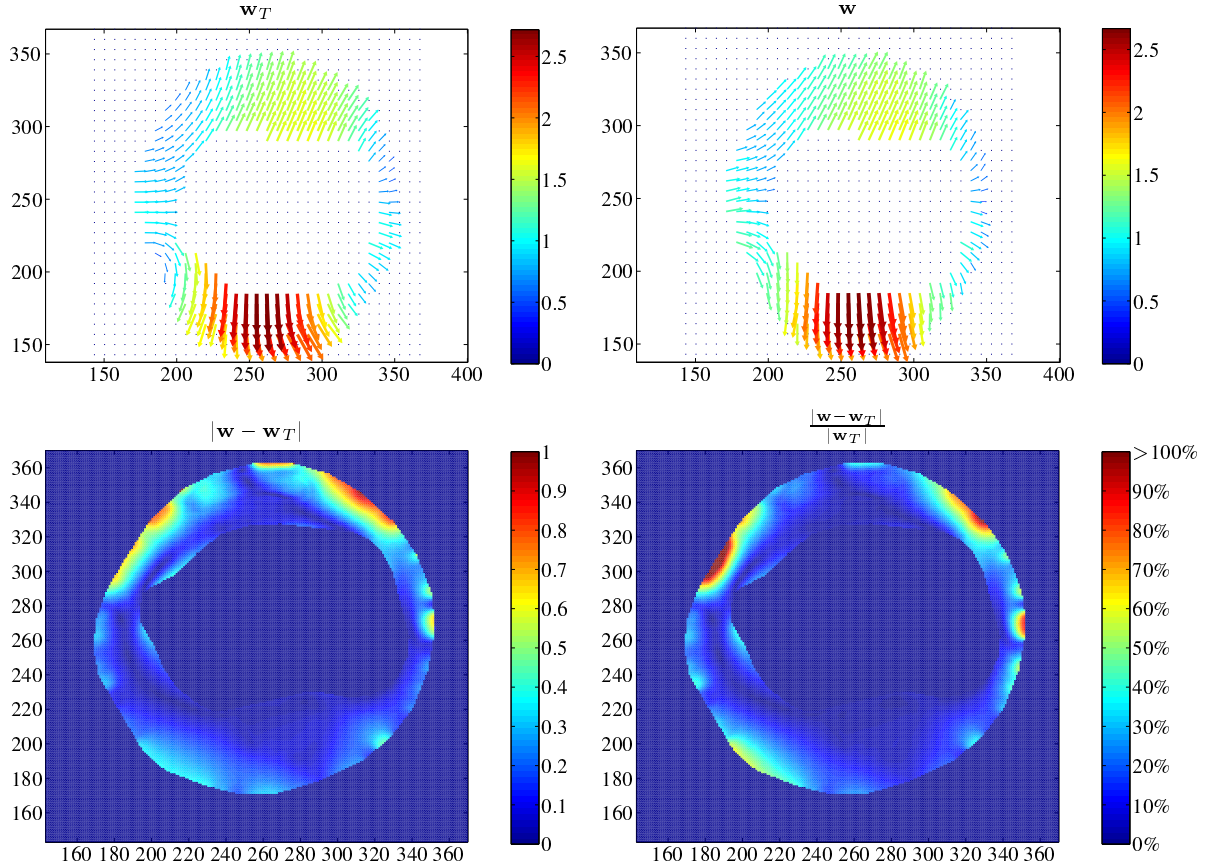


Figure 4.18: Compliant case displacements for the synthetic artery model. (Top-left) Displacement field, w_T , obtained by solving the mechanical problem (ground truth); (top-right) displacement field, w , obtained by solving the optical flow (OF) of the sequence (bottom-left) absolute error of the OF displacement field against the ground truth (in pixels); (bottom-right) relative error of the OF displacement field against the ground truth.

4.4.3 In-vivo artery sequence

By applying the gating and registration methods presented in Chapters 2 and 3 respectively, we extract frames of vessel cross-sections that present atherosclerotic lesions from a sequence of IVUS images. Particularly, we choose 2 lesions with low to no calcium shadows neither stent deployment, to avoid hidden tissue and conditions of low wall pulsatility, respectively. To maximize tissue displacements, the optical flow was estimated between end-diastolic and systolic frames.

The in-vivo results showed larger displacements than the reported in the synthetic cases (compare Figure 4.22 against Figure 4.16 or 4.18). Note that the displacements in synthetic cases rely on experimental ex-vivo measurements of elastic parameters in tissues, while there is not certainty about the relation between material properties in-vivo and ex-vivo. Then, the in-vivo tissue properties may differ from ex-vivo measurements. Also, the observed displacements are coherent with a radial expansion of the lumen, which is expected from a correct flow estimation.

The norm of the stain tensor distinguishes zones with different deformations, which can be used to establish regions composed by different materials. Case 1 (1st column of Figure 4.22) shows three areas with major strains at \overline{OA} , \overline{OB} and \overline{OC} which may result in 3 materials different from the background tissue. Case 2 (2nd column of Figure 4.22) present a calcification at \overline{OC} and a thin fibrous cap between \overline{OA} to \overline{OB} (supported by

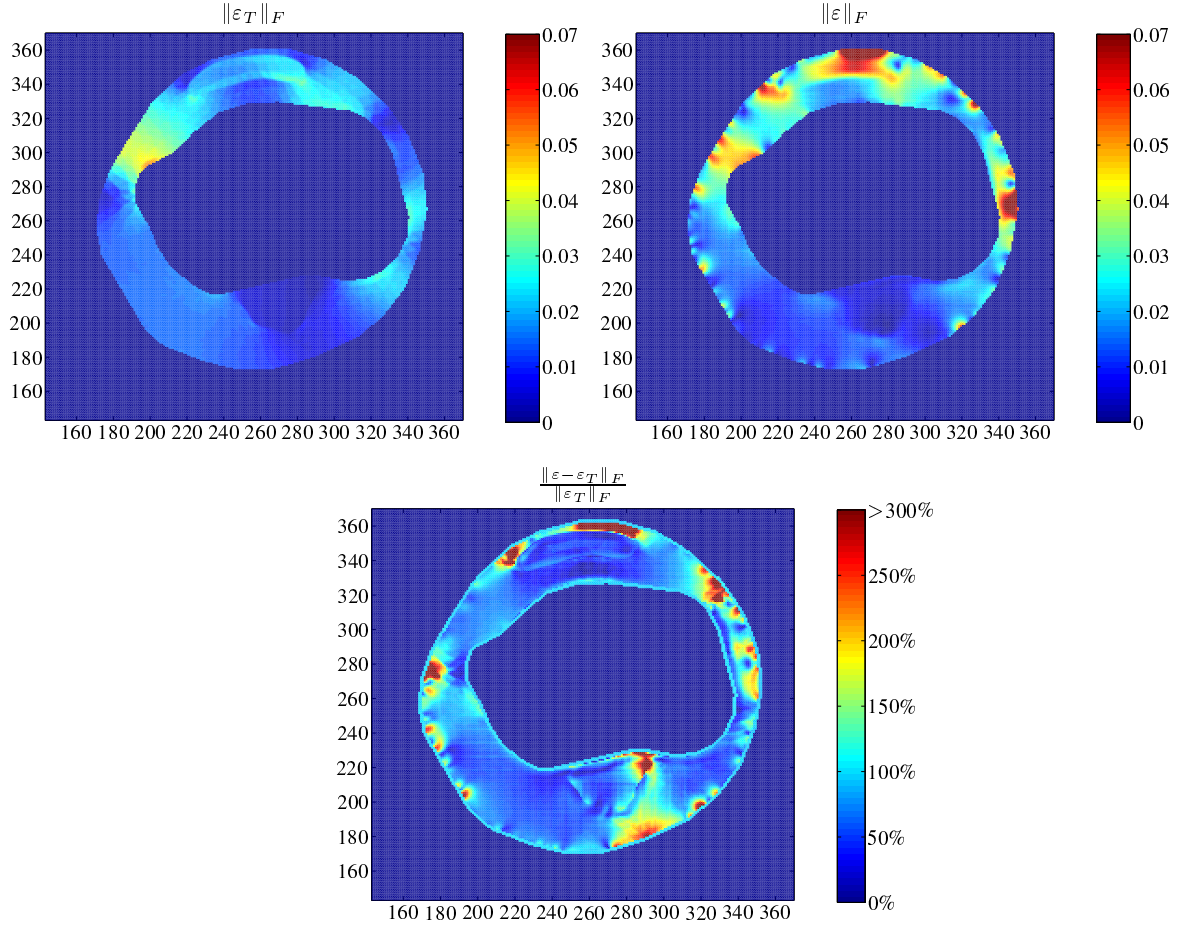


Figure 4.19: Compliant case strains for the synthetic artery model. (Top-left) Norm of the strain field, $\|\varepsilon_T\|_F$, obtained by solving the mechanical problem (ground truth); (top-right) norm of the strain field, $\|\varepsilon\|_F$, obtained by solving the optical flow (OF) of the sequence; (bottom) relative error of the OF strain field against the ground truth. The norm $\|\cdot\|_F$ stands for the Frobenius norm.

the echogenic intensity in the IVUS image), and both tissues are clearly recognizable in the plot of the strain tensor norm.

Besides, an ultimate application of the optical flow is as input for the characterization of material properties, it is important to highlight that the present strain field is an image-based elastography of the tunicas intima and media. The advantage of this elastography method is that no radio-frequency signals are required, allowing its processing with traditional IVUS stations. Also, the gating and registration methods diminish the common errors of elastography or palpography due to transducer migration and rotation.

4.5 Final remarks

By using a novel denoising strategy, we managed to employ optical flow techniques on speckled images. Studies on synthetic images, following noise models and statistics in concordance with the state-of-the-art knowledge, showed that the optical flow was successfully estimated with subpixel precision and a correct flow pattern.

The proposed denoising method, namely maximum likelihood variations (MLV), featured promising capabilities to enhance the signal-to-noise ratio of the IVUS images. The comparisons of MLV against the state-of-the-art method (TVL1) suggested an improved performance of our method yielding larger speckle reduction in terms of image homogeneity

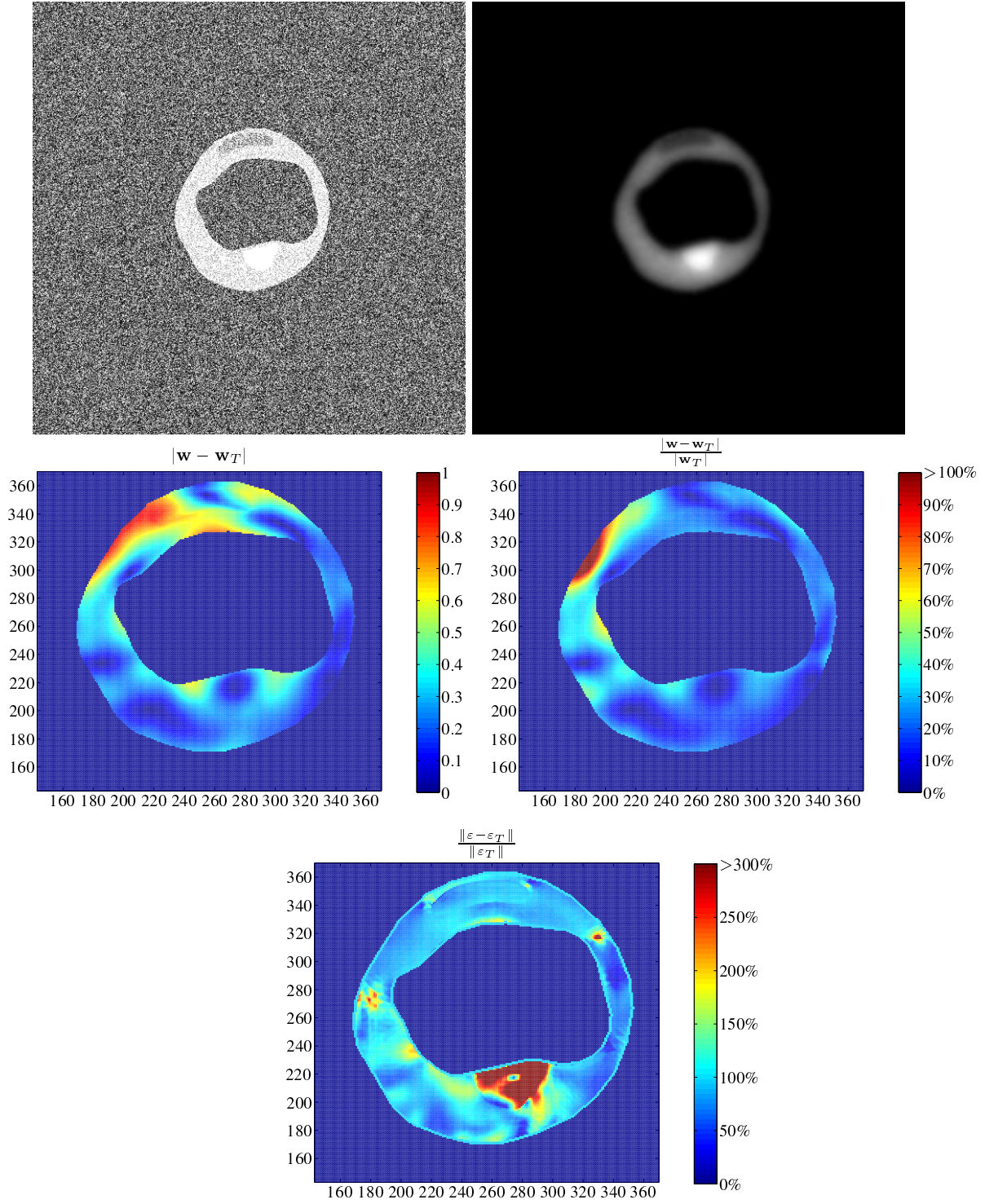


Figure 4.20: Denoising and optical flow estimation using the best denoising parameters ($\alpha = 8$, $a = 1.5$, $b = 1.4$ and $c = 0.1$) in the sense of the error ε_d^{of} . The image sequence is generated using the compliant parameters set and the speckle noise is generated with a generalized gamma distribution with parameters $\alpha = 1.5$, $\gamma = 1.5$ and $\nu = 0.8$. Optical flow (OF) is computed with parameters $\alpha = 0.05$, $\beta = 0.5$, $\rho = 2$, $\kappa^2 = 0.5$ and $M = 2$. (Top-left) First image of the generated sequence; (top-right) first image of the generated sequence after denoising; (middle-left) absolute error of the OF displacement field against the ground truth (in pixels); (middle-right) relative error of the OF displacement field against the ground truth; (bottom) relative error of the OF strain field against the ground truth. The norm $\|\cdot\|$ stands for the Frobenius norm.

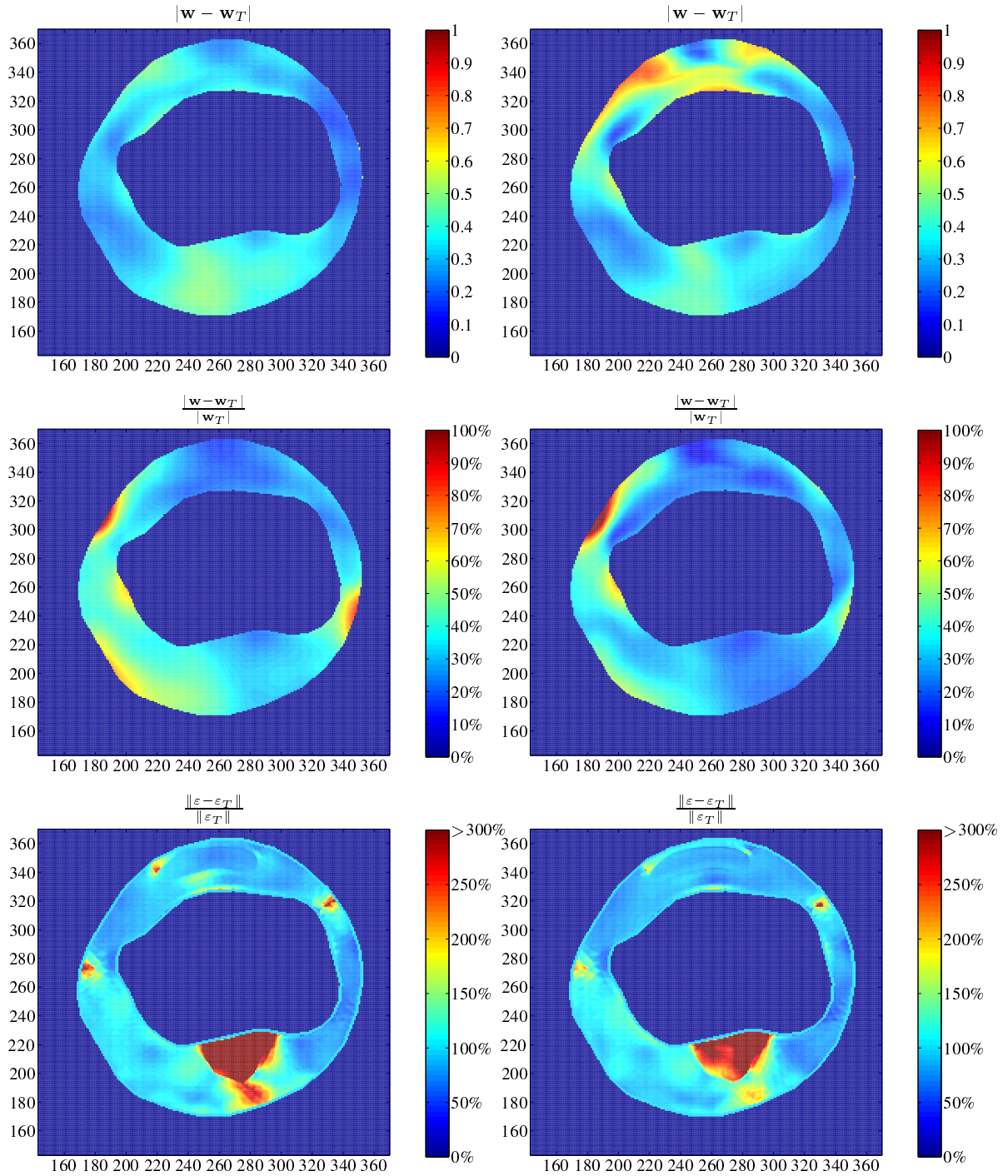


Figure 4.21: Mean errors along 10 different speckled sequences for the stiff (left column) and compliant (right column) cases. The denoising and optical flow parameters were the same as in Figure 4.20. (Top) Absolute error of the optical flow (OF) displacement field against the ground truth (in pixels); (middle) relative error of the OF displacement field against the ground truth; (bottom) relative error of the OF strain field against the ground truth. The norm $\|\cdot\|$ stands for the Frobenius norm.

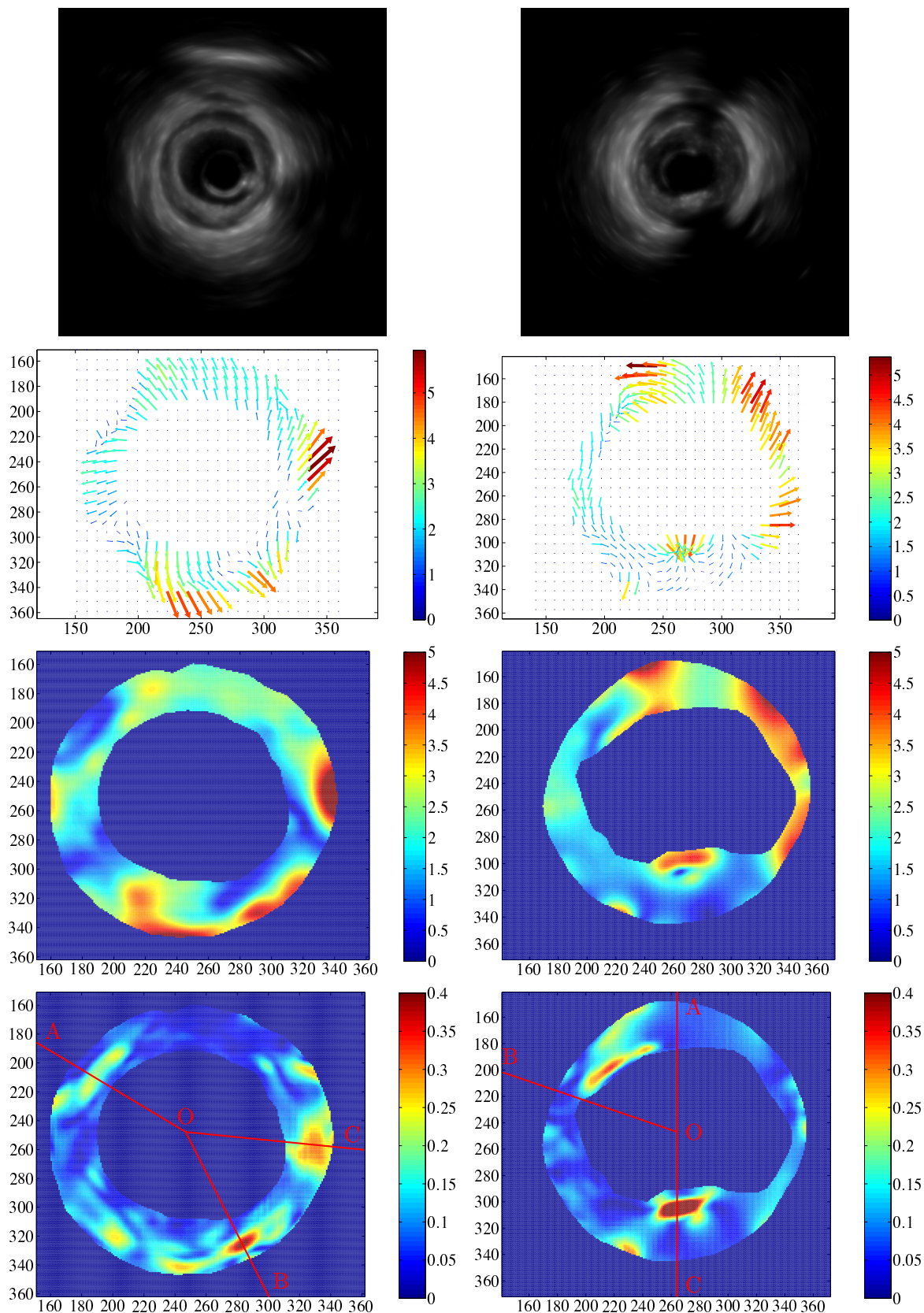


Figure 4.22: Optical flow estimation for two in-vivo image sequences (one case per column). (1st row) First (diastolic) frame of the sequence; (2nd row) optical flow estimation; (3rd row) modulus of the displacements ($|\mathbf{w}|$); (4th row) Frobenius norm of the strain tensor ($\|\varepsilon\|_F$). The denoising is performed with the optimal parameters in the sense of homogeneity ($\alpha = 4$, $a = 1.1$, $b = 1$ and $c = 0.5$) and optical flow is estimated with parameters $\alpha = 0.01$, $\beta = 0.5$, $\rho = 2$, $\kappa^2 = 0.5$ and $M = 4$.

and preservation of the original intensity values. In Sections 4.2.3 and 4.4.2, we established a mechanism based on sensitivity analysis to derive a convenient set of denoising parameters for noise with known statistical distribution. By improving noise models for IVUS images, the MLV will be benefited with more appropriate noise penalization.

Related to the optical flow, it is important to highlight that the estimated flow was directly interpreted as tissue displacement. This may not be the case in some scenarios. Artifacts or scene objects, such as guidewire artifact, calcium shadows and nonuniform rotational distortion (NURD), hide zones of tissue within the image hindering a direct tissue tracking. However, impact of these objects can be reduced, e.g., the guidewire can be removed before IVUS acquisition by the physician, NURD affected sections can be reacquired and results over calcium shadows and NURD sections can be indicated as invalids.

As the techniques presented in this chapter introduce novelty in arterial tissue tracking and featured better denoising than state-of-the-art techniques, further research will be conducted specifically in two lines: (i) experimental characterization of the tissue dependent speckle noise for IVUS; and (ii) optical flow in sequences.

For the first research line, the speckle generated over the synthetic images in Section 4.4.2 has to be improved using statistically different speckles for each kind of tissue. From the works of [293, 327], it is known that the speckle statistics are related to the tissue composition, but the lack of experimental data for vessel wall constituents (values of GG distribution coefficients for each tissue) hinders a coherent noise generation. Then, more experimental data to model the IVUS noise statistics is of paramount importance. Particularly, controlled experiments with ex-vivo specimens, where histology and IVUS data are registered, would allow the characterization of noise signature in each tissue. This would open new research horizons in US images improving image-based segmentation and speckle tracking (as a variation of OF that relaxes the intensity constraint) techniques.

As for the second research line, observe that we have estimated the flow between two frames, and longer sequences can be decomposed in series of frame pairs to estimate the flow at all instants. However, note that the sequence delivers a time coherent flow pattern that would not vary drastically along the cardiac cycle. Thus, there is a temporal consistency in the flow that can be exploited to estimate the sequence flow in a more robust manner. Some approaches have been tested along the development of this work but, yet, more research must be developed around this topic.

Finally, the optical flow coupled with the MLV method was capable to successfully deliver an accurate displacement field, as well as the associated strain field, which endows the IVUS study with kinematic information. As a matter of fact, such kinematic information now attached to the IVUS images makes possible to address the problem of in-vivo tissue characterization as will be seen in forthcoming chapters.

Part II

Biomechanical characterization of the vessel wall

Chapter 5

Anatomy and mechanical models

In the last decade, the technological advances in image acquisition equipments and imaging techniques allowed the visualization of the arterial wall architecture at scales and conditions that revolutionized the understanding of its behavior, organization, remodeling and composition. At the same time, the sustained increase of computational power in low cost equipments enabled the construction of complex mechanical models to perform realistic fluid-structure interaction simulations that integrate physiological conditions, detailed vessel wall structures and complex hemodynamics phenomena [22, 41].

In this chapter, we present state-of-the-art knowledge about the anatomy of the arteries with special focus on the coronary arteries. Also, we detail the atherosclerotic plaque composition that is utmost important to model a stenotic arterial wall. By detailing the underlying composition and organization of the wall in coronary arteries, we derive constitutive models and make assumptions for each constituent material supporting such hypotheses with experimental findings reported in the literature.

Also, we introduce the equilibrium equations for the arterial wall that will allow the characterization of the wall constituents to be performed in Chapter 6.

Finally, we detail the pipeline followed to create a geometric model of the arterial wall from an IVUS image. To appropriately instantiate the presented models, we report the ranges for the physiological and constitutive model parameters in coronary arteries.

5.1 Arterial wall anatomy

The arterial wall is conformed by different types of vascular cells embedded in the denominated extracellular matrix (ECM).

The ECM is composed by several macromolecules (such as elastin, collagen, fibronectin, laminin) immersed in a hydrated gel endowed with intertwined glycosaminoglycans/proteoglycans (GAGs/PGs) chains. The collection of these components creates an organized structural network for scaffold, connectivity, locomotion and control of the in-housed cells [9]. The specific infrastructure of the ECM enables the degradation, proliferation and migration mechanisms necessary for the remodeling and maintenance of the wall. Mechanically, the collagen and elastin fibers are the principal ECM components that resist tensile forces while glycosaminoglycans and elastin resist compressive forces. The GAGs/PGs chains also contribute to the viscoelastic behavior of the vessel wall, principally in the elastic arteries (e.g. the larger arteries). Their principal function is to maintain shape and sustain the stress generated by pulsatile forces [258]. For these reasons, the distribution and quantities of such components are of paramount importance to model a correct mechanical response. In fact, GAG/PGs content tends to increase in hypertension, aging, atherosclerosis and thoracic aortic aneurysms and dissection [151, 268, 272, 346],

evidencing that such components are important contributors to arterial morphogenesis, homeostasis and pathogenesis.

The vascular cells, such as endothelial, smooth muscle and fibroblast, establish the dynamic functionality of the vessel. The endothelial cells are the interface between the vessel wall and the blood. This interface controls the passage of diverse substances (immunologic cells, chemical signal, nutrients, water, among others), sense and mechanotranslate (into chemical signals) shear forces imposed by the blood viscous drag and control the vasomotor tone by releasing vasoconstrictors or vasodilators based on hormonal or mechanical stimuli [4, 269, 276]. The smooth muscle endows the vessel with muscular active capabilities to vary its basal diameter, being capable to contract or relax in response to neural, chemical or mechanical stimuli. Particularly, chemical stimulus can be triggered by the endothelial vasodilators or vasoconstrictors. Such interdependence between these cells allows to act in a wider (and also more complex) range of scenarios along different parts of the arterial wall. Due to the variation of the vessel diameter, smooth muscle cells regulate the blood pressure and blood flow distribution [11] orchestrated by local stimuli, the endocrine system or the autonomic nervous system. Lastly, the fibroblast cells are the source of many of the ECM constituents and so are essential for the maintenance of normal tissue architecture. They also synthesize a variety of proteolytic enzymes and inhibitors, which enables them to control the assembly and turnover of the ECM [221]. Fibroblasts display different phenotypes according to their anatomical site and the underlying ECM state (mechanical and chemical conditions of their environment).

The quantities and distribution of these constituents vary with several factors such as age, type of artery and health condition. For example, the medial layer in a healthy middle aged human consists of approximately 23% elastin, 30% collagen, 43% smooth muscle, and 4% GAGs/PGs by dry weight (in ascending thoracic aortic, [152]) and in a murine (rodent) consists of approximately 26% elastin, 50% collagen, 21% smooth muscle, and 3% GAGs/PGs (in common carotid artery, [31]). It is important to highlight that the architecture and composition of the arterial tunica media do not vary substantially among mammals [339, 340], the structure increases the amount of material layers (as we see later, the denominated lamellar unit) to resist bigger or smaller efforts, hence the percentage of materials remains the same.

5.1.1 Arterial wall architecture

The arterial wall is composed by three distinctively concentric layers denominated as tunicas (see Figure 5.1). In each of these layers, material is organized in specific configurations to provide distinctively functions. Their sizes and proportions vary depending on the vessel size, type (elastic or muscular) and anatomical locus.

The tunica intima is the inner most layer which defines the lumen of the vessel. As principal functions, it controls the passage of nutrients, chemical signals and immunologic cells and acts as a mechanotransducer for blood viscous forces. It is mainly composed by endothelial cells collagen and elastin.

The tunica media is the middle layer and is composed by several concentric units denominated lamellar units. These units present smooth muscle cells arranged circumferentially which allows to control the vascular tone for contraction and dilatation of the lumen. This mechanical active capability is key for regulating pressure and blood flow under different systemic states.

The tunica adventitia is a diffusive layer that is the interface between the vessel and the connectivity tissue. The layer offers scaffold for the tunica media and also houses fibroblast cells that maintain and remodel the ECM constituents in healthy and specially in pathological conditions.

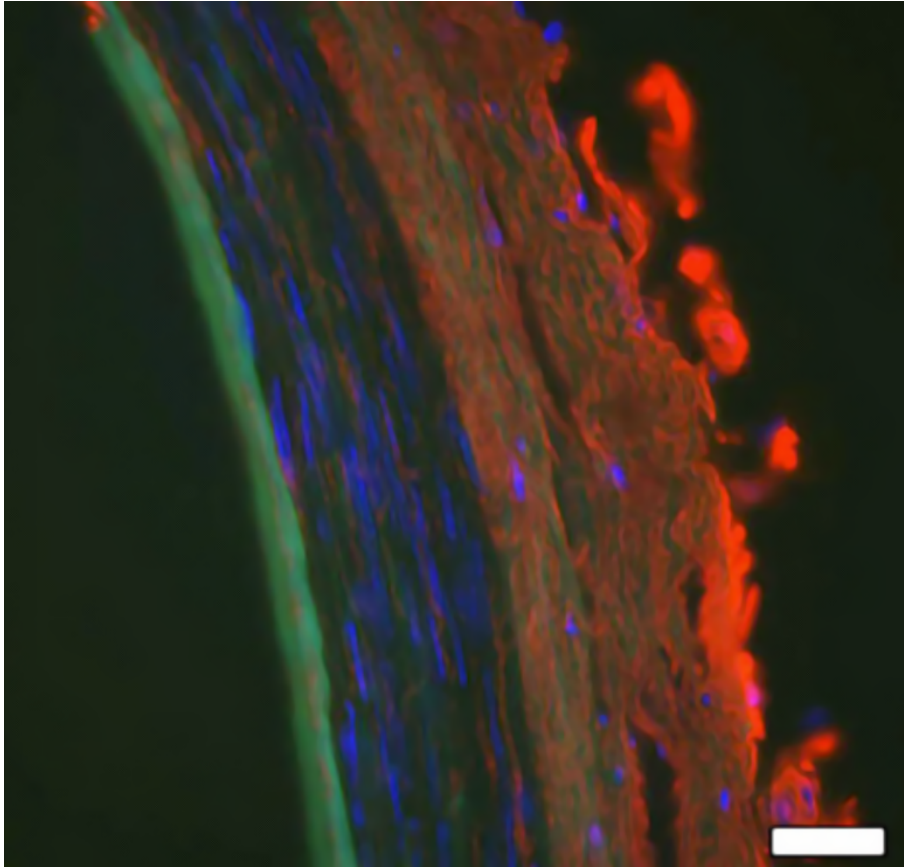


Figure 5.1: Fluorescence microscopy of a human left vertebral artery detailing the tunica intima, media and adventitia (from left to right). Immunohistochemical staining of the arterial wall reveals elastin (green) localized in the internal elastic lamina, cell nuclei (blue, DAPI stain), collagen fibers (red). Reprinted from [276] with permission from Elsevier.

Next, we present the composition of each layer to understand the disposition, function and relationship among the vessel components.

5.1.2 Tunica intima

The tunica intima is composed by three layers: endothelium, basement membrane and subendothelium. Additionally, the endothelial layer is coated by a hair-like glycocalyx layer. In what follows, we detail the composition and main characteristics of each of these constituent layers.

Glycocalyx

The glycocalyx is a polymeric network localized at the apical surface of the endothelium. It acts as a permeable barrier for the macromolecules and regulates leukocytes and thrombocytes adhesion using different kinds of enzymes and proteins. In that manner it controls the homeostasis of the plasma and vessel wall. Another important role are its mechanical sensor capabilities. Due to its fuzz-like geometry, the glycocalyx senses shear forces from the luminal area. One example is the adhesion of leukocytes that exert this kind of forces, and the glycocalyx reacts by releasing nitric oxide to free the leukocyte. Nevertheless, the response may not be purely local to such forces because the anchorage of the glycocalyx to the endothelial cytoskeleton allows to communicate such forces to other components of the wall, as presented in Figure 5.3. This is the case of the blood flow where

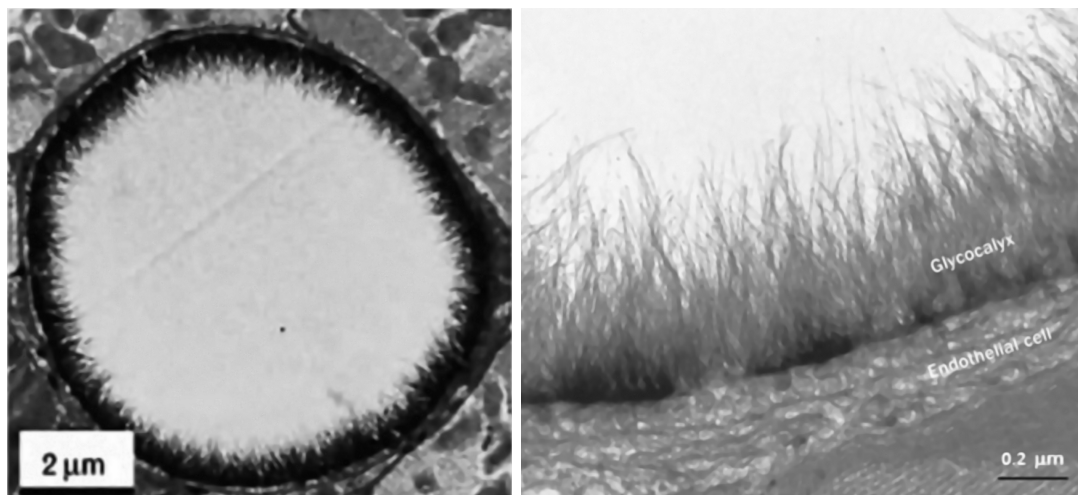


Figure 5.2: (Left) Microscopy depicting the cross-section of a capillary vessel with its glycocalyx layer; (right) microscopy image of the glycocalyx. Reprinted from [276] with permission from Elsevier.

shear stress is sensed by the glycocalyx and, then, can be acknowledged by several vessel wall components due to chemical (cytokines) or mechanical signals. Several authors have proposed association between certain patterns of wall shear stress or glycocalyx thickness and atherosclerotic plaque development [69, 82, 177, 190, 206, 350]. The link between these associations is that the wall shear stress determines the renewal and degradation of the glycocalyx layer [276], e.g., high cholesterol diet has been shown to reduce the glycocalyx thickness in murine carotid artery [317]. In this scenario, the glycocalyx could be an important actor in the genesis and progression of the atherosclerotic plaque.

Endothelium

The endothelium is a single cell thick layer of endothelial cells that acts as interface between the blood and the cardiovascular tissues. Within its numerous physiological functions, we can mention the control of vasomotor tone, blood cell trafficking, hemostatic balance, permeability, proliferation, survival, and innate and adaptive immunity. Also, it is of paramount importance for sensing and reacting to mechanical stimuli triggered by local hemodynamic conditions. As previously presented, the glycocalyx transmits the shear forces exerted by the blood flow over the endothelial cell surface. Nevertheless, as illustrated in Figure 5.3 this is not the only mechanism to sense such forces [227, 271]. There are three principal groups of mechanosensors working directly with the endothelial cells: the membrane structures (ion channels, glycocalyx, prima cilia, tyrosine kinase receptors, caveolae, G proteins and endothelial cytoskeleton), cell-cell adhesion complexes and cell-matrix adhesion complexes.

The biochemical signals, the vessel wall state and the local hemodynamic conditions (sensed by the previously mentioned mechanisms) determine the endothelial cells phenotype. This behavior varies at different organs, vessels or even between neighboring endothelial cells. Even though, two main phenotypes can be considered: a quiescence and an active one. The former stimulates vasodilation, inhibits leukocyte adhesion, platelet aggregation and exhibits anti-inflammatory, anti-coagulant, anti-adhesive, anti-proliferative and anti-oxidant characteristics. In turn, the latter one generally consists of some combination of increased cell adhesiveness, shift in hemostatic balance to the procoagulant side, secretion of inflammatory mediators and change in cell survival/proliferation [276]. The healthy endothelium presents phenotypic heterogeneity along the cardiovascular tree due

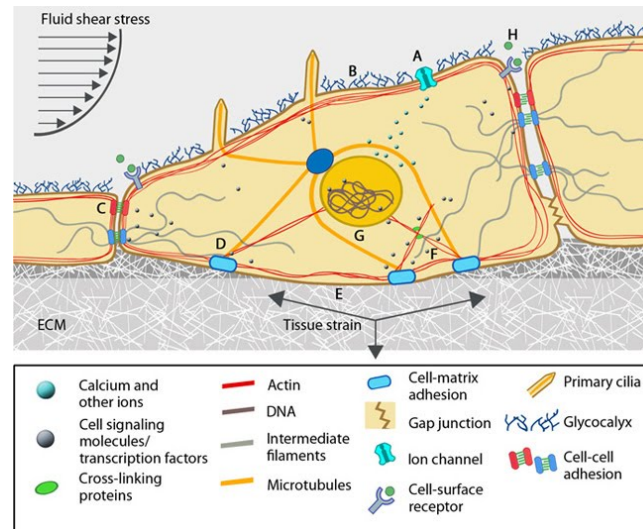


Figure 5.3: Diagram depicting the principal mechanotransducer in the cell and actors in the communication and stimulus reaction processes: (A) ion channels; (B) glycolyx; (C) cell-cell adhesion complexes; (D) cell-matrix adhesion complexes; (F) intracellular cytoskeletal components; (G) cell nucleus senses the mechanical signals and modulate an appropriate response; (H) changes in inter-cellular space is cell-type specific, influencing the concentration of signaling molecules/ proteins that bind cell-surface receptors. Reused from <https://www.mechanobio.info/what-is-mechanobiology> under creative commons attribution-noncommercial-ShareAlike 4.0 International License with permission from MBInfo.

to the changes in the hemodynamic conditions, vessel topology and structure [6]. Conversely, dysfunctional endothelium (associated with pathological cases) present a prevalence of quiescent phenotype [4, 5]. Phenotypic heterogeneity is likely to provide at least 2 evolutionary advantages: (1) it allows the endothelium to comply to the diverse needs of the underlying tissues throughout the body; and (2) it provides the endothelium with the capacity to adapt to different microenvironments [6].

Basement membrane

The basement membrane is a thin lamina endowed by an underlying reticular connective tissue which anchors the endothelium to the vessel wall. It is mainly composed by elastin and collagen arranged in a network of fibers. Additionally to its supporting role, the membrane aids in the angiogenesis inhibition, endothelial cells migration and stores diverse types of cytokines (e.g. growth and degradation enzymes).

Subendothelium

In some elastic arteries (such as coronary arteries), an extra thin layer separates the basement membrane and the internal elastic lamella. It is composed by different types of collagen and dispersed smooth muscle cells. It plays an anti-thrombotic role that is related to the presence of an anti-thrombogenic type of collagen (collagen VIII) in its structure. In elder patients (71.5 ± 7.3 (mean \pm SD) years old), the mechanical contribution of this structure plus intima components is relevant for the load bearing capacity and mechanical strength when compared to the media and adventitia layers. [145, 276].

5.1.3 Tunica media

The media tunica is composed by concentric layers of smooth muscle cells and fenestrated elastic lamellae which are grouped in the denominated lamellar units. In the large vessels, the relation between the total number of these lamellar units and the vessel radius is nearly proportional. The tension per aortic lamellar unit is nearly constant, regardless of vessel diameter or media layer thickness [340]. In fact across mammalian species the load per lamellar unit features small variability of capacity to bear load (1.1 N/m to 3.1 N/m) [340], which seems to be an optimal trade-off (due to natural selection) for the tissue to bear the load without degrade its integrity while maintaining an adequate compliance for a constant diastolic blood flow in arterioles. The most inner and outer tunicas receive a special denomination: the internal elastic lamella and the external elastic lamella. Respectively, they separate the tunica media from tunica intima and adventitia.

Internal and external elastic lamellae

The elastic lamellae are fenestrated membranes of elastin fibers. They restrict the migration of smooth muscle cells while its fenestrae (voids in the membrane) enhance the transport of water, nutrients and electrolytes between the different vessel layers. Two elastic lamellae can be highlighted due to their localization in the tunica media: the internal elastic lamella (IEL) that separates the tunicas media and intima; and the external elastic lamella (EEL) that separates the tunicas media and adventitia. The latter lamella is thicker than the former and van Gieson's stain imaging showed the EEL to be fibrous instead of forming a continuous band [283].

The deterioration of the IEL has been focus of studies aimed to understand its role in the atherosclerosis genesis and progression. Particularly, aging and other pathologies, such as atherosclerosis, have shown to increase the fenestrae area diminishing the stiffness of the lamella [122, 178] and its barrier capabilities. Also, [216] reports that thickening of IEL and disappearance of EEL are encountered in areas with frequent stenoses development.

Lamellar units

The lamellar units play a fundamental role in active and passive mechanical behavior of the vessel wall. A set of these units are piled concentrically forming the tunica media as displayed in Figure 5.4. The amount of lamellar units in the tunica is associated with the pressure load that the vessel supports from the blood in the lumen [341]. The principal components of these units are: the smooth muscle cells (SMC), collagen fibrils, elastin, micro-fibrils and GAGs/PGs chains.

Most lamellar units contains a single layer of SMCs embedded in the so called interlamellar matrix (largely composed by GAGs/PGs chains) that separates the cells to the elastic lamellae at both sides. Even though, the SMCs are anchored to the lamellae by a bundle of micro-fibrils denominated oxytalan (Ox) fibers. In fact, the union between SMC and Ox is considerably strong, remaining its bond stable even in stretched and disrupted specimens from dissected aortas [93]. The SMC can alternatively be anchored in its longitudinal ridges by elastin protrusions of the lamellae (see Figure 5.5). A basal lamina-like envelop the SMC leaving only small parts (if any part at all) of the cells being directly exposed to the ECM. This lamina-like layers could often be seen to connect adjacent SMCs, bridging the gaps separating them. These three prescribed anchorages of the SMC allow the reduction of the vessel wall and luminal areas when SMC contracts longitudinally (active response). Also, they present a passive viscoelastic response to traction forces due to luminal pressure rate increments [142, 186]. Usually, SMC are presented as contractile cells, although there is a spectrum of phenotypes, ranging from the quiescent (contractile) to a proliferative (synthetic) phenotype. Synthetic SMCs are

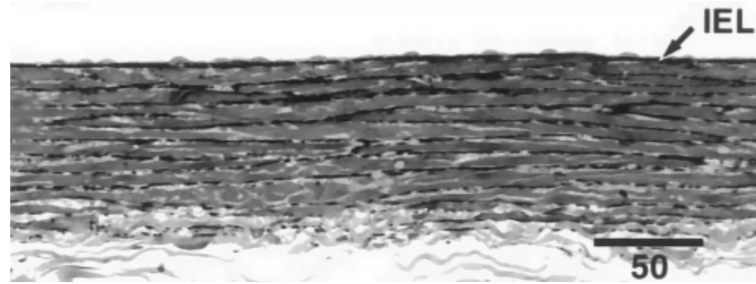


Figure 5.4: Photomicrographs of the left common carotid artery cross-section corresponding to an adult, male, Japanese white rabbit. From the internal elastic lamella until the unorganized tissue, concentric layers of lamellar units are depicted. Reprinted from [215] with permission from Wolters Kluwer Health, Inc.

capable of synthesizing large quantities of ECM, exhibit higher growth rates and higher migratory activity than contractile SMCs and are essential when vessel remodeling or repair is needed [270].

From the elastic lamellae numerous streaks of elastin protrude, conforming a complex network in the lamellar unit (see Figure 5.6). This elastic network is connected to the elastic lamellae only at a limited number of places and loosely envelope the smooth muscle cells [93]. Closely to the elastic lamellae, the collagen is deployed in two families of fibers of longitudinally symmetric directions [289]. The orientation of these collagen families varies greatly across the cardiovascular system, from places such as the aorta thoracic artery where they are oriented at 45 degrees with respect to the longitudinal axis to the common iliac arteries where they are oriented circumferentially. Clearly, the orientation influences notoriously the passive contribution of these fibers to pressure increments. Particularly, healthy coronary arteries exhibit a circumferential orientation of its fibers, although due to atherosclerotic lesions, these fibers adopt more longitudinal orientations [250].

5.1.4 Tunica adventitia

The tunica adventitia presents a less defined organization in comparison to the other tunicas. It is composed by collagen, elastin, vascular cells and perivascular nerves, who are embedded in the adventitial EMC. Collagen is wavier than in the tunica media and does not necessarily present the same orientation. As seen in Figure 5.7, the elastin and collagen fibrils are grouped in bundles with no particular architecture. The predominant vascular cells in this region are fibroblast, myofibroblast and progenitor cells, but also a resident populations of macrophages, T-cells, B-cells, mast cells, and dendritic cells is present for surveillance and innate immune functions. Fibroblasts participate in the maintenance and homeostasis of the vessel wall, but also they differentiate (as well as resident progenitor cells) toward a migratory and contractile myofibroblast phenotype during vessel inflammation [100, 130]. The resulting myofibroblasts migrate to the inflamed tissue to produce cytokines, growth factors and proteases in pathologic conditions such as tissue repair, fibrosis, pathologic organ remodeling, and cancer [100, 249, 259, 301].

Until few years ago, the adventitia functions were only thought to be the contribution to the maintenance and homeostasis of the vessel wall and the passive structural support for the blood vessel to prevent overstretch of the arterial wall under acute loading conditions [332]; nonetheless, it is also a major site of immune surveillance and inflammatory cell trafficking and harbors a dynamic microvasculature, the vasa vasorum, which maintains the medial layer and provides an important gateway for macrophage and leukocyte migration into the intima [203]. Additionally, it is a stem/progenitor cell niche in the artery wall that maintains both endothelial and mural cell progenitors that may be poised

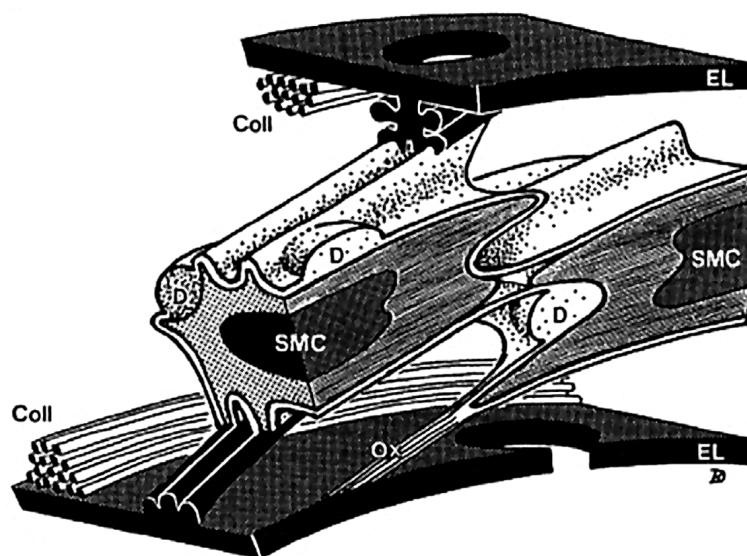


Figure 5.5: Lamellar unit detail. Simplified, schematic representation of two smooth muscle cells (SMC) and two elastic lamellae (EL) with their interconnections. Bundle of collagen fibers (Coll) are closely disposed to the elastic lamellae. Longitudinal surface ridges (but not main cell body) of left smooth muscle cell are connected to both lamellae via long, thin elastin protrusions. For sake of clarity, these protrusions have been depicted far more regular and solid than they appear in human material. Right smooth muscle cell is connected to lower elastic lamella via oxytalan fiber (Ox) that contains fibrillin and type VI collagen (and, especially near smooth muscle cell, also some fibronectin). Thin, fibronectin-positive basal lamina-like layer covers most of cell surface and, in addition, bridges gap between cells. Next to basal lamina-like layers, larger deposits (D) containing type IV collagen and heparan sulfate proteoglycan are found especially at indentations of cell surface. Figure reprinted from [93] with permission from John Wiley & Sons.

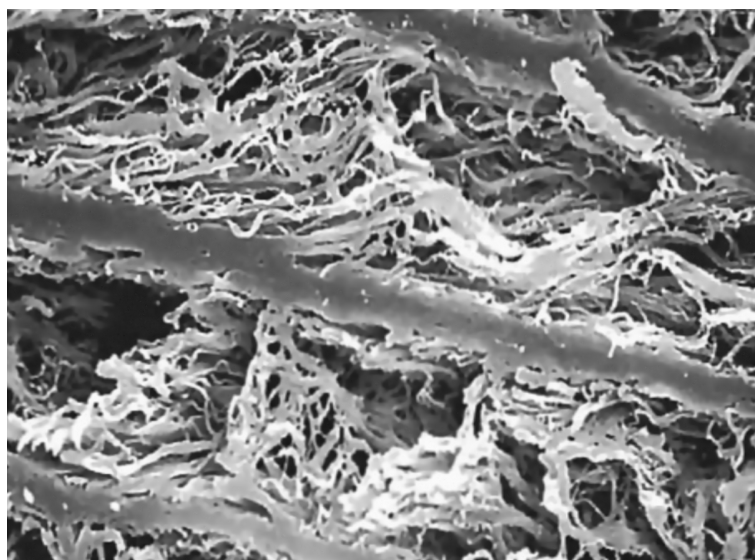


Figure 5.6: Cross-section of the tunica media of a mouse aorta (1500 \times) depicting lamellae and interlamellar elastic fibers. Reprinted from [276] with permission from Elsevier.

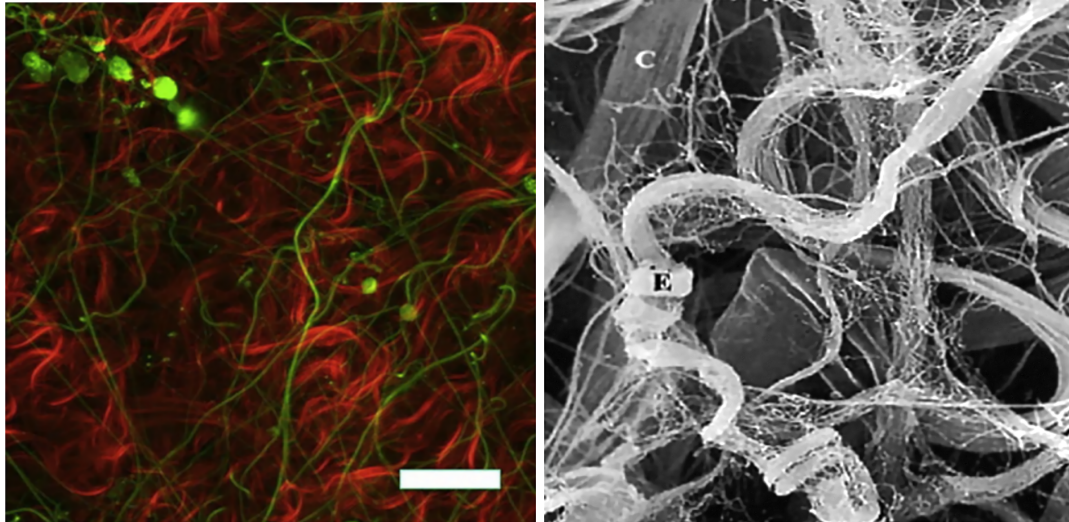


Figure 5.7: (Left) Tunica adventitia of a common carotid artery in a rabbit, imaged using multi-photon microscopy revealing elastin fibers (green) and tortuous collagen fibers (red), bar = $50\mu\text{m}$; (right) scanning electron microscope image of elastin (E) and collagen (C) fibers in adventitia of a mouse aorta. Reprinted from [276] with permission from Elsevier.

to respond to arterial injury; and, also, connects the vessel with the surrounding tissues exchanging signals and cells [59, 148, 203, 204, 253, 352].

5.1.5 Material behavior of vessel constituents

From the arterial architecture described in the previous section, the most mechanically relevant constituents are the elastin (elastic fibers and lamellae), GAG/PGs, collagen fibers and SMCs. For each specific artery in the cardiovascular system, the distribution, orientation and quantity of these constituents varies and also does the size or even the presence of each tunica. As the architecture describes, the distribution of these elements is different for each tunica, leading to heterogeneous mechanical behaviors for the materials across the wall.

The elastin resists tensile and compressive forces and endows arteries with extensibility, elastic recoil, and resilience. Most of the elastin is deposited and arranged during the perinatal period and its regeneration or synthesis after puberty is very limited [88, 276, 326], thus potential reparative processes are generally ineffective [24, 173, 315]. Therefore, damage to the arterial elastin components from causes such as supraphysiological loading during angioplasty or fatigue damage during aging cannot be properly repaired [276]. Due to its deposition in early stages of life, it is assumed to be the main responsible for arterial residual stresses (in collaboration with the GAG/PGs, [26]) and axial pre-stretches [60, 124, 308, 351]. The former appear to maintain a nearly constant transmural distributions of circumferential stress under physiological loads [76, 197, 266] and, together with the latter, contribute significantly to arterial homeostasis [315]. In healthy normotensive conditions, elastin stores most of the elastic energy at lower pressure and axial load levels, endowing the artery with high flexibility [131] at this regime.

The GAG/PGs only represent 2 – 5% of the dry weight of a normal elastic artery, even though, it brings an important mechanical contribution. Some of the PG are negatively charged compounds that are heterogeneously distributed across the arterial wall (presenting a greater concentration in the tunicas intima and media than in the adventitia) [337, 347]. As result of this transmural heterogeneity of fixed-charge density, a Donnan swelling pressure is provoked which contributes to the residual stresses within the arterial

wall [26, 181, 209, 277, 278]. In turn, residual stresses play key roles in homeostasis as well as adaptations to altered hemodynamics [150]. It is hypothesized that consequent pressurized intralamellar spaces present tensed radial elastin fibers attaching SMC to the elastic laminae, facilitating the transmural mechanosensing capabilities of such muscular cells [277]. Hence, GAG/PGs (particularly Hyaluronan) sequesters considerable water into the ECM, contributing to the compressive stiffness and viscoelastic behavior of the arterial wall.

Collagen fibers are a key constituent that only resists tensile forces and, in contrast to the elastin fibers, they are deposited and rearranged along the whole lifetime. Great proportion of these fibers are in a wavy unloaded state at low strains in normotensive conditions. As axial tensile forces are exerted to these fibers during the increase of strain, they are progressively recruited¹ bearing most of the load. This material is notoriously stiffer than other ECM constituents (ultimate tensile strength in the range 50 – 100 MPa, [114]), endowing the mechanical response of the wall with a non-linear behavior [56, 136, 275]. As shown in Figure 5.1, the collagen is present in the three tunicas, being wavier in the adventitia. This architectural characteristic prevents the overstretch of the arterial wall under acute loading conditions [332]. Collagen fibers are organized in two families helically wound along the arterial axis and symmetrically disposed with respect to such axis. The angle between the families follows a distribution that varies between tunicas and arteries [144]. In most arteries, the distribution presents two marked axis-symmetrical modes that allow to simplify the characterization of collagen behavior to two families with homogeneous orientation [143, 144]. The angulation of the fibers appears to be closer to the axial direction in the adventitia, closer to the circumferential direction in the media and in between in the intima, where a third and even a fourth family may arise in the circumferential and axial directions (study performed in thoracic and abdominal aorta and common iliac arteries) [290]. This fiber distribution promotes a different anisotropic behavior in each tunica. Three hypotheses were proposed to explain the specific collagen fiber orientations:

- The fibers are aligned so that, under the mean pressure and an axial pre-stretch, the transmural gradient of the maximum principal Cauchy stress is minimized [113].
- The fibers are adapted during the remodeling process so that the artery layers have optimal load-bearing capability. For this, the two families of collagen fibers are aligned between the principal stretch directions as dictated by the ratio of the magnitudes of the two largest principal stresses [128].
- The fibers are aligned so that the minimum of total potential energy (composed by the sum of the elastic energy stored in the deformed body and the potential energy of the applied forces) is optimized with respect to the angles of the fibers in the tunicas media and adventitia [325].

Particularly, in [263] all three hypotheses were tested for common iliac arteries, recovering the angles observed in previous experiments [290].

The smooth muscle has active and passive mechanical contributions. As previously stated, active SMC endows arteries with the capacity to control the inner radius [315] and, at homeostasis, they are partially contracted (such contraction level is usually referred as basal tone). Along the cardiac cycle, they are cyclically stretched by 10% with a 25-50% mean strain in the healthy arterial wall [219]. Peak force development of these cells occurs at typically $\approx 90\%$ of their distended passive diameter at 100 mmHg, and allows

¹The term *recruit* stands for the moment at which the fiber is completely stretched and axial strains occur in its structure.

constriction up to 200 mmHg [276, 316]. Significant softening occurs when contractile SMCs change to a synthetic state. For SMCs obtained from rat and rabbit thoracic aortas, the normalized stiffness decreases up to 25% and up to 50% after phenotype transformation [226, 236]. This is explained by the structural cell changes between phenotypes, i.e., few filament bundles (which enrich the cell with stiffness) and large amounts of highly deformable organelles in the synthetic SMC. There is scarcity of data about quantification of the viscoelastic behavior of these cells. Between the few works that addressed this issue, [219, 237], conducted stress relaxation tests for SMCs in cultured rat aortic (with no lesions) following rapid stretching with a strain rate of 10%/s. Normalized stiffness measured in the rapid stretch phase was 12.7 ± 2.2 (kPa, mean \pm SD, $n = 11$) and was almost 4 times the stiffness obtained in the quasi-static tensile test. The strain rate in the artery wall during pulsation is $\approx 10\%/s$.

5.2 Atherosclerotic plaque anatomy

The atherosclerotic plaque is an intramural accumulation of intracellular and extracellular lipids, macrophages, T-cells, smooth muscle cells, proteoglycan, collagen, calcium, and necrotic debris, in a vessel. The mechanisms that provoke its genesis and progression are still active fields of research. Two hypotheses about the vascular inflammation that initiates the lesion genesis have been proposed, namely the *inside-out* and *outside-in*.

In the *inside-out* hypothesis, the vascular inflammation is initiated and evolved due to endothelial events and the associated humoral and phenotypic responses. The arterial sites with low or oscillatory endothelial shear stress, located near branching points and along inner curvatures in the cardiovascular system, are likely to present adaptive intimal thickening [291, 305] where the rate of lesion progression remains higher there than at other arterial sites. The low wall shear stress presents an association (yet not completely understood) to the disease initiation due to the injury of the endothelial cells [70]. The affected endothelial cells change from quiescent to active (pro-inflammatory) phenotype in which cell adhesiveness and secretion inflammatory mediators are increased. As result, monocytes homing to the endothelium start to adhere and eventually transmigrate into the vessel wall [191]. Hence, low density lipids (LDLs) in the circulation accumulate in macrophages on the intimal surface and transmigrate to the tunica intima, initiating an inflammatory process [202]. Here, the LDLs molecules are modified by oxydation and aggregation [307] stimulating the adaptive immune response (endothelial cells and SMCs turns to active phenotype, chemoattractants and growth factors are released which stimulate the monocytes homing, migration, and differentiation into macrophages and dendritic cells [30]). The macrophages and dendritic cells present in the lesion serve as deposit of intramural lipids and become foam cells due to mechanisms that are not fully understood [30, 306]. In addition, groups of foam cells form xanthomas (harmless and fully reversible if the stimuli that caused their formation dissipates) which, if located, at sites with accumulation of acellular lipid-rich material, may develop into progressive atherosclerotic lesions [30] due to the formation of necrotic cores.

Conversely, in the *outside-in* hypothesis, the vascular inflammation initiates in the adventitia and advances toward the intima [298, 338]. As reported in [202], several studies have shown increased vasa vasorum neovascularization [123, 135] and macrophage presence [233] in the adventitia after vessel injury but prior neointimal development. The vascularization delivers a conduit for inflammatory cell transport into the vessel wall to promote chronic inflammation and plaque neovascularization, while the adventitia and perivascular tissue become highly populated with neutrophils, macrophages and apoptotic cells [35, 292]. The fibroblasts also located at the adventitia, begin to proliferate, secreting

Strain (%)	CeFb ($n = 12$)	HyFb ($n = 9$)	Ca ($n = 5$)
1	183 ± 248	1740 ± 2630	871 ± 1720
4	594 ± 656	4110 ± 5140	2860 ± 5500
8	1680 ± 1870	10700 ± 13800	7220 ± 13300
12	3380 ± 3800	21100 ± 28600	13500 ± 24300

Table 5.1: Static circumferential modulus (in kPa) for human aortic plaque constituents reported in [198].

extracellular matrix (ECM) and collagen proteins. Particularly, some fibroblasts differentiate into myofibroblasts (see Section 5.1.4) and migrate inward to the intima to generate a neointimal tissue [30]. Once in place, myofibroblasts deposit collagen until apoptosis induced by the cytokine Transforming Growth Factor- β (this mechanism presumably regulates contractile remodeling by self-limiting excessive ECM deposition). Paradoxically, TGF- β is a chemoattractant for myofibroblasts [205] which counteracts the previous regulation processes. The fibroblasts that proliferate in the adventitia, self-regulate their own synthesis mechanisms for collagen to avoid excessive local stiffening of the media [261]. As the myofibroblasts start the deposition of ECM materials, an orchestrated expression of cytokine and inflammatory molecules (yet not completely understood) starts the inflammatory/wound healing process where chemoattractants for monocytes and leukocytes induce the immune cells migration to the intima [156].

By either mechanism (or other yet unknown process), the atherosclerotic plaque is generated in the tunica intima. In Figure 5.8, it is depicted such plaque in murines featuring an heterogenous composition. Three components are discriminated due to their different mechanical behavior: the fibrotic tissue, the lipidic tissue (Lip), and the calcified tissue (Ca). The fibrotic tissue can even be disaggregated in two additional categories: the hypocellular fibrotic (HyFb) tissue which is mainly composed by ECM and collagen fibers; and the cell rich fibrotic (CeFb) tissue similar to the former with the aggregation of smooth muscle cells originated in the inner media [312]. As presented in Figure 5.8, the former fibrotic tissue is reactive with haematoxylin, erythrosine, safran (HES) staining showing an orange tonality, while the latter appears as a pale blue in both HES and oil red-O (ROO) staining. The Lip is reactive with the ROO staining appearing in red tonalities, and calcifications are inert to HES and ROO, leaving a white trail in the interior of the plaque. In the case of the plaque 1, a Lip region (lipid pool) next to the tunica media is contained by the HyFb tissue (fibrotic cap) that is only isolated from the lumen by a layer of CeFb tissue. The plaque 2 is less organized. Most of the lesion is composed by HyFb tissue with Lip inclusions. At the center of the lesion a calcification is presented and, again, the inner most region features CeFb tissue. In both cases, the tunics media and adventitia do not present neither HyFb, CeFb, Lip nor Ca tissue deposition, although the media is considerably thinner in presence of diseased intima (in mean it retracts from $200\mu\text{m}$ to $80\mu\text{m}$ in human coronaries [330]). Even though, the lamellar units seem to preserve their healthy structure.

Mechanical tests of the previous constituents (see Figure 5.9) were reported in [198] and [331]. The experiments showed that the cellular component (myofibroblast or SMC) of the fibrotic tissue greatly modifies the stiffness of the region. In fact, HyFb may reach circumferential modulus higher than calcified regions while CeFb is substantially softer than Ca tissues (see Table 5.1). In terms of the necessary stress for rupture, Ca tissue fails at the smaller levels of stress closely followed by the CeFb. The HyFb has the highest load bearing capacity, which seems to justify the biological purpose of the fibrous cap as lipid pool container.

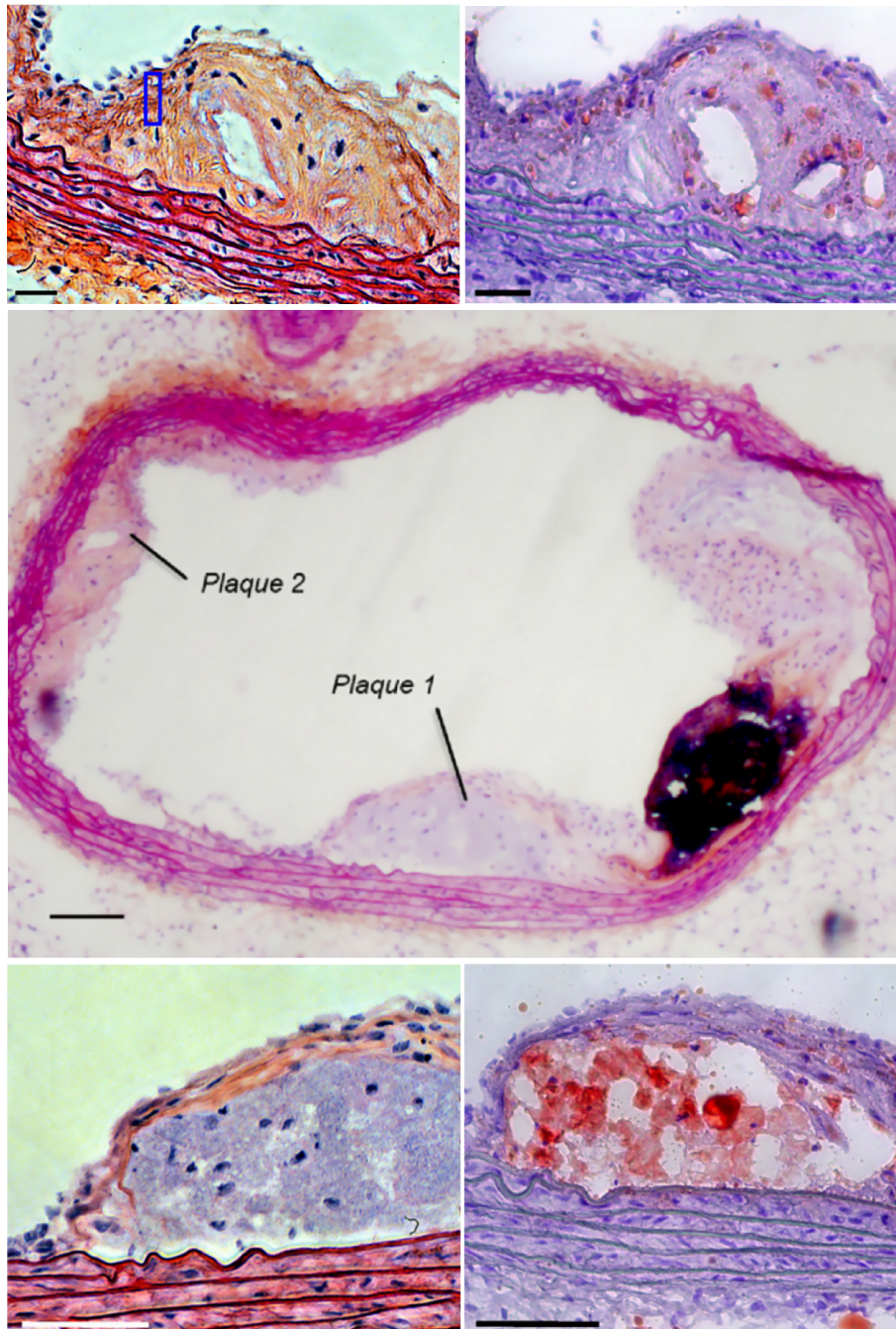


Figure 5.8: Histology of the murine aorta with: (left) a trichrome, haematoxylin, erythrosine, safran (HES) staining the nucleus, cytoplasm and fibrosis in blue, pink and yellow, respectively; and (right) an oil red-O (ROO) staining of lipid deposits in red and a smooth muscular cells (SMC) staining using an anti- α -actin antibody for the evaluation of SMC proliferation and fibrous cap formation. Top and bottom row images depict the plaque 2 and 1, respectively. Reprinted from [312] with permission from Elsevier.

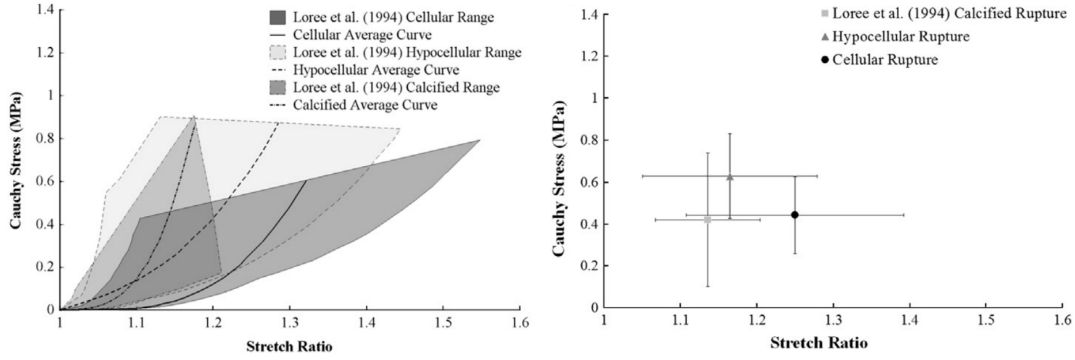


Figure 5.9: Stress-stretch relation for human aortic plaque constituents: (left) Cauchy stress versus stretch ratio and (right) rupture points for cell rich fibrotic (CeFb), hypocellular fibrotic (HyFb) and calcified (Ca) tissues. Reprinted from [331] with permission from Elsevier.

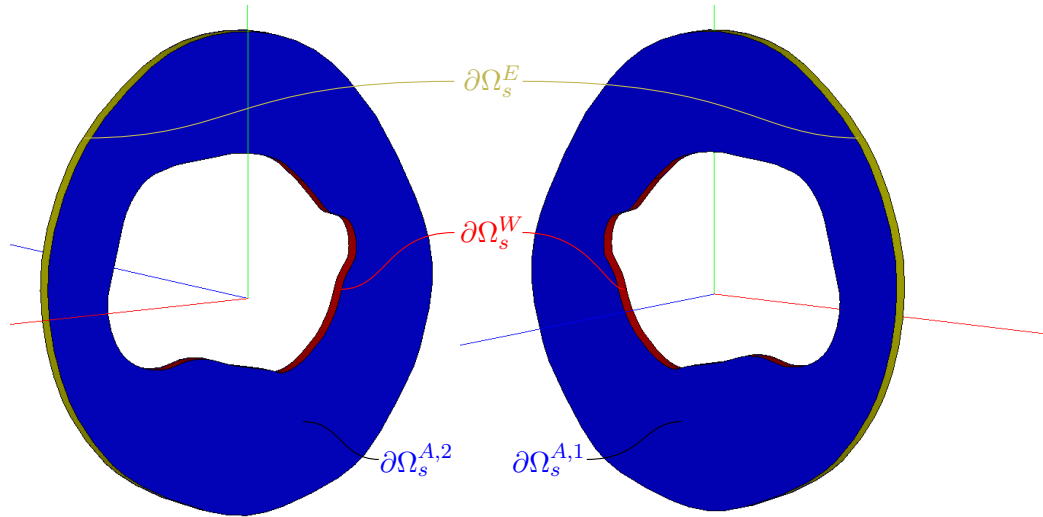


Figure 5.10: Cross-sectional slice of an arterial vessel. Description of the spatial domain Ω_s and boundaries $\partial\Omega_s = \partial\Omega_s^W \cup \partial\Omega_s^E \cup \partial\Omega_s^A$ of the slice.

5.3 Mechanical models for the arterial wall

In this section, we present the elements needed to construct mathematical models for the arterial wall based on continuum mechanics. Let us consider the domain of a vessel cross-sectional slice as a body for which we identify in the Euclidean space its *spatial* configuration denoted by Ω_s with boundary $\partial\Omega_s = \partial\Omega_s^W \cup \partial\Omega_s^E \cup \partial\Omega_s^A$, where $\partial\Omega_s^W$ represents the interface between the vessel and the blood, $\partial\Omega_s^E$ the external surface, and $\partial\Omega_s^A = \bigcup_{i=1}^2 \partial\Omega_s^{A,i}$ stands for the set of 2 cross-sectional (non-physical) boundaries at the axial extremes of a vessel slice (see Figure 5.10). The coordinates at this configuration are denoted by \mathbf{x}_s . A *material* configuration, used as a reference configuration, is denoted by Ω_m , with coordinates \mathbf{x}_m . In the context of hemodynamics, Ω_s stands for the configuration at which mechanical equilibrium is achieved for a given load condition (diastolic, systolic or any other loaded state of the arterial wall). Residual stresses are neglected. Therefore, we assume that the material configuration is always load- and stress-free.

The displacement field from the reference to the spatial configuration is denoted by \mathbf{u} . Then, we can characterize the deformation mapping from Ω_m onto Ω_s and its inverse

by the following expressions,

$$\mathbf{x}_s = \chi_m(\mathbf{x}_m) = \mathbf{x}_m + \mathbf{u}_m, \quad (5.3.1)$$

$$\mathbf{x}_m = \chi_s(\mathbf{x}_s) = \chi_m^{-1}(\mathbf{x}_s) = \mathbf{x}_s - \mathbf{u}_s, \quad (5.3.2)$$

where subscripts m and s denote the descriptions of the fields in the material and spatial configurations, respectively. Thus, the displacement vector field it is given by

$$\mathbf{u}_s(\mathbf{x}_s) = (\mathbf{u}_m(\mathbf{x}_m))_s = \mathbf{u}_m(\chi_m^{-1}(\mathbf{x}_s)). \quad (5.3.3)$$

The gradients of these mappings result

$$\mathbf{F}_m = \nabla_m \chi_m = \mathbf{I} + \nabla_m \mathbf{u}_m, \quad (5.3.4)$$

$$\mathbf{f}_s = \nabla_s \chi_s = \nabla_s \chi_m^{-1} = \mathbf{I} - \nabla_s \mathbf{u}_s, \quad (5.3.5)$$

where ∇_m and ∇_s denote the gradients with respect to material and spatial coordinates, respectively. Observe that $[\mathbf{F}_m^{-1}]_s = \mathbf{f}_s$ and $[\mathbf{f}_s^{-1}]_m = \mathbf{F}_m$.

Further, biological tissues are assumed to behave as incompressible materials, which is mathematically represented by the following kinematical condition

$$\det \mathbf{F}_m = 1. \quad (5.3.6)$$

In a general case the load state of the arterial cross-section can be characterized as follows: a Neumann boundary condition given by the forces exerted by the blood flow over $\partial\Omega_s^W$, i.e. a traction \mathbf{t}_s^W , and by the tethering tractions $\mathbf{t}_s^{A,i}$ acting over $\partial\Omega_s^{A,i}$, $i = 1, 2$. Equivalently, we group the tethering tractions into \mathbf{t}_s^A , which is defined over the whole $\partial\Omega_s^A$. We consider that no load from external tissues $\mathbf{t}_s^E = 0$ is acting on the external surface $\partial\Omega_s^E$. It is important to recall that the traction due to hemodynamic forces \mathbf{t}_s^W constitutes a follower load, and can be split into normal and tangential components by $\mathbf{t}_s^W = t_s^{W,n} \mathbf{n}_s + \mathbf{t}_s^{W,t}$ where $t_s^{W,n} = \mathbf{t}_s^W \cdot \mathbf{n}_s$ is the normal component of the traction and $\mathbf{t}_s^{W,t}$ is the tangent vector which can be characterized as $\mathbf{t}_s^{W,t} = \mathbf{P}_s \mathbf{t}_s^W$, with $\mathbf{P}_s = (\mathbf{I} - \mathbf{n}_s \otimes \mathbf{n}_s)$ being the projection operator to the plane with unit normal vector \mathbf{n}_s . For the application presented in this manuscript, the tangent contribution is considered to be $\mathbf{t}_s^{W,t} = 0$, hence disregarding the shear forces imprinted by the blood flow on the vessel wall. Additionally, we remove rigid motions by constraining orthogonal displacements with respect to the boundary at 3 points over $\partial\Omega_s^W$ (the same points as in 4.14).

The mechanical problem in variational form is presented considering the incompressibility as an additional constraint. Then, an independent variable (the pressure in the solid domain) emerges as a Lagrange multiplier to accommodate this kinematic constraint.

Next, we provide the statement of two variational formulations of mechanical equilibrium which are required for the problem addressed in the present work, and whose difference is rather subtle: the known domain. In the so-called *preload problem*, the given domain is the domain at which the body is at equilibrium (the spatial domain), and the unknown domain is the reference domain used to define the constitutive equations (the material domain). In the so-called *forward problem*, the given domain is the material domain, while the unknown data is the spatial domain. Further details regarding linearization and numerical schemes for these two problems can be found in [22, 41].

5.3.1 Preload problem

Given the equilibrium configuration Ω_s and the load acting on the spatial configuration, the variational equations that govern this problem are those corresponding to the

mechanical equilibrium expressed in the *spatial* domain. Hence, the problem reads: given the loads $\mathbf{t}_s^{W,n}$ and \mathbf{t}_s^A , find $(\mathbf{u}_s, \lambda_s) \in \mathcal{U}_s \times \mathcal{L}_s$ such that $\boldsymbol{\sigma}_s$ satisfies

$$\int_{\Omega_s} [-\lambda_s \operatorname{div} \hat{\mathbf{u}}_s + \boldsymbol{\sigma}_s \cdot \boldsymbol{\varepsilon}_s(\hat{\mathbf{u}}_s)] d\Omega_s = \int_{\partial\Omega_s^W} \mathbf{t}_s^{W,n} \mathbf{n}_s \cdot \hat{\mathbf{u}}_s d\partial\Omega_s^W + \sum_{i=1}^2 \int_{\partial\Omega_s^{A,i}} \mathbf{t}_s^{A,i} \cdot \hat{\mathbf{u}}_s d\partial\Omega_s^{A,i} \quad \forall \hat{\mathbf{u}}_s \in \mathcal{V}_s, \quad (5.3.7)$$

$$\int_{\Omega_s} [1 - \det \mathbf{F}_s^{-1}] \hat{\lambda}_s d\Omega_s = 0 \quad \forall \hat{\lambda}_s \in \mathcal{L}_s, \quad (5.3.8)$$

where $\boldsymbol{\varepsilon}_s(\hat{\mathbf{u}}) = \frac{1}{2}(\nabla_s \hat{\mathbf{u}} + \nabla_s \hat{\mathbf{u}}^T)$ is the strain rate tensor in the *spatial* configuration, $\mathcal{L}_s = L^2(\Omega_s)$ and $\mathcal{U}_s = \{\mathbf{u}_s \in \mathbf{H}^1(\Omega_s), \mathbf{u}_s \text{ satisfies essential b.c.}\}$ are, respectively, the linear space for pressures and the linear manifold associated to kinematically admissible displacements, and $\mathcal{V}_s = \{\hat{\mathbf{u}}_s \in \mathbf{H}^1(\Omega_s), \hat{\mathbf{u}}_s \text{ satisfies homogeneous essential b.c.}\}$ is the space of kinematically admissible variations. Also, $\boldsymbol{\sigma}_s$ can be related to the second Piola-Kirchhoff stress tensor \mathbf{S}_m through

$$\boldsymbol{\sigma}_s = \frac{1}{\det \mathbf{F}_s} \mathbf{F}_s (\mathbf{S}_m(\mathbf{E}_m))_s \mathbf{F}_s^T. \quad (5.3.9)$$

where the Piola-Kirchhoff stress tensor is a function of the Green-Lagrange deformation tensor $\mathbf{E}_m = \frac{1}{2}(\mathbf{F}_m^T \mathbf{F}_m - \mathbf{I})$ via a constitutive equation (see Section 5.4).

5.3.2 Forward problem

When the material (load- and stress-free) configuration Ω_m is known, the variational equations (5.3.7)-(5.3.8) can be evaluated in terms of this reference domain, yielding what we define as the *forward problem*. In fact, the variational equations that govern the equilibrium problem expressed now in the *material* domain Ω_m are written as follows: given the material description of the loads, $\mathbf{t}_m^{W,n}$ and $\mathbf{t}_m^{A,i}$, find $(\mathbf{u}_m, \lambda_m)$ in $\mathcal{U}_m \times \mathcal{L}_m$ such that

$$-\int_{\Omega_m} \lambda_m (\mathbf{F}_m^{-T} \cdot \nabla_m \hat{\mathbf{u}}_m) \det \mathbf{F}_m d\Omega_m + \int_{\Omega_m} (\mathbf{S}_m(\mathbf{E}_m)) \cdot \dot{\mathbf{E}}(\hat{\mathbf{u}}_m) d\Omega_m = \int_{\partial\Omega_m^W} (\mathbf{t}_m^{W,n} \mathbf{F}_m^{-T} \mathbf{n}_0^W \cdot \hat{\mathbf{u}}_m) \det \mathbf{F}_m d\partial\Omega_m^W + \sum_{i=1}^2 \int_{\partial\Omega_m^{A,i}} (\mathbf{t}_m^{A,i} \cdot \hat{\mathbf{u}}_m) |\mathbf{F}_m^{-T} \mathbf{n}_0^{A,i}| \det \mathbf{F}_m d\partial\Omega_m^{A,i} \quad \forall \hat{\mathbf{u}}_m \in \mathcal{V}_m, \quad (5.3.10)$$

$$\int_{\Omega_m} (\det \mathbf{F}_m - 1) \hat{\lambda}_m d\Omega_m = 0 \quad \forall \hat{\lambda}_m \in \mathcal{L}_m, \quad (5.3.11)$$

where $\dot{\mathbf{E}}(\hat{\mathbf{u}}_m) = \frac{1}{2}[\mathbf{F}_m^T(\nabla_m \hat{\mathbf{u}}_m) + (\nabla_m \hat{\mathbf{u}}_m)^T \mathbf{F}_m]$, \mathbf{n}_0 is the unit normal vector in the material configuration and $\mathcal{U}_m, \mathcal{V}_m$ and \mathcal{L}_m are the counterparts of $\mathcal{U}_s, \mathcal{V}_s$ and \mathcal{L}_s , respectively, with functions defined in Ω_m .

We emphasize that the inertial term could be easily incorporated in the solid problem. However, for coronary arteries the stresses associated to inertial forces can be safely

neglected. This is easily justified by a straightforward non-dimensionalization of the equations (consider a cylindrical geometry), which shows that the non-dimensional number α_{in} , representing the ratio between inertial and circumferential stresses is of the order of 10^{-6} . In fact, α_{in} can be approximated by

$$\alpha_{in} = \frac{\rho \Delta r_i h}{T^2 p_i}, \quad (5.3.12)$$

where r_i denotes the inner radius, h the thickness, p_i the internal pressure, Δr_i the inner radius variation, ρ the density of the wall and T the time it takes to achieve the peak pressure from diastole. Given the following values within the physiological range, $r_i = 0.4[cm]$, $\Delta r_i = 0.2r_i$, $h = 0.2r_i$, $p_i = 15 \cdot 10^4[\frac{dyn}{cm^2}]$, $\rho = 1[\frac{gr}{cm^3}]$ and $T = 0.1[s]$, from equation (5.3.12) $\alpha_{in} = 4.267 \cdot 10^{-6}$ is obtained.

5.3.3 The preloaded forward problem

The *forward problem* formulated above is the classical equilibrium problem in solid mechanics when the material configuration is known, while the preload problem is a non-traditional formulation of the very same problem when the equilibrated (deformed) configuration is known. Therefore, both mechanical problems are governed by the same equilibrium equation, and the difference simply lies in the data for the problem, and therefore in the corresponding linearized expressions.

The *preload problem* stated above is a mandatory step towards characterizing the mechanical state, i.e. the stress state, of the arterial wall in a, for instance, geometry obtained from medical images (e.g. the end-diastolic geometry) with a given baseline hemodynamics loads (e.g. the end-diastolic pressure). The material configuration is required because it is used to define constitutive equations, without which the forward problem cannot be properly formulated. In our case, such baseline geometry is obtained from IVUS study, while the baseline hemodynamics loads (the blood pressure) are estimated from patient specific data. Just after solving the preload problem, the baseline mechanical state, that is the stress state due to the preload pressure (i.e. pressure at diastole), is adequately determined and the *forward problem* can be solved to determine the equilibrium configuration for other hemodynamics loads occurring during the cardiac cycle. In that manner both problems are synergically coupled to solve a forward problem from an adequately preloaded configuration.

Note that, given a set of loads for the vessel, the preload problem is solved only once and, then, the *forward problem* is solved for each load in the set.

5.4 Constitutive models

As previously introduce, the arterial wall contains passive (e.g., elastin fibers, collagen fibers, GAGs/PGs) and active (e.g. SMCs) structural components. The extracellular matrix composed mainly by GAGs/PGs and elastin is assumed to be an isotropic neo-hookean material (see Section 5.4.1) because such components do not present any particular orientation. In the works of [277, 278] such model assumption for the GAGs/PGs were tested and fitted with biaxial data from murines showing an excellent agreement at physiological pressure levels. In several works such as [144, 145, 280], the isotropic assumption for the elastin was included in the arterial wall models which fitted with biaxial data from human arteries (coronaries included).

On the other hand, the collagen and SMCs feature marked anisotropy in the tunica media, because of their alignment over the circumferential-axial plane. As the SMCs are circumferentially oriented, collagen fibers are organized in two families helically wound

along the arterial axis and symmetrically disposed with respect to such axis. In our applications, we neglect the SMCs as an independent contribution, although its passive component is embedded within the model for tunica media. In turn, the tunica adventitia lacks of SMCs and the present and less organized collagen fibers are disposed more axially than in the media. For these layers, we use a particular modification of the neo-hookean material introduced in [280], that will be described in Section 5.4.2.

The main components of the atherosclerotic plaque, i.e., fibrotic, lipidic and calcified tissues, are also modeled as isotropic neo-hookean materials (see also Section 5.4.1). In [331], it is shown that fibrotic tissue in illiac plaque presents a quasi isotropic behavior. Different from the fibrotic tissue, the lipidic and calcified tissues do not display such contribution of SMCs neither oriented fibers that endow their structures with anisotropic behavior, what suggests that an isotropic hypothesis for these materials is reasonable.

5.4.1 Neo-Hookean material model

This model is suitable for materials under large deformations where the stress-strain relationship behaves as non-linearly elastic, isotropic and independent of strain rate. Also, the model assumes an ideal elastic material at every strain level which, in physiological ranges, is satisfied by many biological tissues. The stress-strain relationship for a neo-hookean material derives from the strain energy function

$$\psi = \frac{c}{2}(I_1 - 3) \quad (5.4.1)$$

where c is the material parameter that characterizes the stiffness of the material and I_1 is the first invariant of the Cauchy tensor, i.e.,

$$I_1 = \text{tr}(\mathbf{C}_m) \quad (5.4.2)$$

with $\mathbf{C}_m = \mathbf{F}_m^T \mathbf{F}_m$. Using the strain energy function, we can obtain the material description of the second Piola-Kirchhoff stress tensor (and the $\boldsymbol{\sigma}_m$ through (5.3.9)) as

$$\mathbf{S}_m(\mathbf{E}_m) = \frac{\partial \psi}{\partial \mathbf{E}_m}. \quad (5.4.3)$$

5.4.2 Neo-Hookean material model with collagen fibers

For fiber-reinforced materials, the strain energy function of the previous model is complemented with energy terms that contribute specifically to the energy storage of strains at given directions (the fiber family directions). Particularly, in [144] it is proposed to model fibers contribution as an exponential term that is nullified until a certain threshold condition is surpassed. This allows to model the collagen recruitment process² where the threshold condition is the stretch at which the fibers are completely unrolled (usually denominated as recruitment stretch). A later model, [280], introduced a local dispersion for each family of fibers which improves the representation of the fiber spatial distribution. Thus, the strain energy function is defined as

$$\psi = \frac{c}{2}(I_1 - 3) + \frac{k_1}{2k_2} \sum_{i=4,6} \delta_i \left(e^{k_2[(1-\rho)(I_1-3)^2 + \rho(I_i - \lambda_i^0)^2]} - 1 \right) \quad (5.4.4)$$

²A collagen fiber is denominated as *recruited* when it is completely unrolled and further stretches imply in strains of the fiber and therefore in potential energy which is stored in the tissue.

being

$$\delta_i = \begin{cases} 1 & I_i > \lambda_i^0 \\ 0 & \text{otherwise} \end{cases}, \quad (5.4.5)$$

$$I_i = \mathbf{a}_i \cdot (\mathbf{C}_m \mathbf{a}_i), \quad i = 4, 6, \quad (5.4.6)$$

where k_1 and k_2 characterize the stiffness of the collagen fibers, λ_i^0 is the recruitment stretch (set to 1 unless it is reported otherwise), $\rho \in [0, 1]$ is the mixture parameter between isotropic and anisotropic behavior of the fiber families and \mathbf{a}_i , $i = 4, 6$ are the vectors that indicate the orientation of the fibers at the material configuration. Analogously to the previous model, \mathbf{S}_m and $\boldsymbol{\sigma}_m$ are derived from (5.4.4) through the relations (5.4.3) and (5.3.9).

5.5 Coronary arteries settings

5.5.1 Model and physiological parameters

Our focus in the following chapter is the characterization of constituents over the major coronary arteries, i.e., the right (RCA), left main (LM), left anterior descending (LAD) and left circumflex (LCx) coronary arteries. Then, we specify the anatomical variations and physiological ranges previously presented to the case of such coronary arteries.

Those arteries exhibit a luminal diameter that ranges between 1.5 – 5.5mm [330] along their length. Specifically for each artery, diameter is 2.0 – 5.5mm (mean 4mm) for LM; 2.0 – 5.0mm (mean 3.6mm) for LAD; 1.5 – 5.5mm (mean 3.0mm) for LCx; and 1.5 – 5.5mm (mean 3.2mm) for RCA. In healthy LAD arteries, ratios of adventitia, media, and intima thicknesses to total wall thickness are 0.4 ± 0.03 , 0.36 ± 0.03 , and 0.27 ± 0.02 , respectively [145], although due to atherosclerotic lesions remodeling can greatly alter such ratios. In fact, the tunica media underlying healthy intima ranges 125 – 350 μm (mean 200 μm) while for diseased intima it ranges 16 – 190 μm (mean 80 μm) [329]. The variance in the tunica intima is even more dramatic because it is the location of the inflammation process, reaching even to full blockage of the lumen by progressive thickening of such layer. The thickness in the adventitia does not suffer apparent alterations, and in both cases it ranges 300 – 500 μm [329].

The collagen fibers present also characteristic patterns for these arteries. In [145], a similar model to the proposed in Section 5.4.2 was used to fit circumferential and longitudinal stress-stretch responses of 13 (ex-vivo) human LAD specimens without stenosis. It was reported that the angle between the fibers and the circumferential direction is 60.3 ± 18.2 , 20.61 ± 5.5 and 67.0 ± 8.5 degrees. Some evidence has been reported that such angle may vary remarkably (almost 60 degrees) due to remodeling [119, 250], while other works [91] suggest smaller variations (below 10 degrees). In the following chapter, we will fix the fiber angles for each layer within the ranges reported in [145], assuming that the remodeling does not affect the fiber orientation. The three hypothesis described in [263] can be used to estimate the fiber orientation when remodeling, based on fluid-structure interaction between the blood and the vessel wall, happens. Even though, the fiber re-orientation due to vessel remodeling is out of the scope of this thesis.

As previously described in Section 4.4.2, the plaque components present a Young modulus in the ranges: 500 – 2300 kPa for the fibrotic tissue; 5 – 400 kPa for the lipidic tissue; 4000 – 18000 kPa for the calcified tissue. As reported in Table 5.1, fibrotic hypocellular tissue (HyFb) may feature even bigger values within the fibrous cap, presenting a stiffness close to the one of calcified tissue. For the proposed constitutive model presented in Section 5.4.2, experimental fitting was performed in [145] with a population of 13 non-stenotic ex-vivo specimens of human LAD. In Table 5.2, the mean and standard deviation among the 13 specimens for each parameter are reported. Such ranges will be

Tunica	c (kPa)	k_1 (kPa)	k_2	θ (degrees)	ρ
Intima	55.8 ± 21.18	263.66 ± 490.95	170.88 ± 125.47	60.3 ± 18.2	0.51 ± 0.14
Media	2.54 ± 1.26	21.60 ± 7.12	8.21 ± 3.27	20.61 ± 5.5	0.25 ± 0.09
Adventitia	15.12 ± 9.23	38.57 ± 32.53	85.03 ± 58.94	67.0 ± 8.5	0.55 ± 0.18

Table 5.2: Constitutive parameter (mean \pm standard deviation) for tunicas intima, media and adventitia as reported in [145]. The parameter θ corresponds to the opening angle of the fiber family with respect to the circumferential axis. The recruitment stretch was $\lambda_0 = 1$ in all cases for this study.

used to define the parameters of the tunica media and adventitia. In the same study, it is reported an axial in situ stretches of 1.044 ± 0.06 (mean \pm SD) with respect to the load-free length. This prestretch in the coronary arteries diminishes with the aging [145] leading to more compliant and less stressed tissues at advanced ages.

As the coronary vessels branch immediately after the beginning of the aorta, blood pressure is almost the same as the aortic central pressure. Then, we may assume inner pressure loads between 80 – 120mmHg for normotensive patients and 90 – 140mmHg for hypertensive patients.

5.5.2 Model geometry

Using IVUS studies, we derive a geometrical model for a frame of interest (see Figure 5.11). Firstly, the intima-media area is segmented from the image. The segmented surface is extruded 0.1mm in the axial vessel direction. Then, the volume is divided in media and intima tunica, where the media has homogeneous thickness and is the outer layer. An adventitia layer of 300 – 500 μ m thickness is added as an outer layer. If further materials must be detailed in the lumen (for example calcium inclusions, lipid pool areas), we employ the CAD tools in the software Salome 7.8.0 to split the corresponding volumes. The resulting volume is meshed using Netgen 1D-2D-3D embedded in Salome 7.8.0 software and, also, groups of elements, faces and nodes are created to define their constraints and constitutive parameters. The obtained mesh is finally exported in UNV format to our in-house numerical solver.

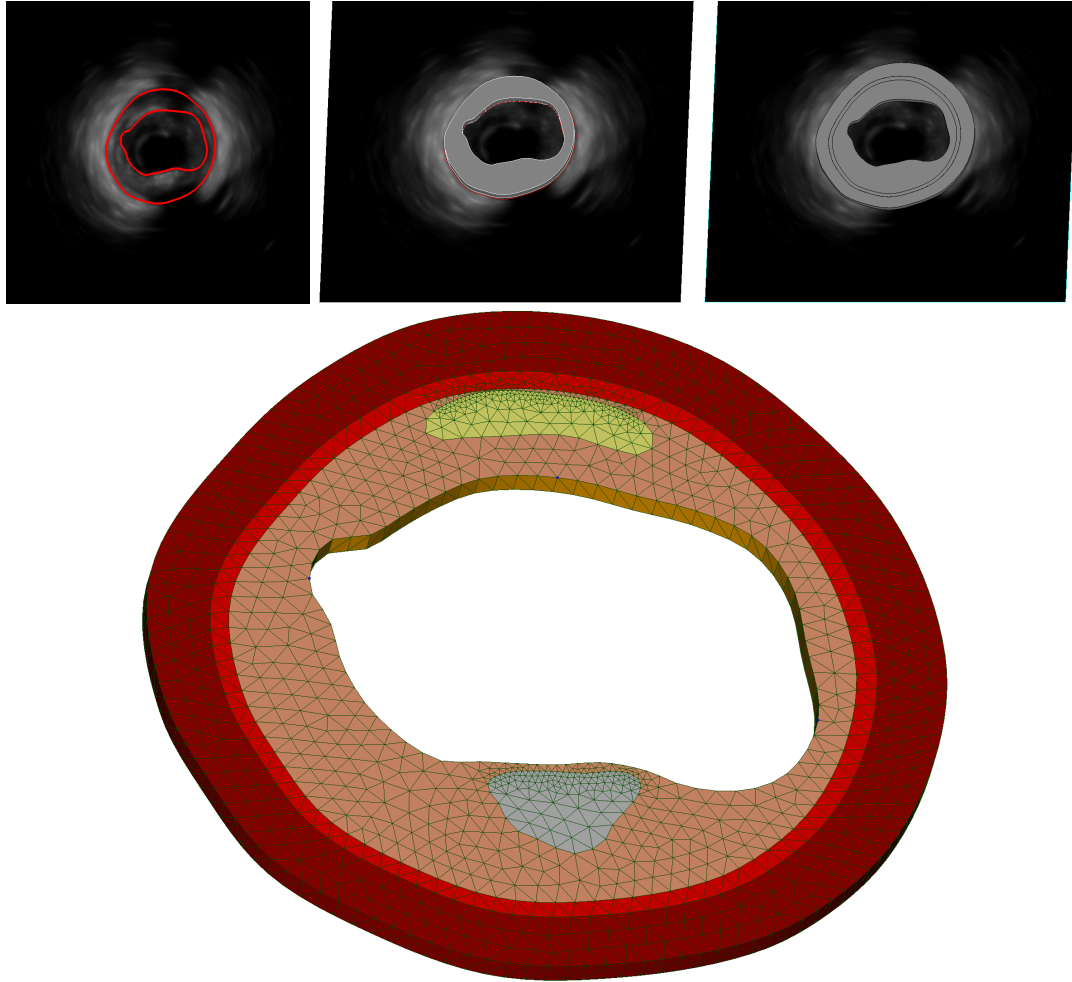


Figure 5.11: Pipeline for geometric model generation: (top-left) segmentation of the intima-media area over the IVUS image; (top-middle) extruded volume of the intima-media area; (top-right) separation of the tunics intima and media and addition of the adventitia; (bottom) final mesh with groups of elements representing the adventitia (dark-red), media (red), fibrotic tissue (light-orange), lipidic tissue (light-yellow) and calcified tissue (gray), and yellow triangular faces depict boundary $\partial\Omega_m^W$ where the blood pressure is prescribed as the load.

Chapter 6

In-vivo estimation of biomechanical parameters

Previous chapters developed the required inputs in terms of image data and models for the data assimilation strategy that will be described in this chapter. This data assimilation process aims to search for the biomechanical parameters of an arterial model such that the deformation of the vessel under physiological conditions obtained from numerical simulations matches the observed displacements retrieved from medical images. To establish a methodology to achieve this, while integrating all the previous chapters elements, is the ultimate goal of this thesis.

For the data assimilation process, it is employed a reduced order unscented Kalman filter (ROUKF) because it is computationally efficient and easily adaptable for model alterations. The efficiency is even more exploited in HPC environments because the iterative steps of the method are embarrassingly parallel. In turn, alterations to the arterial wall model are almost independent to the ROUKF since it is decoupled from the numerical simulation as it will be seen in Section 6.3.

The chapter is structured as follows. In Section 6.1 the state-of-the-art for parameter estimation and data assimilation techniques for biological tissues is scrutinized. In Section 6.2, a self-contained derivation of the ROUKF method is presented. In Section 6.3, the instantiation of the ROUKF for vessel wall characterization is detailed, linking this chapter with the IVUS image processing techniques and the anatomical insights exposed in Chapter 5. In Section 6.4, the methodology is tested in three cases with increasing model complexity towards in-vivo characterization. Finally, the outcomes of this chapter are discussed in Section 6.5.

6.1 State-of-the-art in parameter estimation techniques

The current imaging techniques and diagnostic equipments provide large amounts of data about patient condition, which is the basis for diagnosis and therapeutic risk assessment. Nevertheless, the measurement of several physical quantities or patient specific histology is forbidden in-vivo due to the invasiveness, local accessibility for the equipment or even the resolution of interest. In those cases, we can rely on indirect observation strategies, e.g., measure the displacement of a tissue and infer which are the underlying constituents that best match the observed behavior. Within these indirect methods we have the parameter estimation techniques, which can be classified in two groups: direct parameter estimation and data assimilation.

Direct parameter estimation derives a non-measurable physical quantity from a measurable quantity. This is the case of most elastography/palpography techniques, in which from direct displacement observation of tissues allow the quantification of local deformation

and stress [62, 63, 89, 248, 296]. Another example is the case of the tissue classifiers, which based on the acoustic impedance response of the materials, allow to determine the tissue composition [172, 239, 287].

Data assimilation techniques make use of measurable quantities to adjust a physical model that represents the in-vivo scenario. In that manner, these techniques permit not only to derive specific quantities or constituents, but to study the physical phenomena of the scenario and, even, modify the scenario itself (e.g. simulation of therapeutic procedures or risk scenarios). In turn, measurement errors can be filtered by the physical model being a *quid pro quo* benefit: the measurements instantiate the model and the model filters the measurements. Such techniques can be classified in two categories: variational approaches and sequential filtering approaches.

In the variational approach, a cost functional that measures the difference between the observed measures and the model prediction is constructed. The cost functional depends on the parameters of interest (among other parameters that may be necessary) to render a prediction of the measured variable of the model. Then, the estimated parameters are those such that minimize the cost functional. Several methods available in the literature can be applied to solve such problems. An affine-scaling interior-point Newton method for nonlinear programming with box constraints [80] can be used when an analytical derivative of the functional with respect to parameters is available. Also, Levenberg-Marquardt-Fletcher methods [110] can be employed for least-squares type functionals. A more popular approach is to solve the Karush-Kuhn-Tucker (KKT) necessary conditions [22, 32, 97, 179, 210, 255, 294] involving the solution of an adjoint problem. As these optimization problems are usually non-convex, large-scale trust-region method is a convenient solution for global convergence. Many works have successfully applied such approach. In [179], the viscoelastic parameters of large arteries were estimated using in-silico generated displacement of the vessel wall. Similarly, [210] explored the estimation of the vessel compliance in a 1D model using a 3D fluid-structure interaction (FSI) model to generate the measured displacement of the vessel wall. Using medical data of internal pressure and inner radius of the arteries, [304] used also 1D models to assess the constitutive parameters according to [144] model. The works of [97, 255] formulate the inverse problem from 3D FSI models and analyze the sensitivity in the identification of Young modulus to noise in the measurements of arterial wall displacements. In the latter, data assimilation is performed from flow velocity as well. The main problem of this approach is the amount of evaluations to the cost functional (or its derivative) that must be performed in order to solve the inverse problem (usually ranging from 10^2 to 10^3 [185]). Even more, the use of more realistic models such as 3D FSI models or complex heterogeneous anisotropic solid models are required to render sufficiently accurate displacements, turning the problem extremely challenging in terms of computational cost. For such scenarios, [185] proposes reduced order strategies to solve the Navier Stokes equations in combination with a domain parametrization technique that lowers both the geometrical and computational complexity, leading to faster evaluations of the cost functional. It also presents a Bayesian approach for the inverse problem optimization that lowers even more the computational cost. Other approach is taken in [32], applying model reduction techniques based on a proper orthogonal decomposition to accomplish the solution of 3D FSI in a computationally efficient way. Efficient implementations for solid mechanics problems have also been proposed in [25, 353] using a virtual fields method and a constitutive equation gap functional, respectively.

In turn, the sequential filtering approach (also known as filtering methods) are naturally less computationally demanding and embarrassingly parallel which is their main appealing factor for this kind of problems. Given a set of observations for our model of interest, the method makes a prediction for each observation and, then, corrects it

based on the discrepancies between the model estimation and the observed data. For each prediction-correction step, several variations of the parameters are tested in order to perform a suitable correction based on the prediction statistics. Several methods based on the Kalman filter have been developed to deal with linear and non-linear dynamic problems. In [66, 229, 230] a non-linear extended Kalman filter (EKF) with collocation feedback is applied to identify the Young modulus of different regions of a heart model. The observations used varied between the myocardium velocity [229], displacement [230] and velocity of the heart boundaries [66]. The stability of such methods was studied [229] and in terms of accuracy it is reported that Kalman filtering is optimal for linear systems only, while extended algorithms based on linearized operators may lead to efficient, albeit non-optimal, filtering procedures. [195] also applied EKF to estimate parameters of a reduced order Navier-Stokes model (through an orthogonal decomposition of the velocity field) and fluid concentrations by using observations from electrical impedance tomography. In more recent works, [228] presented a reduced order Kalman filter based on the unscented transform (abbreviated as ROUKF) that offers an interesting alternative to the EKF method. This new approach does not require neither linearization nor tangent operator of the non-linear model, which eases its implementation. Interestingly, the ROUKF features a higher order approximation of the system states statistics delivering more accurate outcomes than EKF. In [33, 34], ROUKF was successfully applied for estimation of Young modulus in arteries with tests in-vivo and in-vitro, showing a simpler and more efficient implementation than EKF.

Based on the efficiency, low computational cost and adaptability (e.g. test different constitutive models) of the sequential approach, such as ROUKF, we choose to implement that strategy for the estimation of biomechanical parameters in coronary arteries.

6.2 Kalman filters

In this section, we expose a self-contained presentation of the Kalman filters, beginning with a linear static system until reaching the formulation for non-linear dynamic systems. The following notation and theoretical development are based on the works of [34, 165, 300, 343].

As a first step, we introduce the least squares approximation of a variable based on a set of noisy observations. This would ease the presentation of the correction step for the Kalman filter which uses an equivalent procedure. Afterwards, we present the classic Kalman filter for linear dynamic problems. Following that, we introduce the unscented and reduced order version of the filter to tackle non-linear problems with efficiency and accuracy.

6.2.1 Weighted least-square approximation

Let us suppose we have an unknown n -vector variable X to estimate and k observations z_i , $i = 1, \dots, k$ of the linear combination of its components. In turn, each of these observations may present a variable error v_i due to the lack of precision of the observation tools. Thus, we formalize this as follows

$$\begin{bmatrix} z_1 \\ \vdots \\ z_k \end{bmatrix} = \begin{bmatrix} H_{1,1}x_1 + \dots + H_{1,n}x_n \\ \vdots \\ H_{k,1}x_1 + \dots + H_{k,n}x_n \end{bmatrix} + \begin{bmatrix} v_1 \\ \vdots \\ v_k \end{bmatrix} \quad (6.2.1)$$

or in compact notation as

$$Z = \mathbf{H}X + V. \quad (6.2.2)$$

where Z is the observation vector, V is the error measurement vector assumed as Gaussian, zero-mean, uncorrelated and white noise and \mathbf{H} is a linear observation operator. As demonstrated by [117], the most probable value of the variable, \hat{X} , will be given by

$$\hat{X} = \arg \min_X \mathcal{J}(X) = \arg \min_X \|Z - \mathbf{H}X\|_{L_2}^2 \quad (6.2.3)$$

denominated the best fit in the sense of least-squares. The minimizer for the least-square cost functional \mathcal{J} is given by

$$\hat{X} = (\mathbf{H}^T \mathbf{H})^{-1} \mathbf{H}^T Z = \mathbf{H}^{-L} Z \quad (6.2.4)$$

where \mathbf{H}^{-L} is the left inverse observation operator and only exist if $k \geq n$ and \mathbf{H} is full rank. Note that we need at least the same number of observations than elements x_i to estimate, and also, n of these observations must be linearly independent to ensure that all x_i are uniquely determined.

Usually not all observations have the same confidence, sensors may present different quality or according to experimental conditions some observations are more reliable than others. Then, we may assume that the error in each observation is zero mean and independent with a known variance $E(v_i^2) = \sigma_i^2$ and define the covariance matrix as

$$\mathbf{R} = \begin{bmatrix} \sigma_1^2 & \cdots & 0 \\ \vdots & & \vdots \\ 0 & \cdots & \sigma_k^2 \end{bmatrix}. \quad (6.2.5)$$

Defining the observation confidence as the inverse of its variance, we can weigh the observations and recast the optimization problem as

$$\hat{X} = \arg \min_X \mathcal{J}^* = \arg \min_X (Z - \mathbf{H}X)^T \mathbf{R}^{-1} (Z - \mathbf{H}X) \quad (6.2.6)$$

where the best estimate is given by

$$\hat{X} = (\mathbf{H}^T \mathbf{R}^{-1} \mathbf{H})^{-1} \mathbf{H}^T \mathbf{R}^{-1} Z. \quad (6.2.7)$$

Note that \mathbf{R} cannot be singular, which implies that every observation must be assumed at least with a small quantity of uncertainty.

In many scenarios, more observations could be added to the minimization procedure over time but the present formulation would need to recompute all matrices, making it inefficient in time-dependent scenarios. Then, we formulate a recursive approach as

$$\hat{X}_k = \hat{X}_{k-1} + \mathbf{K}_k (Z_k - \mathbf{H}_k \hat{X}_{k-1}) \quad (6.2.8)$$

$$Z_k = \mathbf{H}_k X + V_k \quad (6.2.9)$$

where \mathbf{K}_k is denominated as the estimator gain matrix and $(Z_k - \mathbf{H}_k \hat{X}_{k-1})$ is the correction term. Note that the correction term is an estimate of the discrepancies with the previous step and the estimator gain matrix weighs such discrepancies in order to correct the previous estimative \hat{X}_{k-1} , with some optimality criteria. Then, we have to choose an optimality criteria to construct a \mathbf{K}_k . Let us analyze the mean error of estimator (6.2.8),

$$\begin{aligned}
E(X - \hat{X}_k) &= E(X - \hat{X}_{k-1} - \mathbf{K}_k(Z_k - \mathbf{H}\hat{X}_{k-1})) \\
&= E(X - \hat{X}_{k-1} - \mathbf{K}_k(\mathbf{H}_k X + V_k - \mathbf{H}_k \hat{X}_{k-1})) \\
&= E(X - \hat{X}_{k-1} - \mathbf{K}_k \mathbf{H}_k (X - \hat{X}_{k-1}) - \mathbf{K}_k V_k) \\
&= (\mathbf{I} - \mathbf{K}_k \mathbf{H}_k)E(X - \hat{X}_{k-1}) - \mathbf{K}_k E(V_k)
\end{aligned}$$

this implies that for an initial estimate \hat{X}_0 with $E(X - \hat{X}_0) = 0$ then $E(X - \hat{X}_k) = 0$, which means that (6.2.8) is an unbiased estimator regardless the \mathbf{K}_k used. Thus, we focus in the construction of a gain matrix \mathbf{K}_k that minimizes the variance of the estimation error, obtaining not only a zero-mean error estimator but a close to zero as well. For this, we formulate the following optimization problem

$$\mathbf{K}_k = \arg \min_{\tilde{\mathbf{K}}} \text{Tr} \mathbf{P}_k(\tilde{\mathbf{K}}) \quad (6.2.10)$$

where $\text{Tr} \mathbf{P}_k$ is the trace operation of \mathbf{P}_k and, in turn, $\mathbf{P}_k = E[(X - \hat{X}_k)(X - \hat{X}_k)^T]$. Also, \mathbf{P}_k can be defined recursively in terms of \mathbf{P}_{k-1} as

$$\begin{aligned}
\mathbf{P}_k &= E[(X - \hat{X}_k)(X - \hat{X}_k)^T] \\
&= E\left[\left((\mathbf{I} - \mathbf{K}_k \mathbf{H}_k)(X - \hat{X}_{k-1}) - \mathbf{K}_k V_k\right) \left((\mathbf{I} - \mathbf{K}_k \mathbf{H}_k)(X - \hat{X}_{k-1}) - \mathbf{K}_k V_k\right)^T\right] \\
&= (\mathbf{I} - \mathbf{K}_k \mathbf{H}_k)E[(X - \hat{X}_{k-1})(X - \hat{X}_{k-1})^T](\mathbf{I} - \mathbf{K}_k \mathbf{H}_k)^T \\
&\quad - (\mathbf{I} - \mathbf{K}_k \mathbf{H}_k)E[(X - \hat{X}_{k-1})V_k^T]\mathbf{K}_k^T - \mathbf{K}_k E[V_k(X - \hat{X}_{k-1})^T](\mathbf{I} - \mathbf{K}_k \mathbf{H}_k)^T \\
&\quad + \mathbf{K}_k E[V_k V_k^T]\mathbf{K}_k^T
\end{aligned}$$

where V_k and $(X - \hat{X}_{k-1})$ errors are independent and zero-mean, then

$$\begin{aligned}
\mathbf{P}_k &= (\mathbf{I} - \mathbf{K}_k \mathbf{H}_k)E[(X - \hat{X}_{k-1})(X - \hat{X}_{k-1})^T](\mathbf{I} - \mathbf{K}_k \mathbf{H}_k)^T + \mathbf{K}_k E[V_k V_k^T]\mathbf{K}_k^T \\
&= (\mathbf{I} - \mathbf{K}_k \mathbf{H}_k)\mathbf{P}_{k-1}(\mathbf{I} - \mathbf{K}_k \mathbf{H}_k)^T + \mathbf{K}_k \mathbf{R}_k \mathbf{K}_k^T.
\end{aligned} \quad (6.2.11)$$

By using the identity $\frac{\partial \text{Tr}(\mathbf{A}\mathbf{B}\mathbf{A}^T)}{\partial \mathbf{A}} = 2\mathbf{A}\mathbf{B}$ if $\mathbf{B} = \mathbf{B}^T$ and (6.2.11), we find the minimizer for \mathbf{K}_k from (6.2.10) such that satisfies

$$\frac{\partial \mathcal{J}_k}{\partial \mathbf{K}_k} = 2(\mathbf{I} - \mathbf{K}_k \mathbf{H}_k)\mathbf{P}_{k-1}(-\mathbf{H}_k^T) + 2\mathbf{K}_k \mathbf{R}_k = 0 \quad (6.2.12)$$

where by simple algebra is obtained the minimizer

$$\mathbf{K}_k = \mathbf{P}_{k-1} \mathbf{H}_k^T (\mathbf{H}_k \mathbf{P}_{k-1} \mathbf{H}_k^T + \mathbf{R}_k)^{-1}. \quad (6.2.13)$$

Finally, we obtain the system of equations for the recursive weighted least-square approximation to update the estimative \hat{X}_k given a new observation Z_k ,

$$\begin{aligned}
\mathbf{K}_k &= \mathbf{P}_{k-1} \mathbf{H}_k^T (\mathbf{H}_k \mathbf{P}_{k-1} \mathbf{H}_k^T + \mathbf{R}_k)^{-1} \\
\hat{X}_k &= \hat{X}_{k-1} + \mathbf{K}_k (Z_k - \mathbf{H}_k \hat{X}_{k-1}) \\
\mathbf{P}_k &= (\mathbf{I} - \mathbf{K}_k \mathbf{H}_k)\mathbf{P}_{k-1}(\mathbf{I} - \mathbf{K}_k \mathbf{H}_k)^T + \mathbf{K}_k \mathbf{R}_k \mathbf{K}_k^T.
\end{aligned} \quad (6.2.14)$$

6.2.2 Kalman filter

Let us assume that we have to estimate X that is no longer constant but varies along time according to the following discrete dynamic system

$$\begin{aligned} X_k &= \mathbf{A} X_{k-1} + W_k \\ Z_k &= \mathbf{H}_k X_k + V_k \end{aligned} \quad (6.2.15)$$

where \mathbf{A} is the linear forward operator and W_k is the model error vector which is assumed to be Gaussian, zero-mean, uncorrelated and white error. First, we analyze how the mean and variance of the variable X behaves as time evolves, which is key in the Kalman filter formulation. For a given estimate of X at an instant k , the mean is defined as

$$\begin{aligned} \bar{X}_k &= E[X_k] \\ &= E[\mathbf{A} X_{k-1} + W_{k-1}] \\ &= \mathbf{A} E[X_{k-1}] + E[W_{k-1}] \\ &= \mathbf{A} \bar{X}_{k-1} \end{aligned} \quad (6.2.16)$$

obtaining that $\bar{X}_k = \mathbf{A} \bar{X}_{k-1}$. Analogously, the covariance is estimated as

$$\begin{aligned} \mathbf{P}_k &= E[(X_k - \bar{X}_k)(X_k - \bar{X}_k)^T] \\ &= E[(\mathbf{A} X_{k-1} + W_{k-1} - \mathbf{A} \bar{X}_{k-1})(\mathbf{A} X_{k-1} + W_{k-1} - \mathbf{A} \bar{X}_{k-1})^T] \\ &= \mathbf{A} E[(X_{k-1} - \bar{X}_{k-1})(X_{k-1} - \bar{X}_{k-1})^T] \mathbf{A}^T \\ &\quad + \mathbf{A} E[(X_{k-1} - \bar{X}_{k-1})W_{k-1}^T] + E[W_{k-1}(X_{k-1} - \bar{X}_{k-1})^T] \mathbf{A}^T \\ &\quad + E[W_{k-1}W_{k-1}^T] \end{aligned} \quad (6.2.17)$$

given that $(X_{k-1} - \bar{X}_{k-1})$ and W_{k-1} are uncorrelated and $E[W_{k-1}] = 0$, then

$$\begin{aligned} \mathbf{P}_k &= \mathbf{A} E[(X_{k-1} - \bar{X}_{k-1})(X_{k-1} - \bar{X}_{k-1})^T] \mathbf{A}^T + E[W_{k-1}W_{k-1}^T] \\ &= \mathbf{A} \mathbf{P}_{k-1} \mathbf{A}^T + \mathbf{Q}_{k-1} \end{aligned} \quad (6.2.18)$$

where \mathbf{Q}_{k-1} is the covariance matrix of the model error.

Now, suppose that our best initial estimative at $k = 0$ is given by a mean state of X , i.e., $E[X_0] = \hat{X}_0$. Differently from the static case, we can use the forward operator to propagate the estimate from the previous time instant \hat{X}_{k-1} to the current time instant \hat{X}_k satisfying that $\hat{X}_k = E[X_k]$. Note that such estimate is achieved using knowledge of \mathbf{A} regardless Z_k . Exploiting this fact, we can assemble a methodology such that at each time step, a prediction based on previous observations is performed, i.e.,

$$X_k^- = E[X_k | Z_1, \dots, Z_{k-1}], \quad (6.2.19)$$

denominated the *a priori* estimate, and then, correct such prediction based on a new observation Z_k , i.e.,

$$X_k^+ = E[X_k | Z_1, \dots, Z_k], \quad (6.2.20)$$

denominated the *a posteriori* estimate.

The *prediction* step in which we update previous state estimate and its covariance, is given by

$$\begin{aligned} \hat{X}_k^- &= \mathbf{A} \hat{X}_{k-1}^+ \\ \mathbf{P}_k^- &= \mathbf{A} \mathbf{P}_{k-1}^+ \mathbf{A}^T + \mathbf{Q}_{k-1}. \end{aligned} \quad (6.2.21)$$

Similarly as presented in (6.2.14), the *correction* step based in the newest estimate is given by

$$\begin{aligned}
\mathbf{K}_k &= \mathbf{P}_k^- \mathbf{H}_k^T (\mathbf{H}_k \mathbf{P}_k^- \mathbf{H}_k^T + \mathbf{R}_k)^{-1} \\
&= \mathbf{P}_{XZ,k} (\mathbf{P}_{Z,k})^{-1} \\
\hat{X}_k^+ &= \mathbf{A} \hat{X}_k^- + \mathbf{K}_k (Z_k - \mathbf{H}_k \hat{X}_k^-) \\
\hat{\mathbf{P}}_k^+ &= (\mathbf{I} - \mathbf{K}_k \mathbf{H}_k) \mathbf{P}_k^- (\mathbf{I} - \mathbf{K}_k \mathbf{H}_k)^T + \mathbf{K}_k \mathbf{R}_k \mathbf{K}_k^T.
\end{aligned} \tag{6.2.22}$$

where $\mathbf{P}_{XZ,k}$ is the cross covariance between X_k and Z_k and $\mathbf{P}_{Z,k}$ is the covariance of Z_k , in fact

$$\begin{aligned}
\mathbf{P}_{XZ,k} &= E[(X_k - \hat{X}_k^-)(Z_k - \hat{Z}_k)^T] \\
&= E[(X_k - \hat{X}_k^-)(\mathbf{H}_k X_k - \mathbf{H}_k \hat{X}_k^-)^T] \\
&= E[(X_k - \hat{X}_k^-)(X_k - \hat{X}_k^-)^T] \mathbf{H}_k^T \\
&= \mathbf{P}_k^- \mathbf{H}_k^T
\end{aligned} \tag{6.2.23}$$

$$\begin{aligned}
\mathbf{P}_{Z,k} &= E[(Z_k - \hat{Z}_k)(Z_k - \hat{Z}_k)^T] + \mathbf{R}_k \\
&= E[(\mathbf{H}_k X_k - \mathbf{H}_k \hat{X}_k^-)(\mathbf{H}_k X_k - \mathbf{H}_k \hat{X}_k^-)^T] + \mathbf{R}_k \\
&= \mathbf{H}_k E[(X_k - \hat{X}_k^-)(X_k - \hat{X}_k^-)^T] \mathbf{H}_k^T + \mathbf{R}_k \\
&= \mathbf{H}_k \mathbf{P}_k^- \mathbf{H}_k^T + \mathbf{R}_k.
\end{aligned} \tag{6.2.24}$$

The iterative and sequential use of these two steps to update the system state based on incremental observations is the denominated Kalman filter. Some important highlights of the method detailed in [300]:

- If W_k and V_k are Gaussian, zero-mean, uncorrelated and white, then the Kalman filter is the solution of (6.2.15);
- If W_k and V_k are zero-mean, uncorrelated and white, then the Kalman filter is the best *linear* solution of (6.2.15);
- If W_k and V_k are correlated or colored, then the Kalman filter can be modified to solve (6.2.15).

Note that if the forward operator $\mathbf{A} = \mathbf{I}$, i.e., the system is static, we obtain the recursive weighted least-square introduced in the previous Section.

6.2.3 Unscented Kalman filter

Next, we generalize the previous system (6.2.15) for the case that the forward and observation operators are nonlinear, i.e.,

$$\begin{aligned}
X_k &= f(X_{k-1}, t_{k-1}) + W_k \\
Z_k &= h(X_k, t_k) + V_k
\end{aligned} \tag{6.2.25}$$

where $f(\cdot)$ is the nonlinear forward operator, $h(\cdot)$ if the nonlinear observation operator and t_k is the time at the step k . Note that the operator f does not longer propagate the mean as previously shown in (6.2.16), in fact,

$$\begin{aligned}
\bar{X}_k &= E[X_k] \\
&= E[f(X_{k-1}, t_{k-1}) + W_{k-1}] \\
&= E[f(X_{k-1}, t_{k-1})]
\end{aligned} \tag{6.2.26}$$

where $E[f(X_{k-1}, t_{k-1})] \neq f(E[X_{k-1}], t_{k-1})$ since f is not linear to X_k by hypothesis. Then, we have to find a method to propagate the mean and covariance of our state X from a time $k - 1$ to k .

The unscented transform offers a mechanism to sample a PDF (with known mean \bar{X} and covariance \mathbf{P}_X) in M points $\{X^i, i = 1, \dots, M\}$ such that: (i) $\{X^i, i = 1, \dots, M\}$ mean and covariance are the same as the PDF; given a nonlinear operator g , the mean and covariance of the points $\{Y^i = g(X^i), i = 1, \dots, M\}$ are a third-order approximation¹ of the mean and covariance of $y = g(x)$. The sampling points X^i are denominated as *sigma-points* and exist several different sets such that satisfy the third order propagation of the PDF statistics. Particularly, we choose the *spherical sigma-points* [162, 164] because they offer stability for the Kalman filter and only require $N + 1$ samples of the PDF where N is the number of components of the state vector.

The computation of the spherical sigma-points is performed as follows:

1. Choose a weight $w^{(0)} \in [0, 1)$. In this thesis, we always choose $w^{(0)} = 0$ although other values of w can be used to improve the approximation of the fourth and higher order of the mean and covariance [161, 163].
2. Compute the weights $w^{(i)} = \frac{1 - w^{(0)}}{N + 1}, i = 1, \dots, N + 1$.
3. Initialize the 1-element vectors

$$\sigma_0^{(1)} = 0 \quad (6.2.27)$$

$$\sigma_1^{(1)} = -\frac{1}{\sqrt{2w^{(1)}}} \quad (6.2.28)$$

$$\sigma_2^{(1)} = \frac{1}{\sqrt{2w^{(1)}}} \quad (6.2.29)$$

4. Recursively expand the σ vectors for $j = 2, \dots, N$

$$\sigma_i^{(j)} = \begin{cases} \begin{bmatrix} \sigma_0^{(j-1)} \\ 0 \end{bmatrix} & i = 0 \\ \begin{bmatrix} \sigma_i^{(j-1)} \\ 1 \\ -\frac{1}{\sqrt{j(j+1)w^{(1)}}} \end{bmatrix} & i = 1, \dots, j \\ \begin{bmatrix} 0_{j-1} \\ j \\ \frac{1}{\sqrt{j(j+1)w^{(1)}}} \end{bmatrix} & i = j + 1 \end{cases} \quad (6.2.30)$$

where 0_j is a column vector of j zeros and $\sigma_i^{(j)}$ are recursively defined vectors.

5. Compute the sigma points as

$$X^{(i)} = \bar{X} + \sqrt{\mathbf{P}} \sigma_i^{(n)}, \quad i = 0, \dots, N + 1. \quad (6.2.31)$$

As we choose $w^{(0)} = 0$, $X^{(0)}$ is ignored and we effectively obtain $N + 1$ sampling points.

¹The reader is directed to [300] Section 14.2.1 and 14.2.2 for such demonstrations. In the reference, the third order approximation of the mean and covariance of the unscented transform are compared to the Taylor expansion of the nonlinear function g showing the equality of the first fourth terms of the series.

Then, we define the two steps for the unscented Kalman filter by introducing the unscented transform in the steps defined for the linear Kalman filter. The *prediction* step is obtained as

$$\begin{aligned}
\hat{X}_{k-1}^{(i)} &= \hat{X}_{k-1}^+ + \sqrt{\mathbf{P}_{k-1}^+} \sigma_i^{(n)}, \quad i = 0, \dots, N+1 \\
\hat{X}_k^{(i)} &= f(\hat{X}_{k-1}^{(i)}, t_{k-1}) \\
\hat{X}_k^- &= \sum_{i=1}^{N+1} w^{(i)} \hat{X}_k^{(i)} \\
\mathbf{P}_k^- &= \sum_{i=1}^{N+1} w^{(i)} (\hat{X}_k^{(i)} - \hat{X}_k^-) (\hat{X}_k^{(i)} - \hat{X}_k^-)^T + \mathbf{Q}_{k-1}.
\end{aligned} \tag{6.2.32}$$

In turn, the *correction* step is modified as

$$\begin{aligned}
\hat{X}_k^{(i)} &= \hat{X}_k^- + \sqrt{\mathbf{P}_k^-} \sigma_i^{(n)}, \quad i = 0, \dots, N+1 \\
\hat{Z}_k^{(i)} &= h(\hat{X}_k^{(i)}, t_k) \\
\hat{Z}_k &= \sum_{i=1}^{N+1} w^{(i)} \hat{Z}_k^{(i)} \\
\mathbf{P}_{XZ,k} &= \sum_{i=1}^{N+1} w^{(i)} (\hat{X}_k^{(i)} - \hat{X}_k^-) (\hat{Z}_k^{(i)} - \hat{Z}_k)^T \\
\mathbf{P}_{Z,k} &= \sum_{i=1}^{N+1} w^{(i)} (\hat{Z}_k^{(i)} - \hat{Z}_k) (\hat{Z}_k^{(i)} - \hat{Z}_k)^T + \mathbf{R}_k \\
\mathbf{K}_k &= \mathbf{P}_{XZ,k} \mathbf{P}_{Z,k}^{-1} \\
\hat{X}_k^+ &= \hat{X}_k^- + \mathbf{K}_k (Z_k - \hat{Z}_k) \\
\mathbf{P}_k^+ &= \mathbf{P}_k^- - \mathbf{K}_k \mathbf{P}_{Z,k} \mathbf{K}_k^T.
\end{aligned} \tag{6.2.33}$$

The expression $\mathbf{P}_k^+ = \mathbf{P}_k^- - \mathbf{K}_k \mathbf{P}_{Z,k} \mathbf{K}_k^T$ is mathematically identical to definition of \mathbf{P}_k^+ presented in (6.2.22) for linear systems. Its derivation can be found in [300] Section 10.5.2. Here, we need this expression because there is no explicit form for the operator $h(\cdot)$.

6.2.4 Reduced-order unscented Kalman filter (ROUKF)

Suppose that we are interested in estimating only a subset $\theta \subset X^a$ of M parameters, where X^a is the state vector. Henceforth, we simply call as parameters the states that we want to estimate. Thus, we write X^a as

$$X^a = \begin{bmatrix} x_1 \\ \vdots \\ x_N \\ \theta_1 \\ \vdots \\ \theta_M \end{bmatrix} = \begin{bmatrix} X \\ \theta \end{bmatrix} \tag{6.2.34}$$

We are only interested in an accurate prediction and correction of the parameters, then, we only propagate the mean and covariance of these components resulting in the computation of $M+1$ sigma-points. Note that, for each sigma-point we must apply the nonlinear

forward operator that, as shown in the next sections, it is several orders of magnitude more expensive in terms of computations than the whole Kalman filter iteration. As $M + 1 \ll N + M$, we obtain a significant reduction of the computational effort.

Further optimizations can be performed by the following simplification. First, we decompose the covariance matrix \mathbf{P} as

$$\mathbf{P} = \mathbf{L}\mathbf{U}^{-1}\mathbf{L}^T \quad (6.2.35)$$

where \mathbf{U} is a $M \times M$ matrix and L is a $(N + M) \times M$ skinny matrix. As we assume only uncertainty over the parameters (because are the ones that we want to estimate), the initial \mathbf{P}_0^+ features the following structure

$$\mathbf{P}_0^+ = \begin{bmatrix} 0 & 0 \\ 0 & \mathbf{P}^\theta \end{bmatrix} = \begin{bmatrix} \mathbf{L}_0^X \\ \mathbf{L}_0^\theta \end{bmatrix} \mathbf{U}_0^{-1} [(\mathbf{L}_0^X)^T \quad (\mathbf{L}_0^\theta)^T] \quad (6.2.36)$$

where supra-indexes X and θ indicate the states affected by each matrix. Then, the computation of the sigma points in the *prediction* step is decomposed as follows

$$\begin{aligned} \hat{X}_0^{(i)} &= \hat{X}_0^+ + \mathbf{L}_0^X \sqrt{\mathbf{U}_0^{-1} \sigma_i^{(n)}} = \hat{X}_0^+, \quad i = 1, \dots, M + 1 \\ \hat{\theta}_0^{(i)} &= \hat{\theta}_0^+ + \mathbf{L}_0^\theta \sqrt{\mathbf{U}_0^{-1} \sigma_i^{(n)}}, \quad i = 1, \dots, M + 1 \end{aligned} \quad (6.2.37)$$

where the sigma-points maintain the estimate for the states X and only sample across the dimensions of the parameters θ . By using such decomposition, the covariance matrices are rewritten as

$$\begin{aligned} \mathbf{P}_k^- &= \mathbf{L}_k \mathbf{P}_w^{-1} \mathbf{L}_k^T + \mathbf{Q}_{k-1} \\ \mathbf{P}_{Z,k} &= \{\mathbf{HL}\}_k \mathbf{P}_w^{-1} \{\mathbf{HL}\}_k^T + \mathbf{R}_k \\ \mathbf{P}_{XZ,k} &= \mathbf{L}_k \mathbf{P}_w^{-1} \{\mathbf{HL}\}_k^T \end{aligned} \quad (6.2.38)$$

where

$$\begin{aligned} \mathbf{L}_k &= \hat{\mathbf{X}}_k^{(*)} \mathbf{D}_w(\boldsymbol{\sigma}^{(*)})^T \\ \{\mathbf{HL}\}_k &= \hat{\mathbf{Z}}_k^{(*)} \mathbf{D}_w(\boldsymbol{\sigma}^{(*)})^T \\ \mathbf{P}_w &= \boldsymbol{\sigma}^{(*)} \mathbf{D}_w(\boldsymbol{\sigma}^{(*)})^T. \end{aligned} \quad (6.2.39)$$

The matrices $\boldsymbol{\sigma}^{(*)}$, $\hat{\mathbf{X}}_k^{(*)}$, $\hat{\mathbf{Z}}_k^{(*)}$ are the $M \times (M + 1)$ matrices whose columns are the vectors $\sigma^{(i)}$, $\hat{X}_k^{(i)}$, $\hat{Z}_k^{(i)}$ with $i = 1, \dots, M + 1$, respectively. \mathbf{D}_w is the diagonal $(M + 1) \times (M + 1)$ matrix with values $D_{ii} = w_i$, $i = 1, \dots, M + 1$, i.e., the sigma-point weights. Then, a new expression for \mathbf{P}_k^+ is derived as

$$\begin{aligned} \mathbf{P}_k^+ &= \mathbf{P}_k^- - \mathbf{K}_k \mathbf{P}_{Z,k} \mathbf{K}_k^T \\ &= \mathbf{P}_k^- - \mathbf{P}_{XZ,k} \mathbf{P}_{Z,k}^{-1} (\mathbf{P}_{XZ,k})^T \\ &= \mathbf{L}_k \mathbf{P}_w^{-1} \mathbf{L}_k^T + \mathbf{Q}_{k-1} - \mathbf{L}_k \mathbf{P}_w^{-1} \{\mathbf{HL}\}_k^T (\{\mathbf{HL}\}_k \mathbf{P}_w^{-1} \{\mathbf{HL}\}_k^T + \mathbf{R}_k)^{-1} (\mathbf{L}_k \mathbf{P}_w^{-1} \{\mathbf{HL}\}_k^T)^T \\ &= \mathbf{L}_k (\mathbf{P}_w^{-1} - \mathbf{P}_w^{-1} \{\mathbf{HL}\}_k^T (\{\mathbf{HL}\}_k \mathbf{P}_w^{-1} \{\mathbf{HL}\}_k^T + \mathbf{R}_k)^{-1} \{\mathbf{HL}\}_k \mathbf{P}_w^{-1}) \mathbf{L}_k^T + \mathbf{Q}_k \\ &= \mathbf{L}_k (\mathbf{P}_w + \{\mathbf{HL}\}_k^T \mathbf{R}_k^{-1} \{\mathbf{HL}\}_k)^{-1} \mathbf{L}_k^T + \mathbf{Q}_k. \end{aligned} \quad (6.2.40)$$

At the last step, we apply the Woodbury matrix-inversion lemma which states

Lemma 6.2.1 (Woodbury matrix-inversion lemma). *Let $\mathbf{M}_1, \mathbf{M}_{12}, \mathbf{M}_{21}, \mathbf{M}_2$ be matrices with $\mathbf{M}_1, \mathbf{M}_2$ and $\mathbf{M}_2 - \mathbf{M}_{21} \mathbf{M}_1^{-1} \mathbf{M}_{12}$ invertible, then $\mathbf{M}_1 - \mathbf{M}_{12} \mathbf{M}_2^{-1} \mathbf{M}_{21}$ is invertible*

and verifies

$$(\mathbf{M}_1 - \mathbf{M}_{12}\mathbf{M}_2^{-1}\mathbf{M}_{21})^{-1} = \mathbf{M}_1^{-1} + \mathbf{M}_1^{-1}\mathbf{M}_{12}(\mathbf{M}_2 - \mathbf{M}_{21}\mathbf{M}_1^{-1}\mathbf{M}_{12})^{-1}\mathbf{M}_{21}\mathbf{M}_1^{-1}. \quad (6.2.41)$$

Then we define \mathbf{U}_k as

$$\mathbf{U}_k = \mathbf{P}_w + \{\mathbf{HL}\}_k^T \mathbf{R}_k^{-1} \{\mathbf{HL}\}_k \quad (6.2.42)$$

obtaining a reduced expression for \mathbf{P}_k^+ as

$$\mathbf{P}_k^+ = \mathbf{L}_k \mathbf{U}_k^{-1} \mathbf{L}_k^T + \mathbf{Q}_k. \quad (6.2.43)$$

Also, \mathbf{K}_k is rewritten in terms of the decomposed matrices as follows

$$\begin{aligned} \mathbf{K}_k &= \mathbf{P}_{XZ,k} \mathbf{P}_{Z,k}^{-1} \\ &= \mathbf{L}_k \mathbf{P}_w^{-1} \{\mathbf{HL}\}_k^T \left(\{\mathbf{HL}\}_k \mathbf{P}_w^{-1} \{\mathbf{HL}\}_k^T + \mathbf{R}_k \right)^{-1} \\ &= \mathbf{L}_k \mathbf{U}_k^{-1} \mathbf{U}_k \mathbf{P}_w^{-1} \{\mathbf{HL}\}_k^T \left(\{\mathbf{HL}\}_k \mathbf{P}_w^{-1} \{\mathbf{HL}\}_k^T + \mathbf{R}_k \right)^{-1} \\ &= \mathbf{L}_k \mathbf{U}_k^{-1} \left(\mathbf{P}_w + \{\mathbf{HL}\}_k^T \mathbf{R}_k^{-1} \{\mathbf{HL}\}_k \right) \mathbf{P}_w^{-1} \{\mathbf{HL}\}_k^T \left(\{\mathbf{HL}\}_k \mathbf{P}_w^{-1} \{\mathbf{HL}\}_k^T + \mathbf{R}_k \right)^{-1} \\ &= \mathbf{L}_k \mathbf{U}_k^{-1} \left(\{\mathbf{HL}\}_k^T + \{\mathbf{HL}\}_k^T \mathbf{R}_k^{-1} \{\mathbf{HL}\}_k \mathbf{P}_w^{-1} \{\mathbf{HL}\}_k^T \right) \left(\{\mathbf{HL}\}_k \mathbf{P}_w^{-1} \{\mathbf{HL}\}_k^T + \mathbf{R}_k \right)^{-1} \\ &= \mathbf{L}_k \mathbf{U}_k^{-1} \{\mathbf{HL}\}_k^T \mathbf{R}_k^{-1} \left(\mathbf{R}_k + \{\mathbf{HL}\}_k \mathbf{P}_w^{-1} \{\mathbf{HL}\}_k^T \right) \left(\{\mathbf{HL}\}_k \mathbf{P}_w^{-1} \{\mathbf{HL}\}_k^T + \mathbf{R}_k \right)^{-1} \\ &= \mathbf{L}_k \mathbf{U}_k^{-1} \{\mathbf{HL}\}_k^T \mathbf{R}_k^{-1}. \end{aligned} \quad (6.2.44)$$

Using the expressions derived for all operators due to the decomposition $\mathbf{P} = \mathbf{LUL}^T$, we introduce the two step for the reduced-order unscented Kalman filter (ROUKF). The *prediction* step is obtained as

$$\begin{aligned} \hat{X}_{k-1}^{(i)} &= \hat{X}_{k-1}^+ + \mathbf{L}_{k-1}^X \sqrt{\mathbf{U}_{k-1}^{-1}} \sigma_i^{(n)}, \quad i = 1, \dots, M+1 \\ \hat{\theta}_{k-1}^{(i)} &= \hat{\theta}_{k-1}^+ + \mathbf{L}_{k-1}^\theta \sqrt{\mathbf{U}_{k-1}^{-1}} \sigma_i^{(n)}, \quad i = 1, \dots, M+1 \\ \begin{bmatrix} \hat{X}_k^{(i)} \\ \hat{\theta}_k^{(i)} \end{bmatrix} &= f \left(\begin{bmatrix} \hat{X}_{k-1}^{(i)} \\ \hat{\theta}_{k-1}^{(i)} \end{bmatrix}, t_{k-1} \right) \\ \hat{X}_k^- &= \sum_{i=1}^{N+1} w^{(i)} \hat{X}_k^{(i)} \\ \hat{\theta}_k^- &= \sum_{i=1}^{N+1} w^{(i)} \hat{\theta}_k^{(i)} \end{aligned} \quad (6.2.45)$$

For the correction step, we remove the sigma-points re-sampling for the sake of perfor-

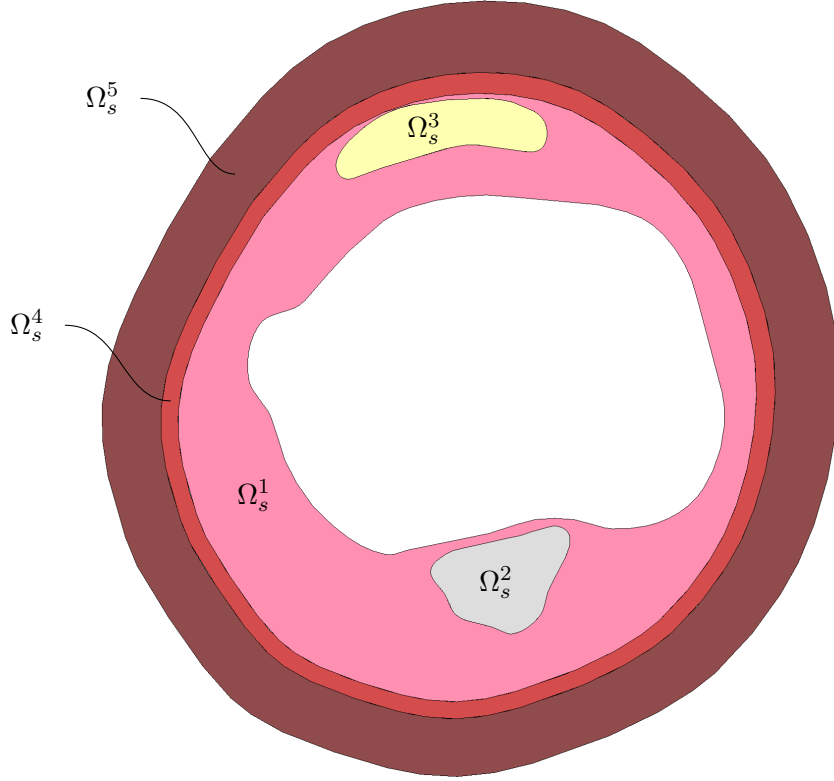


Figure 6.1: Synthetic artery domain composed of 5 regions.

mance. Thus, the *correction* step is obtained as

$$\begin{aligned}
\mathbf{L}_k^X &= \hat{\mathbf{X}}_k^{(*)} \mathbf{D}_w(\boldsymbol{\sigma}^{(*)})^T \\
\mathbf{L}_k^\theta &= \hat{\boldsymbol{\theta}}_k^{(*)} \mathbf{D}_w(\boldsymbol{\sigma}^{(*)})^T \\
\{\mathbf{HL}\}_k &= \hat{\mathbf{Z}}_k^{(*)} \mathbf{D}_w(\boldsymbol{\sigma}^{(*)})^T \\
\mathbf{U}_k &= \mathbf{P}_w + \{\mathbf{HL}\}_k^T \mathbf{R}_k^{-1} \{\mathbf{HL}\}_k \\
\hat{\mathbf{X}}_k^+ &= \hat{\mathbf{X}}_k^- + \mathbf{L}_k^X \mathbf{U}_k^{-1} \{\mathbf{HL}\}_k^T \mathbf{R}_k^{-1} \left(Z_k - \sum_{i=1}^{M+1} w^{(i)} \hat{Z}_k^{(i)} \right) \\
\hat{\boldsymbol{\theta}}_k^+ &= \hat{\boldsymbol{\theta}}_k^- + \mathbf{L}_k^\theta \mathbf{U}_k^{-1} \{\mathbf{HL}\}_k^T \mathbf{R}_k^{-1} \left(Z_k - \sum_{i=1}^{M+1} w^{(i)} \hat{Z}_k^{(i)} \right).
\end{aligned} \tag{6.2.46}$$

Note that we avoid the computation of \mathbf{P}^+ , \mathbf{P}^- and \mathbf{K}_k matrices, instead we compute them partially by using their decomposition in terms of \mathbf{L}_k , \mathbf{U}_k^{-1} , $\{\mathbf{HL}\}_k$ and \mathbf{R}_k . As result we operate with smaller matrices yielding a efficient (in terms of memory usage) and faster method.

6.3 Biomechanical parameter estimation with ROUKF

Using the displacement field \mathbf{u}^{OF} obtained using the optical flow technique as explained in Chapter 4, the mechanical models presented in Chapter 5 and the ROUKF method described in the previous section, we define the constitutive parameter estimation problem for the arterial wall.

Let us define the domain Ω_s with boundary $\partial\Omega_s = \partial\Omega_s^W \cup \partial\Omega_s^E \cup \partial\Omega_s^A$ described in Section 5.3 (see Figure 5.10) and a given domain partition $\Omega_s = \bigcup_{i=1}^R \Omega_s^i$ of R disjoint

regions, each one with its own constitutive parameters (see Figure 6.1). We also know the loads $\mathbf{t}_s^{W,n}$ and the displacement fields \mathbf{u}_s^{OF} (obtained by optical flow techniques) at S different times. Since our problem is static, the time instants in the context of the Kalman filter correspond to the different load levels. Hereafter we refer simply to time instants, but the association with the load level must be kept in mind. By using the mechanical models presented in Chapter 5, we want to estimate the constitutive parameters such that

$$\theta = \arg \min_{\hat{\theta}} \sum_{s=1}^S \|\mathbf{u}_s^{\text{M}}(\hat{\theta}) - \mathbf{u}_s^{\text{OF}}\|_{L_2}^2 \quad (6.3.1)$$

where $\mathbf{u}_s^{\text{M}}(\hat{\theta})$ is the displacement field at the time s obtained by solving the preload and forward problems (described in Section 5.3) with the constitutive parameters $\hat{\theta}$.

This parameter identification problem can be rewritten as the discrete dynamic nonlinear system presented as follows

$$\begin{aligned} X_k^a &= f(X_{k-1}^a, t_{k-1}) + W_k \\ Z_k &= h(X_k, t_k) + V_k \end{aligned} \quad (6.3.2)$$

where X_k is the augmented state vector

$$X_k^a = \begin{bmatrix} \mathbf{u}_{t_k}(x_1) \\ \vdots \\ \mathbf{u}_{t_k}(x_N) \\ \lambda_{t_k}(x_1) \\ \vdots \\ \lambda_{t_k}(x_N) \\ \theta_1 \\ \vdots \\ \theta_M \end{bmatrix} \quad (6.3.3)$$

that contains the displacements \mathbf{u}_{t_k} and pressure λ_{t_k} fields along the vessel wall, and the constitutive parameters of all regions of the domain θ ; $f(X_k^a, t_k)$ is the operator that sequentially solves the preload and forward problem for parameters and initial state conditions in X_k at the time t_k ; W_k are the model errors at the k -th step; $h(X_k^a, t_k) = \mathbf{H}X_k^a$ is a linear operator represented by the block matrix

$$\mathbf{H} = \begin{bmatrix} \mathbf{I}_{N \times N} & \mathbf{0}_{N \times (N+M)} \\ \mathbf{0}_{(N+M) \times N} & \mathbf{0}_{(N+M) \times (N+M)} \end{bmatrix} \quad (6.3.4)$$

where \mathbf{I} is the identity matrix and the sub-indexes of the matrices indicate their size as rows by columns; Z_k is optical flow observation described by the column vector

$$Z_k = \begin{bmatrix} \tilde{\mathbf{u}}_{t_k}^{\text{OF}}(x_1) \\ \vdots \\ \tilde{\mathbf{u}}_{t_k}^{\text{OF}}(x_N) \\ \mathbf{0}_{N+M} \end{bmatrix} \quad (6.3.5)$$

where $\tilde{\mathbf{u}}_{t_k}^{\text{OF}}(x_i)$ is the interpolated value at the spatial position x_i and time t_k of the displacement field given by the optical flow technique; and V_k is the vector of optical flow and interpolation errors for observation vector Z_k .

As presented in Section 6.2.4, we can apply ROUKF to obtain an estimate $\hat{\theta}$ of the

parameters θ . First, we must provide the initial conditions for \mathbf{P}_0^+ , \mathbf{Q}_0 , \mathbf{R}_0 and X_0^a . We will neglect the model error, then $\mathbf{Q}_0 = \mathbf{0}$. To initialize \mathbf{R}_0 , we assume an error variance for the displacement field estimated by optical flow, σ_{OF} , and define the diagonal matrix $\mathbf{R}_0 = \sigma_{\text{OF}} \mathbf{I}$. The states $\mathbf{u}_{t_k}(x_i)$ and $\lambda_{t_k}(x_i)$ will impact the stability and the computational time for solving $f(X_k^a, t_k)$ operator. We choose to initialize $\mathbf{u}_{t_0}(x_i) = \mathbf{0}$ and $\lambda_{t_0}(x_i) = 0$. Lastly, we assume initial parameters $\hat{\theta}_i$ with an error variance of $\sigma_{\hat{\theta}_i}$ from its true value. Thus, we define

$$\begin{aligned} X_0^a &= \begin{bmatrix} 0_{2N} \\ \hat{\theta}_1 \\ \vdots \\ \hat{\theta}_M \end{bmatrix} \\ \mathbf{P}_0^+ &= \mathbf{L}_0 \mathbf{U}_0^{-1} \mathbf{L}_0^T \\ \mathbf{L}_0 &= \begin{bmatrix} \mathbf{0}_{2N \times M} \\ \mathbf{I}_{M \times M} \end{bmatrix} \\ \mathbf{U}_0^{-1} &= \begin{bmatrix} \sigma_{\hat{\theta}_0} & \cdots & 0 \\ \vdots & & \vdots \\ 0 & \cdots & \sigma_{\hat{\theta}_M} \end{bmatrix}. \end{aligned} \tag{6.3.6}$$

In Section 6.3.2, we analyze the appropriate range of values for $\hat{\theta}_i$ and $\sigma_{\hat{\theta}_i}$ based on the experimental constitutive parameters reported in Section 5.5 for the different coronary tissues. At this point, the only uncertainty is how to obtain the partition of the domain Ω_s from an IVUS image, which is address in the following section.

6.3.1 Initialization and tissue regions delimitation

In the present approach, we assume that the regions containing different materials can be identified a priori. The main goal is to split the domain Ω_s in a partition such that tissues with different constitutive behavior remain in regions with different parameters. By using regions with homogeneous tissue composition, we infer the tissue constitution from the estimated parameters $\hat{\theta}$ based on the experimental fitting for these models presented in Section 5.5. We present three alternative criteria to segment the domain Ω_s in subregions of potentially different tissues: an intensity approach, a strain approach and a virtual histology approach. In the first two approaches, we derive a scalar field from the IVUS image in which tissues of similar compositions have a close range of values. Then, we use a K-Means clustering over the scalar field to create the partition.

The intensity approach uses the IVUS image intensities as scalar field. In fact, the intensity represents the pressure amplitude of the acoustic echo reflected by the tissues, which is proportional to the strain and density of the tissue. As strains (disregarding dissipation effects) and density are expected to be homogeneous across the interior of a tissue, it is acceptable to assume that a specific tissue presents a close range of intensities. Here, we choose to use a denoised version of the image using the optimal parameters in the sense of homogeneity (see Sections 4.2.2 and 4.4.2.2), to minimize the intensity distortion due to speckle (from the acquisition) and smoothing (from the denoising). In Figure 6.2, it is shown the resulting partition using K-Means with 3, 5 and 7 bins.

The strain approach exploits the estimated optical flow \mathbf{u}_s^{OF} to compute the first gradient tensor $\varepsilon_s^{\text{OF}} = \nabla \mathbf{u}_s^{\text{OF}}$. Then, we use the Frobenius norm of the $\nabla \mathbf{u}_s^{\text{OF}}$ to derive a single modulus field that will be employed as input for the K-Means clustering. The denoising is performed with the optimal parameters in the sense of homogeneity and the optical flow is computed with parameters $\alpha = 0.01$, $\beta = 0.5$, $\rho = 2$, $\kappa^2 = 0.5$ and $M = 4$

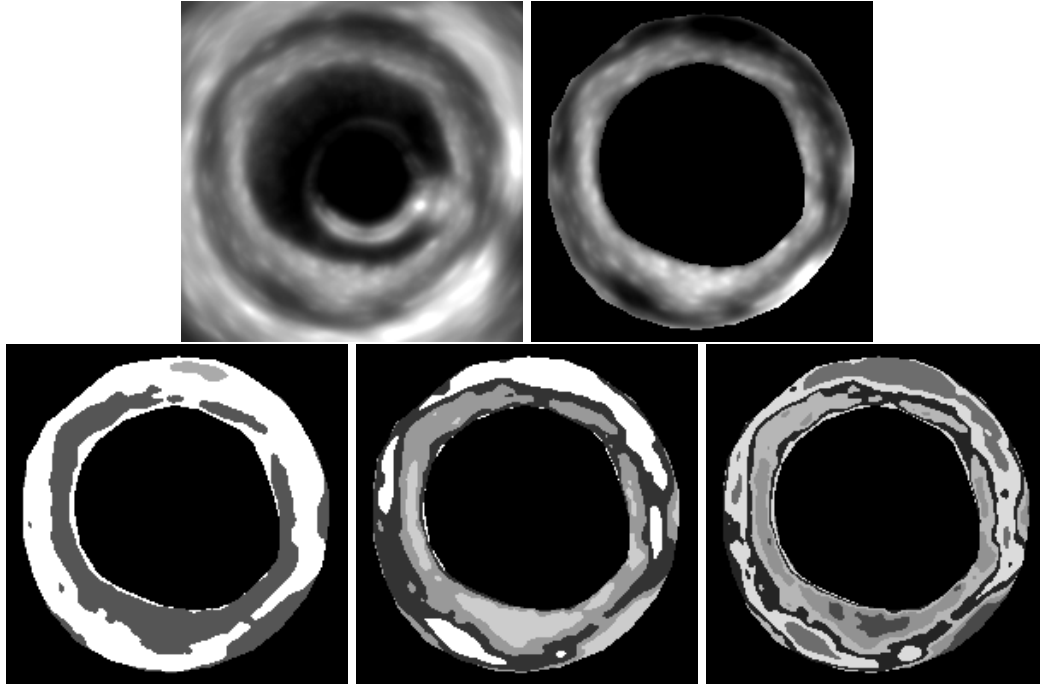


Figure 6.2: K-Means partition based on the IVUS intensity: (left-top) denoised IVUS image, (right-top) segmented vessel wall, (left-bottom) partition with 3 bins, (central-bottom) 5 bins and (right-bottom) 7 bins.

(the same as in 4.22). In Figure 6.3, it is shown the partition using K-Means with 3, 5 and 7 bins.

A third approach, not explored in this thesis, would be the use of virtual histologies (e.g., VH-IVUS, IB-IVUS or iMap). Such data can be obtained from the sonograph after the IVUS acquisition and has been validated against ex-vivo histology, see [115] and reference therein. One drawback of those methods is that only 4 regions can be detected and they may present heterogeneous constitutive parameters, e.g., two areas with fibrotic dense tissue may present a different elasticity (see HyFb in Table 5.1 whose range is quite variable), although the classifier of these strategies may deliver the same region for these materials. In the intensity and strain approaches, this problem can be diminished by increasing the number of bins. Even though, these aspects will be studied in future works.

Note that partitions in Figures 6.2 and 6.3 are qualitatively different with exception of few structures (e.g. the abluminal regions at the middle-top or at the left-bottom). Thus, it is uncertain yet which partition delivers the most reliable assessment, and, moreover, the target solution could eventually rely on a completely different unknown partition. This implies that the partition may change over the optimization process. This is beyond the scope of the present work and will be addressed in the future.

6.3.2 ROUKF parameter setup

Let us define a homogeneous ring-shaped domain Ω_s with the neo-hookean constitutive behavior presented in Section 5.4.1 (see equation (5.4.1)). The inner and outer radius of the ring are 2mm and 2.71mm, respectively. The size and proportions are chosen to approximate an idealized coronary artery. Loads of $\mathbf{t}^{W,n} = 80 \text{ mmHg } \mathbf{n}$ and $\mathbf{t}^{W,n} = 120 \text{ mmHg } \mathbf{n}$ are applied in the inner surface for the preload and forward problem, respectively, simulating a normotensive scenario and tethering tractions $\mathbf{t}_s^{A,i}$ such that an axial stretch of 10% is imposed at the non-physical boundary. The forward operator f , which amounts

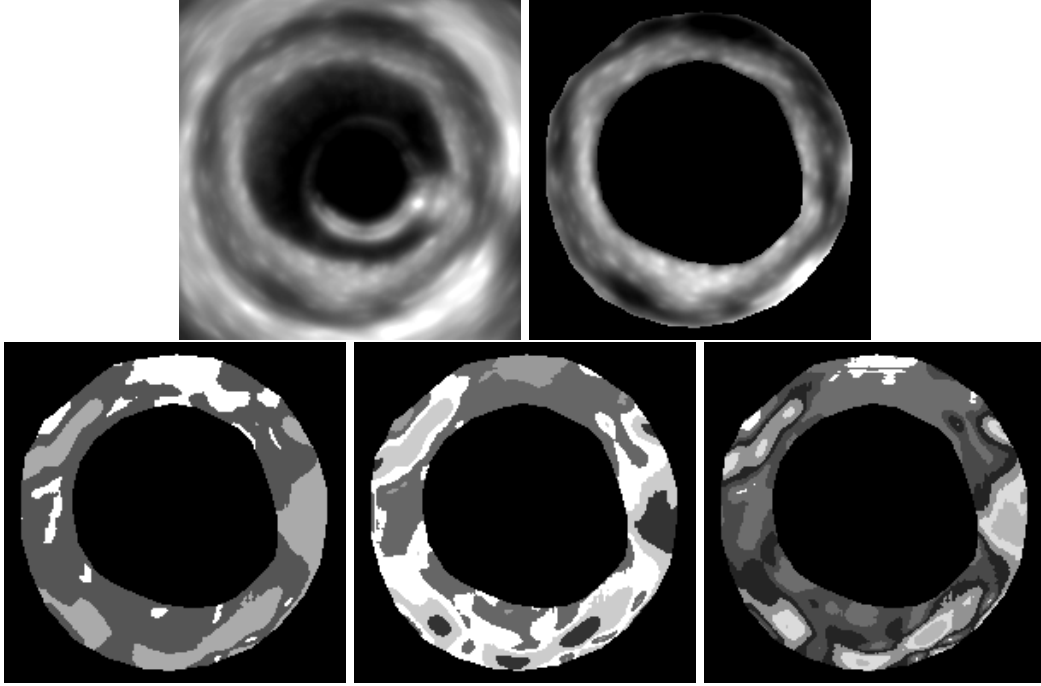


Figure 6.3: K-Means partition based on $\|\nabla \mathbf{u}_s^{\text{OF}}\|_F$: (left-top) denoised IVUS image, (right-top) segmented vessel wall, (left-bottom) partition with 3 bins, (central-bottom) 5 bins and (right-bottom) 7 bins. The parameters for denoising and optical flow are described in 4.22.

to solve the mechanical problems seen in Chapter 5 (see equations (5.3.7), (5.3.8), (5.3.10) and (5.3.11)), is solved with an iterative scheme where at each iteration a Newton-Raphson linearization procedure is applied (further details in [41]). The iterative scheme finishes when $\|\mathbf{u}_s^{m+1} - \mathbf{u}_s^m\|_{L_2} < 10^{-3}$ mm and $\|\lambda_s^{n+1} - \lambda_s^n\|_{L_2} < 10^{-1}$ mmHg. We choose these convergence criteria because they yield a similar precision than the optical flow processing applied to IVUS or OCT images. To avoid negative values for the constitutive parameter c in the neo-hookean model, we define it as $c = 2^{\hat{\theta}}$ (this approach was introduced in [34]) allowing $\hat{\theta}$ to vary in \mathbb{R} (as occurs in the presented formulation (6.2.46) and (6.2.45)) without delivering invalid values for c .²

Using this setting, we create an *in-silico* experiment to analyze: i) the sensitivity of the parameter estimates $\hat{\theta}$ with respect to the σ_Z (the observations uncertainty, previously referred to as σ_{OF}); and ii) the sensitivity of the parameter estimates $\hat{\theta}$ with respect to the σ_θ (the estimate uncertainty). Thus, we generate the observations by computing $Z = h(f(X^t))$ where $X^t = [\mathbf{0}_{2N}, \theta^t]$ is the true augmented state vector with the solution parameters θ^t for the experiment. In this particular case, the domain is homogeneous and the constitutive model has only one parameter (c), then, we only have one parameter to estimate.

To analyze the sensitivity of $\hat{\theta}$ with respect to the observation uncertainty σ_Z , we perform the estimation of the parameter assuming different values σ_Z , ranging from 10^{-1} to 10^{-5} mm. Also, we use three different materials for the ring: cellular fibrotic tissue ($2^{\theta^t} = 5 \cdot 10^5 Pa$), lipidic tissue ($2^{\theta^t} = 1 \cdot 10^5 Pa$) and calcified tissue ($2^{\theta^t} = 4 \cdot 10^6 Pa$). The es-

²The reparametrization $2^{\hat{\theta}}$ modifies the classic statistical meaning of the mean and covariance. We propagate mean and covariance of θ which is not the same as to propagate the mean and covariance of c . Nevertheless, there is a similar statistical meaning for c using these descriptors in an exponential space of coordinates. For example, we must understand the a covariance of $\sigma = 1$ as the same probability of c being half or twice its initial value.

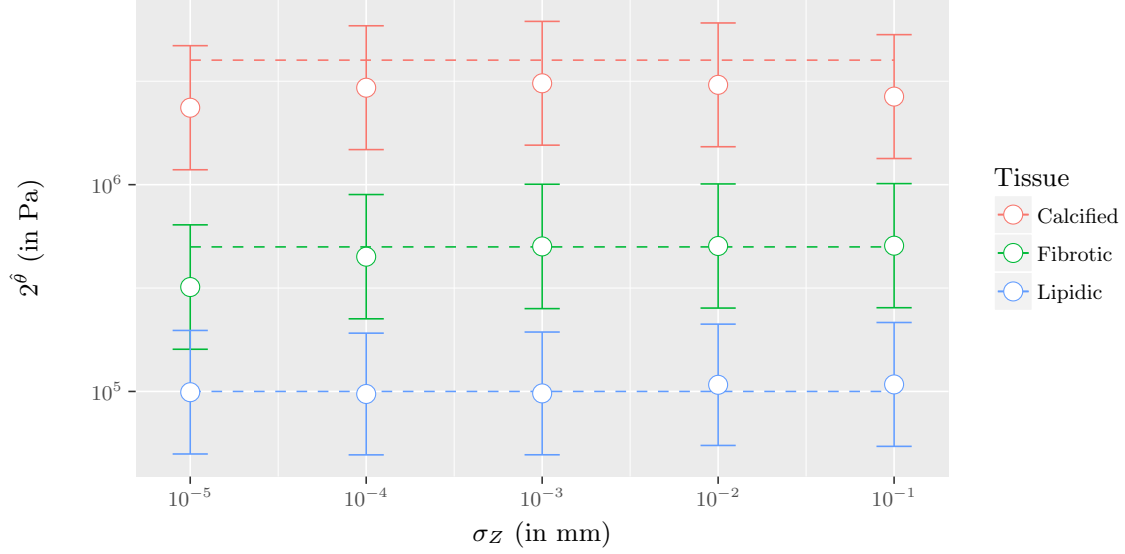


Figure 6.4: Kalman estimate for the experiment of the 1-material ring using observation uncertainties of $\sigma_Z = 10^i$, $i = -5, \dots, -1$ and fixing the parameter uncertainty $\sigma_\theta = 2$. Each dot corresponds to the outcome of a Kalman estimation (after 200 iterations or relative error minor than 10^{-2}). The color indicates the material of the ring at each experiment, the dashed line is 2^{θ^t} value and the whiskers denote the parameter uncertainty computed as $2^{\hat{\theta} \pm \sqrt{\text{diag}(\mathbf{U}^{-1})}}$.

timination of the Kalman filter for the 15 cases is presented in Figure 6.4. The results showed that in all cases the parameter uncertainty interval $\left[2^{\hat{\theta} - \sqrt{\text{diag}(\mathbf{U}^{-1})}}; 2^{\hat{\theta} + \sqrt{\text{diag}(\mathbf{U}^{-1})}}\right]$ contains the true parameter value 2^{θ^t} . Even though, a closer estimate across the three materials is obtained for $\sigma_Z = 10^{-3}$ mm which seems reasonable as it is the precision of the displacements delivered by operator f . We see the larger errors are for the calcified tissue which is the stiffest one and, consequently, the less deformed case (the displacements range is within $[7.76 \cdot 10^{-3}, 8.73 \cdot 10^{-3}]$ mm). Given that the strains are in the same order as the forward operator precision it is expected a poor estimate of the parameter.

In relation with the filter convergence, we observed that as the uncertainty in the observations decreases, the method converges faster. In Figure 6.5, it is shown that as the σ_Z increases its value, the convergence is smoother and slower. Note that the estimator gain matrix is computed as $\mathbf{K}_k = \mathbf{L}_k^\theta \mathbf{U}_k^{-1} \{\mathbf{HL}\}_k^T \mathbf{R}_k^{-1}$ and the only operator that varies in the first iteration of the presented cases is \mathbf{R}_0^{-1} . As the spectral radius of \mathbf{R}_0^{-1} diminishes as σ_Z increases then \mathbf{K}_0 spectral radius diminishes as well, yielding a smaller correction of $\hat{\theta}_k^+$ as presented in the plot. At the same time, since \mathbf{P}_w is constant, the update of $\mathbf{U}_k = \mathbf{P}_w + \{\mathbf{HL}\}_k^T \mathbf{R}_k^{-1} \{\mathbf{HL}\}_k$ is damped by \mathbf{R}_k . This damping effect is evidenced in the evolution of the parameter uncertainty intervals plotted in Figure 6.5. In statistical terms, the lack of confidence in the new observations leads us to reducing its weight at the correction step.

We performed an analogous analysis to study the sensitivity of $\hat{\theta}$ with respect to the parameter uncertainty σ_θ . The uncertainty levels for σ_θ were from 0.25 to 4 and we repeated the experiment for the same three different ring materials (fibrotic, lipidic and calcified tissues). The results showed that the bigger σ_θ , the wider the search space for the parameter, and the faster the method converges when the initial value is off the initial parameter uncertainty interval (see Figures 6.6 and 6.7). On the other hand, high values of

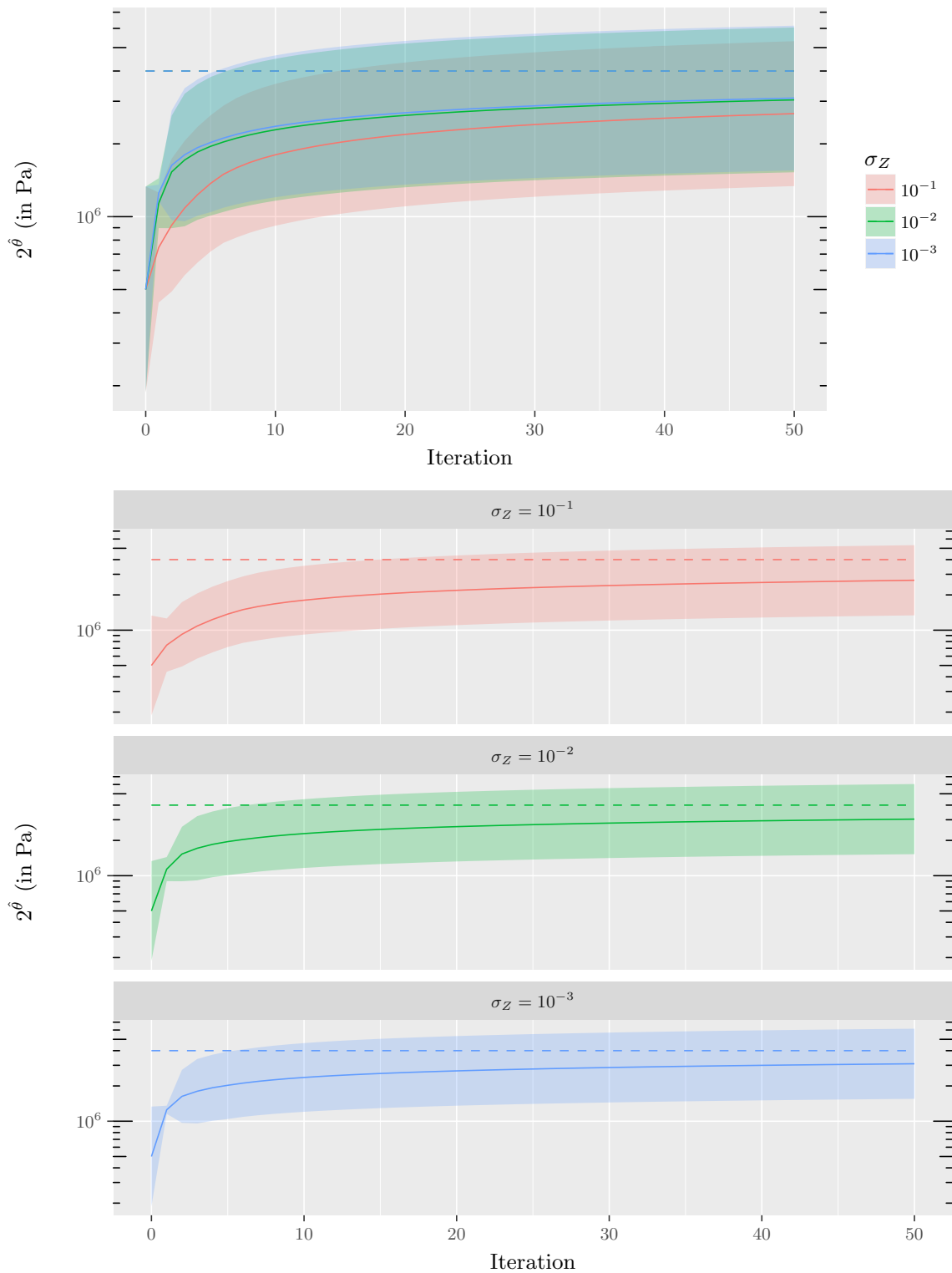


Figure 6.5: Convergence of the Kalman filter for the experiment of the 1-material ring using observation uncertainties of $\sigma_Z = 10^i$, $i = -3, -2, -1$, fixing the parameter uncertainty $\sigma_\theta = 2$ and $2^{\theta^t} = 4 \cdot 10^{-6}$: (top) overlay of the 3 cases; (bottom) each case separately. The dashed line is 2^{θ^t} value, the solid line the Kalman filter estimate $\hat{\theta}$ and the colored ribbon denotes the parameter uncertainty interval $\left[2^{\hat{\theta}-\sqrt{\text{diag}(\mathbf{U}^{-1})}}, 2^{\hat{\theta}+\sqrt{\text{diag}(\mathbf{U}^{-1})}}\right]$.

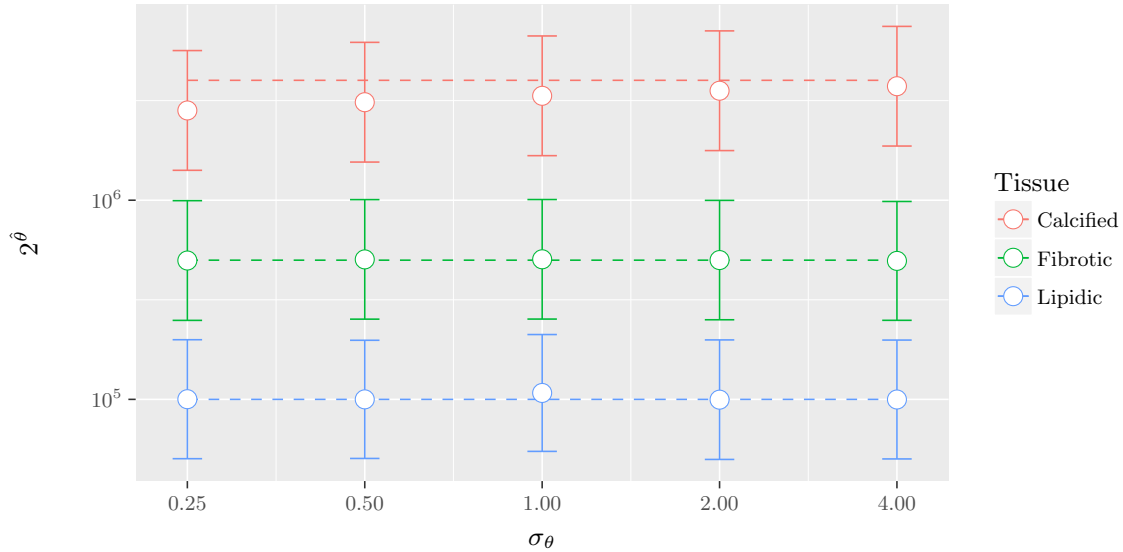


Figure 6.6: Kalman estimate for the experiment of the 1-material ring using parameter uncertainties of $\sigma_\theta = 0.25, 0.5, 1, 2, 4$ and fixing the observation uncertainty $\sigma_Z = 10^{-2}$. Each dot corresponds to the outcome of a Kalman estimation (after 200 iterations or relative error minor than 10^{-2}). The color indicates the material of the ring at each experiment, the dashed line is 2^{θ^t} value and the whiskers denote the parameter uncertainty computed as $2^{\theta \pm \sqrt{\text{diag}(\mathbf{U}^{-1})}}$.

σ_θ may cause an overshooting in the estimation and a slower convergence. In this scenario, the reparametrization deteriorates the convergence even more. The reparametrization imposes an estimation bias to stiffer values due to the fact that displacements are less sensitive with respect to small variations in stiffer than softer materials. Then, the mean observation error (used as correction term in (6.2.46)) is biased closer to the sigma points associated with stiffer materials. This is clearly evidenced in Figure 6.8, where the initial overshooting delays the estimation of the parameter.

Thus, we found a good agreement in term of accuracy and convergence for parameters $\sigma_Z = 10^{-3}$ mm and $\sigma_\theta = 4$. These parameters identify clearly the three different kinds of tissues in this idealized problem. Also, the observations generated *in-silico* present an accuracy of similar order than the obtained (assuming no error carried by the optical flow) through the IVUS image processing. For these reasons, we choose these parameters in the next estimation process. Due to the tendency of the error introduced by the optical flow, we may relax σ_Z for the *in-vivo* estimations.

6.3.3 Media and adventitia modeling

In the previous section, we successfully estimated the constitutive parameters for an isotropic neo-hookean material as described in Section 5.4.1. Such materials correspond to intimal pathological tissues that appear as product of inflammation and remodeling processes. Now, we focus on the materials in the tunicas media and adventitia, which present an anisotropic behavior described by the constitutive equation introduced in equation (5.4.4), see Section 5.4.2. As we are interested only in the estimation of the atherosclerotic plaque composition, we model the tunicas media and adventitia as a single layer to reduce the computational effort and amount of constitutive parameters. Particularly, IVUS images do not deliver a clear delimitation of the adventitia and the poor signal in

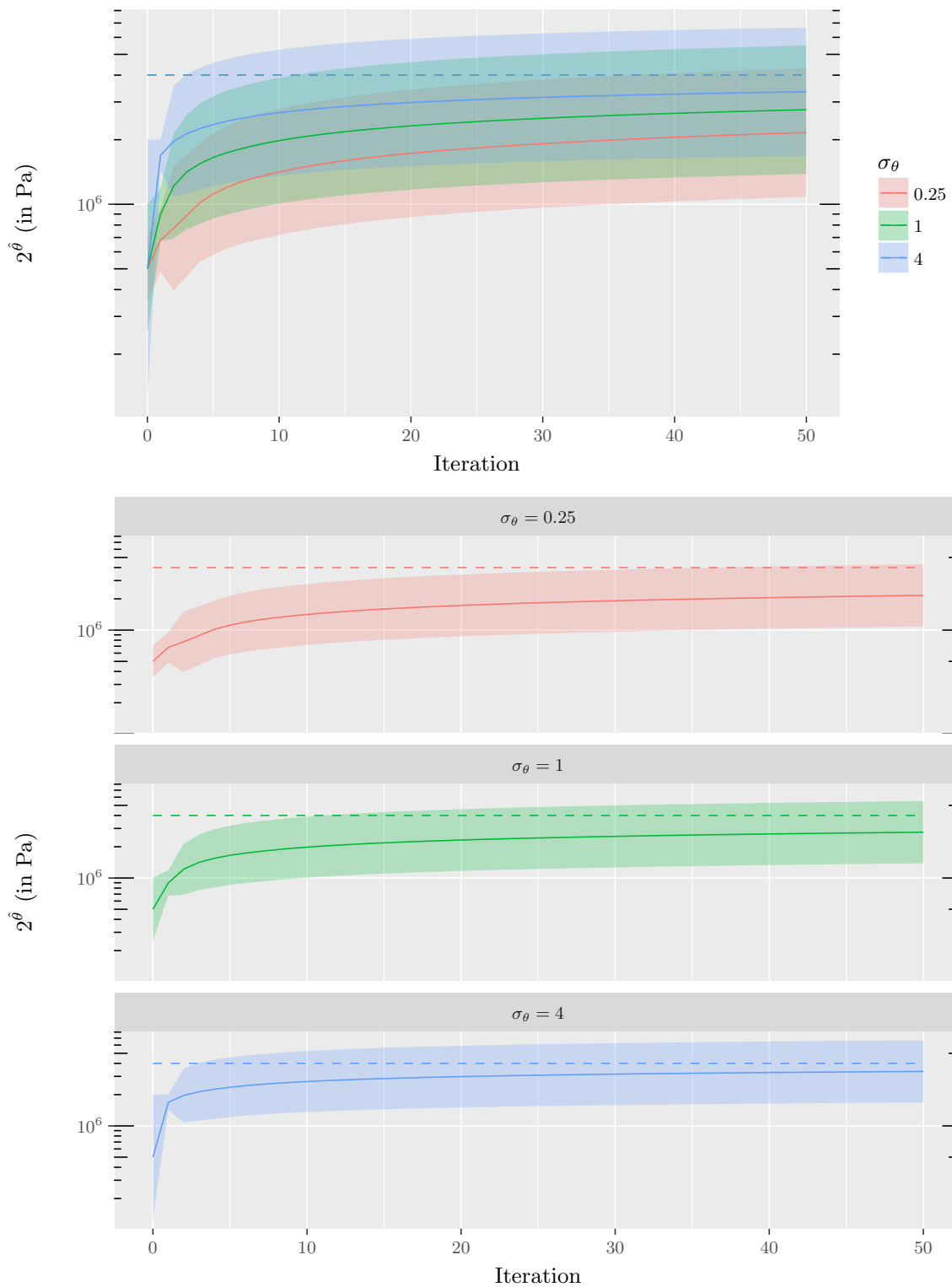


Figure 6.7: Convergence of the Kalman filter for the experiment of the 1-material ring using parameter uncertainties of $\sigma_\theta = 0.25, 1, 4$ and fixing the observation uncertainty $\sigma_Z = 10^{-2}$ and $2^{\theta^t} = 4 \cdot 10^6$: (top) overlay of the 3 cases; (bottom) each case separately. The dashed line is 2^{θ^t} value, the solid line the Kalman filter estimate $\hat{\theta}$ and the colored ribbon denotes the parameter uncertainty interval $[2^{\hat{\theta} - \sqrt{\text{diag}(\mathbf{U}^{-1})}}, 2^{\hat{\theta} + \sqrt{\text{diag}(\mathbf{U}^{-1})}}]$.

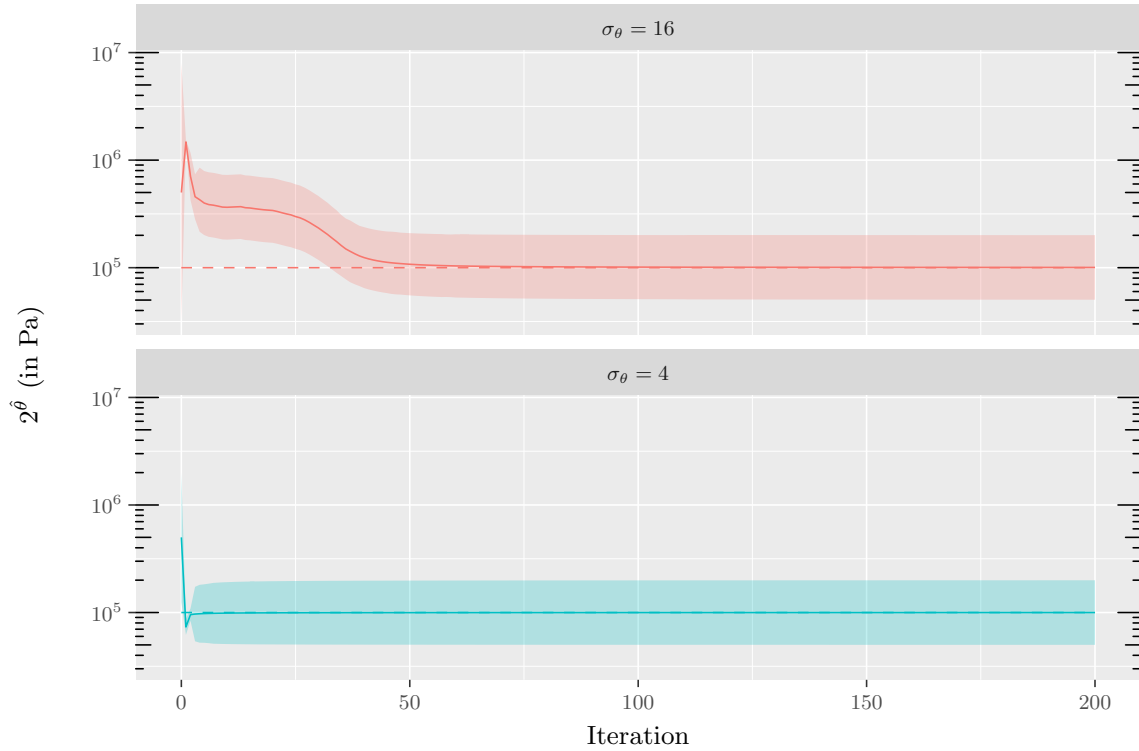


Figure 6.8: Convergence of the Kalman filter for the experiment of the 1-material ring using $\sigma_\theta = 4, 16$, $\sigma_Z = 10^{-2}$ and $2^{\theta^t} = 1 \cdot 10^5$. The dashed line is 2^{θ^t} value, the solid line the Kalman filter estimate $\hat{\theta}$ and the colored ribbon denotes the parameter uncertainty interval $\left[2^{\hat{\theta}-\sqrt{\text{diag}(\mathbf{U}^{-1})}}, 2^{\hat{\theta}+\sqrt{\text{diag}(\mathbf{U}^{-1})}}\right]$.

such region may yield a non-representative or an incomplete displacement field estimation. Furthermore, the nonlinear stress-stretch relation of these layers is very accentuated due to low isotropic and stiff fiber contributions to bear the intimal tractions. This forces the use regularization terms in the preload and forward problem formulated in Section 5.3 (see [22] and [41] for insights of the regularization terms) to stabilize the numerical scheme at expenses of slower convergence.

For such reasons, we choose to construct two synthetic models with fixed parameters to approximate the contributions of such layers and a synthetic model where only constitutive coefficients c and k_1 are optimized using the ROUKF. Note that in the later model, we optimize only the isotropic and anisotropic contribution weights. We choose to optimize these parameters because less tuning of the regularization parameters is required when they are altered during the ROUKF process. Also, the optimization of all constitutive parameters may be unnecessary because of the geometrical uncertainty of this layer on in-vivo studies. Thus, geometry and coefficients of ex-vivo specimens reported in [145] are used as reference. As the tunica media narrows to 0.08mm in average during the atherosclerotic plaque progression (while the adventitia maintains a 0.4mm thickness) and is notoriously more elastic than the adventitia, we choose to neglect its contribution. Thus, we approximate the whole layer as adventitia tissue which bears most of the load. We use the two sets of constitutive parameters described in Table 6.1.

Media/Adventitia model	c (kPa)	k_1 (kPa)	k_2	θ	ρ	λ_0
Soft	4.5	37.06	48.36	65.8	0.4	1
Stiff	29.86	119.25	213.81	53.4	0.6	1
Optimized	–	–	213.81	53.4	0.6	1

Table 6.1: Experimental coefficients reported in [145] for patients VIII (soft model) and X (stiff and optimized model). The optimized model referred to the stiff model where parameters c and k_1 are optimized by the reduced order unscented Kalman filter.

6.4 Cases of study

We study three cases with increasing complexity of the model:

1. **Synthetic idealized artery:** We assume an ideal geometry of an arterial cross section with two concentric layers, modeling the media/adventitia and the intima layer, respectively. An in-silico displacement field is obtained by solving the preload and forward problems. Using such displacements as observations for the ROUKF, we analyze: i) the impact of alternative media/adventitia models; and ii) the capabilities of the ROUKF method to identify the constitutive parameters for different homogeneous intimal tissues.
2. **Synthetic artery with in-vivo geometry:** We segment the media and intima from an IVUS image to create an arterial realistic domain. In this domain, we define a distribution of tissues within the vessel wall and, as before, create an in-silico displacement field solving the preload and forward problems. Finally, we estimate the constitutive parameters with the ROUKF for a normotensive and a hypertensive scenario. In this scenario, we analyze the capabilities of ROUKF to estimate the constitutive parameters in real geometries with heterogeneous composition (although the tissue distribution is synthetic) under physiological ranges of pressure.
3. **In-vivo artery:** We segment the media and intima from an IVUS image acquired at the end-diastolic phase. Differently from the previous case, we split the obtained domain with the K-Means strategies presented in Section 6.3.1. Additionally, we estimate the optical flow between the end-diastolic image (the one used for segmentation) and the systolic image at the same transversal position of the vessel (the image that matches such location is obtained using the gating and registration strategies described in Chapters 2 and 3). Using this in-vivo geometry, we estimate the constitutive parameter of the tissues and infer the vessel composition. This corresponds to a truly in-vivo characterization of the arterial tissues.

6.4.1 Synthetic idealized artery

The idealized artery is a perfect ring with inner and outer radius of 2mm and 2.55mm, and a thickness of 0.04mm. The domain is split in two concentric layers, the inner layer with a radial thickness of 0.2mm models the intima while the outer layer with a radial thickness of 0.35mm models the media and adventitia. Loads of $\mathbf{t}^{W,n} = 80 \mathbf{n}$ mmHg and $\mathbf{t}^{W,n} = 120 \mathbf{n}$ mmHg are applied in the inner surface for the preload and forward problem, respectively, simulating a normotensive scenario and tethering tractions $\mathbf{t}_s^{A,i}$ such that an axial stretch of 10% is imposed at the non-physical boundary. Due to the intrinsic symmetry of the problem, we solve only a quarter of the domain (see Figure

Intimal tissue	Media/Adventitia model	2^{θ^t} (kPa)	$2^{\hat{\theta}}$ (kPa)		ε_c (%)
			Estimation	[LB,UB]	
Fibrotic	Soft	500	598.85	[302.21, 1186.68]	19.77%
Lipidic	Soft	100	179.86	[90.58, 357.16]	79.86%
Calcified	Soft	4000	3915.23	[1965.72, 7798.16]	2.12%
Fibrotic	Stiff	500	456.60	[230.36, 905.05]	8.68%
Lipidic	Stiff	100	56.88	[28.622, 113.043]	43.12%
Calcified	Stiff	4000	3327.88	[1672.70, 6620.89]	16.80%
Fibrotic	Optimized	500	632.42	[316.35, 1264.29]	26.48%
Lipidic	Optimized	100	102.98	[51.51, 105.88]	2.98%
Calcified	Optimized	4000	3937.52	[1984.28, 7813.46]	1.56%

Table 6.2: Estimate of intimal tissues using the soft, stiff and optimized models for the media/adventitia layer. The optimized model estimates the coefficients c and k_1 of the media/adventitia layer using reduced order unscented Kalman filter. The estimate $2^{\hat{\theta}}$ of the true parameter 2^{θ^t} is presented with its uncertainty interval $[LB,UB] = [2^{\hat{\theta}-\sqrt{\text{diag}(\mathbf{U}^{-1})}}; 2^{\hat{\theta}+\sqrt{\text{diag}(\mathbf{U}^{-1})}}]$. The relative error of the elasticity modulus is computed as $\varepsilon_c = (|2^{\theta^t} - 2^{\hat{\theta}}|)/2^{\theta^t}$. The observed displacement Z are generated using a media/adventitia model with coefficients $c = 15.8$ kPa, $k_1 = 25.36$ kPa, $k_2 = 67.85$, $\theta = 70.3^\circ$ and $\rho = 0.7$ (which is elastically a middle term between the soft and stiff models). The Kalman parameters for uncertainty were $\sigma_Z = 10^{-3}$ and $\sigma_\theta = 4$.

6.9) to save computation cost. Two non-physical boundaries appear as result of this simplification where homogeneous Dirichlet conditions are imposed to allow only radial displacements.

This idealized geometry is used to test the media/adventitia models. To be fair with the soft and stiff models, the in-silico displacements are generated with media/adventitia coefficients $c = 15.8$ kPa, $k_1 = 25.36$ kPa, $k_2 = 67.85$, $\theta = 70.3^\circ$ and $\rho = 0.7$, which are a middle term between the two models in terms of elastic response. These coefficients were taken from an ex-vivo specimen as well (see [145], Patient VI). Using such outer layer, three experiments were created each one with a different intimal tissue (with neo-hookean behavior): a fibrotic tissue with $c = 500$ kPa; a lipidic tissue with $c = 100$ kPa; and a calcified tissue with $c = 4000$ kPa. Thus, we estimate the parameters of the intimal tissue using only the in-silico displacements on the intima (reliable data that can potentially be extracted from IVUS). The main focus is to analyze the error in the estimate when using a stiffer, a softer or an optimized model for the media/adventitia. This allows to determine a range of confidence for the estimates made with each model when the media/adventitia coefficients are unknown.

The ROUKF estimation was performed using each of the three media/adventitia models for each of the three intimal tissue experiments. The error in terms of the c parameter, ε_c , (see Table 6.2) indicates that the best estimation for fibrotic tissue is obtained by the stiff model, while for lipidic and calcified tissues it is obtained by the optimized model. The mean error across the three experiments are 87.83, 252.88 and 65.96 kPa for the soft, stiff and optimized models, showing a close agreement between the optimized model and soft model. The relative error of the experiments also presented the optimized model as the most accurate solution, with less than 26.48% of error for all materials. Another interesting outcome from these experiments is the fact that the uncertainty interval always comprises the correct value of c without overlapping with the c value of other type of tissue. However, this is not enough to ensure that all the three

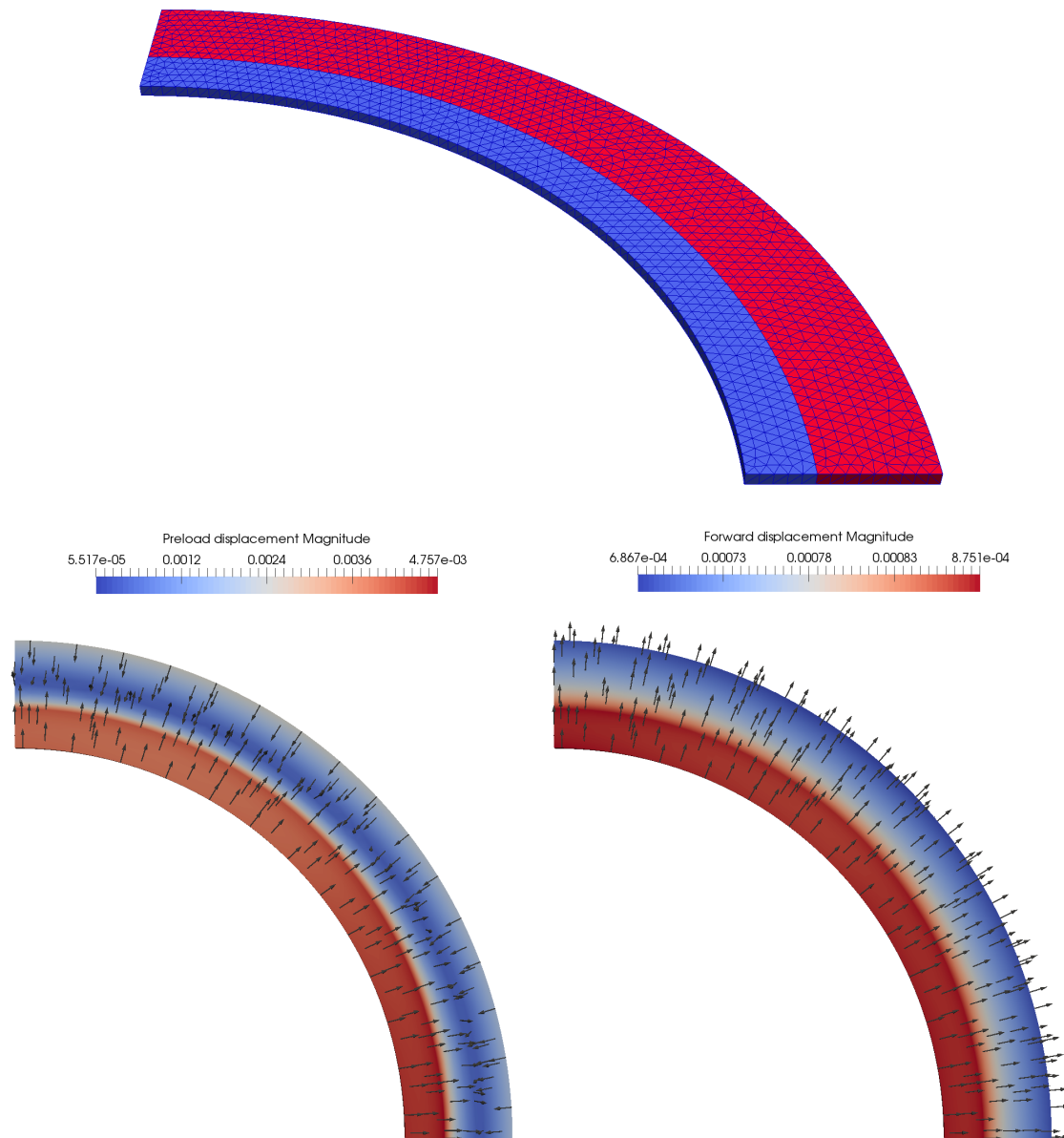


Figure 6.9: Domain discretization for the synthetic idealized artery and in-silico generated displacement fields for the soft media/adventitia model with an homogeneous intimal tissue with $c = 4000$ kPa (calcified tissue). Mesh contains 2469 nodes where (\mathbf{u}, λ) are unknowns, resulting in 9876 degrees of freedom for the preload and forward problems. (Top) Domain discretization used for finite element method numerical scheme, the intima and media/adventitia are the blue and red elements, respectively; (bottom-left) displacements obtained from the preload problem; (bottom-right) displacements obtained from the forward problem. Recall that the vessel is axially stretched by 10% in the configuration Ω_s , then the displacements obtained from the preload problem present an axial component besides the cross-sectional components of displacement.

models will perform successfully in a more realistic situation. This is because of the complexity of the geometry or the material composition (fibro-lipidic materials or small calcium inclusions on other tissue) that an in-vivo scenario may present. In fact, the next case aims to study the performance of the ROUKF estimation in a realistic arterial geometry.

6.4.2 Synthetic artery with in-vivo geometry

A more complex geometry extracted from an IVUS frame segmentation is now employed to assess the performance of the ROUKF on realistic vessel geometries under physiological pressure ranges. The chosen frame corresponds to a lesion with 57.4% stenosis at the end-diastolic phase. The pipeline described in Section 5.5.2 was applied for the construction of the mesh. A manual demarcation of a lipid and calcified areas was performed based on visual inspection of the image intensities. The intima/media layer obtained from the segmentation was considered as intima layer only, since the mechanical contribution of the media with presence of significant plaque (recall that the media thickness diminishes) and in passive conditions (no smooth muscle activation is considered) is negligible when compared to the intimal plaque contribution. The generated mesh of the domain for the numerical simulation is presented in Figure 6.10. This domain partition is not necessarily the in-vivo tissue distribution of this case, although similar to the plaque morphologies analyzed in-vivo where lipid pools and calcifications are located inside fibrotic tissues (see Figure 5.8). Nevertheless, the aim of this scenario is the analysis of the data assimilation procedure on a realistic media/intima geometry, for which the tissue distribution seems morphologically reasonable.

To generate the in-silico displacement field, use an adventitia material with coefficients $c = 15.8$ kPa, $k_1 = 25.36$ kPa, $k_2 = 67.85$, $\theta = 70.3^\circ$ and $\rho = 0.7$ (see equation (5.4.4)) and three neo-hookean materials without fibers (see equation (5.4.1)), a fibrotic material with $c = 500$ kPa, a lipidic material with $c = 100$ kPa and a calcified material with $c = 4000$ kPa. As in the previous case, loads of $\mathbf{t}^{W,n} = 80 \mathbf{n}$ mmHg and $\mathbf{t}^{W,n} = 120 \mathbf{n}$ mmHg are applied in the inner surface for the preload and forward problem in the normotensive scenario and loads of $\mathbf{t}^{W,n} = 90 \mathbf{n}$ mmHg and $\mathbf{t}^{W,n} = 140 \mathbf{n}$ mmHg are applied in the inner surface for the preload and forward problem in the hypertensive scenario. Tethering tractions $\mathbf{t}_s^{A,i}$ at the non-physical boundaries are applied such that an axial stretch of 10% is imposed in the axial direction. The ROUKF optimizes the coefficients (c, k_1) and (c) for the neo-hookean materials with and without fibers. The parameter uncertainties are 1 and 4 for the fibrous and non-fibrous materials, respectively. Such values presented a convenient balance between convergence rate and stability of the method as presented in Sections 6.3.2 and 6.4.1.

The results reported in Table 6.3 show that the method characterizes correctly the properties in the intimal region for the hypertensive case and only misses the calcified tissue for the normotensive case. The reason why the calcification was misidentified, is associated with the small displacement at its locus. In Figure 6.12, it is seen that the displacement in such region is close to $12\mu\text{m}$ in normotensive condition and close to $16\mu\text{m}$ in hypertensive conditions. In turn, as shown in Figure 6.13, the error in such area is similar for both cases ($\approx 3\mu\text{m}$, i.e. a relative error of 25% for the normotensive case and 18.75% for the hypertensive case) degrading more the identification of the normotensive case.

With this example, it has been illustrated that the strategy based on the ROUKF delivers a successful characterization when the displacements in the materials are large enough to analyze the sensitivity of the parameters. This is an important issue to take into consideration when analyzing lesions with large stenosis or calcified rings because

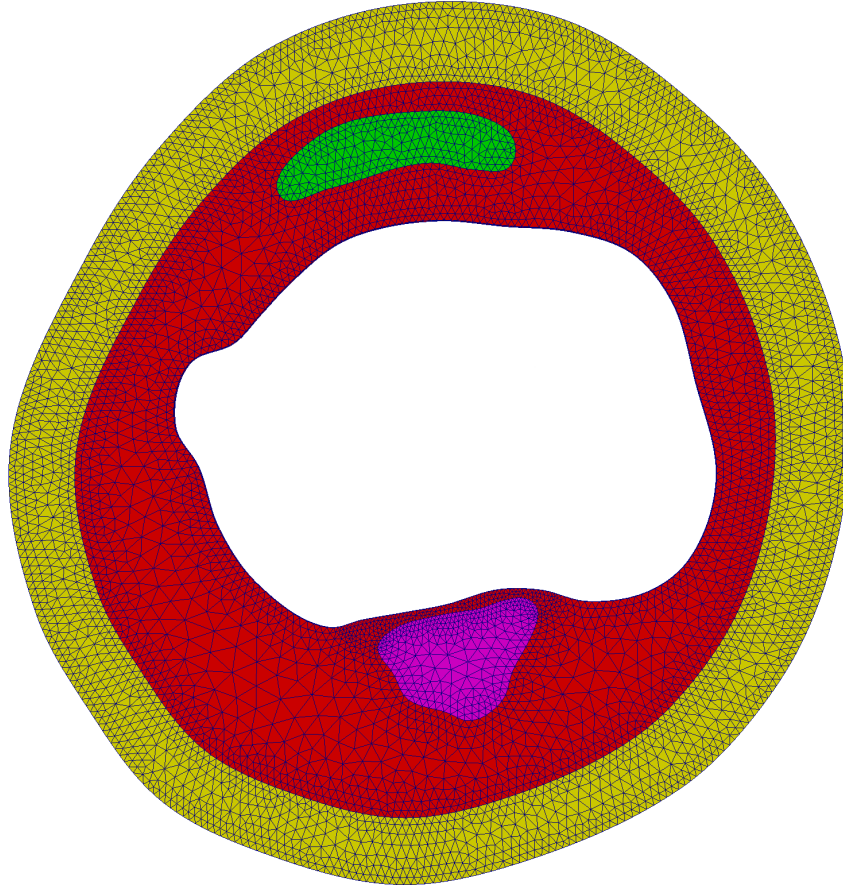


Figure 6.10: Domain discretization for the synthetic artery with in-vivo geometry. The intima is composed by a fibrotic (red), a lipidic (green) and calcified (magenta) partitions, enclosed by the adventitia (yellow) partition. Mesh contains 11602 nodes where (\mathbf{u}, λ) are unknowns, resulting in 46408 degrees of freedom for the preload and forward problems.

Case	Parameter	2^{θ^t} (kPa)	$2^{\hat{\theta}}$ (kPa)		Rel. error ε_c (%)
			Estimation	[LB,UB]	
Normotensive	Fibrotic c	500	663.86	[332.60, 1325.04]	32.77%
	Lipidic c	100	81.10	[40.66, 161.76]	18.9%
	Calcified c	4000	591.13	[295.90, 1180.94]	85, 22%
	Adventitia c	15.8	80.06	[40.16, 159.60]	406, 70%
	Adventitia k_1	25.36	59.72	[29.91, 119.22]	135, 49
Hypertensive	Fibrotic c	500	641.85	[321.51, 1281.35]	28.37%
	Lipidic c	100	96.25	[48.25, 191.98]	3.75%
	Calcified c	4000	3631.12	[1816.99, 7256.53]	9.22%
	Adventitia c	15.8	75.12	[37.66, 149.83]	375.44%
	Adventitia k_1	25.36	7.18	[3.60, 14.33]	71.69%

Table 6.3: ROUKF estimate of the constitutive parameters in the case of a synthetic artery with in-vivo geometry. The estimate $2^{\hat{\theta}}$ of the true parameter 2^{θ^t} is presented with its uncertainty interval $[LB, UB] = [2^{\hat{\theta} - \sqrt{\text{diag}(\mathbf{U}^{-1})}}, 2^{\hat{\theta} + \sqrt{\text{diag}(\mathbf{U}^{-1})}}]$. The parameter estimate relative error is computed as $\varepsilon_c = (|2^{\theta^t} - 2^{\hat{\theta}}|)/2^{\theta^t}$. The Kalman parameters for uncertainty were $\sigma_Z = 10^{-3}$, and $\sigma_\theta = 1$ and $\sigma_\theta = 4$ for materials with and without fibers.

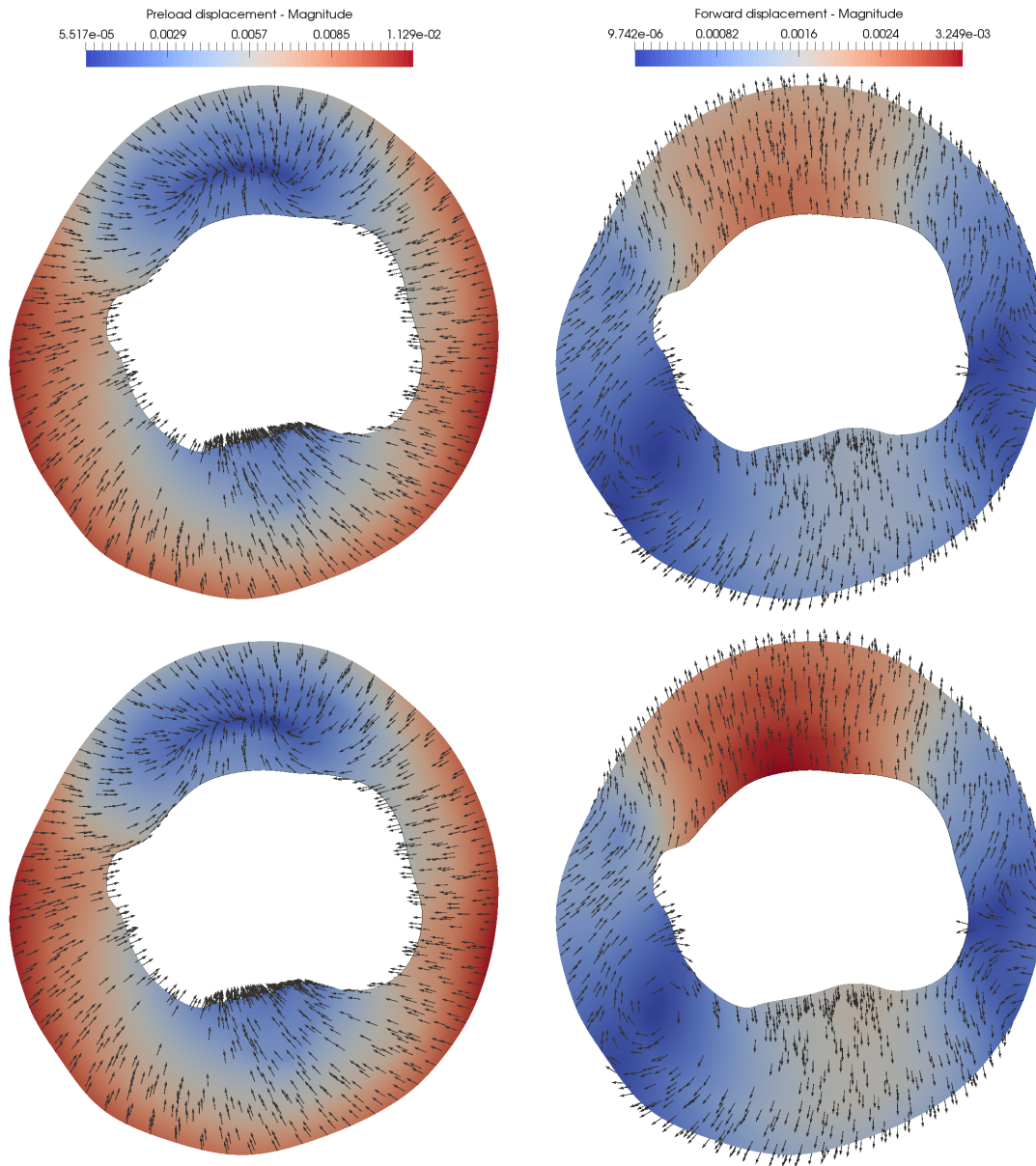


Figure 6.11: In-silico generated displacement fields (in cm) for the normotensive case (first row) and hypertensive case (second row). The columns present the solutions for the preload problem (first column) and for the forward problem (second column). Each column uses the same range and color bar. Recall that the vessel is axially stretched by 10% in the configuration Ω_s , then the displacements obtained from the preload problem present an axial component besides the cross-sectional components of displacement. This is clearly evidenced in the lipidic region at the top center part of the artery, which experiments an important axial retraction at the no-load configuration (Ω_m).

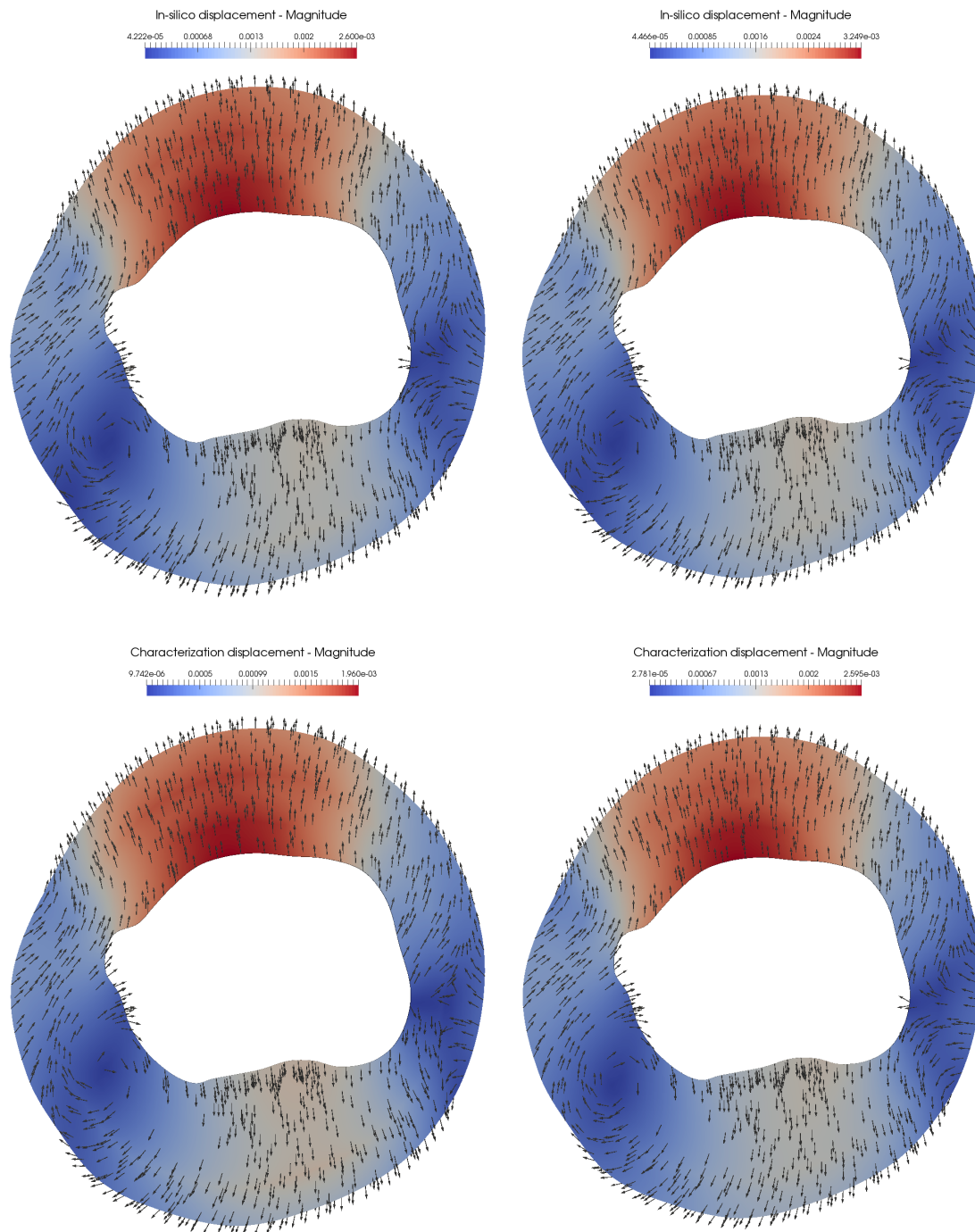


Figure 6.12: Comparison of the displacement field (in cm) for the forward problem obtained by in-silico experiment and as result of the data assimilation process (characterization): (first-column) normotensive case; (second-column) hypertensive case.

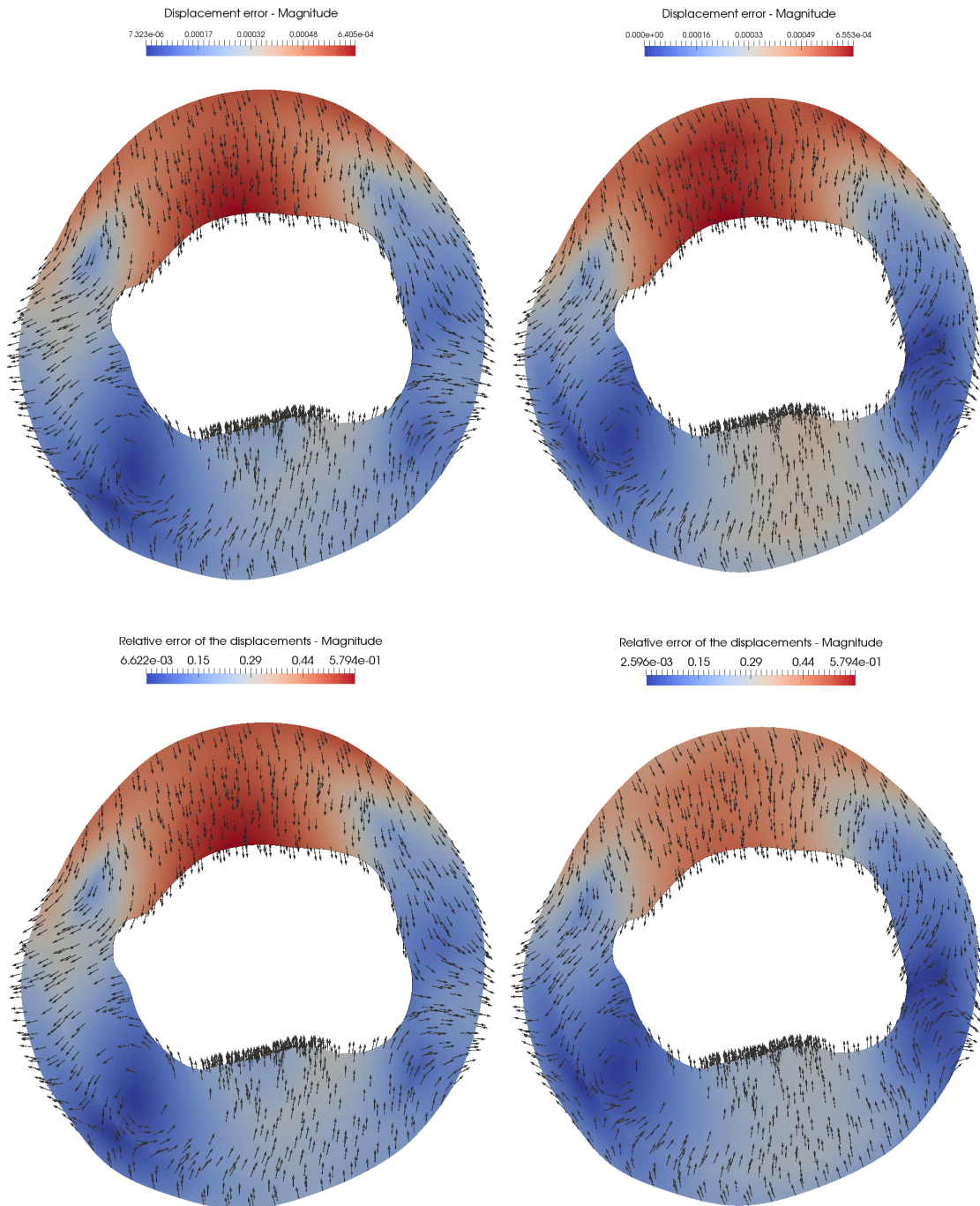


Figure 6.13: Error of the displacement field (in cm) for the forward problem between the in-silico experiment and the result of the data assimilation process (characterization): (first-column) normotensive case; (second-column) hypertensive case; (first-row) absolute error of the displacements in cm; (second-row) relative error of the displacements computed as $\varepsilon_r = |\Omega_s| \frac{\mathbf{u}_s^m - \mathbf{u}_s^t}{\int_{\Omega_s} |\mathbf{u}_s^t| d\Omega}$ where \mathbf{u}_s^t and \mathbf{u}_s^m are the in-silico and estimate displacements respectively.

such characteristics of the vessel wall reduce the compliance and may lead to insufficient input data for a successful characterization.

6.4.3 In-vivo artery

In this last case of study, we use two images of an IVUS studies corresponding to the same cross-sectional area of the vessel at the end-diastolic and systolic phase, respectively (see Figure 6.14). This scenario corresponds to the in-vivo characterization of the biomechanical properties of a patient-specific arterial vessel, which is the ultimate goal of this thesis.

To delineate the partition of the domain, we use the K-means strategy based on the IVUS intensity. The domain contains 2 intimal tissues (2 bins used in the K-means strategy) and an adventitia of thickness $\approx 300\mu\text{m}$, compatible with a typical coronary morphology reported in the literature for atherosclerotic patients [329]. The mesh generated for such partition is shown in Figure 6.15. Additionally, loads of $\mathbf{t}^{W,n} = 80 \mathbf{n}$ mmHg and $\mathbf{t}^{W,n} = 120 \mathbf{n}$ mmHg are respectively applied over the inner surface for the preload and forward problems, and tethering tractions $\mathbf{t}_s^{A,i}$ such that an axial stretch of 5% is imposed in the axial direction. The assumption of normotensive levels of loads was assumed because the patient is medicated to control its pressure during catheterization. The axial stretch of 5% was chosen to obtain similar displacements in the OF observations and in the in-silico simulations used in the characterization process. As reported in [146] the physiological level of axial stretches range from 5 – 10% justifying that the considered loading is physiologically consistent.

The results of the characterization process presented that the intima is composed by two lipidic materials, where the blue partition is slightly more fibrotic (see Table 6.4). The obtained displacement field from the data assimilation procedure (\mathbf{u}^m) showed the larger differences to the observed field (\mathbf{u}_s^{OF}) at the top part of the cross-section, ranging errors between 70 and 148 μm . Such differences can be associated to the error in the domain partition or the absence of surrounding tissues in the model. Inspecting the orientation of the error it seems that a stiffer material (or external tissue to the vessel) is associated to the top right region which advances radially towards the lumen (accordingly to the observations \mathbf{u}_s^{OF}).

The previous analysis of the displacement errors in magnitude and pattern can be useful for the development of domain partitioning techniques, something that seems to be fundamental to obtain a more precise description for the displacements in the data assimilation process. Regions with error higher than a certain threshold can be candidates to conform a partition for a different tissue. Also, models for surrounding tissues as those introduced in [22, 41], will be useful to model epicardium contact, myocardial bridge and other scenarios that reduce the compliance of the vessel surrounding media.

6.5 Final remarks

A data assimilation environment for analysis of arterial models and biomechanical characterization has been developed. The in-silico experiments presented in Section 6.4.1 and 6.4.2 have shown that the methodology is capable to recover biomechanical properties of the intimal tissue when the distribution of the vessel constituents is known and the arterial pressure is large enough to perform observable deformations in the tissues. Also, an in-vivo case showed preliminary results for the biomechanical characterization of a vessel cross-section. Based on this case, some considerations were exposed for further development of the data assimilation technique, such as: i) dynamic strategies for domain partitioning to iteratively enhance the distribution of materials within the arterial wall,

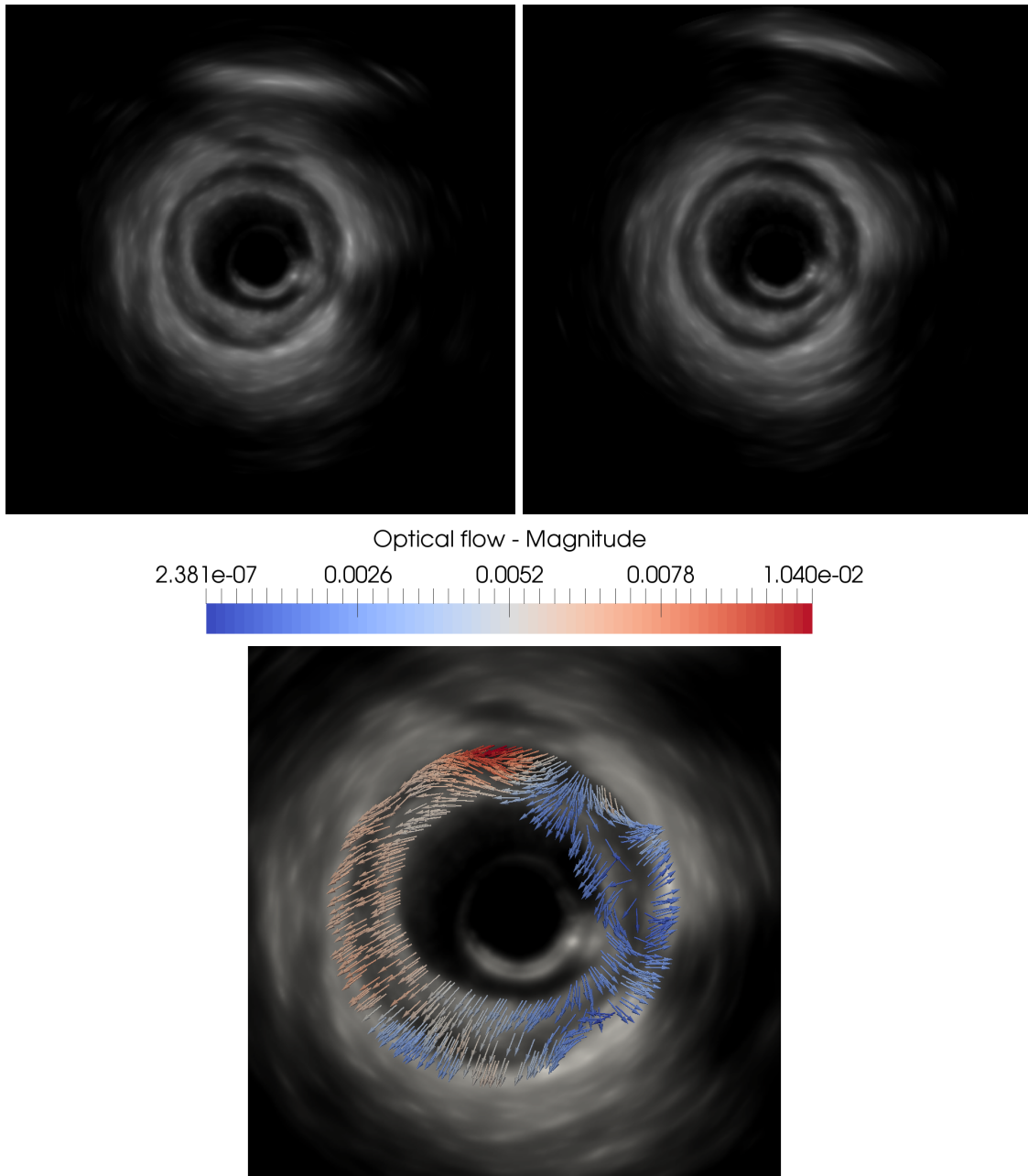


Figure 6.14: IVUS images used for the biomechanical characterization in the case of the in-vivo artery. (Top) Images correspond to an atherosclerotic lesion gated at the cardiac phases \mathcal{I}_{st} (left) and \mathcal{I}_{mo} (right); (bottom) optical flow (in cm) between frames at \mathcal{I}_{st} and \mathcal{I}_{mo} phases, estimated with a Weickert formulation using the numerical scheme proposed in Section 4.3.4.5. The selection and alignment of these images was performed using the gating and registration methods developed in Chapters 2 and 3.

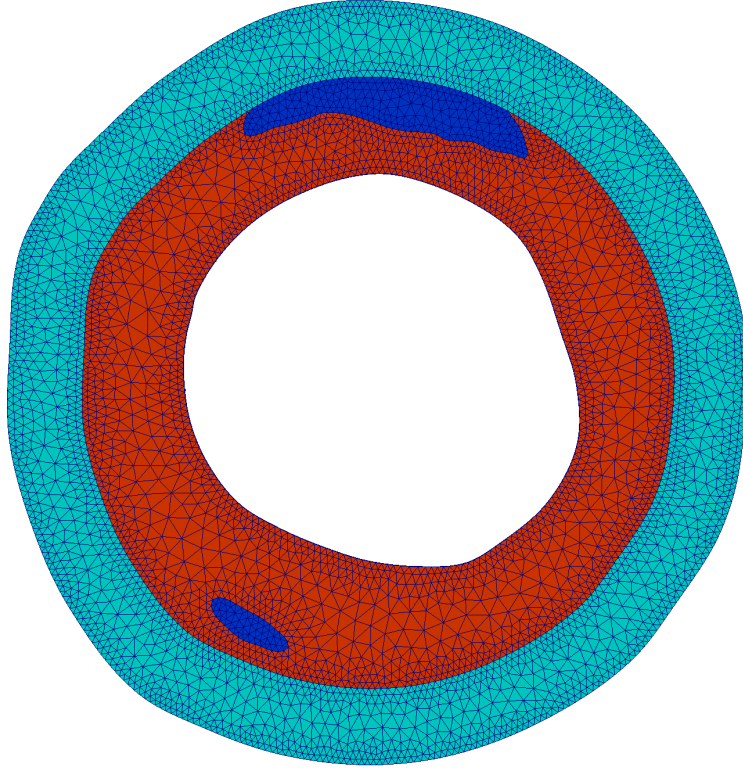


Figure 6.15: Domain discretization for the case of the in-vivo artery. The intima is composed by a material 1 (blue) and a material 2 (red), enclosed by the adventitia (cyan) partition. The mesh for the finite element method was created from the K-Means based on intensity for 2 materials, it contains 8867 nodes where (\mathbf{u}, λ) are unknowns, resulting in 35468 degrees of freedom for the preload and forward problems.

Parameter	$2^{\hat{\theta}}$ (kPa)		Mean relative error by partition
	Estimation	[LB,UB]	
Material 1, c	126.34	[63.85, 250.00]	1.6913
Material 2, c	70.15	[35.38, 139.08]	2.7140
Adventitia c	3.55	[1.78, 7.08]	—
Adventitia k_1	1243.00	[623.96, 2476.23]	—

Table 6.4: Estimate of the reduced order unscented Kalman filter for in-vivo constitutive parameters of a patient-specific artery. The estimate $2^{\hat{\theta}}$ of the partition materials is presented with their uncertainty interval $[LB,UB] = [2^{\hat{\theta}-\sqrt{\text{diag}(\mathbf{U}^{-1})}}; 2^{\hat{\theta}+\sqrt{\text{diag}(\mathbf{U}^{-1})}}]$. The mean relative error for each partition is computed as $\frac{1}{|\Omega_i|} \int_{\Omega_i} \frac{|\mathbf{u}_s^{\text{OF}} - \mathbf{u}_s^m|}{|\mathbf{u}_s^{\text{OF}}|} d\Omega_i$ where Ω_i is the partition of the material i . The Kalman parameters for uncertainty were $\sigma_Z = 10^{-3}$ and $\sigma_\theta = 1$ and $\sigma_\theta = 4$ for materials with and without fibers.

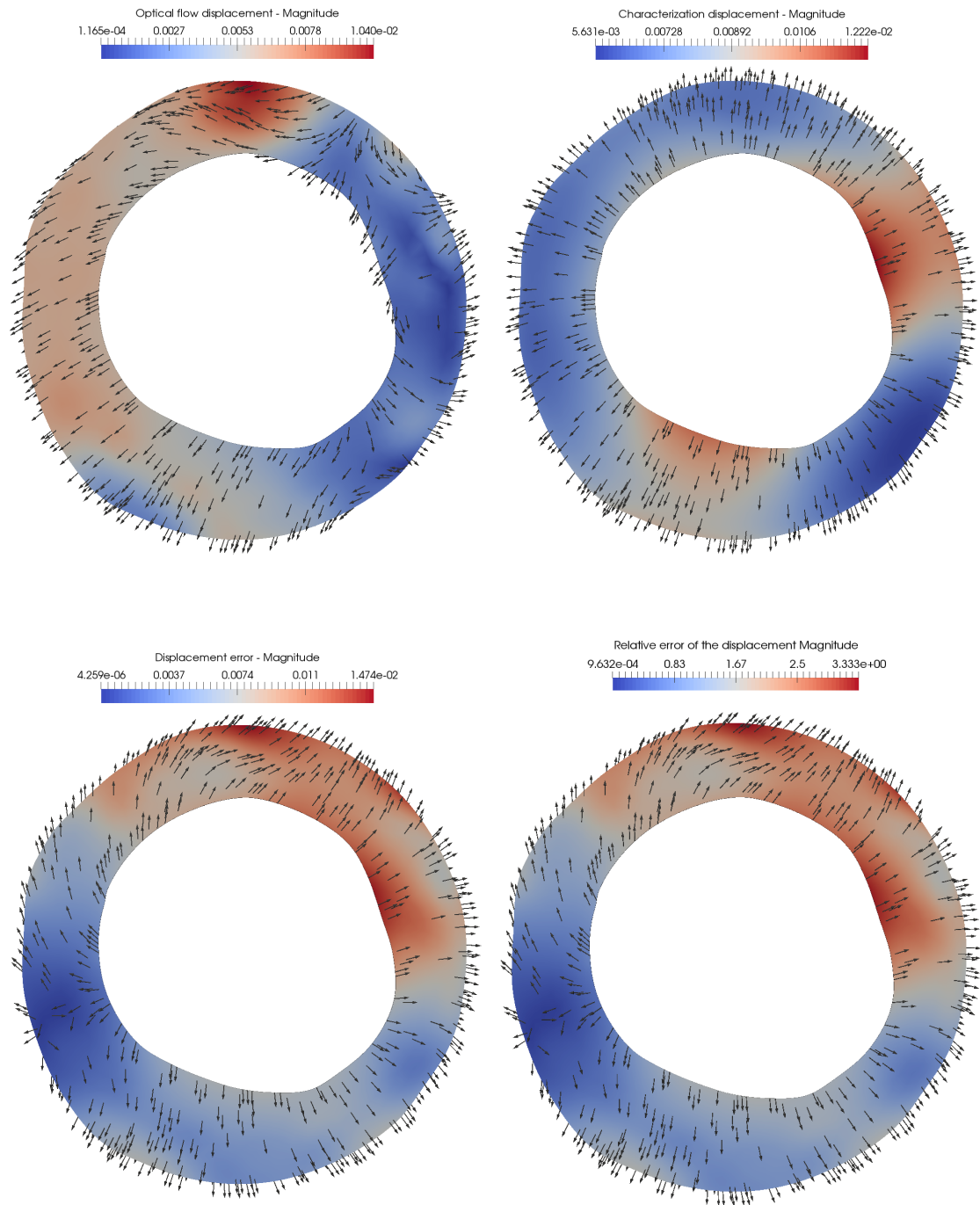


Figure 6.16: Comparison of the displacement field (in cm) recovered from the images by optical flow techniques and the obtained for the forward problem as result of the data assimilation process (characterization): (upper-left) optical flow displacement field \mathbf{u}_s^{OF} ; (upper-right) data assimilation displacement field \mathbf{u}_s^m ; (bottom-left) difference of the displacement fields $\mathbf{u}_s^m - \mathbf{u}_s^{\text{OF}}$; (bottom-right) relative difference of the displacement fields $|\Omega_s| \frac{\mathbf{u}_s^m - \mathbf{u}_s^{\text{OF}}}{\int_{\Omega_s} |\mathbf{u}_s^{\text{OF}}| d\Omega}$.

unveiling the tissue distribution by making use of the disagreement between the observations and the mechanical response; and ii) the use of surrounding tissues models to reproduce the vessel displacement when there is substantial media resistance (epicardium contact, myocardium bridge, among others).

Nevertheless, a complete methodology has been presented that integrates all the elements developed in this thesis. The development of this toolbox for study of biomechanical characterization of the vessel wall successfully completes the goals initial delineated in Chapter 1. This new tools enables several new studies to achieved the in-vivo and patient-specific characterization of the vessel wall tissues, such as: development of shape optimization methods to obtain an in-vivo distribution of the vessel tissues; analysis of the axial and external stress forces along the tissue characterization; assessment of uncertainty of the optical flow observations to establish a heterogeneous distribution of the parameter σ_Z along the image.

Part III

Medical Applications

Chapter 7

Geometric arterial models: IVUS vs. CCTA

The present chapter summarizes some of the clinical contributions derived from the IVUS image processing (introduced in the first part of this manuscript), CCTA image processing (developed in [52]) and the collaboration with the Incor and S rio-Liban s health centers in S o Paulo state, Brazil. The goal is the comparison between the geometric models obtained from coronary angiography fused with intravascular ultrasound (for the sake of simplicity denoted just as IVUS) and coronary computed tomography angiography (CCTA). The construction of such models is further detailed in [212] and [52] for IVUS and CCTA-based approach, respectively. Still, here we describe the fundamental steps in the corresponding processes.

In what follows, two studies are presented: i) a geometric comparison based on features post-processed from the generated geometries; and ii) a comparison of the hemodynamic quantities computed by each model with special focus on the computational estimation of fractional flow reserve (FFR) and of averaged wall shear stress (AWSS). Results of the later study have been published in [54].

7.1 Introduction

Computational fluid dynamics (CFD) [73] is being used to explain the development of atherosclerotic coronary lesion [68] and evaluate its functional significance [232] in term of the computed hemodynamic quantities such as blood flow, pressure gradients and shear stresses. To perform a CFD simulation in a patient-specific scenario, a geometrical model from a given arterial district must be constructed from a medical imaging technique. The most common imaging modalities for coronary arteries are the coronary computed tomography angiography (CCTA), the coronary angiography (AX) and intravascular ultrasound (IVUS). In [212], we developed a methodology to fuse the spatial information from AX with a local and high resolution description of the vessel structures from IVUS. Integrating the gating and registration techniques developed in the present thesis to the previous methodology, it is possible to achieve a spatial and phase consistent geometric model of the coronaries (henceforth referred to as IVUS model).

Several studies compared the diagnostic capabilities of IVUS and CCTA models in terms of lumen area, plaque volume and other classic measurements [108, 118]. However, there are no previous studies comparing a comprehensive set of geometric descriptors for coronary arterial models constructed from IVUS and CCTA. Furthermore, the correctness of hemodynamic simulations is determined, mainly, by two factors: (a) accurate anatomical data provided by three-dimensional coronary model and (b) the suitability of

hypothesis behind the definition of boundary conditions related to patient specific parameters (see [54] for further details). Therefore, our purpose is to compare the geometric features of both models and objectively interpret the impact of geometric differences on CFD simulations.

Additionally, we study the sensitivity of the fractional flow reserve (FFR) with respect to each the geometric model. The FFR is the accepted gold standard for detection of ischemia-related lesion and guide treatment [257], although the need for using drugs to induce maximum hyperemia and its inherently invasive nature (a pressure wire is required) are contributors to low adoption [92]. Despite being non-invasive and already validated [240], the computational assessment of FFR using coronary computed tomography angiography (CCTA) carry some limitations related to this image modality such as lumen underestimation in the presence of stents or calcium [175, 196]. In turn, the use of other image modalities such as quantitative coronary angiography [251] or intravascular ultrasound (IVUS)[61], also allows the computational estimation of FFR. In this context, IVUS brings some advantages, such as high definition of arterial lumen, vascular remodeling [101, 118] and pulsatility [182]; in addition to being associated with decreased use of iodine contrast during percutaneous coronary intervention [208].

7.2 Methods

7.2.1 Study population

Patients with clinical suspicion of atherosclerotic coronary disease who underwent multimodal evaluation with CCTA and IVUS at least, but also FFR in selected cases made up our samples. The left anterior descending (LAD), ramus intermedius (RI), left circumflex (LCx) and right coronary artery (RCA) were analyzed. Imaging data for such vessels were acquired using standardized image acquisition protocols. Data processing and analysis were performed retrospectively using the reconstruction techniques presented in [52] and [212]. The study protocol was approved by the local ethics committees of the centers and is in accordance with the Helsinki Declaration.

Sample for geometric comparison

The study sample consisted of 28 patients (34 arteries) who were indicated to both CCTA and IVUS protocols for diagnostic or therapeutic percutaneous coronary procedure at Sírío-Libanês Hospital, São Paulo, Brazil. Most patients presented mild symptoms (93%). More than 30% of the patients had diabetes and the mean of left ventricular ejection fraction was $64 \pm 7\%$. Details of the study population are outlined in Table 7.1. Regarding stenotic lesion description, the median maximum percentage of diameter stenosis ($\%DS$) by AX was 55% [40-70], whereas median minimum lumen area (MLA) and plaque burden, measured in the IVUS images, were 3.96 mm^2 [3.2-5.1] and 68.5% [56-73], respectively (median [min-max] of the sample).

Sample for hemodynamic comparison

The study sample is a subset of the previous sample, consisting of 11 patients (16 arteries) who were indicated to both CCTA and IVUS protocols with invasive FFR measurements. The time span between both medical studies was 3.4 ± 4.9 days, and the CCTA was always performed before percutaneous coronary procedure. Details of the study population are outlined in Table 7.2.

General information	
Male	23 (82%)
Age (yrs)	64 ± 11
Mean body mass index (kg/m ²)	28 ± 3
Hypertension	16 (57%)
Hyperlipidemia	27 (96%)
Current smoker	9 (32%)
Diabetes mellitus	9 (32%)
Angina type	
Asymptomatic/ Silent ischemia	12 (43%)
Atypical symptoms	14 (50%)
Stable angina	2 (7%)
Cardiovascular history	
Previous PCI	3 (11%)
Previous CABG	2 (7%)
Atrial Fibrillation	3 (11%)
Heart failure	2 (7%)
Calcium score*	218 ± 345
LVEF, %	64 ± 7
Arteries	
Left anterior descending	22 (65%)
Left circumflex	9 (26%)
Ramus intermedius	2 (6%)
Right coronary	1 (3%)
Vessel characteristics	
Percentage diameter stenosis (AX)	55 (40 – 70)
Minimum lumen area (IVUS) (mm ²)	3.96 (3.2 – 5.1)
Plaque burden(%)	68.5 (56 – 73)
Fractional flow reserve**	0.86 (0.78 – 0.93)
Percentage diameter stenosis (CCTA)	50 (40 – 60)

*23 calcium score measurements (5 patients with previous PCI or CABG).

**23 FFR measurements were taken.

Table 7.1: Clinical characteristics of the sample used for the geometric comparison ($n = 28$ patients, 34 arteries). Values are mean ± SD, n (%), or median (IQR). Abbreviations: coronary artery bypass graft (CABG); interquartile range (IQR); percutaneous coronary intervention (PCI); left ventricular ejection fraction (LVEF).

7.2.2 Acquisition and processing of medical images

Due to the intrinsic difference between IVUS and CCTA images, different processing methodologies are employed to retrieve the three-dimensional model of the arterial lumen and its associated axial centerline. While CCTA images deliver three-dimensional arterial models, IVUS must be enriched with spatial information of the pullback path¹ obtained from angiographies (AX). All arterial models were generated from images acquired during end-diastole. Figure 7.2 illustrates the CCTA and IVUS image processing pipeline. For both geometric models, extensions at inlet/outlets were added to reduce boundary effects in the simulation [120].

¹Spatial path followed by the IVUS transducer during the acquisition of the study.

General information	
Male	10 (91%)
Age (yrs)	59 ± 12
Mean body mass index (kg/m^2)	28 ± 4
Resting diastolic pressure (mmHg)	76 ± 5
Resting systolic pressure (mmHg)	120 ± 8
Resting mean systemic pressure (mmHg)	91 ± 6
Resting heart rate (bpm)	72 ± 9
Arteries	
Left anterior descending	10 (62%)
Left circumflex	5 (31%)
Ramus intermedius	1 (7%)
Circulation dominance	
Right	10 (91%)
Co	1 (9%)

Table 7.2: Clinical characteristics of the sample used for the hemodynamic comparison ($n = 11$ patients, 16 arteries). Values are mean \pm standard deviation or n (%).

For each geometric model, the centerline (resolution of 0.5 mm between points) was computed as in [18], and was used to clip the model at the ostium of the artery of interest. From the CCTA model, a region of the centerline was chosen such that it matches the length of the IVUS centerline (see solid surfaces in Figure 7.1). Side branches were removed for comparison purposes. Cross-sectional slices, denoted Γ_s with contour $\partial\Gamma_s$, were extracted at each point over the centerline (see Figure 7.2). Hemodynamic quantities defined in the bulk of the domain were averaged at each section Γ_s , while quantities defined over the surface of the domain were averaged over $\partial\Gamma_s$. We simply refer to these as Γ_s -averaged quantities, and are denoted by $(\bar{\cdot})$.

7.2.2.1 Intra-vascular ultrasound

IVUS images were acquired with the Atlantis™ SR Pro Imaging Catheter 40 MHz synchronized with an ECG signal and connected to an iLab™ Ultrasound Imaging System (Boston Scientific Corporation, Natick, MA, USA). The acquisition was performed with a frame rate of 30 FPS during an automated constant velocity pullback at 0.5mm/s. The acquisition finalizes at the ostium of the aorta in every run. The IVUS frames of 512×512 pixels yield a resolution of $17.5\mu\text{m} \times 17.5\mu\text{m}$ per pixel. Overall, multiple IVUS runs were performed on 28 patients resulting in 34 IVUS studies (one for each reconstructed artery) with synchronized ECG signal. In addition, the IVUS study is gated to retrieve the images at the end-diastolic phase (see Chapter 2). The vessel geometry is defined in a system of intrinsic transducer coordinates which requires integration with angiographic images to adequately place the model in the three-dimensional space.

Two orthogonal AX films were acquired synchronized with the ECG signal when the IVUS sensor was at the initial pullback position. The views were taken along the cranial-caudal plane for left coronary vessels and along the right-left oblique plane for right coronary arteries. These positions minimize dye overlapping between the coronary vessels and heart chambers as well. The films span over 8 heartbeats to ensure the acquisition along the whole respiratory period. Finally, a specialist selected images from the films at the same respiratory phase (full exhalation) and at the end-diastolic cardiac phase, to perform a time-space consistent reconstruction of the vessel.

An in-house software developed in Matlab™ was used to retrieve the end-diastolic cardiac phase from IVUS images. Luminal area (from all end-diastolic IVUS frames) was

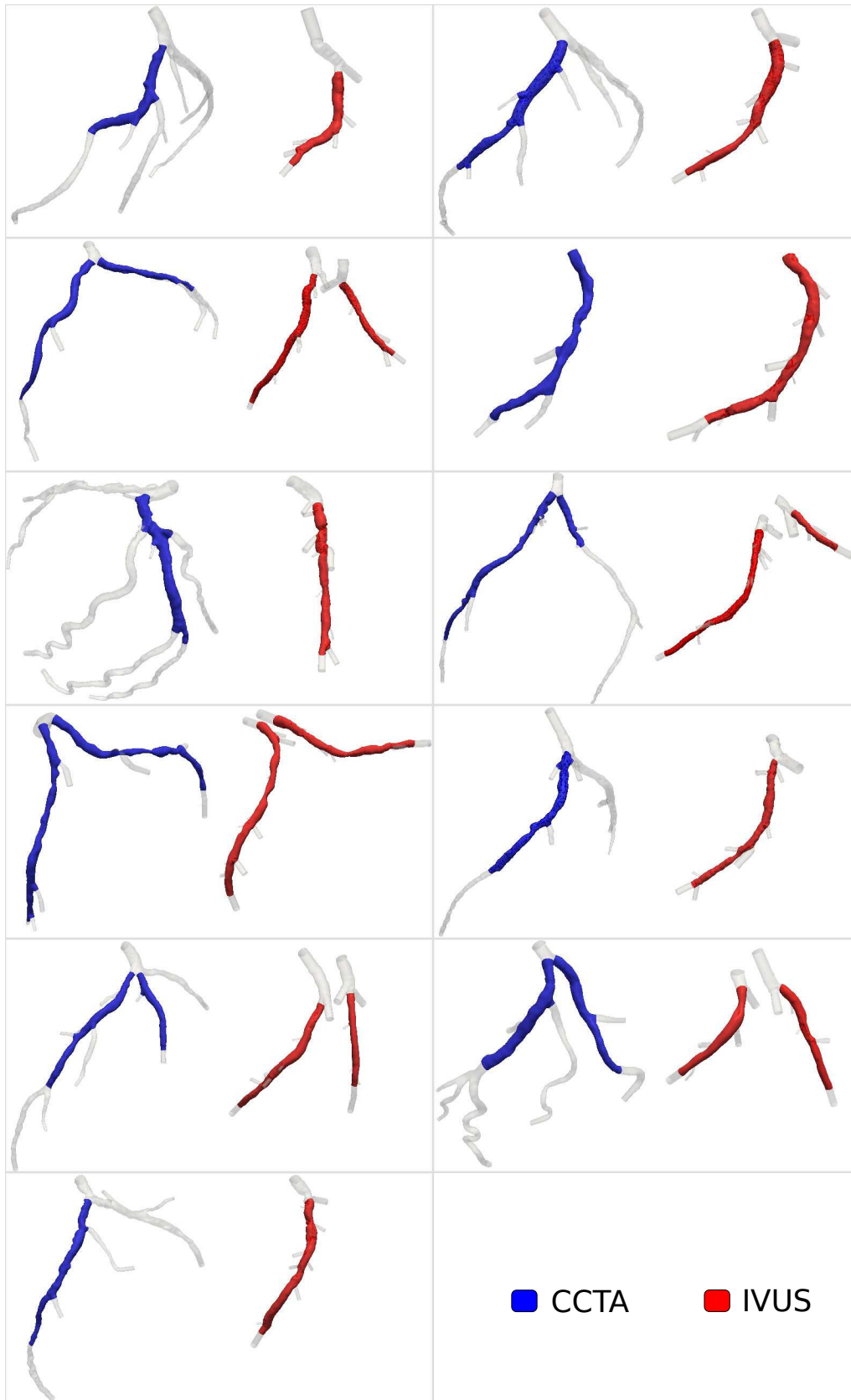


Figure 7.1: Geometric models of 16 arteries used in the study for hemodynamic comparison. The lumen geometries used for computational simulations are shown with transparency. Regions for comparison are highlighted with solid colors blue for CCTA and red for IVUS.

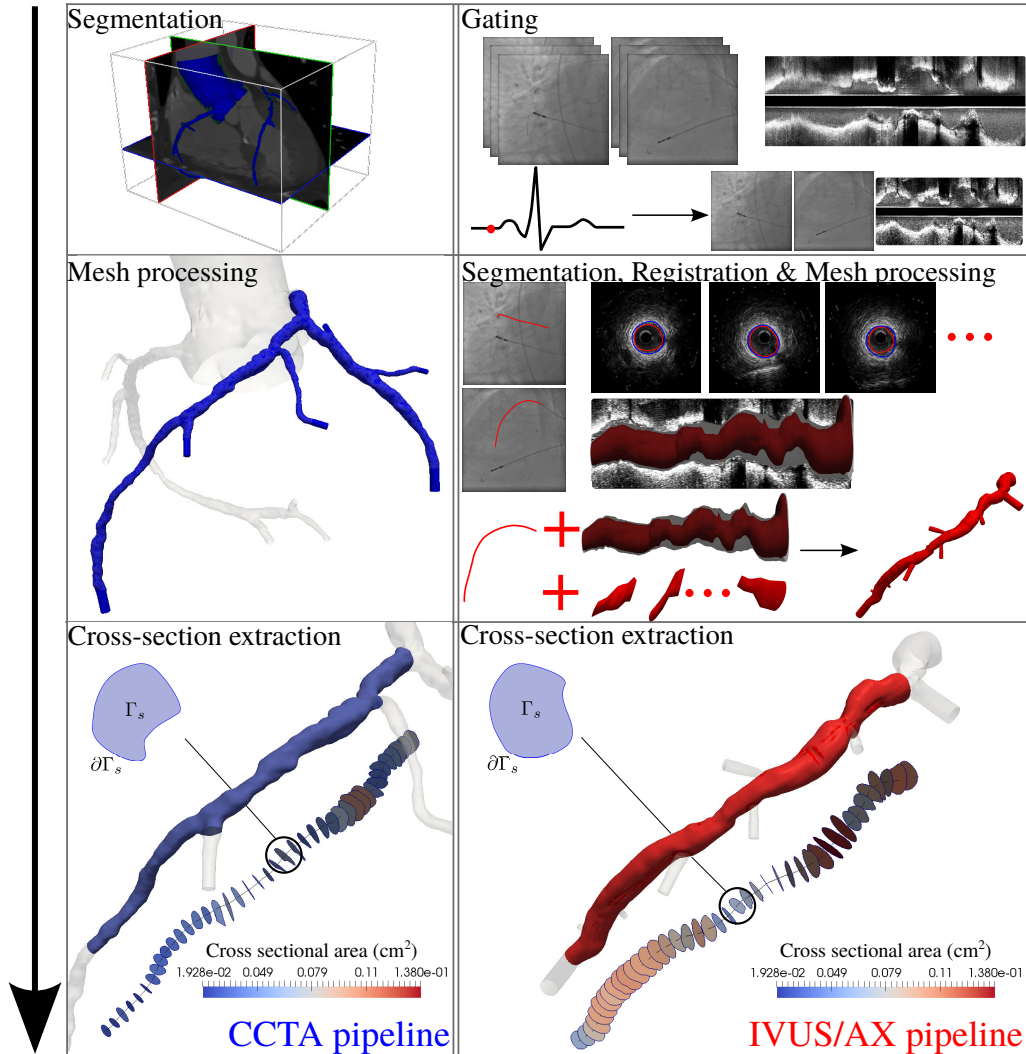


Figure 7.2: Complete processing pipeline from medical images to geometric models. The CCTA procedure is presented in the left column and the IVUS procedure is shown in the right column.

manually segmented by a specialist using cubic splines. The length of the segmented pull-backs was 153.81 ± 45.76 gated frames, which corresponds to 67.19 ± 17.89 mm of vessel length. Then, the transducer path was segmented from the orthogonal AX images using a biplane snakes method [231]. The segmented cross-sectional areas were positioned in the transversal plane of the recovered transducer path, using an inter-frame spacing dictated by the acquisition time of the frame and by the pullback velocity. Segmentation of side branches from IVUS images was also manually performed, creating a mesh in intrinsic transducer coordinates for each branch. These branches were spatially positioned in the transversal plane already determined for the parent vessel.

To account for catheter rotations, all contours are rotated around the axis described by the transducer path. The rotation angle of each frame is the one that minimizes the mismatch between the projected luminal area from IVUS and the AX contrast in the same part of the vessel. After this process, a specialist verifies and, if necessary, corrects the rotation angle by matching the branches and main artery with the projection resulting in the AX.

At this point, IVUS processed data consist in several disconnected meshes, one for the parent vessel and one for each branch. Each mesh is improved applying the following

processes: i) smoothing using a Laplacian algorithm with no shrinking restriction (a relaxation factor of 0.63 and 30 iterations are used) [183]; ii) addition of tube extensions at inlet/outlets (at boundaries near bifurcations or in boundaries with non-convex enclosing curves) to reduce boundary effects in the simulation [120], such extensions have circular cross-section with the same area of the boundaries that are extending in the direction of the outward normal; iii) adaptive refinement as a function of the vessel radius. Then, all surfaces are merged using union surface operations described in [265]. Finally, a tetrahedral volume mesh is constructed for the CFD simulations using also VMTK [1]. The number of side branches was manually performed by an expert.

7.2.2.2 Coronary computed tomography angiography

CCTA images were acquired in a 320-row scanner system (Aquilion ONE, Toshiba Medical Systems, Japan). All acquisitions were ECG-triggered prospectively at end-diastolic phase (75% of the cardiac cycle) to keep the lowest possible radiation dose. The acquisition scheme followed standard practice protocols [53], ensuring heart rate lower to 65 bpm.

For each patient, the arterial lumen is segmented by implicit deformable models [19]. First, a curvature anisotropic filter is applied over a region of interest [336]. Initialization of the level-set method is performed in individual arteries using a colliding front algorithm [19]. The segmented lumen is defined using a marching cubes method [200]. This procedure results in a triangulated raw surface of the coronary tree which is improved following the same procedure described in Section 7.2.2.1. All image and mesh processing stages are performed using VMTK [1], ImageLab [126] and HeMoLab [183] softwares.

An advantage of CCTA images is that the coronary network can be retrieved from a single tomography. The degree of detail, i.e. number of small arteries, of such network depends on image quality and artifacts. The number of side branches for each artery is counted from such network.

7.2.3 Invasive FFR measurements

FFR invasive measurement was performed according to routine clinical practice utilizing the PressureWire Certus™ (St Jude Medical Systems). The FFR was performed only in vessels demonstrating an intermediate stenosis and with clinical indication for FFR evaluation. Transcatheter aortic and intracoronary pressure tracings were equalized. After administration of nitroglycerin, the guidewire was advanced into the distal portion of respective coronary artery and distal to the index lesion. The ratio of the mean pressure in the distal portion of coronary over the mean pressure in the aorta (P_d/P_a) was continuously recorded. Adenosine was either injected intravenously at a constant rate of 140 mg/kg/min or as an intracoronary bolus (300 μ g for the right coronary artery and average of 990 μ g for the left coronary artery), and the lowest P_d/P_a value in steady state after adenosine application was documented as FFR result. FFR was considered diagnostic of ischemia at a threshold of < 0.80 .

7.2.4 Flow Simulations

Blood flow was modeled using the Navier-Stokes equations with rigid vessel wall boundaries. Let Ω be the domain occupied by the coronary vessels, with boundary Γ_w representing the arterial wall, Γ_p the proximal boundary and Γ_i , $i = 1, \dots, N_o$, the N_o

outlet boundaries, and \mathbf{n} the normal vector. Then, we must find the velocity and pressure fields (\mathbf{v}, p) such that

$$\begin{cases} \rho \frac{\partial \mathbf{v}}{\partial t} + \rho(\nabla \mathbf{v})\mathbf{v} - \mu \Delta \mathbf{v} + \nabla p = 0 & \text{in } \Omega \\ \operatorname{div} \mathbf{v} = 0 & \text{in } \Omega \\ \mathbf{v} = 0 & \text{on } \Gamma_w \\ \mathbf{t}_p = -P_p \mathbf{n} & \text{on } \Gamma_p, \\ + \text{Resistance boundary conditions (see [52])} & \text{on } \cup_{i=1}^{N_o} \Gamma_i, \\ + \text{Initial conditions} & \text{in } \Omega \end{cases} \quad (7.2.1)$$

where ρ and μ are blood density and viscosity, \mathbf{t}_p are the homogeneous tractions imposed at Γ_p , P_p is the mean systemic blood pressure and the resistance boundary conditions are homogeneous tractions \mathbf{t}_i imposed at the outlets $\cup_{i=1}^{N_o} \Gamma_i$. The variables P_p and \mathbf{t}_i are constant or variable in time if the blood flow simulation is steady or pulsatile, respectively. The resistance boundary conditions are responsible for the flow distribution over the arterial network and are estimated relying in two assumptions: (i) the pressure drop is only due to peripheral bed resistances; and ii) the Murray's law, with a certain exponent γ , holds. Details of the estimation and justification of such conditions are given in [52, 54]. Particularly, the parameters were defined as $\rho = 1.05 \text{ g/cm}^3$, $\mu = 0.04 \text{ cP}$ and $\gamma = 2.66$. For simulations at maximum myocardial hyperemia, hyperemic blood flow is estimated from patient data. Given the IVUS and CCTA models of a coronary artery, boundary conditions are prescribed such that the same amount of blood volume flows through the compared arteries. Therefore, differences in hemodynamics variables such as FFR or time average wall shear stress (AWSS) are caused by the difference in the geometric models.

To solve the equations (7.2.1), the variational form of system is approximated using an implicit backward Euler finite-difference method in time and a fully coupled velocity-pressure finite element method in space [23, 149]. Tetrahedral meshes were constructed using the VMTK library [1]. Computer simulations were performed with an in-house fully parallel solver. For pulsatile simulations, the time step was $\Delta t = 5 \cdot 10^{-4} \text{ s}$, and homogeneous initial conditions were used. Mesh independence tests were performed. Models of IVUS and CCTA contained $2.05 \pm 1.18 \text{ M}$ and $1.52 \pm 0.43 \text{ M}$ degrees of freedom, respectively.

7.2.5 Statistical analysis

The analyses were performed on a per-vessel basis. Features and indexes are expressed as mean \pm SD describing the correlation between modalities in terms of the Spearman coefficient ρ , Bland-Altman relative bias and limits of agreement. Centerlines were scaled down to a normalized centerline with parametric arc-length coordinate $s \in [0, 1]$, and re-sampled to 200 points for each centerline for comparison purposes.

Hemodynamic comparisons along the region of interest focused on the magnitude of velocity $\bar{v} = \|\bar{\mathbf{v}}\|$ and pressure \bar{p} , lumen area A (D the diameter), Reynolds number $\operatorname{Re} = \frac{\rho \bar{v} D}{\mu}$, time average wall shear stress $\overline{\text{AWSS}}$, oscillatory shear index $\overline{\text{OSI}}$, flow rate \bar{Q} and fractional flow reserve ($\overline{\text{FFR}} = \bar{p}/P_p^H$). The hemodynamic time-dependent quantities were averaged over the last cardiac cycle (first cardiac cycle were periodicity of the solution is achieved). Also, the branch count in the regions of interest, and the fraction of flow at the outlet relative to the total flow rate coming into the coronary tree, denoted FFOI, were compared. Point-wise comparison between Γ_s -averaged quantities was performed. Paired nonparametric Mann-Whitney U-Test (two tailed) and Bland-Altman (BA) analysis of differences were used to show statistical discrepancies between variables from IVUS and CCTA simulations.

Invasive measurements of FFR were available for each vessel of the set. The pressure wire location in the arterial models is manually determined by an expert from the associated angiographic image. A region Ω_{FFR} of approximately 2 mm of length is used to average the FFR field which is used as the computational estimation of FFR. Due to poor image quality, only 1 CCTA model did not reach the measurement domain Ω_{FFR} . In turn, 11 IVUS models did not reach the Ω_{FFR} , because IVUS pullbacks started more proximally than the pressure wire locus at the moment of the FFR test.

7.3 Results

The results for the geometric and computational hemodynamic comparisons are reported in Table 7.3 and Table 7.4, respectively. The correlation was analyzed in terms of the Spearman's correlation because not all features present a normal distribution (which invalidates the Pearson's correlation analysis). Also, it was analyzed the agreement between the two modalities in the sense of Bland-Altman. To ease the comparison across different features, the quantities were normalized by the average value between IVUS and CCTA means. In that manner, the bias and limits of agreement are interpreted as a factor of disagreement between the modalities.

7.3.1 Geometric comparison

The results of the geometric comparison between modalities is detailed in Table 7.3. It is shown a good correlation ($\rho > 0.6$ and $p < 0.01$) between the following characteristics: aspect ratio, bending energy, twisting energy, total curvature, total torsion, total combined curvature, lumen area and volume.

Due to the presence of the IVUS catheter, the three-dimensional model obtained by IVUS may undergo vessel straightening. Analyzing the entire sample, total curvature is smaller in IVUS than CCTA model (4.312 vs 4.784 mm^{-1} , $p < 0.01$) with relative difference of $-18 \pm 36\%$. In Figure 7.3, we present two angiographies that evidence the previous finding. In the images, it is seen that the LCx and LAD arteries feature higher curvature when the transducer is not deployed yet (e.g. sites marked by the arrows). Particularly, a more pronounced rectification is seen in the LCx comparing to the LAD.

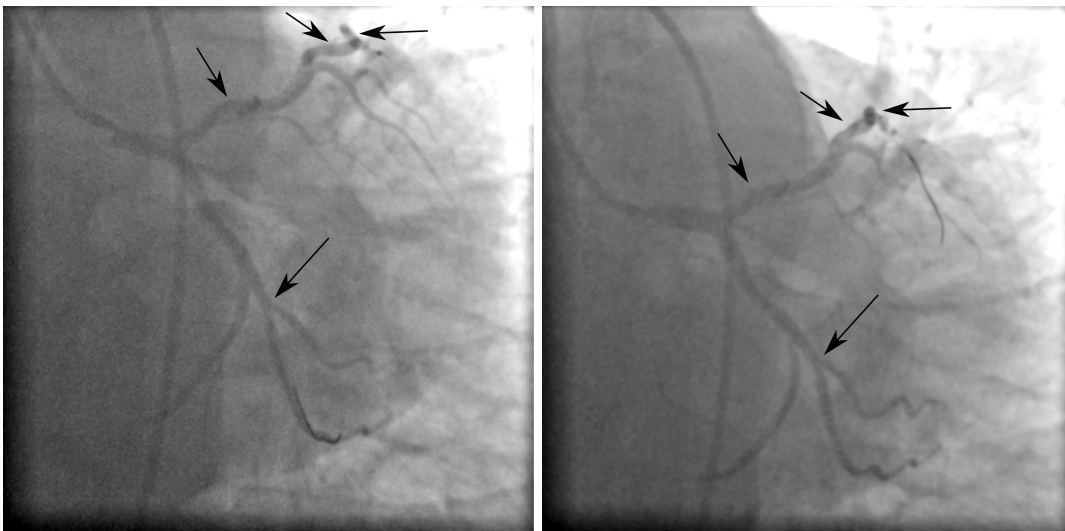


Figure 7.3: Rectification of the vessel due to catheterization: (left) transducer deployment at the left anterior descending coronary artery; (right) transducer deployment at the left circumflex coronary artery.

Geometrical feature	IVUS	CCTA	ρ	Rel. Bias	Rel. LA
Length (mm)	53.877 ± 14.84	53.877 ± 14.84	1	0	0
Tortuosity*	0.118 ± 0.095	0.112 ± 0.058	0.597	-0.059	[-0.733, 0.616]
Mean radius (mm)	1.37 ± 0.162	1.26 ± 0.198	0.467	-0.086	[-0.204, 0.031]
Aspect Ratio	39.608 ± 11.759	43.807 ± 14.689	0.938	0.101	[-0.057, 0.258]
Fractal dimension*	1.029 ± 0.022	1.027 ± 0.014	0.274	-0.002	[-0.022, 0.018]
Torsion Ratio	0.212 ± 0.145	0.177 ± 0.111	0.491	-0.185	[-0.842, 0.472]
Bending Energy	5.162 ± 5.356	6.349 ± 5.128	0.679	0.206	[-0.347, 0.759]
Twisting Energy	390.555 ± 299.848	328.613 ± 255.467	0.771	-0.172	[-0.765, 0.420]
Total Curvature (mm ⁻¹)	4.312 ± 1.878	4.784 ± 1.797	0.648	0.010	[-0.156, 0.363]
Total Torsion (mm ⁻¹)	25.825 ± 11.198	23.796 ± 8.550	0.755	-0.073	[-0.374, 0.227]
Total Combined Curvature (mm ⁻¹)	27.099 ± 11.587	25.710 ± 8.673	0.776	-0.053	[-0.327, 0.222]
Area (mm ²)	534.48 ± 175.90	495.55 ± 164.09	0.906	-0.076	[-0.210, 0.059]
Volume (mm ³)	408.314 ± 177.877	347.012 ± 165.698	0.749	-0.162	[-0.431, 0.106]
Mean Cross-Sectional Area(mm ²)*	7.466 ± 2.023	6.598 ± 2.148	0.469	-0.123	[-0.337, 0.091]
Branch count	5.441 ± 2.017	2.235 ± 1.285	0.437	-0.835	[-1.327, -0.344]

Table 7.3: Statistical analysis of all geometrical features. Mean ± standard deviation are shown for each model and for the relative bias. The bias (CCTA-IVUS) and the limits of agreements (mean±SD) for the Bland-Altman analysis were normalized by the average between IVUS and CCTA means. Features with ρ non statistically significant ($p \geq 0.01$) are indicated by the marker *. Details of the definition of each feature is given in [53].

Among the geometrical features that affect hemodynamic variables, the ones related to the lumen area are the most important. In comparison to CCTA, the IVUS model showed bigger mean radius (1.37 vs 1.26mm, $p < 0.01$), mean cross-sectional area (7.466 vs 6.598 mm², $p = 0.02$), volume of lumen (408.314 vs 347.012 mm³, $p < 0.01$) and area of lumen (534.48 vs 495.55 mm², $p < 0.01$) with relative differences of $8 \pm 10\%$, $10 \pm 19\%$, $13 \pm 27\%$, $6 \pm 11\%$, respectively. These results suggest the systematic underestimation of lumen in CCTA models. Conversely, CCTA has a $18 \pm 36\%$ higher total curvature, a $8 \pm 10\%$ lower average radius and a $10 \pm 19\%$ lower average cross-sectional area. The amount of lateral branches can also influence hemodynamic variables. The IVUS model has a higher lateral branch count than CCTA (5.441 vs 2.235; $p < 0.01$) with relative difference of $58 \pm 26\%$.

7.3.2 Hemodynamic comparison

The statistical analysis for the sample specified in Section 7.2.1 is presented in Table 7.4. It was found that A , \bar{p} and $\overline{\text{OSI}}$ are larger in IVUS than CCTA, while \bar{v} , Re and $\overline{\text{AWSS}}$ are smaller. Such results are confirmed through the U-test with statistical significance of $p < 0.01$. The Bland-Altman analysis (CCTA – IVUS) shows that all variables have significant correlation ($p < 0.01$) with moderate ($0.35 < \rho < 0.6$) to high ($\rho \geq 0.6$) values of the Spearman's correlation coefficient. Figure 7.4 presents the mean \pm SD of the computed hemodynamic quantities for the entire sample, along the normalized centerline.

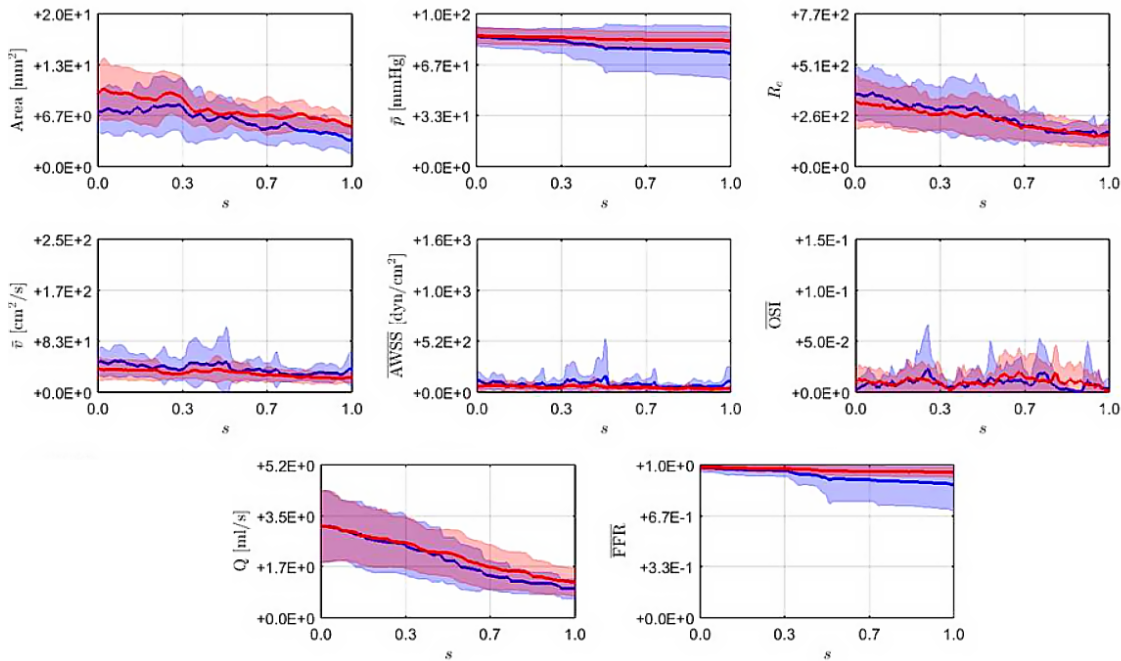


Figure 7.4: Mean (solid lines) and standard deviation (light areas) along the normalized arc length of the centerline for each quantity of interest. Red and blue stand for IVUS and CCTA, respectively.

The smallest relative biases were found for the $\overline{\text{FFR}}$ (-4%), \bar{p} (-5%), Q (-8%) and Re (+8%) while the biggest are seen in $\overline{\text{AWSS}}$ (47%) and $\overline{\text{OSI}}$ (-15%). However, $\overline{\text{OSI}}$ value is relatively small for all cases which hinders a significant comparison. The standard deviation of the bias indicates that \bar{p} and $\overline{\text{FFR}}$ are the less sensitive with respect to the imaging modality (SD 12%), in contrast to $\overline{\text{AWSS}}$ and $\overline{\text{OSI}}$, where SD reaches 140% and 215% respectively. As in the geometric comparison, the area was larger in IVUS, whereas

Hemodynamic quantity	IVUS	CCTA	ρ	Rel. Bias	Rel. IA
A [mm ²]	7.55±2.77	6.07±2.92	0.51	-0.22±0.39	[-0.98, 0.55]
\bar{p} [mmHg]	84±5	79±13	0.92	-0.05±0.12	[-0.29, 0.18]
Re	238±184	257±125	0.74	0.08±0.34	[-0.60, 0.75]
\bar{v} [cm ² /s]	31±14	38±23	0.54	0.23±0.58	[-0.91, 1.37]
$\overline{\text{AWSS}}$ [dyn/cm ²]	49±38	79±92	0.41	0.47±1.39	[-2.25, 3.19]
OSI	0.010±0.015	0.009±0.017	0.38	-0.15±2.15	[-4.36, 4.05]
$\overline{\text{FFR}}$	0.97±0.03	0.93±0.12	0.60	-0.04±0.11	[-0.27, 0.18]
Q [ml/s]	2.15±1.00	1.99±1.06	0.80	-0.08±0.30	[-0.66, 0.51]
Branch count	5.69±2.33	2.5±1.21	0.61	-0.75±0.44	[-1.19, -0.31]
FFOI*	0.21±0.08	0.17±0.09	0.20	-0.11±0.37	[-0.48, 0.26]

Table 7.4: Statistical analysis of all Γ_s -averaged quantities. Mean \pm standard deviation are shown for each model and for the relative bias. The bias (CCTA-IVUS) and the limits of agreements (mean \pm SD) for the Bland-Altman analysis were normalized by the average between IVUS and CCTA means. Only for the fraction of flow between outlet and total inflow (FFOI), the ρ was not statistically significant ($p > 0.05$), which is indicated by the marker *. For all other variables, the Spearman's correlation coefficient ρ is significant ($p < 0.01$).

\bar{v} was larger in CCTA models. This is not a straightforward consequence because the topology of the arterial tree is different between the modalities. In fact, main artery flow rate Q at distal locations may vary because IVUS models feature, in average, 3 more side branches than CCTA models, promoting the blood deviation through proximal branches. Despite this, Q continues to be higher in IVUS, which implies that the flow deviation is actually more significant in the CCTA model. This is also appreciated in the low correlation of FFOI.

Visual inspection of Figure 7.4 shows how the different variables differ in the proximal, mid and distal thirds of the arterial models. Particularly, focusing on the $\overline{\text{FFR}}$ and $\overline{\text{AWSS}}$, differences in the three portions of the arterial segments are reported in Table 7.5. For both variables, correlation decreases towards the distal section. While the $\overline{\text{FFR}}$ relative bias and dispersion increases from proximal to distal thirds, the $\overline{\text{AWSS}}$ results in larger bias in the last two-thirds. Furthermore, arterial tapering is far from linear, and differences in the area between models impact directly in the discrepancies of hemodynamic variables between models. To illustrate such behavior, Figure 7.5 presents scatter plots of discrepancies in $\overline{\text{FFR}}$ and $\overline{\text{AWSS}}$ as a function of the discrepancy in the lumen area (CCTA – IVUS for both cases). As expected, differences in the area are proportional to deviation in the $\overline{\text{AWSS}}$. In turn, deviations in the $\overline{\text{FFR}}$ depend not only of local difference in lumen area, but also on the cumulative pressure drop caused by discrepancies in the lumen area at proximal locations. For instance, discrepancies in the second third of the vessels are caused by lumen area differences at the first third of the vessel.

Hemodynamic Index	IVUS	CCTA	ρ	Rel. Bias	Rel. LA
$\overline{\text{FFR}}$					
Proximal	0.98±0.02	0.97±0.03	0.69	-0.01±0.03	[-0.07, 0.05]
Mid	0.96±0.03	0.92±0.11	0.51	-0.04±0.11	[-0.27, 0.18]
Distal	0.96±0.03	0.89±0.16	0.39	-0.07±0.16	[-0.38, 0.24]
$\overline{\text{AWSS}}$ [dyn/cm ²]					
Proximal	55±40	81± 68	0.54	0.38±0.98	[-1.54, 2.29]
Mid	54±43	93±126	0.43	0.53±1.63	[-2.67, 3.73]
Distal	37±24	63± 66	0.17	0.51±1.33	[-2.01, 3.11]

Table 7.5: Statistical analysis of Γ_s -averaged quantities in the proximal, mid and distal thirds of geometric models. Mean \pm standard deviation are shown for each model and for the relative bias. The bias (CCTA-IVUS) and the limits of agreements (mean \pm SD) for the Bland-Altman analysis were normalized by the average between IVUS and CCTA means. All statistical tests, including correlations were statistically significant ($p < 0.01$).

Regarding invasive FFR measurements for the 16 arteries, the in-vivo measure of FFR was 0.86 ± 0.08 . The computational estimation of the FFR delivered a mean of 0.85 ± 0.16 with CCTA models (with correlation $\rho = 0.70$, $p < 0.01$, and mean difference 0.01 ± 0.18) and 0.95 ± 0.03 for the IVUS models (with correlation $\rho = 0.61$, $p = 0.014$, and mean difference -0.08 ± 0.07).

7.4 Discussion

The unique findings of our study were the geometric confrontation of two three-dimensional models by CCTA and IVUS exposing their differences markedly. Furthermore, accurate description of arterial geometry is relevant for diagnostic evaluation of coronary artery disease (CAD) with classic lumen measurements [29, 262] or such as a CAD risk

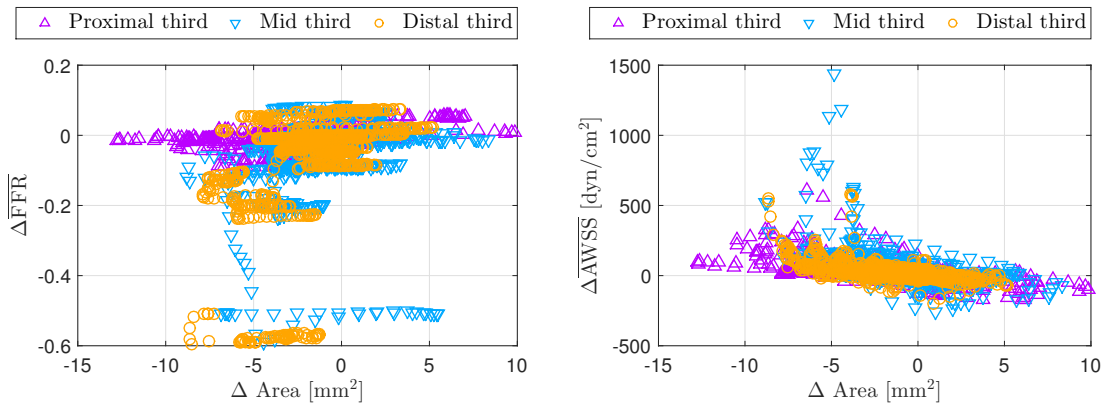


Figure 7.5: Scatter plots featuring differences between IVUS and CCTA models: (left) $\overline{\Delta FFR}$ and (right) $\overline{\Delta AWSS}$, against differences in area, in the entire sample. The position, i.e. proximal, mid and distal third, are identified.

factor [166, 171, 207]. Features of each model can influence on interpretation of the other and emphasize some aspects to improve plaque evaluation and flow simulations. While it is possible to retrieve the correct spatial information of the coronary arteries provided by CCTA; on the other hand, the IVUS delivers a more refined anatomical vasculature in terms of lumen area and branch count. The higher confidence in the geometrical description of the lumen in IVUS images is not only due to the higher resolution, but also by the fact that the images display the physical boundary of the lumen, whereas the CCTA visualizes only the contrast within the lumen (which can be attenuated distally). A clear phase consistent description of the vessel in IVUS can only be achieved by using the gating technique presented in Chapter 2. Without such preliminary processing, the lumen area and the spatial position may present severe oscillations due to the vessel deformation along the cardiac cycle. However, IVUS clinical procedure focuses on one (or two) arterial vessel, and inclusion of branches in the geometric models is an arduous task. In this aspect, CCTA segmentation of lateral branches and, overall, a global topological description, is easier.

With respect to the vascular lumen, the IVUS model realizes a larger mean radius, cross-sectional area, volume and area of lumen in the full sample. In fact, if we analyze the relative errors, the mean radius and cross-sectional area are 8% and 10% higher in IVUS than CCTA, respectively. These findings remained in accordance with earlier studies. We found that the underestimation of the vascular lumen by CCTA is critical, being 6% smaller in total area lumen and 13% smaller in total volume of the whole vessel. This might be explained by: i) low image resolution of CCTA; ii) effect of calcium in lumen measurements [45, 141, 242, 318]; and iii) the natural tapering of vessels may be distorted due to attenuation of contrast intensity in distal regions [74]. Hoffmann et al. [140] showed that CCTA can underestimate the lumen in comparison with QCA, especially in the presence of large calcified plaques which appear enlarged (blooming effect). Kruk et al. [175] showed that CCTA significantly underestimated coronary lumen area within calcified lesions by a mean of 5%. The mean calcium score of our sample is 218, lower than other studies which detected lumen underestimation in CCTA (DeFACTO study at 381 and Kruk et al. at 433) [175, 240]; and the mean total length of analyzed arteries are 54mm in IVUS and CCTA ($p = 0.2$), just contemplating the proximal and middle portions of coronary arteries, avoiding the use of distal portions which commonly result in impairment of image quality on CCTA. Likewise, it was previously shown that in cases of ambiguous lesions CCTA correlates better with the IVUS than angiography [246]. Nevertheless, we

still had smaller lumen in CCTA in all geometric features analyzed.

Despite the poor results achieved in the estimation of lesion significance with anatomic data, the intravascular image modalities are often used for this purpose [328]. In fact, the capabilities for the estimation of lesion significance strongly depend on the methodological aspects behind the definition of patient-specific physiology, which is hard to quantify in clinical routine. However, CFD simulations allow the integration of the anatomy and physiology to evaluate the coronary lesions and have obtained much improvement notably with image extracted from CCTA. CFD simulations depend on the geometry of the arterial domain and on boundary conditions. Moreover, under many hypotheses the latter depends on the former. Therefore, the impact of geometric discrepancies between two coronary models (CCTA and IVUS) over hemodynamic variables is of the utmost importance to understand CFD outcomes. Despite the growing interest in FFR by anatomical methods, the recent DeFACTO study obtained disappointing results. Due to exponential relationship between the area of the stenosis and coronary resistance, even small errors can result in substantial inaccuracy of FFR values. In this work, CCTA underestimate the mean cross-sectional area in a 11.6%, which consequently overestimates the degree of stenoses [240]. It may be speculated that the computational FFR method, irrespective of the accuracy of blood flow models, remains subject to imperfect lumen delineation within lesions. The overestimation of lesions may be associated not only to the presence of calcium, but as importantly, to a smaller lumen. Kruk et al. [176] demonstrated that the coexistence of calcium arc exceeding 47° and mean lumen diameter of < 2.9 mm as the most accurate marker of excessive lumen underestimation by coronary CCTA.

Most of the coronary lesions included in our sample are intermediate lesions, and this is the case where the functional evaluation is necessary and the image quality really matters. In general, we obtained a good correlation of all area and volumetric features (with certain disagreement in the mean cross-sectional area) between the IVUS and the gold standard for spatial information, CCTA. Some differences were found in curvature due to coronary rectification produced by IVUS catheter and tapering overestimation in CCTA due to distal contrast attenuation and calcium artifacts. Thus, some concerns have to be taken into account in: extremely tortuous vessels in IVUS (not included in this study) where significant underestimation of curvature and lumen volume (ghost lesions) can be found; and in the excessive tapering in distal regions for the CCTA models.

Regarding the computational hemodynamic comparison, it is seen that the smaller lumen area consistently yields larger blood velocity, forcing the pressure to drop more markedly in CCTA than in IVUS models. Focusing on the pressure and FFR, the sensitivity to the imaging modality increases as we move distally. The underestimated lumen area of the CCTA models also results in larger AWSS, for roughly the same flow rate. Differently from the pressure and FFR, the bias and limits of agreement of the wall shear stress are extremely wide, which indicate that wall shear stress estimation from CCTA is to be carefully regarded when correlating this to coronary disease, at least under hyperemic conditions. In turn, the oscillatory shear index featured small values in both imaging modalities, which is consistent with the fact that no retrograde flow occurs along the cardiac cycle. Although it is not the focus of this work, the comparison between invasive FFR to computational FFR shows promising results. The better correlation with CCTA models is explained by the fact that the used IVUS computational domains did not reach the FFR acquisition site. Then, the pressure drop was underestimated because the FFR was estimated at a more proximal site of the artery.

7.4.1 Limitations

Due to the unblinded nature of the comparison of the FFR and small sample size, it was not carried out a comparison of FFR-CCTA and FFR-IVUS with the FFR measured

by a pressure wire. The present study has a relatively small number of vessels to generalize the obtained findings. Nevertheless, collecting the amount of data for each patient is an extremely complex task, and the results reported here have helped to elucidate some of the main drawbacks when trying to simulate coronary blood flow under hyperemic conditions. Strengths and weaknesses of each modality in terms of the geometric and hemodynamic features were highlighted, as well as some concerns to take into account when interpreting results from CCTA or IVUS models.

The study is retrospective by image processing of data already acquired in daily routine catheterization laboratory, and there may be subtle differences in the image acquisition for each patient such as the presence or absence of sedation interfering with hemodynamic and breaths.

7.5 Final remarks

In this chapter, we presented a geometric and computation hemodynamic comparison in coronary arteries performed on top of geometric models constructed from IVUS and CCTA imaging modalities. A good correlation between modalities was found in global geometrical descriptors such as area and volume. It was observed that the major factor affecting hemodynamics was arterial geometry, more specifically, lumen cross-sectional area which is distally underestimated by CCTA models. Wall shear stress and blood velocity were significantly sensitive to the lumen radius. In turn, pressure and FFR were less sensitive, although pressure drop is systematically higher in CCTA models. As consequence of the smaller lumen area rendered by CCTA, and even featuring less proximal side branches, these models are more affected by coronary steal phenomenon than IVUS ones. This fact implies that the IVUS model carries more flow rate than the CCTA model in the major vessel of interest, which counterbalances the effect of IVUS having a larger lumen area for the computational FFR assessment.

The statistical analysis indicates that care must be taken when drawing conclusions from computational simulations of coronary flow. As in some cases the agreement in both modalities was quite good, certain calcified lesion or excessive tapering produced in CCTA may lead to overestimation of blood velocity, wall shear stresses, pressure drop and, finally, underestimation of FFR. Also, excessive tortuous vessels may present ghost lesions or artificial straightening in IVUS models leading to less reliable AWSS estimations.

Chapter 8

Conclusions

This chapter acts as a counterpoint of the introduction, it exposes the advance along the roadmap initially traced detailing the contributions obtained and the goals achieved. In this denouement, we draw general conclusions for each of the three parts of the manuscript with the intent of integrating the independent conclusions outlined at the end of each chapter. Ultimately, a general conclusion of this thesis is elaborated, establishing its significance in the context of the state-of-the-art.

8.1 Contributions

Several methods were developed to achieve the biomechanic characterization of the vessel wall. Their usage far exceeds the current methodology, allowing diverse applications in research and clinical practice. Next, it is detailed each contribution of this work and their potential uses:

Gating method for IVUS A novel method that integrates frame motion descriptors was proposed. The combination of uncorrelated descriptors improved the accuracy to estimate the vessel motion. Based on the inferred motion and knowledge of the cardiac phases, it was developed a methodology to gate not one but several cardiac phases from an IVUS study. The method can also be used for

- Visualization of the vessel deformation along the cardiac cycle: it is available new gated studies showing the vessel at different cardiac phases, then a temporal sequence for the longitudinal view of the vessel is straightforwardly available;
- Removal of artifacts from longitudinal view associated with the entanglement of all cardiac phases (saw-tooth artifact);
- Creation of motion free IVUS sequences: A gated phase presents lower to no motion between the frames, aligning the vessel structures from one frame to the next one. This eases segmentation or structure recognition tasks;
- Time-coherent reconstruction of the vessel from IVUS images: As the gated sequences contains all frames for the same cardiac phase, the spatial description of the vessel in such sequences is temporally-coherent and allows to reconstruct the vessel in a specific cardiac phase.

Registration of cardiac phases Using the previous gating method, several IVUS sub-sequences are obtained, each one corresponding to a specific cardiac phase. To obtain the frames across these sub-sequence that are associated with the same vessel cross-section, it was developed a novel method of longitudinal and transversal registration. This endows the previous gating with a semi-rigid mapping (non-rigid longitudinally and rigid transversally) of the vessel structures along the cardiac cycle. The method can be used for

- Recovering of the deformation of a vessel cross-section along the cardiac cycle;
- Quantification of the longitudinal deformation of the vessel along the cardiac cycle (see Sections 3.3.5 and 3.3.6);
- Quantification of the transversal motion at each vessel cross-section which can be used as an additional feature in geometrical studies as the one presented in Chapter 7;
- Accurate spatio-temporal reconstruction of the vessel: Additionally to the classic end-diastolic phase reconstruction of the vessel, it can be reconstructed all other phases with neither longitudinal nor transversal displacement between the cross-sections.
- Estimation of the local pulsatility of the vessel.

Denosing method for IVUS A novel denosing method was specifically developed to remove speckle noise originated from high-frequency ultrasonic images. By knowing that the IVUS noise follows a generalized gamma distribution, it was created a log-likelihood estimator for such images. Using this estimator, it was derived a tailored denosing method. By varying the log-likelihood estimator to other type of noises, the same methodology allowed the creation of noise specific denosing methods. The method can be used for

- Improving segmentation and structure recognition methods;
- Improving optical flow performance;
- Enhancing the visualization of structure of the vessel wall;

Data assimilation environment for the setup and analysis of arterial models

A data assimilation environment was carefully developed in this work integrating displacement data extracted from medical images. We use data assimilation techniques already employed in the literature for linear elastic arterial models [33, 34]. Nevertheless, the setup here proposed integrates the data assimilation strategy with more realistic arterial models and vessel conditions such as axial strain, preload and external tissue (the later was not analyzed in this work) [22, 41]. The data assimilation environment can be used for

- The study of the axial strain level on patient-specific arteries by adding this parameter to the data assimilation process;
- The study of the external tissues contributions on patient-specific arteries by adding the associated parameters to the data assimilation process;
- Identification of the material distribution on patient-specific arteries by performing a domain partitioning adaptive process. Some criteria for domain partitioning can be the discrepancy between the OF observation and the mechanical displacements after the data assimilation process.

8.2 Partial conclusions

Each chapter presented partial and independent conclusions. Here, we summarize and integrate the outcomes of the chapters in each part of the thesis, highlighting the most important findings.

8.2.1 Image processing of IVUS studies

Novel methods for gating, registration and denoising tailored specifically for IVUS were developed in this work. The gating and denoising methods showed to outperform the state-of-the-art alternatives for the IVUS processing in the processed phantom and IVUS studies. In turn, the registration and gating methods were validated against a ground truth manually constructed by specialists from more than 50 IVUS studies (52 and 61, respectively). In both cases, the automatic methods showed an accuracy comparable to the specialists. The denoising method presented an interesting methodology for the construction of a family of specific purpose methods to enhance images with known noise statistics.

Additionally, methods of optical flow from the literature were studied focusing their applicability to IVUS images. The Weickert method, which showed to be the more promising strategy, was implemented using a parallel and efficient numerical scheme. As other optical flow methods, the Weickert approach diminishes its performance in the presence of noise. The denoising method showed to remove the speckle delivering more consistent patterns for optical flow computation.

As a general result of this part of the thesis, the developed automatic methods have enabled extraction of the displacement field for a vessel cross-section of interest, in several cardiac phases. This delivers an unprecedented tool for IVUS processing with the following features: i) rearrangement of the study data by cardiac phase; ii) quantification of the longitudinal displacement of each vessel cross-section along the cardiac cycle; and iii) extraction of sequences along the cardiac cycle for a vessel cross-section of interest, this is fundamental to study the stresses within atherosclerotic lesions.

8.2.2 Biomechanical characterization of the vessel wall

A self-contained description of the vessel anatomy and atherosclerotic plaque histopathology was presented focusing in the coronary vessels. From this review, modeling decisions and hypotheses were taken to determine adequate models for vessel and plaque tissue representation. Physiological ranges in coronary arteries for the parameters of such models were also reported to establish a proper numerical setup for solid mechanics simulations. Based on previous works [22, 41], vessel preload and axial stretch were taken into account to obtain more realistic physiological conditions. Hence, a pipeline to construct patient-specific geometrical models of the vessel wall suitable for solid mechanics simulations was developed.

The patient-specific geometrical models and numerical simulations under realistic physiological conditions, were combined with the data assimilation technique known as reduced order unscented Kalman filter. In-silico experiments were used to test the capabilities of the method to estimate constitutive parameters of the vessel wall when the displacement field of the arterial wall between two cardiac phases is known. From these experiments, it was seen that parameters for plaque materials can be estimated as long as the pressure difference between the cardiac phases deforms the tissues “sufficiently”. The necessary deformation has to be observable (more than a pixel in the IVUS image) and higher than the expected observation noise (which is modeled by the observation uncertainty parameter). Preliminary in-vivo experiments were presented showing the successful

integration of the Kalman strategy with the optical flow estimated as proposed in the first part of this work. Further research is required to dynamically perform domain partitioning towards a correct identification of the materials distribution. As the preliminary results suggest, an accurate domain partition (as well as the inclusion of other modeling factors such as surrounding tissues) is essential to successfully reproduce the observed displacement field, which is a mandatory condition for the estimation of the vessel wall parameters.

The developed tools in this part of the thesis settle a framework for the study of the biomechanical characterization of the vessel wall. Thus, further work is still to be done to adjust the current methodology and models for in-vivo scenario. This motivates to future work described in Section 8.4.

8.2.3 Medical applications

The collaboration with other members of the HeMoLab group and physicians allowed to apply the here developed tools (and also previous developed tools [212]) in studies with relevance in the clinical practice. The image processing tools enabled the reconstruction of patient-specific geometrical models for coronary arteries where geometric and hemodynamic features were estimated.

The studies delivered insights about the differences obtained with CCTA and IVUS image modalities. The study was centered in the analysis of the weaknesses and strengths of each imaging technique. A complete comparison between the geometric and hemodynamic features obtained with each modality was reported. The features were estimated in a small sample of 28 patients (and a sub-group of 11 patients for the hemodynamic comparison) targeting a more individual comparison and interpretation of the cases. The most notable outcomes revealed that CCTA models are less accurate in zones near calcified lesions while IVUS models present a less accurate description of the vessel curvature due to the rectification provoked by the catheter.

Further medical studies are currently in progress using the gating and registration methods for the computational assessment of fractional flow reserve and quantification of the axial deformation of the vessel during stent deployment.

8.3 General conclusions

A methodology towards in-vivo mechanical characterization of the vessel wall was developed. It is a bridge from the IVUS study to a patient-specific geometrical model that incorporates the displacements observed in the medical images. All image processing steps that yield such data are completely automatized allowing the processing of large amount of patients without human intervention. Hence, a data assimilation scheme was proposed, which has shown to be capable of estimating the mechanical properties of a model when precise observations and tissues distribution are given. Further research has to be conducted to obtain a patient-specific and in-vivo mechanical characterization of the vessel wall. Sensitivity studies regarding the estimated parameters with respect to the domain partition error, more ex-vivo data regarding axial stretch, mechanical properties of the adventitia in a wide sample of the population and the study of the incorporation of surrounding tissues for the analyzed vessel, are in order.

An advantage of the proposed methodology is that, beyond from the mechanical characterization of the vessel wall, other typical features of arterial vessels can potentially be studied such as the surrounding tissue distribution, axial stretches, or any other phenomenon that can be modeled in terms of specific parameters of the mechanical or geometrical model. Also, the constitutive laws of the materials can be changed without

any modification to the methodology, only the data assimilation parameters to be optimized. Furthermore, the present methodology is highly decoupled allowing to work in any of the stages (for example, proposing optical flow alternatives to enhance the quality of the observations) without compromising the rest of the steps.

Related to the goals traced at the beginning of this work, all of them were successfully achieved and several publications were produced in congresses, journals and books, reporting the partial contributions along the production of this manuscript. In addition, other parts of this work are pending to be published in the near future. Also, contributions beyond the initial roadmap were produced due to the team work with other members of the HeMoLab group, e.g., the results presented in Chapter 7.

The collaboration with institutions such as Incor and Sirio Libanés, constituted a challenge for this work, and endowed this thesis with large amounts of data for validation of the image processing methods, as well as enriched the diverse discussions regarding clinical results and presented possibilities to develop closely related works that were published in congresses and journals. Hence, such collaboration motivated the writing of the anatomical and atherosclerotic plaque description by the knowledge acquired from researchers in these institutions, as well as from members of the HeMoLab group along the post-graduation program. As result of working side-by-side with such professionals, this work earned an extra dimension of multi-disciplinarity.

Also, the availability of the HPC environment (MACCHPC and Santos Dumont clusters) at LNCC allowed the processing of computationally demanding task consuming thousands of allocation units. The use of these resources is materialized in: i) the parameters study of the gating, registration, denoising and optical flow methods; ii) the validations of the gating and registration methods; and iii) the computational fluid dynamics simulations used in the medical applications.

8.4 Future works

The present methodology opens several new possibilities for future works such as: i) the enhancement of the methods used in the different stages, ii) the use of developed components for clinical studies; and iii) the increase of models complexity to engage further research in the mechanical characterization of vessels. Next, the future works which branch out from this thesis are addressed:

- The integration of the developed image processing tools in this work and a previous one [212] in a unified software for the manipulation of IVUS studies, allowing to recover geometric models, perform mechanical parameter estimation of the vessel wall components, gating, examination of a fixed cross-section of the vessel along the cardiac cycle, among other tasks.
- The development of non-rigid registration techniques based on optical flow.
- The development of a generalized methodology to obtain denoising methods, specific to remove noise with known probability density functions.
- The development of new optical flow solutions that combine temporal data from several frames to obtain a more robust estimate of the vessel wall displacement.
- The extension of the optical flow method to estimate the flow between the different gated cardiac phases.
- The development of methods for domain partitioning that are based on the displacement error obtained from the data assimilation process presented in Chapter 6.

- The study of different constitutive laws to model the tissues and analyze their impact on the outcome of the data assimilation process. In particular, models with physically meaningful parameters would allow to extract more biological information about the vessel and its inner structures, e.g., the collagen fiber orientation, quantification of GAG/PGs proportion in the tissue, among others.
- The study of the surrounding tissues of the coronary arteries and their mechanical contribution to the vessel stress state along the cardiac cycle. Poor knowledge is reported about the coronary vessels fixation to the epicardium and other surrounding tissues, the insights in this topic will contribute to the anatomical and mechanical description of the coronary vessels.
- The extension of the data assimilation process to 3D geometries for the whole vessel of interest.
- The estimation of axial stretch in healthy places of the coronary arteries by using the proposed data assimilation process.
- The study of axial deformation of the coronary vessels when a stent is deployed. There is no report of this phenomenon in the literature and it is medically relevant to assess: i) the condition of the vessel after implantation, ii) the success of the stent deployment; and iii) the stent design to use in each specific scenario.

Appendix A

Guidewire detection

For simplicity, the polar representation of the frames, $\hat{J}_k(r, \theta)$, $r = 1, \dots, R$, $\theta = 1, \dots, S$, is employed for the identification of artifacts. To preserve the IVUS frame quality and avoid oversampling, we choose $R = 256$ and $S = 256$, given that the IVUS transducer performs 256 individual radial scans of 256 pixels of resolution through the acquisition of each frame [224].

The down-ring artifact fixed in size and space affects a rounded central region of the image at a neighborhood of the transducer. Then, we identify, by visual inspection, this region along 45 IVUS studies as the first 45 lines of the polar representation. Thus, the mask in polar coordinates for the down-ring artifact is the same for all frames, and is defined as

$$\hat{M}_{\text{DR}}(r, \theta) \begin{cases} 0 & r > 45, \\ 1 & 0 < r \leq 45. \end{cases} \quad (\text{A.0.1})$$

The guidewire artifact is identified through a semi-automatic approach. First, two rows enclosing the artifact must be marked in the frames J_l , $l \in \mathcal{L} = \{100 \times m + 1, m = 0, \dots, \lfloor \frac{\# \text{ study frames}}{100} \rfloor\}$ of the IVUS study. Then, each of the enclosed regions, denoted as R_{UGW}^l , is used to detect the guidewire position in the subsequent 99 frames. Given the low shape variation of this artifact signature along adjacent frames, normalized cross-correlation and a sliding window (in polar space) are used to assess the angular displacement of the artifact. Let us define $R_{\text{W}}(\hat{J}_k, \theta_k)$ as the region in \hat{J}_k enclosed at the same position of the previous R_{UGW}^l but angularly displaced θ_k pixels. Also, we consider \hat{J}_k to be cyclic in its second argument with period equal to S , i. e., the pixels $\hat{J}_k(r, S + m) = \hat{J}_k(r, m)$. Then, the guidewire region for the frame \hat{J}_k is calculated as follows

$$R_{\text{GW}}^k = \arg \max_{\theta_k \in [-M, M]} c(R_{\text{UGW}}^l, R_{\text{W}}(\hat{J}_k, \theta_k)), \quad (\text{A.0.2})$$

where l is the maximum value in \mathcal{L} such that $l < k$. To reduce computational cost, the search range is reduced to $M = 30$ due to the small in-plane motion of the guidewire along the 99 frames. Finally, the mask in polar coordinates for the guidewire artifact is defined as

$$\hat{M}_{\text{GW}}^k(r, \theta) = \begin{cases} 0 & (r, \theta) \notin R_{\text{GW}}^k \\ 1 & (r, \theta) \in R_{\text{GW}}^k. \end{cases} \quad (\text{A.0.3})$$

After identification of the guidewire artifact, an expert assesses the correctness of the solution and adjusts it if necessary. For all the studies processed no adjustment was needed. The success in the guidewire identification is related to the particular artifact pattern. It presents a saturation in the guidewire location and a clear drop in intensity over the metal boundaries. Although it was not reported for the processed studies, bare-metal stents and calcifications may project shadows similar to the guidewire, potentially

misleading the artifact identification. More complete studies including different plaque morphologies and histologies must be performed in order to guarantee the success of the algorithm under different scenarios.

Appendix B

Discrete gradient ascendant method

To use a gradient ascendant method for the functional \mathcal{F} over \mathcal{U} , we must find a continuum representation of space, say $\tilde{\mathcal{U}}$, to evaluate the function in non-defined coordinates of \mathcal{U} (i.e., $\tau_i \notin [\tau_i^{\text{MIN}}, \tau_i^{\text{MAX}}]$ or $\theta \neq i \frac{\pi}{128}, i = 0, \dots, 255$). A straightforward solution that avoids spurious minima in the non-defined elements of \mathcal{U} , is to perform a linear interpolation of the defined values. Given that each evaluation of the function $\mathcal{F}(\Xi)$ implies the rotation, translation and cross-correlation computation over an image, we choose approximations for $\mathcal{F}(\tilde{\Xi})$ and $\nabla \mathcal{F}(\tilde{\Xi}), \tilde{\Xi} \in \tilde{\mathcal{U}}$ that minimize the evaluations. In that manner, $\mathcal{F}(\tilde{\Xi})$ is estimated with the four nearest defined values $\mathcal{F}(\Xi), \Xi \in \mathcal{U}$ by applying barycentric interpolation. The gradient $\nabla \mathcal{F}(\tilde{\Xi})$ is approximated as

$$\nabla \mathcal{F}(\tilde{\Xi}) = \left(\frac{\partial \mathcal{F}}{\partial \tau_x}(\tilde{\Xi}), \frac{\partial \mathcal{F}}{\partial \tau_y}(\tilde{\Xi}), \frac{\partial \mathcal{F}}{\partial \theta}(\tilde{\Xi}) \right) \quad (\text{B.0.1})$$

being

$$\frac{\partial \mathcal{F}}{\partial \eta}(\tilde{\Xi}) = \omega_\eta(\tilde{\Xi}) \frac{\mathcal{F}(\Xi + \Delta\eta) - \mathcal{F}(\Xi)}{\Delta\eta} + (1 - \omega_\eta(\tilde{\Xi})) \frac{\mathcal{F}(\Xi) - \mathcal{F}(\Xi - \Delta\eta)}{\Delta\eta},$$

$$\eta \in \{\tau_x, \tau_y, \theta\}, \quad (\text{B.0.2})$$

where Ξ is the nearest (in the sense of the \mathcal{U} norm, see Eq. (3.3.1)) defined coordinate to $\tilde{\Xi}$ in \mathcal{U} , $\Delta\tau_x = \Delta\tau_y = 1$, $\Delta\theta = \pi/128$ and ω is defined as follows

$$\omega_\eta(\tilde{\Xi}) = \frac{\tilde{\Xi} \cdot \check{\eta} - \Xi \cdot \check{\eta}}{\Delta\eta} + \frac{1}{2}, \quad (\text{B.0.3})$$

where $\check{\eta}$ is the η versor and \cdot stands for the standard inner product. We choose this approximation for the gradient because it only requires seven evaluations of the function $\mathcal{F}(\Xi)$.

Finally, we use a gradient ascend method with the backtracking line search over $\tilde{\mathcal{U}}$. This method offers a suitable trade-off between the convergence ratio and the amount of $\mathcal{F}(\Xi)$ evaluations.

Appendix C

Application of variational calculus

In this appendix, we detail the variational calculus used with the development of some optimization problems introduced in the manuscript. For each of them, we show the necessary and sufficient conditions for optimization and, then, we derive the Euler-Lagrange equations associated to the problems.

C.1 Maximum likelihood variations

Given the minimization problem presented in Section 4.2.2, stated as

$$I_d = \arg \min_{\tilde{I}} \int_{\Omega} \left(-c(I_o(x, y), \tilde{I}(x, y)) + \alpha |\nabla \tilde{I}(x, y)| \right) d\Omega, \quad (\text{C.1.1})$$

where

$$c(I_o(x, y), \tilde{I}(x, y)) = \gamma \nu (I_o(x, y) - I_d(x, y)) - \frac{1}{\delta \gamma} e^{\gamma(I_o(x, y) - I_d(x, y))}, \quad (\text{C.1.2})$$

we have to find the minimizer function $\tilde{I}(x, y) \in \mathcal{U}$, where

$$\mathcal{U} = \{ \tilde{I}(x, y) \in \mathbb{R}^{n, m}; \tilde{I}(x, y), \nabla \tilde{I}(x, y) \text{ are square-integrable functions} \}. \quad (\text{C.1.3})$$

To ease the readability, let us simply denote $I(x, y)$ as I . Introducing C.1.2 in C.1.1, we obtain the following functional

$$\mathcal{F}(\tilde{I}) = \int_{\Omega} \left(-\gamma \nu (I_o - \tilde{I}) + \frac{1}{\delta \gamma} e^{\gamma(I_o - \tilde{I})} + \alpha |\nabla \tilde{I}| \right) d\Omega. \quad (\text{C.1.4})$$

We use variational calculus to analyze the necessary and sufficient conditions for the function to be a minimizer. Thus, we perturb the function \tilde{I} as $\tilde{I} + \tau \eta$ with $\eta \in \mathcal{U}$.

The resulting perturbed functional is presented as follows

$$\mathcal{F}(\tilde{I} + \tau \eta) = \int_{\Omega} \left(-\gamma \nu (I_o - \tilde{I}) + \gamma \nu \tau \eta + \frac{1}{\delta \gamma} e^{\gamma(I_o - \tilde{I})} e^{-\gamma \tau \eta} + \alpha |\nabla \tilde{I} - \tau \nabla \eta| \right) d\Omega. \quad (\text{C.1.5})$$

The necessary condition is obtained when the first Gâteaux derivative of \mathcal{F} is nullified for any admissible perturbation η , i.e., $\delta \mathcal{F}(\tilde{I}, \eta) = 0, \forall \eta \in \mathcal{U}$. Then, we calculate such

condition as follows

$$\begin{aligned}
\delta\mathcal{F}(\tilde{I}, \eta) &= \left. \frac{\partial\mathcal{F}(\tilde{I} + \tau\eta)}{\partial\tau} \right|_{\tau=0} \\
&= \int_{\Omega} \left(\gamma\nu\eta - \frac{\gamma}{\delta\gamma} e^{\gamma(I_o - \tilde{I})} \eta + \alpha \frac{1}{|\nabla\tilde{I}|} \left(\frac{\partial\tilde{I}}{\partial x} \frac{\partial\eta}{\partial x} + \frac{\partial\tilde{I}}{\partial y} \frac{\partial\eta}{\partial y} \right) \right) d\Omega \quad (\text{C.1.6}) \\
&= \int_{\Omega} \left(\gamma\nu\eta - \frac{\gamma}{\delta\gamma} e^{\gamma(I_o - \tilde{I})} \eta + \alpha \frac{\nabla\tilde{I} \cdot \nabla\eta}{|\nabla\tilde{I}|} \right) d\Omega = 0, \quad \forall \eta \in \mathcal{U}.
\end{aligned}$$

To determine if the extreme in $\delta\mathcal{F}(\tilde{I}, \eta) = 0$ is maximum or minimum, we inspect the sign of the second Gâteaux derivative $\delta^2\mathcal{F}(\tilde{I}, \eta)$ obtained as follows

$$\begin{aligned}
\delta^2\mathcal{F}(\tilde{I}, \eta) &= \left. \frac{\partial^2\mathcal{F}(\tilde{I} + \tau\eta)}{\partial\tau^2} \right|_{\tau=0} \quad (\text{C.1.7}) \\
&= \int_{\Omega} \left[\frac{\gamma^2}{\delta\gamma} e^{\gamma(I_o - \tilde{I})} \eta^2 + \alpha \frac{\nabla\eta \cdot \nabla\eta}{|\nabla\tilde{I}|} + \alpha \nabla\tilde{I} \cdot \nabla\eta \delta \left(\frac{1}{|\nabla\tilde{I} + \tau\eta|} \right) \right] d\Omega
\end{aligned}$$

where

$$\begin{aligned}
\delta \left(\frac{1}{|\nabla\tilde{I} + \tau\eta|} \right) &= \left. \frac{\partial}{\partial\tau} \left(\left(\frac{\partial\tilde{I}}{\partial x} + \tau \frac{\partial\eta}{\partial x} \right)^2 + \left(\frac{\partial\tilde{I}}{\partial y} + \tau \frac{\partial\eta}{\partial y} \right)^2 \right)^{-1/2} \right|_{\tau=0} \quad (\text{C.1.8}) \\
&= -\frac{1}{|\nabla\tilde{I}|^3} \nabla\tilde{I} \cdot \nabla\eta.
\end{aligned}$$

Replacing C.1.8 in C.1.7 and rearranging terms

$$\begin{aligned}
\delta^2\mathcal{F}(\tilde{I}, \eta) &= \int_{\Omega} \left[\frac{\gamma^2}{\delta\gamma} e^{\gamma(I_o - \tilde{I})} \eta^2 + \alpha \frac{\nabla\eta \cdot \nabla\eta}{|\nabla\tilde{I}|} - \alpha \frac{1}{|\nabla\tilde{I}|^3} (\nabla\tilde{I} \cdot \nabla\eta)^2 \right] d\Omega \quad (\text{C.1.9}) \\
&= \int_{\Omega} \left[\frac{\gamma^2}{\delta\gamma} e^{\gamma(I_o - \tilde{I})} \eta^2 + \frac{\alpha}{|\nabla\tilde{I}|} \left(\nabla\eta \cdot \nabla\eta - \left(\frac{\nabla\tilde{I}}{|\nabla\tilde{I}|} \cdot \nabla\eta \right)^2 \right) \right] d\Omega.
\end{aligned}$$

Note that the first term of the integral is always positive, and the second term is positive if

$$\begin{aligned}
\frac{\alpha}{|\nabla\tilde{I}|} \left(\nabla\eta \cdot \nabla\eta - \left(\frac{\nabla\tilde{I}}{|\nabla\tilde{I}|} \cdot \nabla\eta \right)^2 \right) &\geq 0 \\
\nabla\eta \cdot \nabla\eta - \left(\frac{\nabla\tilde{I}}{|\nabla\tilde{I}|} \cdot \nabla\eta \right)^2 &\geq 0 \quad (\text{C.1.10}) \\
\nabla\eta \cdot \nabla\eta &\geq \left(\frac{\nabla\tilde{I}}{|\nabla\tilde{I}|} \cdot \nabla\eta \right)^2 \\
|\nabla\eta| |\nabla\eta| \cos\theta &\geq \left(\left| \frac{\nabla\tilde{I}}{|\nabla\tilde{I}|} \right| |\nabla\eta| \cos\theta \right)^2 \\
|\nabla\eta|^2 &\geq |\nabla\eta|^2 (\cos\theta)^2
\end{aligned}$$

where θ is the angle between $\frac{\nabla\tilde{I}}{|\nabla\tilde{I}|}$ and $\nabla\eta$. As $(\cos\theta)^2 \leq 1 \Rightarrow |\nabla\eta|^2 \geq |\nabla\eta|^2 (\cos\theta)^2 \Rightarrow$ the second term is always positive. As both terms are always positive, then $\delta^2\mathcal{F}(\tilde{I}, \eta) \geq 0, \forall \eta \in \mathcal{U}$, implying that $\delta\mathcal{F}(\tilde{I}, \eta) = 0$ is a minimum. Note that only $\eta = 0$ nullifies the first term since $\gamma \neq 0$ (from the definition of generalized gamma distribution). Also, the

second term can be rewritten as

$$\frac{\alpha}{|\nabla \tilde{I}|} |\nabla \eta|^2 \left(1 - (\cos \theta)^2\right) \quad (\text{C.1.11})$$

where only spatially homogeneous η variations or $\nabla \eta \parallel \nabla I$ nullifies such term. Then, both terms are nullified at the same time if and only if $\eta = 0$, implying that the uniqueness of the minimum.

Finally, we integrate by parts C.1.6 as follows

$$\delta \mathcal{F}(\tilde{I}, \eta) = \alpha \frac{\nabla \tilde{I}}{|\nabla \tilde{I}|} \cdot \mathbf{n} \eta \Big|_{\partial \Omega} + \int_{\Omega} \left[\gamma \nu \eta - \frac{\gamma}{\delta \gamma} e^{\gamma(I_o - \tilde{I})} \eta - \alpha \operatorname{div} \left(\frac{\nabla \tilde{I}}{|\nabla \tilde{I}|} \right) \eta \right] d\Omega = 0, \quad \forall \eta \in \mathcal{V}, \quad (\text{C.1.12})$$

where \mathbf{n} is the normal vector to the boundary $\partial \Omega$. By the fundamental lemma of the variational calculus, we obtain the following Euler-Lagrange equations for C.1.1

$$\gamma \nu - \frac{\gamma}{\delta \gamma} e^{\gamma(I_o - \tilde{I})} - \alpha \frac{\operatorname{div}(\nabla \tilde{I})}{|\nabla \tilde{I}|} - \alpha \frac{1}{|\nabla I|^3} \nabla^2 I : (\nabla I \otimes \nabla I) = 0 \quad \text{in } \Omega \quad (\text{C.1.13})$$

$$\nabla \tilde{I} \cdot \mathbf{n} = 0 \quad \text{on } \partial \Omega \quad (\text{C.1.14})$$

To decrease the computation cost, we neglect the second order term assuming that the modulus of the image gradient varies smoothly. Thus, the simplified Euler-Lagrange equations are the following

$$\gamma \nu - \frac{\gamma}{\delta \gamma} e^{\gamma(I_o - \tilde{I})} - \alpha \frac{\operatorname{div}(\nabla \tilde{I})}{|\nabla \tilde{I}|} = 0 \quad \text{in } \Omega \quad (\text{C.1.15})$$

$$\nabla \tilde{I} \cdot \mathbf{n} = 0 \quad \text{on } \partial \Omega. \quad (\text{C.1.16})$$

C.2 Optical flow based on Weickert strategies

The optical flow strategy presented in Section 4.3.4.4, results in the minimization of the following functional

$$\mathcal{E}(\tilde{\mathbf{w}}) = \int_{\Omega} \left[\psi \left(\left(\nabla_{\rho} I \cdot \tilde{\mathbf{w}} + \frac{\partial_{\rho} I}{\partial t} \right)^2 \right) + \alpha \psi \left(\|\nabla(\mathbf{w} + \tilde{\mathbf{w}})\|_F^2 \right) \right] d\Omega \quad (\text{C.2.1})$$

where $\|\cdot\|_F$ is the Frobenius norm and $\psi(x)$ function is defined as

$$\psi(x) = 2\kappa^2 \sqrt{1 + \frac{x}{\kappa^2}}. \quad (\text{C.2.2})$$

Note the drop of the supra-index m in C.2.1 for the sake of readability.

As in the previous Section, we use variational calculus to analyze the necessary and sufficient conditions for the minimizer. Thus, we perturb the function $\tilde{\mathbf{w}}$ as $\tilde{\mathbf{w}} + \tau \boldsymbol{\eta}$ with $\boldsymbol{\eta} \in \mathcal{V}$ where

$$\mathcal{V} = \{\boldsymbol{\eta} \in \mathbb{R}^{2,n,m}; \boldsymbol{\eta}, \nabla \boldsymbol{\eta} \text{ are square-integrable functions}\}. \quad (\text{C.2.3})$$

The resulting perturbed functional is

$$\begin{aligned} \mathcal{E}(\tilde{\mathbf{w}} + \tau\boldsymbol{\eta}) &= \int_{\Omega} \left[\psi \left(\left(\nabla_{\rho} I \cdot \tilde{\mathbf{w}} + \nabla_{\rho} I \cdot \tau\boldsymbol{\eta} + \frac{\partial_{\rho} I}{\partial t} \right)^2 \right) \right. \\ &\quad \left. + \alpha \psi \left(\left\| \nabla(\mathbf{w} + \tilde{\mathbf{w}}) + \tau \nabla \boldsymbol{\eta} \right\|_F^2 \right) \right] d\Omega \end{aligned} \quad (\text{C.2.4})$$

The necessary condition for optimization of the \mathcal{E} is obtained when the first Gâteaux derivative of \mathcal{E} is nullified for any admissible perturbation $\boldsymbol{\eta}$, i.e., $\delta \mathcal{E}(\tilde{\mathbf{w}}, \boldsymbol{\eta}) = 0, \forall \boldsymbol{\eta} \in \mathcal{V}$. Then, we calculate such condition as follows

$$\begin{aligned} \delta \mathcal{E}(\tilde{\mathbf{w}}, \boldsymbol{\eta}) &= \left. \frac{\partial \mathcal{E}(\tilde{\mathbf{w}} + \tau\boldsymbol{\eta})}{\partial \tau} \right|_{\tau=0} \\ &= \int_{\Omega} \left[\psi' \left(\left(\nabla_{\rho} I \cdot \tilde{\mathbf{w}} + \frac{\partial_{\rho} I}{\partial t} \right)^2 \right) 2 \left(\nabla_{\rho} I \cdot \tilde{\mathbf{w}} + \frac{\partial_{\rho} I}{\partial t} \right) \nabla_{\rho} I \cdot \boldsymbol{\eta} \right. \\ &\quad \left. + \alpha \psi' \left(\nabla(\mathbf{w} + \tilde{\mathbf{w}}) : \nabla(\mathbf{w} + \tilde{\mathbf{w}}) \right) 2 \left(\nabla(\mathbf{w} + \tilde{\mathbf{w}}) : \nabla \boldsymbol{\eta} \right) \right] d\Omega = 0, \quad \forall \boldsymbol{\eta} \in \mathcal{V}. \end{aligned} \quad (\text{C.2.5})$$

where $:$ denotes the Frobenius inner product.

To determine if the extreme in $\delta \mathcal{E}(\tilde{\mathbf{w}}, \boldsymbol{\eta}) = 0$ is maximum or minimum, we inspect the sign of the second Gâteaux derivative $\delta^2 \mathcal{E}(\tilde{\mathbf{w}}, \boldsymbol{\eta})$ obtained as follows

$$\begin{aligned} \delta^2 \mathcal{E}(\tilde{\mathbf{w}}, \boldsymbol{\eta}) &= \left. \frac{\partial^2 \mathcal{E}(\tilde{\mathbf{w}} + \tau\boldsymbol{\eta})}{\partial \tau^2} \right|_{\tau=0} \\ &= \int_{\Omega} \left[\psi'' \left(\left(\nabla_{\rho} I \cdot \tilde{\mathbf{w}} + \frac{\partial_{\rho} I}{\partial t} \right)^2 \right) 4 \left(\nabla_{\rho} I \cdot \tilde{\mathbf{w}} + \frac{\partial_{\rho} I}{\partial t} \right)^2 (\nabla_{\rho} I \cdot \boldsymbol{\eta})^2 \right. \\ &\quad + \psi' \left(\left(\nabla_{\rho} I \cdot \tilde{\mathbf{w}} + \frac{\partial_{\rho} I}{\partial t} \right)^2 \right) 2 (\nabla_{\rho} I \cdot \boldsymbol{\eta})^2 \\ &\quad + \alpha \psi'' \left(\nabla(\mathbf{w} + \tilde{\mathbf{w}}) : \nabla(\mathbf{w} + \tilde{\mathbf{w}}) \right) 4 \left(\nabla(\mathbf{w} + \tilde{\mathbf{w}}) : \nabla \boldsymbol{\eta} \right)^2 \\ &\quad \left. + \alpha \psi' \left(\nabla(\mathbf{w} + \tilde{\mathbf{w}}) : \nabla(\mathbf{w} + \tilde{\mathbf{w}}) \right) 2 \left(\nabla \boldsymbol{\eta} : \nabla \boldsymbol{\eta} \right) \right] d\Omega \end{aligned} \quad (\text{C.2.6})$$

For convenience, we analyze the integral sign by taking two term at the time. The first two terms are positive if only if

$$\begin{aligned} &\psi'' \left(\left(\nabla_{\rho} I \cdot \tilde{\mathbf{w}} + \frac{\partial_{\rho} I}{\partial t} \right)^2 \right) 4 \left(\nabla_{\rho} I \cdot \tilde{\mathbf{w}} + \frac{\partial_{\rho} I}{\partial t} \right)^2 (\nabla_{\rho} I \cdot \boldsymbol{\eta})^2 \\ &\quad + \psi' \left(\left(\nabla_{\rho} I \cdot \tilde{\mathbf{w}} + \frac{\partial_{\rho} I}{\partial t} \right)^2 \right) 2 (\nabla_{\rho} I \cdot \boldsymbol{\eta})^2 \geq 0 \end{aligned} \quad (\text{C.2.7})$$

by changing variables $x = \left(\nabla_{\rho} I \cdot \tilde{\mathbf{w}} + \frac{\partial_{\rho} I}{\partial t} \right)^2$, then

$$\begin{aligned}
4x \psi''(x) (\nabla_{\rho} I \cdot \boldsymbol{\eta})^2 + 2\psi'(x) (\nabla_{\rho} I \cdot \boldsymbol{\eta})^2 &\geq 0 \\
2x \psi''(x) + \psi'(x) &\geq 0 \\
2x \left(-\frac{1}{2\kappa^2(1 + \frac{x}{\kappa^2})^{3/2}} \right) + \left(1 + \frac{x}{\kappa^2} \right)^{-1/2} &\geq 0 \\
\left(1 + \frac{x}{\kappa^2} \right)^{-1/2} &\geq \frac{x}{\kappa^2(1 + \frac{x}{\kappa^2})^{3/2}} \\
1 &\geq \frac{x}{\kappa^2 + x}
\end{aligned} \tag{C.2.8}$$

which is always true since $x = \left(\nabla_{\rho} I \cdot \tilde{\mathbf{w}} + \frac{\partial_{\rho} I}{\partial t} \right)^2 \geq 0$, then the sum of the first two terms is always positive. Now let us analyze the second two terms, which its sum is positive if and only if

$$\begin{aligned}
\alpha \psi'' \left(\|\nabla(\mathbf{w} + \tilde{\mathbf{w}})\|_F^2 \right) 4 \left(\nabla(\mathbf{w} + \tilde{\mathbf{w}}) : \nabla \boldsymbol{\eta} \right)^2 + \alpha \psi' \left(\|\nabla(\mathbf{w} + \tilde{\mathbf{w}})\|_F^2 \right) 2 \left(\|\nabla \boldsymbol{\eta}\|_F^2 \right) &\geq 0 \\
\psi' \left(\|\nabla(\mathbf{w} + \tilde{\mathbf{w}})\|_F^2 \right) \left(\|\nabla \boldsymbol{\eta}\|_F^2 \right) &\geq -2 \psi'' \left(\|\nabla(\mathbf{w} + \tilde{\mathbf{w}})\|_F^2 \right) \left(\nabla(\mathbf{w} + \tilde{\mathbf{w}}) : \nabla \boldsymbol{\eta} \right)^2.
\end{aligned} \tag{C.2.9}$$

Consider the change of variable $x = \|\nabla(\mathbf{w} + \tilde{\mathbf{w}})\|_F^2$, then

$$\begin{aligned}
\psi'(x) \left(\|\nabla \boldsymbol{\eta}\|_F^2 \right) &\geq -2 \psi''(x) \left(\nabla(\mathbf{w} + \tilde{\mathbf{w}}) : \nabla \boldsymbol{\eta} \right)^2 \\
\left(1 + \frac{x}{\kappa^2} \right)^{-1/2} \left(\|\nabla \boldsymbol{\eta}\|_F^2 \right) &\geq -2 \left(-\frac{1}{2\kappa^2(1 + \frac{x}{\kappa^2})^{3/2}} \right) \left(\nabla(\mathbf{w} + \tilde{\mathbf{w}}) : \nabla \boldsymbol{\eta} \right)^2 \\
(\kappa^2 + x) \left(\|\nabla \boldsymbol{\eta}\|_F^2 \right) &\geq \left(\nabla(\mathbf{w} + \tilde{\mathbf{w}}) : \nabla \boldsymbol{\eta} \right)^2 \\
\kappa^2 \|\nabla \boldsymbol{\eta}\|_F^2 + \|\nabla(\mathbf{w} + \tilde{\mathbf{w}})\|_F^2 \|\nabla \boldsymbol{\eta}\|_F^2 &\geq \left(\nabla(\mathbf{w} + \tilde{\mathbf{w}}) : \nabla \boldsymbol{\eta} \right)^2
\end{aligned} \tag{C.2.10}$$

Assuming the worst case scenario where $\kappa = 0$, and expressing the previous equation in terms of the Frobenius inner product, we obtain that

$$\left(\nabla(\mathbf{w} + \tilde{\mathbf{w}}) : \nabla(\mathbf{w} + \tilde{\mathbf{w}}) \right) \left(\nabla \boldsymbol{\eta} : \nabla \boldsymbol{\eta} \right) \geq \left(\nabla(\mathbf{w} + \tilde{\mathbf{w}}) : \nabla \boldsymbol{\eta} \right)^2 \tag{C.2.11}$$

which is the Cauchy-Schwarz inequality, then the sum of the second two terms is also positive. Thus, $\delta^2 \mathcal{E}(\tilde{\mathbf{w}}, \boldsymbol{\eta}) \geq 0, \forall \boldsymbol{\eta} \in \mathcal{V}$, implying that $\delta \mathcal{E}(\tilde{\mathbf{w}}, \boldsymbol{\eta}) = 0$ is necessary and sufficient condition for minimization.

In that manner, we integrate C.2.5 as follows

$$\begin{aligned}
\delta \mathcal{E}(\tilde{\mathbf{w}}, \boldsymbol{\eta}) &= \alpha \psi' \left(\|\nabla(\mathbf{w} + \tilde{\mathbf{w}})\|_F^2 \right) \left(\nabla(\mathbf{w} + \tilde{\mathbf{w}}) \right) \mathbf{n} \cdot \boldsymbol{\eta} \Big|_{\partial \Omega} \\
&\quad + \int_{\Omega} \left[\psi' \left(\left(\nabla_{\rho} I \cdot \tilde{\mathbf{w}} + \frac{\partial_{\rho} I}{\partial t} \right)^2 \right) \left(\nabla_{\rho} I \cdot \tilde{\mathbf{w}} + \frac{\partial_{\rho} I}{\partial t} \right) \nabla_{\rho} I \right. \\
&\quad \left. - \alpha \operatorname{div} \left(\psi' \left(\|\nabla(\mathbf{w} + \tilde{\mathbf{w}})\|_F^2 \right) \nabla(\mathbf{w} + \tilde{\mathbf{w}}) \right) \right] \cdot \boldsymbol{\eta} \, d\Omega = 0, \quad \forall \boldsymbol{\eta} \in \mathcal{V},
\end{aligned} \tag{C.2.12}$$

where \mathbf{n} is the normal vector to the boundary $\partial\Omega$. By the fundamental lemma of the variational calculus, we obtain the following Euler-Lagrange equations for the minimization of C.2.1 as

$$\begin{aligned} & \psi' \left(\left(\nabla_{\rho} I \cdot \tilde{\mathbf{w}} + \frac{\partial_{\rho} I}{\partial t} \right)^2 \right) \left(\nabla_{\rho} I \cdot \tilde{\mathbf{w}} + \frac{\partial_{\rho} I}{\partial t} \right) \nabla_{\rho} I \\ -\alpha \operatorname{div} & \left(\psi' \left(\|\nabla(\mathbf{w} + \tilde{\mathbf{w}})\|_F^2 \right) (\nabla(\mathbf{w} + \tilde{\mathbf{w}})) \right) = 0 && \text{in } \Omega && \text{(C.2.13)} \end{aligned}$$

$$(\nabla(\mathbf{w} + \tilde{\mathbf{w}}))\mathbf{n} = \mathbf{0} \quad \text{on } \partial\Omega. \quad \text{(C.2.14)}$$

Medical glossary

anamnesis

a patient's account of a medical history. 2

angiogenesis

formation of new blood vessels. This process involves the migration, growth, and differentiation of endothelial cells, which line the inside wall of blood vessels. 95

angioplasty

minimally invasive, endovascular procedure to widen narrowed or obstructed arteries or veins, typically to treat arterial atherosclerosis. 99

apical

relating to or denoting an apex (the top or highest part of something, especially one forming a point). 93

atherosclerosis

specific form of arteriosclerosis in which the arterial wall thickens as a result of invasion and accumulation of white blood cells (foam cell) and proliferation of intimal-smooth-muscle cell creating an atheromatous (fibrofatty) plaque. 92, 96

atherosclerotic plaque

nucleation of materials in the vessel wall as consequence of the arteriosclerotic vascular disease. 91, 94, 101, 102, 108

collagen

main structural protein in the extracellular space in the various connective tissues in animal bodies. 91–93, 95–102, 107–109

coronary steal

phenomenon where an alteration of circulation patterns lead to a reduction in the blood directed to the coronary circulation. 156

cytokine

any of a number of substances that are secreted by certain cells of the immune system and have an effect on other cells. E.g. interferon, interleukin, and growth factors. 94, 95, 97, 102

differentiate

to change from relatively generalized to specialized kinds, during development. 97, 102

elastin

highly elastic protein in connective tissue and allows many tissues in the body to resume their shape after stretching or contracting. 91–93, 95–100, 107

extracellular matrix

collection of extracellular molecules secreted by cells that provides structural and biochemical support to the surrounding cells. 91, 102, 107

fibronectin

high-molecular weight (≈ 440 kDa) glycoprotein of the extracellular matrix that binds to membrane-spanning receptor proteins called integrins. 91, 98

genotype

set of genes in an organism's DNA which is responsible for a particular trait. 2

glycosaminoglycan

any of a group of compounds occurring chiefly as components of connective tissue. They are complex polysaccharides containing amino groups. 91

homeostasis

tendency toward a relatively stable equilibrium between interdependent elements, especially as maintained by physiological processes. 92, 93, 97, 99, 100

hyperemia

increase of blood flow to different tissues in the body. 148

hypertensive

having or denoting a high blood pressure. 110

lamella

thin plate-like structure. 95–99

laminin

high-molecular weight (≈ 400 to ≈ 900 kDa) protein of the extracellular matrix. It is a major component of the basal lamina (one of the layers of the basement membrane), a protein network foundation for most cells and organs. 91

leukocyte

colorless cell that circulates in the blood and body fluids and is involved in counter-acting foreign substances and disease; a white (blood) cell. 93, 94, 97, 102

morphogenesis

origin and development of morphological characteristics. 92

normotensive

having or denoting a normal blood pressure. 99, 100, 110

pathogenesis

biological mechanism (or mechanisms) that leads to the diseased state. The term can also describe the origin and development of the disease, and whether it is acute, chronic, or recurrent. 92

phenotype

set of observable characteristics of an individual resulting from the interaction of its genotype with the environment. 2, 92, 94–97, 101

physiological

characteristic of or appropriate to an organism's healthy or normal functioning. 91, 94, 99, 107–109

protease

any of a group of enzymes that catalyze the hydrolytic degradation of proteins or polypeptides to smaller amino acid polymers. 97

proteoglycan

compound consisting of a protein bonded to glycosaminoglycan groups, present especially in connective tissue. 91, 98, 101

protrusion

something that extends from, above or beyond a surface or boundary. 96, 98

stenosis

abnormal narrowing in a blood vessel or other tubular organ or structure. 8, 15, 23, 96, 109

thrombocyte

component of blood whose function (along with the coagulation factors) is to stop bleeding by clumping and clotting blood vessel injuries; a platelet. 93

tunica

layer, coat, sheath, or similar covering. 92, 93, 96–102, 107–111

vasoconstrictor

agents that promote constriction of blood vessels plural. 92

vasodilation

dilatation of blood vessels. 94

vasodilator

agents that promote dilatation of blood vessels. 92

vasomotor tone

amount of tension in the smooth muscle inside the walls of blood vessels, particularly in arteries. 3, 92, 94

Bibliography

- [1] The Vascular Modeling Toolkit website, 2015.
- [2] A. Hernández-Sabaté et al. Image-based cardiac phase retrieval in intravascular ultrasound sequences. IEEE Trans. Ultrason. Ferroelectrics Freq. Contr., 58(1):60–72, 2011.
- [3] J. G. Abbott and F. L. Thurstone. Acoustic speckle: Theory and experimental analysis. Ultrason. Imag., 324(4):303–324, 1979.
- [4] W. Aird. Spatial and temporal dynamics of the endothelium. Journal of Thrombosis and Haemostasis, 3(7):1392–1406, 2005.
- [5] W. C. Aird. Endothelial cell dynamics and complexity theory. Critical care medicine, 30(5):S180–S185, 2002.
- [6] W. C. Aird. Phenotypic heterogeneity of the endothelium i. structure, function, and mechanisms. Circulation research, 100(2):158–173, 2007.
- [7] M. Alberti et al. Automatic non-rigid temporal alignment of IVUS sequences. In Medical Image Computing and Computer-Assisted Intervention MICCAI 2012, pages 642–650. Springer, 2012.
- [8] M. Alberti et al. Automatic non-rigid temporal alignment of intravascular ultrasound sequences: method and quantitative validation. Ultrasound. Med. Biol., 39(9):1698–712, 2013.
- [9] B. Alberts, A. Johnson, J. Lewis, M. Raff, K. Roberts, and P. Walter. The extracellular matrix of animals. Garland Science, 2002.
- [10] M. Alessandrini, B. Heyde, S. Queiros, S. Cygan, M. Zontak, O. Somphone, O. Bernard, M. De Craene, M. O’Donnell, and J. D’hooge. Detailed Evaluation of Five 3d Speckle Tracking Algorithms using Synthetic Echocardiographic Recordings. IEEE Transactions on Medical Imaging, pages 1–1, 2016.
- [11] M. R. Alexander and G. K. Owens. Epigenetic control of smooth muscle cell differentiation and phenotypic switching in vascular development and disease. Annual review of physiology, 74:13–40, 2012.
- [12] L. Alvarez, J. Weickert, and J. Snchez. Reliable Estimation of Dense Optical Flow Fields with Large Displacements. International Journal of Computer Vision, 39(1):41–56, 2000.
- [13] J. Amores and P. Radeva. Non-rigid registration of vessel structures in IVUS images. Pattern. Recogn. Image Anal., pages 45–52, 2003.
- [14] J. Amores and P. Radeva. Registration and retrieval of highly elastic bodies using contextual information. Pattern Recognition Letters, 26:1720–1731, 2003.

- [15] J. Amores and P. Radeva. Retrieval of IVUS images using contextual information and elastic matching. *Int. J. Intell. Syst.*, 20(5):541–559, May 2005.
- [16] P. Anandan. A computational framework and an algorithm for the measurement of visual motion. *International Journal of Computer Vision*, 2(3):283–310, 1989.
- [17] E. D. Angelini and O. Gerard. Review of myocardial motion estimation methods from optical flow tracking on ultrasound data. In *Engineering in Medicine and Biology Society, 2006. EMBS'06. 28th Annual International Conference of the IEEE*, pages 1537–1540. IEEE, 2006.
- [18] L. Antiga, B. Ene-Iordache, and A. Remuzzi. Computational geometry for patient-specific reconstruction and meshing of blood vessels from MR and CT angiography. *IEEE Transactions on Medical Imaging*, 22(5):674–684, May 2003.
- [19] L. Antiga, M. Piccinelli, L. Botti, B. Ene-Iordache, A. Remuzzi, and D. A. Steinman. An image-based modeling framework for patient-specific computational hemodynamics. *Medical & Biological Engineering & Computing*, 46(11):1097–1112, November 2008.
- [20] T. Araki et al. A comparative approach of four different image registration techniques for quantitative assessment of coronary artery calcium lesions using intravascular ultrasound. *Computer Methods and Programs in Biomedicine*, 118(2):158–172, 2015.
- [21] A. Arbab-Zadeh, A. N. DeMaria, W. F. Penny, R. J. Russo, B. J. Kimura, and V. Bhargava. Axial movement of the intravascular ultrasound probe during the cardiac cycle: implications for three-dimensional reconstruction and measurements of coronary dimensions. *American Heart Journal*, 138(5 Pt 1):865–72, November 1999.
- [22] G. D. Ares. *Integrative Computational Modeling & In-vivo Characterization of Residual Deformations in Hemodynamics*. PhD thesis, National Laboratory for Scientific Computing, 2016.
- [23] D. Arnold, F. Brezzi, and M. Fortin. A stable finite element for the Stokes equations. *Calcolo*, (21), 1984.
- [24] S. M. Arribas, A. Hinek, and M. C. González. Elastic fibres and vascular structure in hypertension. *Pharmacology & therapeutics*, 111(3):771–791, 2006.
- [25] S. Avril, P. Badel, and A. Duprey. Anisotropic and hyperelastic identification of in vitro human arteries from full-field optical measurements. *Journal of biomechanics*, 43(15):2978–2985, 2010.
- [26] E. U. Azeloglu, M. B. Albro, V. A. Thimmappa, G. A. Ateshian, and K. D. Costa. Heterogeneous transmural proteoglycan distribution provides a mechanism for regulating residual stresses in the aorta. *American Journal of Physiology-Heart and Circulatory Physiology*, 294(3):H1197–H1205, 2008.
- [27] A. Bab-Hadiashar and D. Suter. Robust optic flow computation. *International Journal of Computer Vision*, 29(1):59–77, 1998.
- [28] R. A. Baldewsing, C. L. de Korte, J. A. Schaar, F. Mastik, and A. F. van Der Steen. A finite element model for performing intravascular ultrasound elastography of human atherosclerotic coronary arteries. *Ultrasound in medicine & biology*, 30(6):803–813, 2004.

- [29] I. Ben-Dor, M. Mahmoudi, T. Deksis, A. B. Bui, M. A. Gaglia, M. A. Gonzalez, G. Maluenda, G. Sardi, R. Romaguera, A. Laynez, et al. Correlation between fractional flow reserve and intravascularultrasound lumen area in intermediate coronary artery stenosis. *Cardiovascular Revascularization Medicine*, 12(3):e41, 2011.
- [30] J. F. Bentzon, F. Otsuka, R. Virmani, and E. Falk. Mechanisms of plaque formation and rupture. *Circulation research*, 114(12):1852–1866, 2014.
- [31] M. Bersi, M. Collins, E. Wilson, and J. Humphrey. Disparate changes in the mechanical properties of murine carotid arteries and aorta in response to chronic infusion of angiotensin-ii. *International journal of advances in engineering sciences and applied mathematics*, 4(4):228–240, 2012.
- [32] L. Bertagna and A. Veneziani. A model reduction approach for the variational estimation of vascular compliance by solving an inverse fluid–structure interaction problem. *Inverse Problems*, 30(5):055006, 2014.
- [33] C. Bertoglio, D. Barber, N. Gaddum, I. Valverde, M. Rutten, P. Beerbaum, P. Moireau, R. Hose, and J.-F. Gerbeau. Identification of artery wall stiffness: In vitro validation and in vivo results of a data assimilation procedure applied to a 3d fluid–structure interaction model. *Journal of biomechanics*, 47(5):1027–1034, 2014.
- [34] C. Bertoglio, P. Moireau, and J.-F. Gerbeau. Sequential parameter estimation for fluid–structure problems: Application to hemodynamics. *International Journal for Numerical Methods in Biomedical Engineering*, 28(4):434–455, 2012.
- [35] P. J. Best, D. Hasdai, G. Sangiorgi, R. S. Schwartz, D. R. Holmes, R. D. Simari, and A. Lerman. Apoptosis basic concepts and implications in coronary artery disease. *Arteriosclerosis, thrombosis, and vascular biology*, 19(1):14–22, 1999.
- [36] J. Bigün, G. Granlund, and J. Wiklund. Multidimensional orientation estimation with applications to texture analysis and optical flow. *IEEE Transactions on Pattern Analysis & Machine Intelligence*, 8:775–790, 1991.
- [37] M. J. Black. Recursive non-linear estimation of discontinuous flow fields. In *Computer VisionECCV’94*, pages 138–145. Springer, 1994.
- [38] M. J. Black and P. Anandan. Robust dynamic motion estimation over time. In *Proceedings CVPR’91*, pages 296–302, 1991.
- [39] M. J. Black and P. Anandan. The robust estimation of multiple motions: Parametric and piecewise-smooth flow fields. *Computer vision and image understanding*, 63(1):75–104, 1996.
- [40] M. J. Black and A. D. Jepson. Estimating optical flow in segmented images using variable-order parametric models with local deformations. *IEEE Transactions on Pattern Analysis and Machine Intelligence*, 18(10):972–986, 1996.
- [41] P. J. Blanco, G. D. Ares, S. A. Urquiza, and R. A. Feijóo. On the effect of preload and pre-stretch on hemodynamic simulations: an integrative approach. *Biomechanics and modeling in mechanobiology*, 15(3):593–627, 2016.
- [42] P. J. Blanco, S. M. Watanabe, E. A. Dari, M. A. R. F. Passos, and R. A. Feijóo. Blood flow distribution in an anatomically detailed arterial network model: criteria and algorithms. *Biomechanics and Modeling in Mechanobiology*, 13(6):1303–1330, November 2014.

- [43] P. J. Blanco, S. M. Watanabe, M. A. R. F. Passos, P. A. Lemos, and R. A. Feijóo. An Anatomically Detailed Arterial Network Model for One-Dimensional Computational Hemodynamics. IEEE Transactions on Biomedical Engineering, 62(2):736–753, February 2015.
- [44] G. V. Born and P. D. Richardson. Mechanical properties of human atherosclerotic lesions. In Pathobiology of the human atherosclerotic plaque, pages 413–423. Springer, 1990.
- [45] H. Brodoefel, C. Burgstahler, I. Tsiflikas, A. Reimann, S. Schroeder, C. D. Claussen, M. Heuschmid, and A. F. Kopp. Dual-source ct: Effect of heart rate, heart rate variability, and calcification on image quality and diagnostic accuracy 1. Radiology, 247(2):346–355, 2008.
- [46] T. Brox, A. Bruhn, N. Papenberg, and J. Weickert. High accuracy optical flow estimation based on a theory for warping. In Computer Vision-ECCV 2004, pages 25–36. Springer, 2004.
- [47] A. Bruhn, J. Weickert, and C. Schnörr. Lucas / Kanade Meets Horn / Schunck : Combining Local and Global Optic Flow Methods. International Journal of Computer Vision, 61(3):211–231, 2005.
- [48] A. Bruhn and J. Weickert. Towards ultimate motion estimation: Combining highest accuracy with real-time performance. In Computer Vision, 2005. ICCV 2005. Tenth IEEE International Conference on, volume 1, pages 749–755. IEEE, 2005.
- [49] A. Bruhn, J. Weickert, C. Feddern, T. Kohlberger, and C. Schnrr. Real-time optic flow computation with variational methods. In Computer Analysis of Images and Patterns, pages 222–229. Springer, 2003.
- [50] A. Bruhn, J. Weickert, and C. Schnrr. Combining the advantages of local and global optic flow methods. In Pattern Recognition, pages 454–462. Springer, 2002.
- [51] A. Bruhn, J. Weickert, and C. Schnrr. Lucas/kanade meets horn/schunck: Combining local and global optic flow methods. International Journal of Computer Vision, 61:211–231, 2005.
- [52] C. A. Bulant. Computational models for the geometric and functional analysis of coronary circulation. PhD thesis, National Laboratory for Scientific Computing, 2017.
- [53] C. A. Bulant, P. J. Blanco, T. P. Lima, A. N. Assunção, G. Liberato, J. R. Parga, L. F. R. Ávila, A. C. Pereira, R. A. Feijóo, and P. A. Lemos. A computational framework to characterize and compare the geometry of coronary networks. International Journal for Numerical Methods in Biomedical Engineering, 2016. Accepted. DOI: 10.1002/cnm.2800,.
- [54] C. Bulant, P. Blanco, G. M. Talou, C. G. Bezerra, P. Lemos, and R. Feijóo. A head-to-head comparison between ct-and ivus-derived coronary blood flow models. Journal of Biomechanics, 2016.
- [55] A. P. Burke, F. D. Kolodgie, A. Farb, D. K. Weber, G. T. Malcom, J. Smialek, and R. Virmani. Healed plaque ruptures and sudden coronary death. Circulation, 103(7):934–940, 2001.
- [56] A. C. Burton. Relation of structure to function of the tissues of the wall of blood vessels. Physiological reviews, 34(4):619–642, 1954.

- [57] C. Gatta et al. Robust image-based ivus pullbacks gating. In Medical Image Computing and Computer-Assisted Intervention - MICCAI 2008, volume 11, pages 518–525. Springer Berlin Heidelberg, 2008.
- [58] C. Gatta et al. Real-time gating of ivus sequences based on motion blur analysis: method and quantitative validation. In Medical Image Computing and Computer-Assisted Intervention - MICCAI 2010, volume 13, pages 59–67. Springer Berlin Heidelberg, 2010.
- [59] P. Campagnolo, D. Cesselli, A. A. H. Zen, A. P. Beltrami, N. Kränkel, R. Katare, G. Angelini, C. Emanuelli, and P. Madeddu. Human adult vena saphena contains perivascular progenitor cells endowed with clonogenic and proangiogenic potential. Circulation, 121(15):1735–1745, 2010.
- [60] L. Cardamone, A. Valentin, J. Eberth, and J. Humphrey. Origin of axial prestretch and residual stress in arteries. Biomechanics and modeling in mechanobiology, 8(6):431–446, 2009.
- [61] S. Carrizo, X. Xie, R. Peinado-Peinado, A. Sánchez-Recalde, S. Jiménez-Valero, G. Galeote-Garcia, and R. Moreno. Functional assessment of coronary artery disease by intravascular ultrasound and computational fluid dynamics simulation. Revista Portuguesa de Cardiologia (English Edition), 33(10):645–e1, 2014.
- [62] E. I. Céspedes, C. L. de Korte, and A. F. van der Steen. Intraluminal ultrasonic palpation: assessment of local and cross-sectional tissue stiffness. Ultrasound in medicine & biology, 26(3):385–96, March 2000.
- [63] E. Céspedes, C. de Korte, A. van der Steen, C. von Birgelen, and C. Lance. Intravascular elastography: principles and potentials. Seminars in interventional cardiology : SIIC, 2(1):5562, March 1997.
- [64] A. Chambolle. An algorithm for total variation minimization and applications. Journal of Mathematical imaging and vision, 20(1-2):89–97, 2004.
- [65] T. F. Chan, G. H. Golub, and P. Mulet. A Nonlinear Primal-Dual Method for Total Variation-Based Image Restoration. SIAM Journal on Scientific Computing, 20(6):1964–1977, January 1999.
- [66] D. Chapelle, P. Moireau, and P. Le Tallec. Robust filtering for joint state parameter estimation for distributed mechanical systems. Discrete and Continuous Dynamical Systems-Series A, 23(1-2):65–84, 2009.
- [67] P. Charbonnier, L. Blanc-Féraud, G. Aubert, and M. Barlaud. Two deterministic half-quadratic regularization algorithms for computed imaging. In Image Processing, 1994. Proceedings. ICIP-94., IEEE International Conference, volume 2, pages 168–172. IEEE, 1994.
- [68] Y. Chatzizisis, A. Coskun, M. Jonas, E. Edelman, C. Feldman, and P. Stone. Role of endothelial shear stress in the natural history of coronary atherosclerosis and vascular remodeling. Molecular, cellular, and vascular behavior. Journal of the American College of Cardiology, 49:2379–2393, 2007.
- [69] C. Cheng, D. Tempel, R. van Haperen, A. van der Baan, F. Grosveld, M. J. Daemen, R. Krams, and R. de Crom. Atherosclerotic lesion size and vulnerability are determined by patterns of fluid shear stress. Circulation, 113(23):2744–2753, 2006.

- [70] C. Cheng, D. Tempel, R. van Haperen, A. van der Baan, F. Grosveld, M. J. Daemen, R. Krams, and R. de Crom. Atherosclerotic lesion size and vulnerability are determined by patterns of fluid shear stress. Circulation, 113(23):2744–2753, 2006.
- [71] G. C. Cheng, H. M. Loree, R. D. Kamm, M. C. Fishbein, and R. T. Lee. Distribution of circumferential stress in ruptured and stable atherosclerotic lesions. A structural analysis with histopathological correlation. Circulation, 87(4):1179–1187, April 1993.
- [72] G. C. Cheng, H. M. Loree, R. D. Kamm, M. C. Fishbein, and R. T. Lee. Distribution of circumferential stress in ruptured and stable atherosclerotic lesions. a structural analysis with histopathological correlation. Circulation, 87(4):1179–1187, 1993.
- [73] G. Choi, J. Lee, H.-J. Kim, J.-B. Park, S. Sankaran, H. Otake, J.-H. Doh, C.-W. Nam, E.-S. Shin, C. Taylor, and B.-K. Koo. Coronary artery axial plaque stress and its relationship with lesion geometry. Application of computational fluid dynamics to coronary CT angiography. Journal of the American College of Cardiology: Cardiovascular Imaging, 8:1156–1166, 2015.
- [74] B. J. Chow, M. Kass, O. Gagné, L. Chen, Y. Yam, A. Dick, and G. A. Wells. Can differences in corrected coronary opacification measured with computed tomography predict resting coronary artery flow? Journal of the American College of Cardiology, 57(11):1280–1288, 2011.
- [75] P. S. Chowdhury and R. G. Ramos. Coronary-stent fracture. New England Journal of Medicine, 347(8):581–581, 2002.
- [76] C. Chuong and Y. Fung. Residual stress in arteries. In Frontiers in Biomechanics, pages 117–129. Springer, 1986.
- [77] F. Ciompi, O. Pujol, C. Gatta, O. Rodríguez-Leor, J. Mauri-Ferré, and P. Radeva. Fusing in-vitro and in-vivo intravascular ultrasound data for plaque characterization. The international journal of cardiovascular imaging, 26(7):763–79, October 2010.
- [78] B. Cohen and I. Dinstein. New maximum likelihood motion estimation schemes for noisy ultrasound images. Pattern Recognition, 35(2):455–463, February 2002.
- [79] I. Cohen. Nonlinear variational method for optical flow computation. In Proceedings of the scandinavian conference on image analysis, volume 1, pages 523–523, 1993.
- [80] T. F. Coleman and Y. Li. An interior trust region approach for nonlinear minimization subject to bounds. SIAM Journal on optimization, 6(2):418–445, 1996.
- [81] F. Crea and G. Liuzzo. Pathogenesis of acute coronary syndromes. Journal of the American College of Cardiology, 61(1):1–11, 2013.
- [82] K. S. Cunningham and A. I. Gotlieb. The role of shear stress in the pathogenesis of atherosclerosis. Laboratory investigation, 85(1):9–23, 2005.
- [83] M. G. Danilouchkine, F. Mastik, and a. F. W. van der Steen. A study of coronary artery rotational motion with dense scale-space optical flow in intravascular ultrasound. Physics in Medicine and Biology, 54(6):1397–418, March 2009.
- [84] M. Danilouchkine. Interframe registration of IVUS images due to catheter rotation with feature-based optical flow. In S. Y. Emelianov and S. A. McAleavey, editors, Medical Imaging, volume 6513, pages 65130V–65130V–10. International Society for Optics and Photonics, March 2007.

- [85] M. Danilouchkine. P3A-5 Two Methods for Catheter Motion Correction in IVUS Palpography. In Ultrasonics Symposium, pages 1724–1727. IEEE, 2007.
- [86] M. G. Danilouchkine, F. Mastik, and A. F. W. van der Steen. Accuracy in prediction of catheter rotation in ivus with feature-based optical flow-a phantom study. IEEE Trans. Inform. Technol. Biomed., 12(3):356–65, May 2008.
- [87] M. G. Danilouchkine, F. Mastik, and A. F. W. van der Steen. Improving IVUS palpography by incorporation of motion compensation based on block matching and optical flow. IEEE Trans. Ultrason., Ferroelect., Freq. Contr., 55(11):2392–404, November 2008.
- [88] E. C. Davis. Elastic lamina growth in the developing mouse aorta. Journal of Histochemistry & Cytochemistry, 43(11):1115–1123, 1995.
- [89] C. L. de Korte, E. Cespedes, A. F. van der Steen, G. Pasterkamp, and N. Bom. Intravascular ultrasound elastography: assessment and imaging of elastic properties of diseased arteries and vulnerable plaque. European Journal of Ultrasound, 7(3):219 – 224, 1998.
- [90] de Korte CL. Intravascular ultrasound elastography. PhD thesis, Erasmus University Rotterdam, 1999.
- [91] J.-O. Deguchi, E. Aikawa, P. Libby, J. R. Vachon, M. Inada, S. M. Krane, P. Whitaker, and M. Aikawa. Matrix metalloproteinase-13/collagenase-3 deletion promotes collagen accumulation and organization in mouse atherosclerotic plaques. Circulation, 112(17):2708–2715, 2005.
- [92] G. J. Dehmer, D. Weaver, M. T. Roe, S. Milford-Beland, S. Fitzgerald, A. Hermann, J. Messenger, I. Moussa, K. Garratt, J. Rumsfeld, et al. A contemporary view of diagnostic cardiac catheterization and percutaneous coronary intervention in the united states: a report from the cathpci registry of the national cardiovascular data registry, 2010 through june 2011. Journal of the American College of Cardiology, 60(20):2017–2031, 2012.
- [93] K. P. Dingemans, P. Teeling, J. H. Lagendijk, and A. E. Becker. Extracellular matrix of the human aortic media: an ultrastructural histochemical and immunohistochemical study of the adult aortic media. The Anatomical Record, 258(1):1–14, 2000.
- [94] M. Doyley, F. Mastik, and C. D. Korte. Advancing intravascular ultrasonic palpation toward clinical applications. Ultrasound. Med. Biol., 27(11):1471–1480, 2001.
- [95] Q. Duan, E. D. Angelini, S. L. Herz, O. Gerard, P. Allain, C. M. Ingrassia, K. D. Costa, J. W. Holmes, S. Homma, and A. F. Laine. Tracking of LV endocardial surface on real-time three-dimensional ultrasound with optical flow. In Functional Imaging and Modeling of the Heart, pages 434–445. Springer, 2005.
- [96] V. Dutt and J. F. Greenleaf. Ultrasound echo envelope analysis using a homodyned k distribution signal model. Ultrasonic Imaging, 16(4):265–287, 1994.
- [97] M. DElia, L. Mirabella, T. Passerini, M. Perego, M. Piccinelli, C. Vergara, and A. Veneziani. Applications of variational data assimilation in computational hemodynamics. In Modeling of Physiological Flows, pages 363–394. Springer, 2012.

- [98] M. Elad and A. Feuer. Recursive Optical Flow Estimation Adaptive Filtering Approach. Journal of Visual Communication and Image Representation, 9(2):119–138, June 1998.
- [99] L. D. Enochson and R. K. Otnes. Programming and analysis for digital time series data. Shock and Vibration Information Center [Washington], 1969.
- [100] A. Enzerink and A. Vaheri. Fibroblast activation in vascular inflammation. Journal of Thrombosis and Haemostasis, 9(4):619–626, 2011.
- [101] B. A. Falcão, J. L. A. Falcão, G. R. Morais, R. C. Silva, A. C. Lopes, P. R. Soares, J. Mariani Jr, R. Kalil-Filho, E. R. Edelman, and P. A. Lemos. A novel algorithm to quantify coronary remodeling using inferred normal dimensions. Arquivos brasileiros de cardiologia, 105(4):390–398, 2015.
- [102] G. Farneäck. Very high accuracy velocity estimation using orientation tensors, parametric motion, and simultaneous segmentation of the motion field. In Eighth IEEE International Conference on Computer Vision, volume 1, pages 171–177. IEEE, 2001.
- [103] G. Farneäck. Two-Frame Motion Estimation Based on Polynomial Expansion. In Image analysis, pages 363–370, 2003.
- [104] G. H. Farneäck. Fast and accurate motion estimation using orientation tensors and parametric motion models. In Pattern Recognition, volume 1, pages 135–139, 2000.
- [105] G. Farneäck. Polynomial expansion for orientation and motion estimation. PhD thesis, Linköping University, Sweden, 2002.
- [106] D. Fernandes and M. Sekine. Suppression of weibull radar clutter. IEICE transactions on communications, 76(10):1231–1235, 1993.
- [107] A. V. Finn, M. Nakano, J. Narula, F. D. Kolodgie, and R. Virmani. Concept of vulnerable/unstable plaque. Arteriosclerosis, thrombosis, and vascular biology, 30(7):1282–1292, 2010.
- [108] C. Fischer, E. Hulthen, P. Belur, R. Smith, S. Voros, and T. C. Villines. Coronary CT angiography versus intravascular ultrasound for estimation of coronary stenosis and atherosclerotic plaque burden: A meta-analysis. Journal of Cardiovascular Computed Tomography, 7(4):256–266, July 2013.
- [109] D. J. Fleet and A. D. Jepson. Computation of component image velocity from local phase information. International Journal of Computer Vision, 5(1):77–104, August 1990.
- [110] R. Fletcher. A modified marquardt subroutine for non-linear least squares. Theoretical Physics Division, Atomic Energy Research Establishment, 1971.
- [111] I. Fontaine, M. Bertrand, and G. Cloutier. A system-based approach to modeling the ultrasound signal backscattered by red blood cells. Biophysical Journal, 77(5):2387–2399, 1999.
- [112] A. Franquet, S. Avril, R. Le Riche, P. Badel, F. C. Schneider, Zhi Yong Li, C. Boissier, and J. P. Favre. A New Method for the In Vivo Identification of Mechanical Properties in Arteries From Cine MRI Images: Theoretical Framework and Validation. IEEE Transactions on Medical Imaging, 32(8):1448–1461, August 2013.

- [113] Y. Fung. What principle governs the stress distribution in living organs? biomechanics in china, japan, and usa. In Proceedings of Wuhan Conference, Science Press, Beijing, China, 1983.
- [114] Y.-c. Fung. Biomechanics: mechanical properties of living tissues. Springer Science & Business Media, 2013.
- [115] H. M. García-García, B. D. Gogas, P. W. Serruys, and N. Bruining. Ivus-based imaging modalities for tissue characterization: similarities and differences. The international journal of cardiovascular imaging, 27(2):215–224, 2011.
- [116] C. Gatta, O. Pujol, O. Rodriguez Leor, J. Mauri Ferre, and P. Radeva. Fast rigid registration of vascular structures in IVUS sequences. IEEE Trans. Inform. Technol. Biomed., 13(6):1006–11, November 2009.
- [117] C. F. Gauss. Theory of the motion of the heavenly bodies moving about the sun in conic sections: a translation of Carl Frdr. Gauss" Theoria motus": With an appendix. By Ch. H. Davis. Little, Brown and Comp., 1857.
- [118] S. Gauss, S. Achenbach, T. Pflederer, A. Schuhbäck, W. G. Daniel, and M. Marwan. Assessment of coronary artery remodelling by dual-source ct: a head-to-head comparison with intravascular ultrasound. Heart, 97(12):991–997, 2011.
- [119] S. D. Giattina, B. K. Courtney, P. R. Herz, M. Harman, S. Shortkroff, D. L. Stamper, B. Liu, J. G. Fujimoto, and M. E. Brezinski. Assessment of coronary plaque collagen with polarization sensitive optical coherence tomography (ps-oct). International journal of cardiology, 107(3):400–409, 2006.
- [120] F. Gijzen, J. Schuurbiens, A. van der Giessen, M. Schaap, A. van der Steen, and J. Wentzel. 3D reconstruction techniques of human coronary bifurcations for shear stress computations. Journal of Biomechanics, 47:39–43, 2014.
- [121] P. Giudice, T. Attisano, M. Di Maio, E. Bellino, M. Polito, C. Baldi, F. Vigorito, M. Di Muro, S. Tomasello, A. Galassi, et al. Coronary vasomotion dysfunction after everolimus-eluting stent implantation. Interventional Medicine and Applied Science, 6(4):178–182, 2014.
- [122] J. M. González, A. M. Briones, B. Starcher, M. Conde, B. Somoza, C. Daly, E. Vila, I. McGrath, M. C. González, and S. M. Arribas. Influence of elastin on rat small artery mechanical properties. Experimental physiology, 90(4):463–468, 2005.
- [123] M. Gössl, D. Versari, D. Mannheim, E. L. Ritman, L. O. Lerman, and A. Lerman. Increased spatial vasa vasorum density in the proximal lad in hypercholesterolemia—implications for vulnerable plaque-development. Atherosclerosis, 192(2):246–252, 2007.
- [124] S. Greenwald, J. Moore, A. Rachev, T. Kane, and J.-J. Meister. Experimental investigation of the distribution of residual strains in the artery wall. Journal of biomechanical engineering, 119(4):438–444, 1997.
- [125] H. Zhu. Retrieval of cardiac phase from ivus sequences. In Medical Imaging 2003, pages 135–146. International Society for Optics and Photonics, 2003.
- [126] M. Hadlich, G. Oliveira, R. Feijóo, C. Azevedo, B. Tura, P. Ziemer, P. Blanco, G. Pina, M. Meira, and N. de Souza e Silva. Software livre e de código aberto para avaliação de imagens de angiotomografia de coronárias. Arquivos Brasileiros de Cardiologia, 99:944–951, 2012.

- [127] M. Hamilos, J. Sarma, M. Ostojic, T. Cuisset, G. Sarno, N. Melikian, A. Ntalianis, O. Muller, E. Barbato, B. Beleslin, et al. Interference of drug-eluting stents with endothelium-dependent coronary vasomotion evidence for device-specific responses. Circulation: Cardiovascular Interventions, 1(3):193–200, 2008.
- [128] I. Hariton, T. Gasser, G. Holzapfel, et al. Stress-driven collagen fiber remodeling in arterial walls. Biomechanics and modeling in mechanobiology, 6(3):163–175, 2007.
- [129] F. Harris. On the use of windows for harmonic analysis with the discrete fourier transform. Proceedings of the IEEE, 66(1):51–83, 1978.
- [130] M. J. Haurani and P. J. Pagano. Adventitial fibroblast reactive oxygen species as autocrine and paracrine mediators of remodeling: bellwether for vascular disease? Cardiovascular research, 75(4):679–689, 2007.
- [131] E. D. Hay. Cell biology of extracellular matrix. Springer Science & Business Media, 2013.
- [132] D. Heeger. Model for the extraction of image flow. Journal of the Optical Society of America A, 4(8):1455–1471, 1987.
- [133] F. Heitz and P. Bouthemy. Multimodal estimation of discontinuous optical flow using Markov random fields. Pattern Analysis and Machine Intelligence, IEEE Transactions on, 15(12):1217–1232, 1993.
- [134] A. Hernandez-Sabate, D. Gil, E. Fernandez-Nofrerias, P. Radeva, and E. Marti. Approaching artery rigid dynamics in IVUS. IEEE Trans. Med. Imag., 28(11):1670–80, November 2009.
- [135] J. Herrmann, L. O. Lerman, M. Rodriguez-Porcel, D. R. Holmes, D. M. Richardson, E. L. Ritman, and A. Lerman. Coronary vasa vasorum neovascularization precedes epicardial endothelial dysfunction in experimental hypercholesterolemia. Cardiovascular research, 51(4):762–766, 2001.
- [136] M. R. Hill, X. Duan, G. A. Gibson, S. Watkins, and A. M. Robertson. A theoretical and non-destructive experimental approach for direct inclusion of measured collagen orientation and recruitment into mechanical models of the artery wall. Journal of biomechanics, 45(5):762–771, 2012.
- [137] T. Hiro, T. Fujii, S. Yoshitake, T. Kawabata, K. Yasumoto, and M. Matsuzaki. Assessment of lipid content of atherosclerotic plaque by intravascular ultrasound using fractal analysis. In J Am Coll Cardiol, volume 35, pages 38A–38A. ELSEVIER SCIENCE INC 655 AVENUE OF THE AMERICAS, NEW YORK, NY 10010 USA, 2000.
- [138] T. Hiro. Three stars of the constellation of color intravascular ultrasound in the space of tissue characterization of coronary plaque. J Cardiol, 61(2):186–187, 2013.
- [139] T. Hiro, T. Fujii, K. Yasumoto, T. Murata, A. Murashige, and M. Matsuzaki. Detection of fibrous cap in atherosclerotic plaque by intravascular ultrasound by use of color mapping of angle-dependent echo-intensity variation. Circulation, 103(9):1206–1211, 2001.
- [140] U. Hoffmann, M. Ferencik, R. C. Cury, and A. J. Pena. Coronary ct angiography. Journal of Nuclear Medicine, 47(5):797–806, 2006.

- [141] U. Hoffmann, F. Moselewski, R. C. Cury, M. Ferencik, I.-k. Jang, L. J. Diaz, S. Abbara, T. J. Brady, and S. Achenbach. Predictive value of 16-slice multidetector spiral computed tomography to detect significant obstructive coronary artery disease in patients at high risk for coronary artery disease. Circulation, 110(17):2638–2643, 2004.
- [142] G. A. Holzapfel, T. C. Gasser, and M. Stadler. A structural model for the viscoelastic behavior of arterial walls: continuum formulation and finite element analysis. European Journal of Mechanics-A/Solids, 21(3):441–463, 2002.
- [143] G. A. Holzapfel and T. C. Gasser. A viscoelastic model for fiber-reinforced composites at finite strains: Continuum basis, computational aspects and applications. Computer methods in applied mechanics and engineering, 190(34):4379–4403, 2001.
- [144] G. A. Holzapfel, T. C. Gasser, and R. W. Ogden. A new constitutive framework for arterial wall mechanics and a comparative study of material models. Journal of elasticity and the physical science of solids, 61(1-3):1–48, 2000.
- [145] G. A. Holzapfel, G. Sommer, C. T. Gasser, and P. Regitnig. Determination of layer-specific mechanical properties of human coronary arteries with nonatherosclerotic intimal thickening and related constitutive modeling. American Journal of Physiology-Heart and Circulatory Physiology, 289(5):H2048–H2058, 2005.
- [146] G. A. Holzapfel, G. Sommer, C. T. Gasser, and P. Regitnig. Determination of layer-specific mechanical properties of human coronary arteries with nonatherosclerotic intimal thickening and related constitutive modeling. American Journal of Physiology-Heart and Circulatory Physiology, 289(5):H2048–H2058, 2005.
- [147] B. Horn and B. Schunck. Determining optical flow. Artificial intelligence, 1981.
- [148] Y. Hu, Z. Zhang, E. Torsney, A. R. Afzal, F. Davison, B. Metzler, and Q. Xu. Abundant progenitor cells in the adventitia contribute to atherosclerosis of vein grafts in apoe-deficient mice. The Journal of clinical investigation, 113(9):1258–1265, 2004.
- [149] T. Hughes, L. Franca, and M. Mallet. A new finite element formulation for computational fluid dynamics: VI. Convergence analysis of the generalized SUPG formulation for linear time-dependent multidimensional advective-diffusive systems. Computer Methods in Applied Mechanics and Engineering, (63):97–112, 1987.
- [150] J. D. Humphrey. Cardiovascular solid mechanics: cells, tissues, and organs. Springer Science & Business Media, 2013.
- [151] J. Humphrey. Possible mechanical roles of glycosaminoglycans in thoracic aortic dissection and associations with dysregulated transforming growth factor- β . Journal of vascular research, 50(1):1–10, 2012.
- [152] D. C. Iliopoulos, E. P. Kritharis, A. T. Giagini, S. A. Papadodima, and D. P. Sokolis. Ascending thoracic aortic aneurysms are associated with compositional remodeling and vessel stiffening but not weakening in age-matched subjects. The Journal of thoracic and cardiovascular surgery, 137(1):101–109, 2009.
- [153] G. H. S. Initiatives. Shifting Paradigm: How BRICS are Reshaping Global Health and Development. 2012.

- [154] M. F. Insana, R. F. Wagner, B. S. Garra, D. G. Brown, and T. H. Shawker. Analysis of ultrasound image texture via generalized rician statistics. Optical Engineering, 25(6):256743–256743, 1986.
- [155] J. Barajas et al. Cardiac phase extraction in ivus sequences using 1-d gabor filters. In Engineering in Medicine and Biology Society, 29th Annual International Conference of the IEEE, pages 343–346. IEEE, 2007.
- [156] A. Jabs, E.-i. Okamoto, J. Vinten-Johansen, G. Bauriedel, and J. N. Wilcox. Sequential patterns of chemokine-and chemokine receptor-synthesis following vessel wall injury in porcine coronary arteries. Atherosclerosis, 192(1):75–84, 2007.
- [157] E. Jakeman and R. Tough. Generalized k distribution: a statistical model for weak scattering. Journal of the Optical Society of America A, 4(9):1764–1772, 1987.
- [158] C. Janssen, C. de Korte, M. van der Heiden, C. Wapenaar, and a.F.W. van der Steen. Angle matching in intravascular elastography. Ultrasonics, 38(1-8):417–423, March 2000.
- [159] P. Jordán. Image-Based Mechanical Characterization of Soft Tissue using Three Dimensional Ultrasound. PhD thesis, MIT-Harvard, 2001.
- [160] P. Jordán, S. Socrate, T. E. Zickler, and R. D. Howe. A Nonrigid Image Registration Framework for Identification of Tissue Mechanical Parameters. In Medical Image Computing and Computer-Assisted InterventionMICCAI 2008, pages 930–938. Springer, 2008.
- [161] S. Julier, J. Uhlmann, and H. F. Durrant-Whyte. Technical notes and correspondence.. IEEE Transactions on automatic control, 45(3):477, 2000.
- [162] S. J. Julier. The spherical simplex unscented transformation. In American Control Conference, 2003. Proceedings of the 2003, volume 3, pages 2430–2434. IEEE, 2003.
- [163] S. J. Julier and J. K. Uhlmann. Reduced sigma point filters for the propagation of means and covariances through nonlinear transformations. In Proceedings of the 2002 American Control Conference (IEEE Cat. No. CH37301), volume 2, pages 887–892. IEEE, 2002.
- [164] S. J. Julier and J. K. Uhlmann. Unscented filtering and nonlinear estimation. Proceedings of the IEEE, 92(3):401–422, 2004.
- [165] T. Kailath, A. H. Sayed, and B. Hassibi. Linear estimation, volume 1. Prentice Hall Upper Saddle River, NJ, 2000.
- [166] S. Kamangar, G. Kalimuthu, I. Anjum Badruddin, A. Badarudin, N. Salman Ahmed, and T. Khan. Numerical investigation of the effect of stenosis geometry on the coronary diagnostic parameters. The Scientific World Journal, 2014, 2014.
- [167] K. Karamanidis, A. Travlou, P. Krauss, and U. Jaekel. Use of a LucasKanade-Based Template Tracking Algorithm to Examine In Vivo Tendon Excursion during Voluntary Contraction Using Ultrasonography. Ultrasound in Medicine & Biology, April 2016.
- [168] A. Karimi, M. Navidbakhsh, and A. Shojaei. A combination of histological analyses and uniaxial tensile tests to determine the material coefficients of the healthy and atherosclerotic human coronary arteries. Tissue and Cell, 47(2):152–158, 2015.

- [169] A. Katouzian, E. D. Angelini, S. G. Carlier, J. S. Suri, N. Navab, and A. F. Laine. A state-of-the-art review on segmentation algorithms in intravascular ultrasound (IVUS) images. IEEE Trans. Inform. Technol. Biomed., 16(5):823–34, September 2012.
- [170] A. Katouzian, A. Karamalis, J. Lissauskas, A. Eslami, and N. Navab. Ivus-histology image registration. In Biomedical Image Registration, pages 141–149. Springer Berlin Heidelberg, 2012.
- [171] S. Katranas, A. L. KeLeKiS, A. Antoniadis, A. G. ZiAKAS, and G. d GiAnnoGLou. Differences in stress forces and geometry between left and right coronary artery: a pathophysiological aspect of atherosclerosis heterogeneity. The Hellenic Journal of Cardiology, 56(3):217–223, 2015.
- [172] M. Kawasaki, H. Takatsu, T. Noda, K. Sano, Y. Ito, K. Hayakawa, K. Tsuchiya, M. Arai, K. Nishigaki, G. Takemura, S. Minatoguchi, T. Fujiwara, and H. Fujiwara. In Vivo Quantitative Tissue Characterization of Human Coronary Arterial Plaques by Use of Integrated Backscatter Intravascular Ultrasound and Comparison With Angioscopic Findings. Circulation, 105(21):2487–2492, May 2002.
- [173] A. Krettek, G. K. Sukhova, and P. Libby. Elastogenesis in human arterial disease a role for macrophages in disordered elastin synthesis. Arteriosclerosis, thrombosis, and vascular biology, 23(4):582–587, 2003.
- [174] J. Krücker et al. Rapid elastic image registration for 3-D ultrasound. IEEE transactions on medical imaging, 21(11):1384–94, 2002.
- [175] M. Kruk, D. Noll, S. Achenbach, G. S. Mintz, J. Pregowski, E. Kaczmarska, K. Kryczka, R. Pracon, Z. Dzielińska, J. Śleszycka, et al. Impact of coronary artery calcium characteristics on accuracy of ct angiography. JACC: Cardiovascular Imaging, 7(1):49–58, 2014.
- [176] M. Kruk, L. Wardziak, G. S. Mintz, S. Achenbach, J. Pregowski, W. Ruzyllo, Z. Dzielinska, M. Demkow, A. Witkowski, and C. Kepka. Accuracy of coronary computed tomography angiography vs intravascular ultrasound for evaluation of vessel area. Journal of Cardiovascular Computed Tomography, 8(2):141–148, March 2014.
- [177] D. N. Ku, D. P. Giddens, C. K. Zarins, and S. Glagov. Pulsatile flow and atherosclerosis in the human carotid bifurcation. positive correlation between plaque location and low oscillating shear stress. Arteriosclerosis, thrombosis, and vascular biology, 5(3):293–302, 1985.
- [178] H. M. Kwon, G. Sangiorgi, L. G. Spagnoli, K. Miyauchi, D. R. Holmes, R. S. Schwartz, and A. Lerman. Experimental hypercholesterolemia induces ultrastructural changes in the internal elastic lamina of porcine coronary arteries. Atherosclerosis, 139(2):283–289, 1998.
- [179] P.-Y. Lagrée. An inverse technique to deduce the elasticity of a large artery. The European Physical Journal Applied Physics, 9(2):153–163, 2000.
- [180] S.-H. Lai and B. C. Vemuri. Reliable and efficient computation of optical flow. International Journal of Computer Vision, 29(2):87–105, 1998.
- [181] W. M. Lai, J. Hou, and V. C. Mow. A triphasic theory for the swelling and deformation behaviors of articular cartilage. Journal of biomechanical engineering, 113(3):245–258, 1991.

- [182] J. P. Lane, L. E. Perkins, A. J. Sheehy, E. J. Pacheco, M. P. Frie, B. J. Lambert, R. J. Rapoza, and R. Virmani. Lumen gain and restoration of pulsatility after implantation of a bioresorbable vascular scaffold in porcine coronary arteries. JACC: Cardiovascular Interventions, 7(6):688–695, 2014.
- [183] I. Larrabide, P. Blanco, S. Urquiza, E. Dari, M. Vénere, N. de Souza e Silva, and R. Feijóo. Hemolab hemodynamics modelling laboratory: An application for modelling the human cardiovascular system. Computers in Biology and Medicine, 42:993–1004, 2012.
- [184] L. J. Laslett, P. Alagona, B. A. Clark, J. P. Drozda, F. Saldivar, S. R. Wilson, C. Poe, and M. Hart. The worldwide environment of cardiovascular disease: prevalence, diagnosis, therapy, and policy issues: a report from the american college of cardiology. Journal of the American College of Cardiology, 60(25):S1–S49, 2012.
- [185] T. Lassila, A. Manzoni, A. Quarteroni, and G. Rozza. A reduced computational and geometrical framework for inverse problems in hemodynamics. International journal for numerical methods in biomedical engineering, 29(7):741–776, 2013.
- [186] B. M. Learoyd and M. G. Taylor. Alterations with age in the viscoelastic properties of human arterial walls. Circulation research, 18(3):278–292, 1966.
- [187] R. T. Lee, S. G. Richardson, H. M. Loree, A. J. Grodzinsky, S. A. Gharib, F. J. Schoen, and N. Pandian. Prediction of mechanical properties of human atherosclerotic tissue by high-frequency intravascular ultrasound imaging. an in vitro study. Arteriosclerosis, Thrombosis, and Vascular Biology, 12(1):1–5, 1992.
- [188] R. T. Lee, F. J. Schoen, H. M. Loree, M. W. Lark, and P. Libby. Circumferential stress and matrix metalloproteinase 1 in human coronary atherosclerosis implications for plaque rupture. Arteriosclerosis, thrombosis, and vascular biology, 16(8):1070–1073, 1996.
- [189] K. E. Leung, R. Baldewsing, F. Mastik, J. A. Schaar, A. Gisolf, V. der Steen, A. F. Ton, et al. Motion compensation for intravascular ultrasound palpography. IEEE Trans. Ultrason., Ferroelect., Freq. Contr., 53(7):1269–1280, 2006.
- [190] J. Lewis, R. G. Taylor, N. Jones, R. St Clair, and J. Cornhill. Endothelial surface characteristics in pigeon coronary artery atherosclerosis. i. cellular alterations during the initial stages of dietary cholesterol challenge. Laboratory investigation; a journal of technical methods and pathology, 46(2):123–138, 1982.
- [191] A. C. Li and C. K. Glass. The macrophage foam cell as a target for therapeutic intervention. Nature medicine, 8(11):1235–1242, 2002.
- [192] P. C. Li, C. J. Cheng, and C. K. Yeh. On velocity estimation using speckle decorrelation. IEEE Trans. Ultrason., Ferroelect., Freq. Contr., 48(4):1084–1091, 2001.
- [193] Y. Liang, H. Zhu, and M. H. Friedman. Estimation of the transverse strain tensor in the arterial wall using IVUS image registration. Ultrasound. Med. Biol., 34(11):1832–45, November 2008.
- [194] Y. Liang, H. Zhu, T. Gehrig, and M. H. Friedman. Measurement of the transverse strain tensor in the coronary arterial wall from clinical intravascular ultrasound images. Journal of Biomechanics, 41(14):2906–2911, October 2008.

- [195] A. Lipponen, A. Seppänen, and J. Kaipio. Reduced-order estimation of nonstationary flows with electrical impedance tomography. Inverse Problems, 26(7):074010, 2010.
- [196] L. Liu, W. Yang, Y. Nagahara, Y. Li, S. R. Lamooki, T. Muramatsu, P. Kitslaar, M. Sarai, Y. Ozaki, P. Barlis, et al. The impact of image resolution on computation of fractional flow reserve: coronary computed tomography angiography versus 3-dimensional quantitative coronary angiography. The international journal of cardiovascular imaging, 32(3):513–523, 2016.
- [197] S. Liu and Y. Fung. Zero-stress states of arteries. Journal of biomechanical engineering, 110(1):82–84, 1988.
- [198] H. M. Loree, A. J. Grodzinsky, S. Y. Park, L. J. Gibson, and R. T. Lee. Static circumferential tangential modulus of human atherosclerotic tissue. Journal of biomechanics, 27(2):195–204, 1994.
- [199] H. M. Loree, B. J. Tobias, L. J. Gibson, R. D. Kamm, D. M. Small, and R. T. Lee. Mechanical properties of model atherosclerotic lesion lipid pools. Arterioscler., Thromb., Vasc. Biol., 14(2):230–234, 1994.
- [200] W. E. Lorensen and H. E. Cline. Marching cubes: A high resolution 3d surface construction algorithm. Computer Graphics, 21(4):163–169, 1987.
- [201] B. D. Lucas, T. Kanade, and others. An iterative image registration technique with an application to stereo vision. In IJCAI, volume 81, pages 674–679, 1981.
- [202] K. Maiellaro and W. R. Taylor. The role of the adventitia in vascular inflammation. Cardiovascular research, 75(4):640–648, 2007.
- [203] M. W. Majesky, X. R. Dong, V. Hoglund, W. M. Mahoney, and G. Daum. The adventitia a dynamic interface containing resident progenitor cells. Arteriosclerosis, thrombosis, and vascular biology, 31(7):1530–1539, 2011.
- [204] M. W. Majesky, X. R. Dong, J. N. Regan, and V. J. Hoglund. Vascular smooth muscle progenitor cells building and repairing blood vessels. Circulation research, 108(3):365–377, 2011.
- [205] M. W. Majesky, V. Lindner, D. R. Twardzik, S. M. Schwartz, and M. A. Reidy. Production of transforming growth factor beta 1 during repair of arterial injury. Journal of Clinical Investigation, 88(3):904, 1991.
- [206] A. M. Malek, S. L. Alper, and S. Izumo. Hemodynamic shear stress and its role in atherosclerosis. JAMA, 282(21):2035–2042, 1999.
- [207] M. Malvè, A. Gharib, S. Yazdani, G. Finet, M. Martínez, R. Pettigrew, and J. Ohayon. Tortuosity of coronary bifurcation as a potential local risk factor for atherosclerosis: Cfd steady state study based on in vivo dynamic ct measurements. Annals of biomedical engineering, 43(1):82–93, 2015.
- [208] J. Mariani, C. Guedes, P. Soares, S. Zalc, C. M. Campos, A. C. Lopes, A. G. Spadaro, M. A. Perin, A. Esteves Filho, C. K. Takimura, et al. Intravascular ultrasound guidance to minimize the use of iodine contrast in percutaneous coronary intervention: the mozart (minimizing contrast utilization with ivus guidance in coronary angioplasty) randomized controlled trial. JACC: Cardiovascular Interventions, 7(11):1287–1293, 2014.

- [209] A. Maroudas. Balance between swelling pressure and collagen tension in normal and degenerate cartilage. *Nature*, 260(5554):808–809, 1976.
- [210] V. Martin, F. Clément, A. Decoene, and J.-F. Gerbeau. Parameter identification for a one-dimensional blood flow model. In *ESAIM: Proceedings*, volume 14, pages 174–200. EDP Sciences, 2005.
- [211] G. D. Maso Talou, P. J. Blanco, I. Larrabide, C. G. Bezerra, P. A. Lemos, and R. A. Feijóo. Registration methods for ivus: Transversal and longitudinal transducer motion compensation. *IEEE Transactions on Biomedical Engineering*, 64(4), Apr 2016.
- [212] G. D. Maso Talou. Ivus images segmentation driven by active contours and spacio-temporal reconstruction of the coronary vessels aided by angiographies. Master’s thesis, National Laboratory for Scientific Computing, Mar 2013.
- [213] G. D. Maso Talou, P. J. Blanco, I. Larrabide, C. G. Bezerra, P. A. Lemos, and R. A. Feijóo. Combining transversal and longitudinal registration in ivus studies. In *International Conference on Medical Image Computing and Computer-Assisted Intervention*, pages 346–353. Springer International Publishing, 2015.
- [214] G. D. Maso Talou, I. Larrabide, P. J. Blanco, C. G. Bezerra, P. A. Lemos, and R. A. Feijóo. Improving cardiac phase extraction in ivus studies by integration of gating methods. *IEEE Transactions on Biomedical Engineering*, 62(12):2867 – 2877, 2015.
- [215] H. Masuda, Y.-J. Zhuang, T. M. Singh, K. Kawamura, M. Murakami, C. K. Zarins, and S. Glagov. Adaptive remodeling of internal elastic lamina and endothelial lining during flow-induced arterial enlargement. *Arteriosclerosis, thrombosis, and vascular biology*, 19(10):2298–2307, 1999.
- [216] T. Masuoka, N. Hayashi, E. Hori, N. Kuwayama, O. Ohtani, and S. Endo. Distribution of internal elastic lamina and external elastic lamina in the internal carotid artery: possible relationship with atherosclerosis. *Neurologia medico-chirurgica*, 50(3):179–182, 2010.
- [217] C. Mathers, G. Stevens, W. R. Mahanani, J. Ho, D. M. Fat, and D. Hogan. Who methods and data sources for country-level causes of death 2000-2015. Technical report, World Health Organization, 2016.
- [218] M. Matsumoto, P. A. Lemos, and S. S. Furuie. IVUS coronary volume alignment for distinct phases. In S. A. McAleavey and J. D’hooge, editors, *SPIE Medical Imaging*, volume 7265, pages 72650X–72650X–7. International Society for Optics and Photonics, February 2009.
- [219] T. Matsumoto and K. Nagayama. Tensile properties of vascular smooth muscle cells: bridging vascular and cellular biomechanics. *Journal of biomechanics*, 45(5):745–755, 2012.
- [220] E. Mémin and P. Pérez. Dense estimation and object-based segmentation of the optical flow with robust techniques. *Image Processing, IEEE Transactions on*, 7(5):703–719, 1998.
- [221] S. Meran and R. Steadman. Fibroblasts and myofibroblasts in renal fibrosis. *International journal of experimental pathology*, 92(3):158–167, 2011.

- [222] O. V. Michailovich and A. Tannenbaum. Despeckling of medical ultrasound images. Ultrasonics, Ferroelectrics, and Frequency Control, IEEE Transactions on, 53(1):64–78, 2006.
- [223] I. Miki, S. Krucinski, and J. D. Thomas. Segmentation and tracking in echocardiographic sequences: active contours guided by optical flow estimates. Medical Imaging, IEEE Transactions on, 17(2):274–284, 1998.
- [224] G. S. Mintz, S. E. Nissen, W. D. Anderson, S. R. Bailey, R. Erbel, P. J. Fitzgerald, F. J. Pinto, K. Rosenfield, R. J. Siegel, E. M. Tuzcu, et al. American college of cardiology clinical expert consensus document on standards for acquisition, measurement and reporting of intravascular ultrasound studies (ivus). a report of the american college of cardiology task force on clinical expert consensus documents developed in collaboration with the european society of cardiology endorsed by the society of cardiac angiography and interventions. Journal of the American College of Cardiology, 37(5):1478–1492, 2001.
- [225] H. Mita, H. Kanai, and Y. Koiwa. Cross-sectional elastic imaging of arterial wall using intravascular ultrasonography. Japanese Journal of Applied Physics, 40(7):4753–4762, 2001.
- [226] H. Miyazaki, Y. Hasegawa, and K. Hayashi. Tensile properties of contractile and synthetic vascular smooth muscle cells. JSME International Journal Series C, 45(4):870–879, 2002.
- [227] M. R. Mofrad and R. D. Kamm. Cellular mechanotransduction: diverse perspectives from molecules to tissues. Cambridge University Press, 2009.
- [228] P. Moireau and D. Chapelle. Reduced-order unscented kalman filtering with application to parameter identification in large-dimensional systems. ESAIM: Control, Optimisation and Calculus of Variations, 17(2):380–405, 2011.
- [229] P. Moireau, D. Chapelle, and P. Le Tallec. Joint state and parameter estimation for distributed mechanical systems. Computer methods in applied mechanics and engineering, 197(6):659–677, 2008.
- [230] P. Moireau, D. Chapelle, and P. Le Tallec. Filtering for distributed mechanical systems using position measurements: perspectives in medical imaging. Inverse problems, 25(3):035010, 2009.
- [231] M. Molina, G. P. Prause, P. Radeva, and M. Sonka. 3d catheter path reconstruction from biplane angiograms. In Medical Imaging’98, pages 504–512. International Society for Optics and Photonics, 1998.
- [232] P. D. Morris, F. N. van de Vosse, P. V. Lawford, D. R. Hose, and J. P. Gunn. virtual(computed) fractional flow reserve: current challenges and limitations. JACC: Cardiovascular Interventions, 8(8):1009–1017, 2015.
- [233] K. S. Moulton, K. Vakili, D. Zurakowski, M. Soliman, C. Butterfield, E. Sylvain, K.-M. Lo, S. Gillies, K. Javaherian, and J. Folkman. Inhibition of plaque neovascularization reduces macrophage accumulation and progression of advanced atherosclerosis. Proceedings of the National Academy of Sciences, 100(8):4736–4741, 2003.
- [234] A. Murashige, T. Hiro, T. Fujii, K. Imoto, T. Murata, Y. Fukumoto, and M. Matsuzaki. Detection of lipid-laden atherosclerotic plaque by wavelet analysis of radiofrequency intravascular ultrasound signals in vitro validation and preliminary in vivo application. J Am Coll Cardiol, 45(12):1954–1960, 2005.

- [235] N. Bruining et al. Ecg-gated versus nongated three-dimensional intracoronary ultrasound analysis: implications for volumetric measurements. Catheterization and cardiovascular diagnosis, 43(3):254–260, 1998.
- [236] K. Nagayama, Y. Nagano, M. Sato, and T. Matsumoto. Effect of actin filament distribution on tensile properties of smooth muscle cells obtained from rat thoracic aortas. Journal of biomechanics, 39(2):293–301, 2006.
- [237] K. Nagayama, S. Yanagihara, and T. Matsumoto. Actin filaments affect on not only elasticity but also late viscous response in stress relaxation of single isolated aortic smooth muscle cells (possible effect of active reorganization of actin filaments). Journal of Biomechanical Science and Engineering, 2(3):93–104, 2007.
- [238] H.-H. Nagel and W. Enkelmann. An investigation of smoothness constraints for the estimation of displacement vector fields from image sequences. Pattern Analysis and Machine Intelligence, IEEE Transactions on, (5):565–593, 1986.
- [239] A. Nair, B. D. Kuban, E. M. Tuzcu, P. Schoenhagen, S. E. Nissen, and D. G. Vince. Coronary Plaque Classification With Intravascular Ultrasound Radiofrequency Data Analysis. Circulation, 106(17):2200–2206, October 2002.
- [240] R. Nakazato, H.-B. Park, D. S. Berman, H. Gransar, B.-K. Koo, A. Erglis, F. Y. Lin, A. M. Dunning, M. J. Budoff, J. Malpeso, et al. Noninvasive fractional flow reserve derived from computed tomography angiography for coronary lesions of intermediate stenosis severity. Circulation: Cardiovascular Imaging, 6(6):881–889, 2013.
- [241] P. Nesi. Variational approach to optical flow estimation managing discontinuities. Image and Vision Computing, 11(7):419–439, 1993.
- [242] D. Noll, M. Kruk, J. Prgowski, E. Kaczmarek, K. Kryczka, R. Pracon, M. Skwarek, Z. Dzielińska, J. Petryka, M. Spiewak, et al. Lumen and calcium characteristics within calcified coronary lesions. comparison of computed tomography coronary angiography versus intravascular ultrasound. Postepy Kardiologii Interwencyjnej, 9:1–8, 2013.
- [243] K. Oakeson. Quantification of cross-sectional artery wall motion with IVUS image registration. In W. F. Walker and S. Y. Emelianov, editors, Medical Imaging 2004, volume 5373, pages 119–130. International Society for Optics and Photonics, April 2004.
- [244] J. Ohayon, O. Dubreuil, P. Tracqui, S. Le Floc’h, G. Rioufol, L. Chalabreysse, F. Thivolet, R. I. Pettigrew, and G. Finet. Influence of residual stress/strain on the biomechanical stability of vulnerable coronary plaques: potential impact for evaluating the risk of plaque rupture. Am. J. Physiol., 293(3):H1987–96, September 2007.
- [245] N. Ohta. Uncertainty models of the gradient constraint for optical flow computation. IEICE Transactions on Information and Systems, E79(D7):958–962, 1996.
- [246] T. Okabe, W. G. Weigold, G. S. Mintz, R. Roswell, S. Joshi, S. Y. Lee, B. Lee, D. H. Steinberg, P. Roy, T. L. P. Slottow, et al. Comparison of intravascular ultrasound to contrast-enhanced 64-slice computed tomography to assess the significance of angiographically ambiguous coronary narrowings. The American journal of cardiology, 102(8):994–1001, 2008.

- [247] E. P. Ong and M. Spann. Robust optical flow computation based on least-median-of-squares regression. *International Journal of Computer Vision*, 31(1):51–82, 1999.
- [248] J. Ophir, I. Céspedes, H. Ponnekanti, Y. Yazdi, and X. Li. Elastography: A method for imaging the elasticity in biological tissues. *Ultrasonic Imaging*, 13:111–134, 1991.
- [249] A. Orimo and R. A. Weinberg. Stromal fibroblasts in cancer: a novel tumor-promoting cell type. *Cell Cycle*, 5(15):1597–1601, 2006.
- [250] C. Pagiatakis, R. Galaz, J.-C. Tardif, and R. Mongrain. A comparison between the principal stress direction and collagen fiber orientation in coronary atherosclerotic plaque fibrous caps. *Medical & biological engineering & computing*, 53(6):545–555, 2015.
- [251] M. I. Papafaklis, T. Muramatsu, Y. Ishibashi, L. S. Lakkas, S. Nakatani, C. V. Bourantas, J. Ligthart, Y. Onuma, M. Echavarria-Pinto, G. Tsirka, et al. Fast virtual functional assessment of intermediate coronary lesions using routine angiographic data and blood flow simulation in humans: comparison with pressure wire-fractional flow reserve. *EuroIntervention: journal of EuroPCR in collaboration with the Working Group on Interventional Cardiology of the European Society of Cardiology*, 10(5):574–583, 2014.
- [252] A. Papoulis and S. U. Pillai. *Probability, random variables, and stochastic processes*. Tata McGraw-Hill Education, 2002.
- [253] J. N. Passman, X. R. Dong, S.-P. Wu, C. T. Maguire, K. A. Hogan, V. L. Bautch, and M. W. Majesky. A sonic hedgehog signaling domain in the arterial adventitia supports resident $\text{sc}\alpha^+$ smooth muscle progenitor cells. *Proceedings of the National Academy of Sciences*, 105(27):9349–9354, 2008.
- [254] I. Patras, M. Worring, and R. vandenBoomgaard. Dense Motion Estimation Using Regularization Constraints on Local Parametric Models. *IEEE Transactions on Image Processing*, 13(11):1432–1443, November 2004.
- [255] M. Perego, A. Veneziani, and C. Vergara. A variational approach for estimating the compliance of the cardiovascular tissue: An inverse fluid-structure interaction problem. *SIAM Journal on Scientific Computing*, 33(3):1181–1211, 2011.
- [256] J. S. Pérez, E. Meinhardt-Llopis, and G. Facciolo. Tv-l1 optical flow estimation. *Image Processing On Line*, 2013:137–150, 2013.
- [257] N. H. Pijls, W. F. Fearon, P. A. Tonino, U. Siebert, F. Ikeno, B. Bornschein, M. van’t Veer, V. Klauss, G. Manoharan, T. Engstrøm, et al. Fractional flow reserve versus angiography for guiding percutaneous coronary intervention in patients with multivessel coronary artery disease: 2-year follow-up of the fame (fractional flow reserve versus angiography for multivessel evaluation) study. *Journal of the American College of Cardiology*, 56(3):177–184, 2010.
- [258] A. R. Poole. Proteoglycans in health and disease: structures and functions. *Biochemical Journal*, 236(1):1, 1986.
- [259] D. Powell, R. Mifflin, J. Valentich, S. Crowe, J. Saada, and A. West. Myofibroblasts. i. paracrine cells important in health and disease. *American Journal of Physiology-Cell Physiology*, 277(1):C1–C19, 1999.

- [260] M. Proesmans, L. Van Gool, E. Pauwels, and A. Oosterlinck. Determination of optical flow and its discontinuities using non-linear diffusion. In Computer VisionECCV'94, pages 294–304. Springer, 1994.
- [261] P. Pyagay, M. Heroult, Q. Wang, W. Lehnert, J. Belden, L. Liaw, R. E. Friesel, and V. Lindner. Collagen triple helix repeat containing 1, a novel secreted protein in injured and diseased arteries, inhibits collagen expression and promotes cell migration. Circulation research, 96(2):261–268, 2005.
- [262] S. A. Pyxaras, S. Tu, E. Barbato, G. Barbati, L. Di Serafino, F. De Vroey, G. Toth, F. Mangiacapra, G. Sinagra, B. De Bruyne, et al. Quantitative angiography and optical coherence tomography for the functional assessment of nonobstructive coronary stenoses: comparison with fractional flow reserve. American heart journal, 166(6):1010–1018, 2013.
- [263] N. Qi, H. Gao, R. W. Ogden, N. A. Hill, G. A. Holzapfel, H.-C. Han, and X. Luo. Investigation of the optimal collagen fibre orientation in human iliac arteries. Journal of the mechanical behavior of biomedical materials, 52:108–119, 2015.
- [264] Qi Duan, S. Herz, C. Ingrassia, K. Costa, J. Holmes, A. Laine, E. Angelini, O. Gerard, and S. Homma. Dynamic Cardiac Information From Optical Flow Using Four Dimensional Ultrasound. pages 4465–4468. IEEE, 2005.
- [265] C. Quammen, C. Weigle, and R. Taylor. Boolean operations on surfaces in vtk without external libraries. Insight Journal, 797:1–12, 2011.
- [266] A. Rachev and S. Greenwald. Residual strains in conduit arteries. Journal of biomechanics, 36(5):661–670, 2003.
- [267] B. I. Raju and M. A. Srinivasan. Statistics of envelope of high-frequency ultrasonic backscatter from human skin in vivo. Ultrasonics, Ferroelectrics, and Frequency Control, IEEE Transactions on, 49(7):871–882, 2002.
- [268] L. M. Rasmussen, Y. G. Wolf, and E. Ruoslahti. Vascular smooth muscle cells from injured rat aortas display elevated matrix production associated with transforming growth factor-beta activity. The American journal of pathology, 147(4):1041, 1995.
- [269] E. R. Regan and W. C. Aird. Dynamical systems approach to endothelial heterogeneity. Circulation research, 111(1):110–130, 2012.
- [270] S. Rensen, P. Doevendans, and G. Van Eys. Regulation and characteristics of vascular smooth muscle cell phenotypic diversity. Netherlands Heart Journal, 15(3):100–108, 2007.
- [271] N. Resnick, H. Yahav, A. Shay-Salit, M. Shushy, S. Schubert, L. C. M. Zilberman, and E. Wofovitz. Fluid shear stress and the vascular endothelium: for better and for worse. Progress in biophysics and molecular biology, 81(3):177–199, 2003.
- [272] R. H. Reynertson, R. T. Parmley, L. Rodén, and S. Oparil. Proteoglycans and hypertension ia biochemical and ultrastructural study of aorta glycosaminoglycans in spontaneously hypertensive rats. Collagen and related research, 6(1):77–101, 1986.
- [273] M. S. Richards and M. M. Dooley. Non-Rigid Image Registration Based Strain Estimator for Intravascular Ultrasound Elastography. Ultrasound in Medicine & Biology, 39(3):515–533, mar 2013.

- [274] P. D. Richardson, M. Davies, and G. Born. Influence of plaque configuration and stress distribution on fissuring of coronary atherosclerotic plaques. The Lancet, 334(8669):941–944, 1989.
- [275] M. R. Roach and A. C. Burton. The reason for the shape of the distensibility curves of arteries. Canadian journal of biochemistry and physiology, 35(8):681–690, 1957.
- [276] A. M. Robertson and P. N. Watton. Chapter 8 - mechanobiology of the arterial wall. In S. M. Becker and A. V. Kuznetsov, editors, Transport in Biological Media, pages 275 – 347. Elsevier, Boston, 2013.
- [277] S. Roccabianca, C. Bellini, and J. Humphrey. Computational modelling suggests good, bad and ugly roles of glycosaminoglycans in arterial wall mechanics and mechanobiology. Journal of The Royal Society Interface, 11(97):20140397, 2014.
- [278] S. Roccabianca, G. A. Ateshian, and J. D. Humphrey. Biomechanical roles of medial pooling of glycosaminoglycans in thoracic aortic dissection. Biomechanics and modeling in mechanobiology, 13(1):13–25, 2014.
- [279] A. Roche, G. Malandain, and N. Ayache. Unifying maximum likelihood approaches in medical image registration. PhD thesis, Inria, 1999.
- [280] J. F. Rodríguez, C. Ruiz, M. Doblaré, and G. A. Holzapfel. Mechanical stresses in abdominal aortic aneurysms: influence of diameter, asymmetry, and material anisotropy. Journal of biomechanical engineering, 130(2):021023, 2008.
- [281] M. Rosales, P. Radeva, O. Rodriguez-Leor, and D. Gil. Modelling of image-catheter motion for 3-D IVUS. Medical Image Analysis, 13(1):91–104, February 2009.
- [282] L. I. Rudin, S. Osher, and E. Fatemi. Nonlinear total variation based noise removal algorithms. Physica D: Nonlinear Phenomena, 60(1-4):259–268, November 1992.
- [283] P. Ruengsakulrach, R. Sinclair, M. Komeda, J. Raman, I. Gordon, and B. Buxton. Comparative histopathology of radial artery versus internal thoracic artery and risk factors for development of intimal hyperplasia and atherosclerosis. Circulation, 100(suppl 2):II–139, 1999.
- [284] S. A. De Winter et al. A novel retrospective gating method for intracoronary ultrasound images based on image properties. In Computers in Cardiology, 2003, pages 13–16. IEEE, 2003.
- [285] S. K. Nadkarni et al. Image-based cardiac gating for three-dimensional intravascular ultrasound imaging. Ultrasound in Medicine and Biology, 31(1):53–63, 2005.
- [286] S. M. O’Malley et al. Image-based gating of intravascular ultrasound pullback sequences. Information Technology in Biomedicine, IEEE Transactions on, 12(3):299–306, 2008.
- [287] S. Sathyanarayana, S. Carlier, W. Li, and L. Thomas. Characterisation of atherosclerotic plaque by spectral similarity of radiofrequency intravascular ultrasound signals. EuroIntervention, 5(1):133–139, May 2009.
- [288] C. Schnörr. On functionals with greyvalue-controlled smoothness terms for determining optical flow. Pattern Analysis and Machine Intelligence, IEEE Transactions on, 15(10):1074–1079, 1993.

- [289] A. J. Schrieffl, A. J. Reinisch, S. Sankaran, D. M. Pierce, and G. A. Holzapfel. Quantitative assessment of collagen fibre orientations from two-dimensional images of soft biological tissues. Journal of The Royal Society Interface, 9(76):3081–3093, 2012.
- [290] A. J. Schrieffl, G. Zeindlinger, D. M. Pierce, P. Regitnig, and G. A. Holzapfel. Determination of the layer-specific distributed collagen fibre orientations in human thoracic and abdominal aortas and common iliac arteries. Journal of the Royal Society Interface, page rsif20110727, 2011.
- [291] S. M. Schwartz, E. R. OBrien, et al. The intima soil for atherosclerosis and restenosis. Circulation research, 77(3):445–465, 1995.
- [292] N. A. Scott, G. D. Cipolla, C. E. Ross, B. Dunn, F. H. Martin, L. Simonet, and J. N. Wilcox. Identification of a potential role for the adventitia in vascular lesion formation after balloon overstretch injury of porcine coronary arteries. Circulation, 93(12):2178–2187, 1996.
- [293] C. Sehgal. Quantitative relationship between tissue composition and scattering of ultrasound. The Journal of the Acoustical Society of America, 94(4):1944–1952, 1993.
- [294] M. Sermesant, P. Moireau, O. Camara, J. Sainte-Marie, R. Andriantsimiavona, R. Cimrman, D. L. Hill, D. Chapelle, and R. Razavi. Cardiac function estimation from mri using a heart model and data assimilation: advances and difficulties. Medical Image Analysis, 10(4):642–656, 2006.
- [295] P. M. Shankar. A general statistical model for ultrasonic backscattering from tissues. Ultrasonics, Ferroelectrics, and Frequency Control, IEEE Transactions on, 47(3):727–736, 2000.
- [296] B. M. Shapo, J. R. Crowe, R. Erkamp, S. Y. Emelianov, M. J. Eberle, and M. O’Donnell. Strain imaging of coronary arteries with intraluminal ultrasound: experiments on an inhomogeneous phantom. Ultrasonic Imaging, 18(3):173–91, July 1996.
- [297] Y. Shi, F. J. de Ana, S. J. Chetcuti, and M. O’Donnell. Motion artifact reduction for IVUS-based thermal strain imaging. IEEE Transactions on Ultrasonics, Ferroelectrics, and Frequency, 52(8):1312–9, August 2005.
- [298] Y. Shi, J. E. O’Brien, A. Fard, J. D. Mannion, D. Wang, and A. Zaleski. Adventitial myofibroblasts contribute to neointimal formation in injured porcine coronary arteries. Circulation, 94(7):1655–1664, 1996.
- [299] D. Shulman and J.-Y. Herv. Regularization of discontinuous flow fields. In Visual Motion, 1989., Proceedings. Workshop on, pages 81–86. IEEE, 1989.
- [300] D. Simon. Optimal state estimation: Kalman, H infinity, and nonlinear approaches. John Wiley & Sons, 2006.
- [301] R. S. Smith, T. J. Smith, T. M. Blieden, and R. P. Phipps. Fibroblasts as sentinel cells. synthesis of chemokines and regulation of inflammation. The American journal of pathology, 151(2):317, 1997.
- [302] S. Smith, J. Ralston, and K. Taubert. Urbanization and cardiovascular disease: Raising heart-healthy children in todays cities. Geneva: The World Heart Federation, 2012.

- [303] E. W. Stacy. A generalization of the gamma distribution. The Annals of Mathematical Statistics, pages 1187–1192, 1962.
- [304] J. Stålhand. Determination of human arterial wall parameters from clinical data. Biomechanics and modeling in mechanobiology, 8(2):141–148, 2009.
- [305] H. C. Stary, D. H. Blankenhorn, A. B. Chandler, S. Glagov, W. Insull Jr, M. Richardson, M. E. Rosenfeld, S. A. Schaffer, C. J. Schwartz, and W. D. Wagner. A definition of the intima of human arteries and of its atherosclerosis-prone regions. a report from the committee on vascular lesions of the council on arteriosclerosis, american heart association. Circulation, 85(1):391, 1992.
- [306] D. Steinberg. The ldl modification hypothesis of atherogenesis: an update. Journal of lipid research, 50(Supplement):S376–S381, 2009.
- [307] D. Steinberg and J. L. Witztum. Oxidized low-density lipoprotein and atherosclerosis. Arteriosclerosis, Thrombosis, and Vascular Biology, 30(12):2311–2316, 2010.
- [308] N. Stergiopoulos, S. Vulliamoz, A. Rachev, J.-J. Meister, and S. Greenwald. Assessing the homogeneity of the elastic properties and composition of the pig aortic media. Journal of vascular research, 38(3):237–246, 2001.
- [309] J. Stoitsis, S. Golemati, A. Dimopoulos, and K. Nikita. Analysis and quantification of arterial wall motion from B-mode ultrasound images comparison of block-matching and optical flow. In Engineering in Medicine and Biology 27th Annual Conference, Shanghai, China, September 2005.
- [310] L. Timmins et al. Framework to co-register longitudinal virtual histology-intravascular ultrasound data in the circumferential direction. IEEE Transactions on Medical Imaging, 32(11):1989–1996, 2013.
- [311] M. Togni, S. Windecker, R. Cocchia, P. Wenaweser, S. Cook, M. Billinger, B. Meier, and O. M. Hess. Sirolimus-eluting stents associated with paradoxical coronary vasoconstriction. Journal of the American College of Cardiology, 46(2):231–236, 2005.
- [312] P. Tracqui, A. Broisat, J. Toczek, N. Mesnier, J. Ohayon, and L. Riou. Mapping elasticity moduli of atherosclerotic plaque in situ via atomic force microscopy. Journal of structural biology, 174(1):115–123, 2011.
- [313] T. H. Tuthill, R. H. Sperry, and K. J. Parker. Deviations from Rayleigh statistics in ultrasound speckle. Ultrasonic imaging, 10(2):81–89, 1988.
- [314] S. Uras, F. Giroso, A. Verri, and V. Torre. A computational approach to motion perception. Biological Cybernetics, 60(2):79–87, 1988.
- [315] A. Valentín, J. Humphrey, and G. A. Holzapfel. A multi-layered computational model of coupled elastin degradation, vasoactive dysfunction, and collagenous stiffening in aortic aging. Annals of biomedical engineering, 39(7):2027–2045, 2011.
- [316] J. van den Akker, B. G. Tuna, A. Pisteu, A. J. Sleutel, E. N. Bakker, and E. van Bavel. Vascular smooth muscle cells remodel collagen matrices by long-distance action and anisotropic interaction. Medical & biological engineering & computing, 50(7):701–715, 2012.
- [317] B. M. van den Berg, J. A. Spaan, T. M. Rolf, and H. Vink. Atherogenic region and diet diminish glycocalyx dimension and increase intima-to-media ratios at murine carotid artery bifurcation. American Journal of Physiology-Heart and Circulatory Physiology, 290(2):H915–H920, 2006.

- [318] A. L. Vavere, A. Arbab-Zadeh, C. E. Rochitte, M. Dewey, H. Niinuma, I. Gottlieb, M. E. Clouse, D. E. Bush, J. W. Hoe, A. De Roos, et al. Coronary artery stenoses: accuracy of 64-detector row ct angiography in segments with mild, moderate, or severe calcification: a subanalysis of the core-64 trial. Radiology, 261(1):100–108, 2011.
- [319] A. I. Veress, J. F. Cornhill, E. E. Herderick, and J. D. Thomas. Age-related development of atherosclerotic plaque stress: a population-based finite-element analysis. Coronary artery disease, 9(1):13–19, 1998.
- [320] P. A. Viola. Alignment by Maximization of Mutual Information. PhD Thesis, Massachusetts Institute of Technology, 1995.
- [321] R. Virmani, F. D. Kolodgie, A. P. Burke, A. Farb, and S. M. Schwartz. Lessons from sudden coronary death. Arteriosclerosis, thrombosis, and vascular biology, 20(5):1262–1275, 2000.
- [322] C. von Birgelen et al. Electrocardiogram-gated intravascular ultrasound image acquisition after coronary stent deployment facilitates on-line three-dimensional reconstruction and automated lumen quantification. Journal of the American College of Cardiology, 30(2):436–43, August 1997.
- [323] A. Vukicevic et al. Computer methods for follow-up study of hemodynamic and disease progression in the stented coronary artery by fusing IVUS and X-ray angiography. Medical and Biological Engineering and Computing, 52(6):539–556, 2014.
- [324] C. Wachinger et al. Registration Strategies and Similarity Measures for Three-dimensional Ultrasound Mosaicing. Academic Radiology, 15(11):1404–1415, November 2008.
- [325] T. Waffenschmidt and A. Menzel. Extremal states of energy of a double-layered thick-walled tube—application to residually stressed arteries. Journal of the mechanical behavior of biomedical materials, 29:635–654, 2014.
- [326] J. E. Wagenseil and R. P. Mecham. New insights into elastic fiber assembly. Birth Defects Research Part C: Embryo Today: Reviews, 81(4):229–240, 2007.
- [327] R. F. Wagner, S. W. Smith, J. M. Sandrik, and H. Lopez. Statistics of speckle in ultrasound b-scans. IEEE transactions on Sonics and Ultrasonics, 3:156–163, 1983.
- [328] R. Waksman, J. Legutko, J. Singh, Q. Orlando, S. Marso, T. Schloss, J. Tugaoen, J. DeVries, N. Palmer, M. Haude, et al. First: fractional flow reserve and intravascular ultrasound relationship study. Journal of the American College of Cardiology, 61(9):917–923, 2013.
- [329] B. Waller. The eccentric coronary atherosclerotic plaque: morphologic observations and clinical relevance. Clinical cardiology, 12(1):14–20, 1989.
- [330] B. F. Waller, C. M. Orr, J. D. Slack, C. A. Pinkerton, J. Van Tassel, and T. Peters. Anatomy, histology, and pathology of coronary arteries: A review relevant to new interventional and imaging techniques part i. Clinical cardiology, 15(6):451–457, 1992.
- [331] M. Walsh, E. Cunnane, J. Mulvihill, A. Akyildiz, F. Gijssen, and G. A. Holzapfel. Uniaxial tensile testing approaches for characterisation of atherosclerotic plaques. Journal of biomechanics, 47(4):793–804, 2014.

- [332] H. D. Wang, M. T. Rätsep, A. Chapman, and R. Boyd. Adventitial fibroblasts in vascular structure and function: the role of oxidative stress and beyond this review is one of a selection of papers published in a special issue on oxidative stress in health and disease. Canadian journal of physiology and pharmacology, 88(3):177–186, 2010.
- [333] J. Weber and J. Malik. Robust computation of optical flow in a multi-scale differential framework. International Journal of Computer Vision, 14(1):67–81, 1995.
- [334] J. Weickert and C. Schnrr. A theoretical framework for convex regularizers in PDE-based computation of image motion. International Journal of Computer Vision, 45(3):245–264, 2001.
- [335] J. Weickert and C. Schnrr. Variational optic flow computation with a spatio-temporal smoothness constraint. Journal of mathematical imaging and vision, 14(3):245–255, 2001.
- [336] R. T. Whitaker and X. Xue. Variable-conductance, level-set curvature for image denoising. In Image Processing, 2001. Proceedings. 2001 International Conference on, volume 3, pages 142–145. IEEE, 2001.
- [337] T. N. Wight. Vessel proteoglycans and thrombogenesis. Progress in hemostasis and thrombosis, 5:1, 1980.
- [338] J. N. Wilcox, R. Waksman, S. B. King, and N. A. Scott. The role of the adventitia in the arterial response to angioplasty: the effect of intravascular radiation. International Journal of Radiation Oncology * Biology * Physics, 36(4):789–796, 1996.
- [339] H. Wolinsky and S. Glagov. Structural basis for the static mechanical properties of the aortic media. Circulation research, 14(5):400–413, 1964.
- [340] H. Wolinsky and S. Glagov. A lamellar unit of aortic medial structure and function in mammals. Circulation research, 20(1):99–111, 1967.
- [341] H. Wolinsky and S. Glagov. A lamellar unit of aortic medial structure and function in mammals. Circulation research, 20(1):99–111, 1967.
- [342] K. Wu, H. Shu, and J.-L. Dillenseger. Region and boundary feature estimation on ultrasound images using moment invariants. Comput Meth Prog Bio, November 2013.
- [343] N. Xiao. Simulation of 3-D Blood Flow in the Full Systemic Arterial Tree and Computational Frameworks for Efficient Parameter Estimation. PhD thesis, PhD thesis, Stanford University. 98, 80, 2013.
- [344] Y. Yacoob and L. S. Davis. Temporal Multi-Scale Models for Flow and Acceleration. International Journal of Computer Vision, 32(2):147–163, September 1999.
- [345] R. Yamada, H. Okura, T. Kume, Y. Neishi, T. Kawamoto, Y. Miyamoto, K. Imai, K. Saito, A. Hayashida, and K. Yoshida. A comparison between 40MHz intravascular ultrasound iMap imaging system and integrated backscatter intravascular ultrasound. J Cardiol, 61(2):149–154, December 2012.
- [346] S. N. Yang, M. L. Burch, L. R. Tannock, S. Evanko, N. Osman, and P. J. Little. Transforming growth factor- β regulation of proteoglycan synthesis in vascular smooth muscle: Contribution to lipid binding and accelerated atherosclerosis in diabetes. Journal of diabetes, 2(4):233–242, 2010.

- [347] L. Y. Yao, C. Moody, E. Schönherr, T. N. Wight, and L. J. Sandell. Identification of the proteoglycan versican in aorta and smooth muscle cells by dna sequence analysis, in situ hybridization and immunohistochemistry. Matrix Biology, 14(3):213–225, 1994.
- [348] C. Zach, T. Pock, and H. Bischof. A Duality Based Approach for Realtime TV-L1 Optical Flow. In Pattern Recognition, pages 214–223. Springer Berlin Heidelberg, 2007.
- [349] T. Zakaria, Z. Qin, and R. L. Maurice. Optical-flow-based b-mode elastography: application in the hypertensive rat carotid. Medical Imaging, IEEE Transactions on, 29(2):570–578, 2010.
- [350] C. K. Zarins, D. P. Giddens, B. Bharadvaj, V. S. Sottiurai, R. F. Mabon, and S. Glagov. Carotid bifurcation atherosclerosis. quantitative correlation of plaque localization with flow velocity profiles and wall shear stress. Circulation research, 53(4):502–514, 1983.
- [351] P. J. Zeller and T. C. Skalak. Contribution of individual structural components in determining the zero-stress state in small arteries. Journal of vascular research, 35(1):8–17, 1998.
- [352] E. Zengin, F. Chalajour, U. M. Gehling, W. D. Ito, H. Treede, H. Lauke, J. Weil, H. Reichenspurner, N. Kilic, and S. Ergün. Vascular wall resident progenitor cells: a source for postnatal vasculogenesis. Development, 133(8):1543–1551, 2006.
- [353] J. M. P. Zerpa and A. Canelas. Efficient formulations of the material identification problem using full-field measurements. Computational Mechanics, pages 1–21, 2016.
- [354] L. Zhang et al. Side-Branch Guided Registration of Intravascular Ultrasound Pullbacks in Coronary Arteries. In MICCAI Workshop in Computing and Visualization for IntraVascular Imaging and Computer Assisted Stenting (CVII-STENT), 2014.
- [355] L. Zhang et al. Simultaneous Registration of Location and Orientation in Intravascular Ultrasound Pullbacks Pairs Via 3D Graph-Based Optimization. IEEE Trans. Med. Imag., 34(12):2550–2561, 2015.
- [356] S. Zheng and W. Jianjian. Compensation of in-plane rigid motion for in vivo intracoronary ultrasound image sequence. Computers in Biology and Medicine, 43(9):1077–85, September 2013.

Academic bibliography of the author

Published articles in scientific journals:

- Maso Talou, G. D., Larrabide, I., Blanco, P. J., Guedes Bezerra, C., Lemos, P. A. and Feijóo, R. A., *Improving cardiac phase extraction in IVUS studies by integration of gating methods*, IEEE Transactions on Biomedical Engineering 62.12 (2015): 2867-2877.
- Guedes Bezerra, C., Maso Talou, G.D., Bulant, C.A., Falco, B.D.A.A., Mariani, J., Blanco, P.J., Feijóo, R.A. and Lemos, P.A., *Three-dimensional reconstruction of coronary arteries based on the integration of intravascular ultrasound and conventional angiography*, Revista Brasileira de Cardiologia Invasiva (English Edition) 23.2 (2015): 134-138.
- Bulant, C. A., Blanco, P. J., Maso Talou, G. D., Guedes Bezerra, C., Lemos, P. A. and Feijóo, R. A., *A head-to-head comparison between CT-and IVUS-derived coronary blood flow models*, Journal of Biomechanics 51 (2016): 65-76.
- Maso Talou, G. D., Blanco, P. J., Larrabide, I., Guedes Bezerra, C., Lemos, P. A. and Feijóo, R. A., *Registration Methods for IVUS: Transversal and Longitudinal Transducer Motion Compensation*, IEEE Transactions on Biomedical Engineering 64.4 (2017): 890-903.

Published articles in proceedings:

- Maso Talou, G. D. , Larrabide, I., Lemos, P. A., Blanco, P. J., Feijóo, R. A., *Decomposition of IVUS Studies in Cardiac Phases*, Proceedings of the 1st Biomedical Signal Analysis Conference (2014), Florianopolis, Brazil.
- Maso Talou, G. D. , Blanco, P. J., Larrabide, I., Guedes Bezerra, C., Lemos, P. A., Feijóo, R. A., *Detailed reconstruction for coronary arteries integrating angiographies and IVUS studies*, XXXIV Congresso da Sociedade Brasileira de Computação (2014), Brasilia, Brazil.
- Maso Talou, G. D., Bulant, C. A., Blanco, P.J., Larrabide, I., Guedes Bezerra, C., Lemos, P.A. and Feijóo, R.A., *Detailed 3D reconstruction and geometrical characterization of the coronary arteries from IVUS+AX studies*, Congreso de Matemática Aplicada, Computacional e Industrial 5 (2015), Tandil, Argentina.
- Maso Talou, G. D., Pérez Zerpa, J. M., Blanco, P. J., Canelas, A. and Feijóo, R.A., *IVUS image conditioning for in-vivo characterization of arterial tissue*, VI International Conference on Computational Bioengineering (2015), Barcelona, Spain.

- Maso Talou, G. D., Blanco, P.J., Larrabide, I., Bezerra, C.G., Lemos, P.A. and Feijóo, R.A., *Combining Transversal and Longitudinal Registration in IVUS Studies*, International Conference on Medical Image Computing and Computer-Assisted Intervention, Springer International Publishing (2015), Munich, Germany.
- Guedes Bezerra, C., Bulant, C. A., Maso Talou, G. D., Mariani, J., Falcão, B., Pinton, F. A., Feijóo, R. A. and Lemos, P. A., *TCT-535 Coronary computed tomography angiography (CCTA) blood flow model, how we can improve it? Insights based on comparison with intravascular ultrasound (IVUS) tridimensional model*, Journal of the American College of Cardiology 68.18S (2016):B216, Washington DC, USA.
- Guedes Bezerra, C., Maso Talou, G. D., Bulant, C. A., Mariani, J., Pinton, F.A., Falco, B., Feijóo, R. A. and Lemos, P. A., *TCT-573 Head-to-head comparison between coronary computed tomography angiography (CCTA) and intravascular ultrasound (IVUS) tridimensional models: a geometric point of view*, Journal of the American College of Cardiology 68.18 (2016):B232, Washington DC, USA.